Astronomy Unit
School of Physics and Astronomy
Queen Mary University of London

Exploring The Architectures Of Planetary Systems That Form In Thermally Evolving Viscous Disc Models

Gavin Arthur Leonard Coleman

Submitted in partial fulfillment of the requirements of the Degree of Doctor of Philosophy

Declaration

I, Gavin Arthur Leonard Coleman, confirm that the research included within this thesis is my own work or that where it has been carried out in collaboration with, or supported by others, that this is duly acknowledged below and my contribution indicated. Previously published material is also acknowledged below.

I attest that I have exercised reasonable care to ensure that the work is original, and does not to the best of my knowledge break any UK law, infringe any third party's copyright or other Intellectual Property Right, or contain any confidential material.

I accept that the College has the right to use plagiarism detection software to check the electronic version of the thesis.

I confirm that this thesis has not been previously submitted for the award of a degree by this or any other university.

Signature:
Date:

All the work in this thesis has been undertaken in collaboration with my supervisor, Professor Richard Nelson. Unless otherwise stated, all simulations and figures have been completed by the author. This work was supported by an STFC PhD studentship.

Work in this thesis has been published in the following peer-reviewed papers, in collaboration with the listed authors:

Nelson, R. P., Hellary, P., Fendyke, S. M. and **Coleman, G. A. L.** (2014). *Planetary system formation in thermally evolving viscous protoplanetary discs.* Phil. Trans. R. Soc. A, 372

Coleman, G. A. L. and Nelson, R. P. (2014). *On the formation of planetary systems via oligarchic growth in thermally evolving viscous disc.* MNRAS; 445:479-499

Coleman, G. A. L. and Nelson, R. P. (2016a). *On the formation of compact planetary systems via concurrent core accretion and migration.* MNRAS; 457:2480-2500

Coleman, G. A. L. and Nelson, R. P. (2016b). *Giant planet formation in radially structured protoplanetary discs.* MNRAS; 460:2779-2795

Abstract

The diversity in observed planets and planetary systems has raised the question of whether they can be explained by a single model of planet formation or whether multiple models are required. The work presented in this thesis aims to examine the oligarchic growth scenario, to determine whether the core accretion model, where planets form bottom-up, can recreate the observed diversity. I begin by exploring how changing model parameters such as disc mass and metallicity influence the types of planetary systems that emerge. I show that rapid inward migration leads to very few planets with masses $m_{\rm p} > 10\,{\rm M}_{\oplus}$ surviving, with surviving planetary systems typically containing numerous low-mass planets. I examine what conditions are required for giant planets to form and survive migration, finding that for a planet similar to Jupiter to form and survive, it must form at an orbital radius $r_{\rm p} > 10\,{\rm au}$.

In the second project in this thesis, I update the physical models before examining whether a broader range of parameters can produce planetary systems similar to those observed. I find that compact systems of low-mass planets form in simulations if there is sufficient solid material in the disc or if planetesimals are small, thus having increased mobility. I also find that giant planets can form when the solid abundance and mobility of planetesimals are high, however they all undergo large-scale migration into the magnetospheric cavity located close to the star.

For the final project of this thesis, I examined the effects that disc radial structuring has on the formation of giant planets. I find that by including radial structures, numerous giant planets are able to form at large orbital radii and survive migration. The observed period valley between 10–100 days is also recreated, of which I attribute to disc dispersal late in the disc's lifetime.

Acknowledgements

My first acknowledgement must be my supervisor, Professor Richard Nelson. Your faith in me, and the advice you have given from your years of experience have been invaluable during my studies, and so I thank you for that.

I shall also like to thank Guillem Anglada-Escudé for the many insightful discussions throughout my time here. They have given me many new ideas in how to approach my current and future studies. I am also thankful to Guillem for allowing me the opportunity to take part in the exciting *Pale Red Dot* project.

I should also like to acknowledge my friends and workers in the SCR bar for making my stay in London be as enjoyable as possible (and also for putting up with me going on about *Pale Red Dot* so much).

My thanks also to academics and administrative staff at the school for your hard work in making the running of the department as smooth and enjoyable as possible, especially given the number of relocations and renovations that we have undergone.

Lastly I would like to thank my friends and family for their continued support and encouragement throughout my studies.

Contents

List of Figures

List of Tables

1 Introduction

1.1 Known Planets

In recent years the number of extrasolar planets, planets that orbit stars other than the Sun, has increased dramatically. The first of these extrasolar planets, or exoplanets for short, were *PSR B1257+12 b* and *c* (recently named *Draugr* and *Poltergeist* by the IAU (2015)), confirmed in 1992 through observing timing variations in the signals received from the central pulsar (Wolszczan & Frail, 1992). Three years later, the first exoplanet orbiting a main-sequence star was discovered by Mayor & Queloz (1995). This planet, *51 Pegasi b* (also known as *Dimidium*) discovered using the radial velocity technique described below, has a mass of approximately half that of Jupiter, but orbits its parent star with a period of only 4.23 days. The discovery of this planet established a new class of exoplanets, *hot Jupiters*. Over the next 10 years, a further 150 exoplanets were discovered, with the majority of these being giant planets either orbiting as hot Jupiters (Butler et al., 1997), or as long-period Jupiters (exoplanets of mass comparable to Jupiter orbiting with periods greater than 100 days) (Mayor et al., 2004). The discovery of mainly giant planets, showing little diversity in the types of planets dissimilar to that seen in the Solar System, inspired numerous missions and instruments, such as; *Corot*, *Kepler*, *HARPS*, with the aim of improving the diversity of exoplanets discovered, allowing the Solar Systems' place in the Galaxy to be put into perspective. Over the past 10 years, these missions have dramatically increased the number of exoplanets confirmed to 1629 (Han et al., 2014). *Kepler* alone has discovered 942 of these to date, thanks in part to its continued observation of a region in the constellations *Cygnus* and *Lyra* for over 3 years. A wide diversity in the properties (both orbital and physical) of these newly discovered exoplanets is now apparent, as well as a wide diversity in planetary system architectures. Diversity in exoplanet properties ranges from short period super-Earths such as *Corot-7b* (4.8 Earth masses with period 0.85 days) (Léger et al., 2009) and *Kepler-10 b* (4.55 Earth masses with period 0.84 days) (Batalha et al., 2011) to the very long period massive planets detected via direct

imaging such as *Beta Pic b* (8 Jupiter masses with semi-major axis 9 au)(Lagrange et al., 2009) and *HR 8799 b* (7 Jupiter masses with semimajor axis 67 au)(Marois et al., 2008).

1.1.1 Planetary System Architectures

It is not only important to discuss the diversity amongst exoplanets, but also the types of planetary systems they reside in. Over 63% of exoplanets discovered are found in multi-planet systems (Han et al., 2014), with *KIC 11442793* containing seven planets, the most populated planetary system known apart from the Solar System (Cabrera et al., 2014). *KIC 11442793* has been likened to a compact Solar System, with two giant planets orbiting on long periods, exterior to an inner system of five smaller planets. Not every planetary system is similar to the Solar System. Thus observing the diversity in planetary system architectures, and their respective occurrence rates is of great importance in understanding how common the Solar System is in the Galaxy. As mentioned, there is a compact analogue to the Solar System (*KIC 11442793*), but as yet, no other planetary systems hold any significant common properties to the Solar System.

Planetary systems containing hot Jupiters (*51 Pegasi* for example) were among the first to be discovered since they contain large signals for multiple detection techniques. More recently, further searches have been performed attempting to discover how lonely hot Jupiters are. Many hot Jupiter systems have been found to contain giant planets on longer periods, (e.g. *HD 187123*, Butler et al., 1998; Wright et al., 2009). However it is currently difficult to discover low-mass companions to hot Jupiters, mainly due to their signals being significantly weaker and harder to detect. Recent work however has been able to discover super-Earth and Neptune mass companions to a hot Jupiter. *Wasp-47* was originally known to contain a hot Jupiter with a 4.2 day period (Hellier et al., 2012), but more recent analysis using *HARPS* and *K2* (the successor to the *Kepler* mission (Howell et al., 2014)) has since discovered a super-Earth orbiting interior, and a hot Neptune orbiting just exterior (Becker et al., 2015), whilst a cold Jupiter in the same system was also recently discovered (Neveu-VanMalle et al., 2016).

Numerous Systems of cold Jupiters have also been discovered, again due to the strong signals they impart on observed stellar radial velocities. Systems with cold Jupiters range from containing a single cold Jupiter (e.g. *16 Cygni B*, Cochran et al., 1997), to also containing low-mass companions (e.g. *Kepler-68*, Gilliland et al., 2013), or in many cases, multiple cold Jupiters (e.g. *HR 8799*, Marois et al.,

2008). Again the planetary systems found here are by no means complete, as more planets could be found in the future when these systems are analysed with greater precision.

Another type of planetary system recently discovered by *Kepler* are low-mass compact planetary systems. *Kepler-11* is the best known of these systems where six planets, all smaller in size than Neptune, orbit their parent star with periods less than 120 days, with five of the planets having periods less than 50 days (Lissauer et al., 2011). Though the planets in these systems appear to be compact, a paucity of first order mean-motion resonances has been observed, with very few systems being in strict mean-motion resonance (Fabrycky et al., 2014). The period ratio distribution shows features in the vicinity of 2:1 and 3:2 resonances, suggesting that they have been dynamically important in the past, but some systems have been found to be in strict mean motion resonances, *Kepler-60* for example (Steffen et al., 2012). Another characteristic of some of these systems is the diversity in densities, especially those of neighbouring planets thought to have similar formation histories (Jontof-Hutter et al., 2015; Marcy et al., 2014; Wu & Lithwick, 2013), of which *Kepler-36* provides a good example where two planets orbiting close to the 7:6 resonance have dramatically different densities (Carter et al., 2012). It has also been questioned whether giant planets and compact systems are mutually exclusive or whether they can both form in tandem. Recent work has shown that long period giant planets may be present around stars with low-mass compact systems (Uehara et al., 2016).

The observed exoplanet diversity raises the question as to whether a single model of planet formation can explain the origins of these systems or whether multiple models that operate under different conditions are required. For example a model of core accretion close to the central star operating on long time-scales could explain the planets at short periods (Hubickyj et al., 2005; Pollack et al., 1996), while gravitational collapse of fragments at large orbital radii on short time-scales might explain the formation of long-period giant planets (Boss, 1997; Forgan & Rice, 2013; Stamatellos & Whitworth, 2008). Another complication for these models, is the necessity for them to explain the diversity in planetary system architectures as well as that amongst the internal composition of the planets.

A large body of related work that has used n-body simulations to examine planet formation, in the presence of a gas disc, has been published in recent years. For example, Papaloizou & Larwood (2000) examined planetary growth through planet-planet collisions using n-body simulations combined with models for migration and

eccentricity/ inclination damping. McNeil et al. (2005) and Daisaka et al. (2006) examined the effects of type I migration on terrestrial planet formation. Fogg & Nelson (2007, 2009) examined the influence of type I migration on the formation of terrestrial planets in the presence of migrating Jovian-mass planets. Terquem & Papaloizou (2007) examined the formation of hot super-Earths and Neptunes using n-body simulations combined with a prescription for type I migration, and a disc model that included an inner cavity created by the stellar magnetosphere. McNeil & Nelson (2009, 2010) performed large-scale simulations of oligarchic growth to examine the formation of systems containing multiple super-Earths and Neptune-mass planets, such as *Gliese 581* and *HD 69830*. More recently, Hellary & Nelson (2012) examined the influence of disc-induced corotation torques experienced by low mass planets on the formation of planetary systems, using simple disc models with power-law surface density and temperature profiles. Cossou et al. (2013) have examined how planet convergence zones, generated by the combined action of outwardly directed corotation torques and inwardly directed Lindblad torques, are shifted in multiple planet systems by the influence of orbital eccentricity on the strength of the corotation torque. In follow-on work, Pierens et al. (2013) have examined how corotation torques can assist in the formation of giant planet cores.

An alternative approach to simulating planet formation using n-body simulations has been planetary population synthesis modelling, as exemplified by Ida & Lin (2010); Ida et al. (2013); Miguel et al. (2011a,b); Mordasini et al. (2009, 2012). These Monte-Carlo approaches have the advantage of computational speed over n-body simulations, enabling coverage of large areas of parameter space, hence allowing statistical comparisons to be made with observations. Computational efficiency also allows sophisticated models of gaseous envelope accretion to be incorporated (e.g. Mordasini et al., 2009). One significant disadvantage associated with these Monte-Carlo approaches is that planet-planet interactions are generally neglected, although recent work has started to address this issue (Alibert et al., 2013; Ida & Lin, 2010). The medium-term trajectory of this subject area is clearly towards convergence between the population synthesis and full n-body approaches.

To begin answering the question of how observed planetary systems form, global models of planet formation that allow the formation and evolution of these systems over a large range of orbital length scales need to be constructed. In this thesis, I present the results of simulations of oligarchic growth, performed using the *Mercury-6* symplectic integrator (Chambers, 1999) that compute the dynamical evolution and collisional accretion of a system of planetary embryos and planetes-

imals. This is combined with a 1-D viscous disc model that incorporates thermal evolution through stellar irradiation, viscous dissipation and blackbody cooling. The migration of low mass planets is modelled through implementation of the torque prescriptions given by Paardekooper et al. (2011), including the effects of corotation torque saturation. Gap formation and type II migration of gap forming planets is modelled self-consistently using the impulse-approximation approach first introduced by Lin & Papaloizou (1986). The simulations also incorporate models for gas-envelope accretion, enhanced planetesimal capture by planetary atmospheres, and gas disc dispersal through photoevaporation over Myr time-scales. In chapter 3, I explore the range of model parameters including disc mass, metallicity and planetesimal radii to examine their influence on the types of planetary systems that emerge. I update the physical models and use this updated version in chapter 4 to examine whether or not the models can produce planetary systems that are similar to those that have been observed, and if so under which set of conditions (e.g. disc mass, metallicity, planetesimal/boulder sizes) do these systems form. For my third and final project presented in chapter 5, I address the question of whether or not radial structuring of a protoplanetary disc, because of spatial and temporal variations in the viscous stress, can prevent accreting giant planet cores from rapidly migrating inwards because of the 'planet traps' created by the surface density variations (Masset et al., 2006).

1.2 Detection Methods for Extrasolar planets

Before I can begin to examine the formation of planetary systems, it is important to understand the techniques, and their associated biases, that have been used in discovering the current exoplanet population. Currently there are six known methods that are used for detecting exoplanets. This section contains a short overview of these techniques, whilst a more thorough review has been published by Wright & Gaudi (2013). Figure 1.1 shows the masses and periods of currently confirmed exoplanets, where colour-coding denotes the method of discovery, whilst table 1.1 shows a quantitative comparison of the number of exoplanets discovered by each method.

1.2.1 Transit Method

If an exoplanet's orbital plane appears edge on to an observer, i.e. its inclination (the angle of the orbital plane relative to an observer), is $\sim 90^o$, then it will pass in

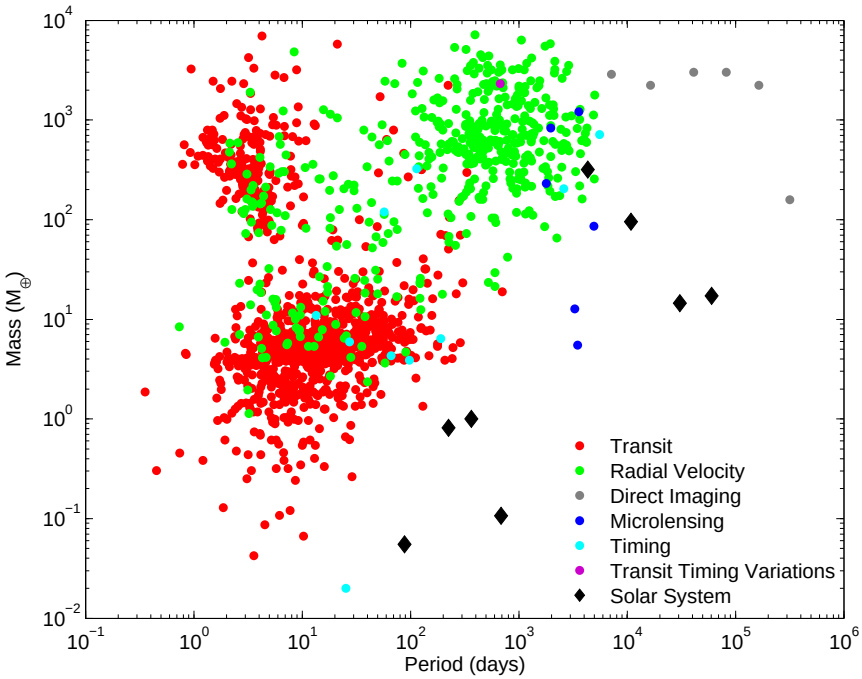

Figure 1.1: Mass versus period plot for observed planets, with different colours denoting different detection techniques. This plot was produced by the author on 21st March 2016 using data from the exoplanets.org website (Han et al., 2014)

front of its parent star causing a reduction in observed stellar flux. The likelihood of an exoplanet having an orbit that crosses the line of sight between the observer and parent star is proportional to the ratio of a star's radius and the semi-major axis of the exoplanet. Thus the probability of detection decreases the further away an exoplanet orbits its parent star, making the transit method most effective for planets orbiting close to their parent star. The reduction in observed stellar flux that an exoplanet induces is directly proportional to the ratio of cross-sectional areas from the planet to the star, given as:

$$\frac{\Delta F_*}{F_*} = \left(\frac{R_\mathrm{p}}{R_*}\right)^2 \tag{1.1}$$

Since small planets have small cross-sectional areas compared to their parent stars, they induce extremely small dips in observed fluxes. For example, a planet the size of Jupiter will cause a drop of just 1 % in the flux of a solar type star, whilst an Earth sized planet would only give rise to a 0.01% drop. The small reduction in flux caused by a transiting Earth sized planet is comparable to the cumulation of numerous systematics, such as stellar jitter. It is necessary to observe the star for multiple

Method	Planets confirmed
Transit	1124
Radial Velocity	470
Direct Imaging	8
Microlensing	16
Timing	10
Transit Timing Variations	1
Total	1629

Table 1.1: A comparison of the number of exoplanets detected by different detection methods. This table was produced by the author on 21st March 2016 using data from the exoplanets.org website (Han et al., 2014)

orbital periods of the transiting planet, as this gives a sufficient signal to noise, allowing the systematic effects to be modelled and discounted in an accurate fashion. It is also necessary to have multiple observations of the same transit signature, i.e. at different epochs, so that the orbital period of the transit signature can be interpreted accurately. Typically 3 or more transits are required for confirmation of a planet causing a reduction of $\sim 1\%$ of the stars flux, whilst even more are required when the reduction in flux caused by a transiting planet is comparable to the systematic effects. Other tests are also required to discount false positive signatures, such as eclipsing binaries or blended objects, as without the exclusion of these "detections", planetary distributions and occurrence rates would be inaccurate, affecting theories of planet formation, migration and evolution which rely on observations to test their conclusions.

Due to these reasons of probability of detection and false positive likelihood, it is necessary to continuously monitor a large number of stars for a long period of time in order to build sufficient statistics to detect potential exoplanets. For example the *Kepler* mission performed a transit survey of approximately 150,000 stars for 3.5 years in the constellations *Cygnus* and *Lyra*. With the requirement for 3 transits per signature, the exoplanet with the longest orbital period detected by *Kepler* is *KIC 11442793 h* with an orbital period of 331.6 days (Cabrera et al., 2014), though *Kepler-421 b* with an orbital period of 704.2 days has been confirmed with only 2 observed transits through statistical validation (Kipping et al., 2014). Figure 1.2 shows an example light curve from the *Kepler* mission, showing the transits for six planets orbiting *Kepler-11* (Lissauer et al., 2011), whilst transit timing variations have been analysed to obtain mass estimates for these planets.

Additional information such as the orbital eccentricity of the planet can be determined from the shape of the transit (Seager & Mallén-Ornelas, 2003), though

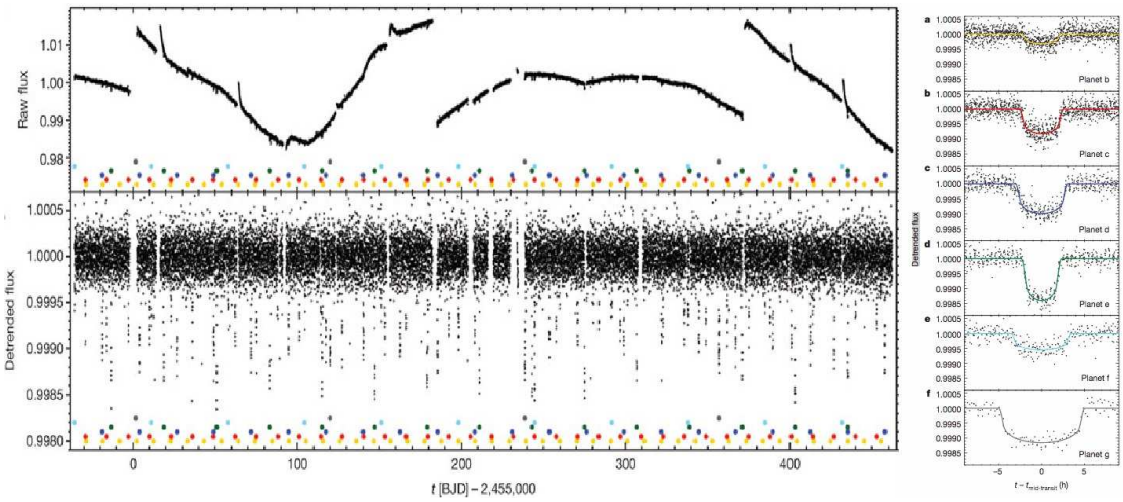

Figure 1.2: The light curve for *Kepler-11* showing 6 transiting planets (Lissauer et al., 2011).

additional effects such as limb darkening need to be taken into account (Csizmadia et al., 2013). The properties of an exoplanet's atmosphere can also be extracted when an exoplanet passes in front of its parent star, as well as when it passes behind the star, the latter known as a secondary eclipse. Firstly, as the exoplanet passes in front of the star, light from the star must pass through the exoplanet's atmosphere, where high-resolution spectroscopy can determine elements or compounds that are present in the atmosphere causing absorption lines in the stellar spectrum. Further analysis of transit ingresses/egresses can yield information about the atmosphere's structure, whilst an exoplanet's orbital inclination relative to the parent star's rotational axis can be determined through the Rossiter-McLaughlin effect (McLaughlin, 1924; Rossiter, 1924). Recently, atmospheric wind speeds have been extracted on a handful of hot Jupiters through further investigation into Rossiter-McLaughlin observations (Louden & Wheatley, 2015).

1.2.1.1 Transit Timing Variations

As the number of transiting exoplanets has dramatically increased, especially those in planetary systems containing multiple planets, it has become fruitful to analyse and determine the effect that each planet has on its neighbours. Transit timing variations are observables that show the variations in observed transit times, as well as transit durations. As planets orbit their parent star, they perturb the orbits of nearby planets, affecting their orbital periods, and thus their transit times. Analysis of these variations can yield planet masses, e.g. *Kepler-11* (Lissauer et al., 2011), or can also discover non-transiting planets such as *Kepler-419c* (Dawson et al., 2014).

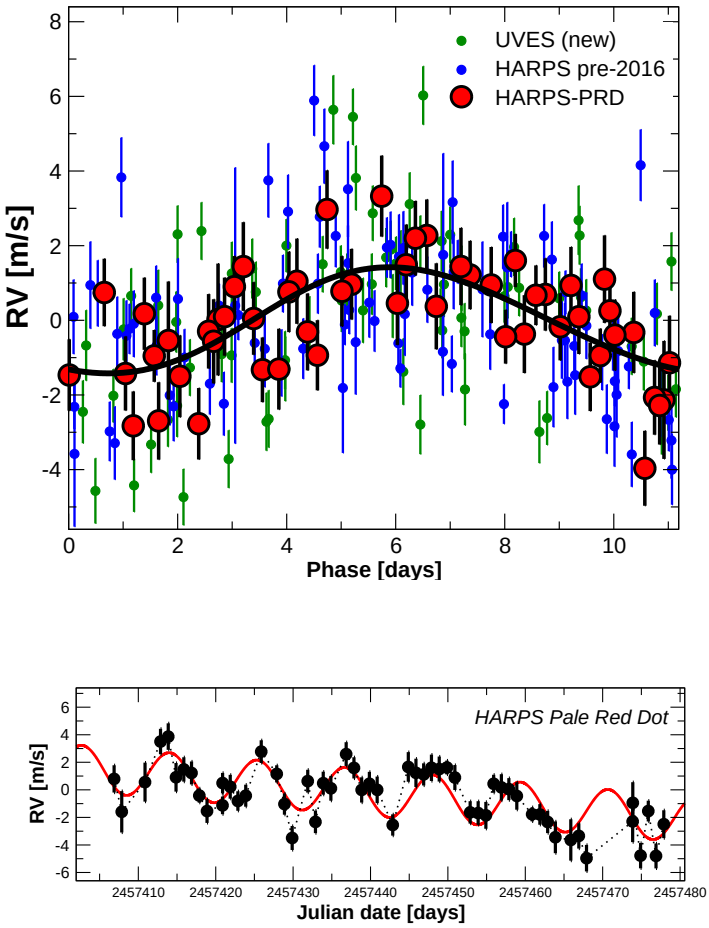

Figure 1.3: Top panel: Phase-folded radial velocity measurements centered around the expected orbital period of *Proxima b*. Bottom panel: Radial velocity measurements from the recent *Pale Red Dot* campaign Anglada-Escudé et al. (2016)

1.2.2 Radial Velocity Surveys

When planets orbit their parent star, they exert their own gravitational influence on the star, causing both the star and the planet to orbit the centre of mass of the combined system. If the orbital plane of the planet is not perfectly aligned with that of the sky, then an observer would note periodic Doppler shifting of the spectral lines in the light of the parent star due to its motion along the line of sight. This radial velocity is dependant on a number of factors in the planetary system as shown below,

$$v_{\text{radial}} = \frac{m_{\text{p}}}{M_*}\sqrt{\frac{GM_*}{r}}\sin i \tag{1.2}$$

where m_{p} is the mass of the planet, M_* is the stellar mass, and r is the radial

distance between the planet and star. As can be seen the magnitude of the radial velocity signal depends on the mass ratio between the planet and star, and their radial separation. This results in the radial velocity method being effective at finding planets that either have large masses, or are orbiting close to their parent star. Since the radial velocity measured is only a line of sight measurement, the estimated mass of the planet is only a minimum mass. The orbital period of the planet can be determined from the periodicity of the signal, since the contribution to the line of sight velocity from the planet will oscillate between positive and negative values as the star orbits the centre of mass of the system. Figure 1.3 shows the radial velocity signal from a planet (*Proxima b*) with mass $m_{\rm p}{\rm sini} \sim 1.3\,{\rm M}_{\oplus}$ and a period of ~ 11 days orbiting *Proxima Centauri* (Anglada-Escudé et al., 2016). When there are multiple planets in a system, each periodic signal can be decomposed from the radial velocity measurements, assuming that there is high enough signal to noise. Within the Solar system for example, Jupiter is responsible for Solar motion about the barycentre of 12 m/s whilst the Earth induces a reflex motion of only 0.1m/s.

There are a number of factors that affect radial velocity observations, making it more difficult to confirm a planetary signal. These include: long term stellar variability, granulation of the stellar surface, stellar flaring events, instrumentation noise, atmospheric seeing and telluric contamination. The culmination of these different factors generally result in a typical noise level of $\sim 1 - 2$m/s, making it difficult to detect Earth-like planets. Only when an extremely large number of observations are made, such that there is high signal to noise, is it possible to average out the noise and detect low-mass exoplanets.

This technique resulted in the first exoplanet discovery around a solar type star, *Pegasus 51 b* (Mayor & Queloz, 1995). Since that discovery 470 exoplanets have been discovered using this technique, allowing statistically significant occurrence rates to be formulated (Cumming et al., 2008; Santos et al., 2004).

Since radial velocity data only gives the line of sight radial velocity, the mass determination of a perturbing exoplanet depends on its orbital inclination relative to the line of sight measured from the plane of the sky. If the radial velocity data is coupled with transit detections of the same exoplanet then this degeneracy breaks, since $i \sim 90^{o}$ for a transiting exoplanet. Combination of the mass from radial velocity measurements and radius from transit measurements, yields the density of the planet, enabling conclusions about the bulk composition to be made.

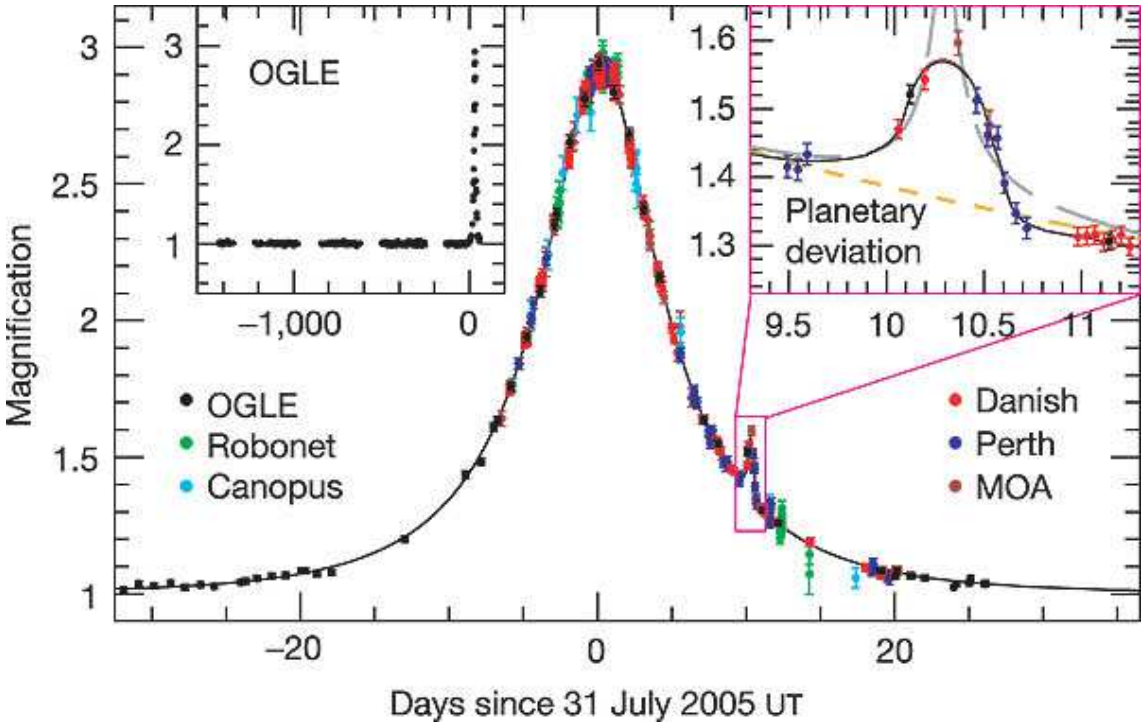

Figure 1.4: The microlensing event for planet *OGLE-05-390L b* (Beaulieu et al., 2006).

1.2.3 Microlensing

If a foreground star passes through the line of sight between an observer and a background object, the curvature of space-time due to the mass of the foreground star can create a lensing effect, distorting the image of the background object. This distortion more precisely causes the background to appear as a ring with a radius equal to the Einstein ring radius of the foreground star. As it is generally not possible to resolve the lensing event, this appears simply as an increase, then decrease, in brightness of the background object as it passes through the "lens". If a planet is orbiting the foreground lens star, and its projected separation is comparable to the Einstein ring radius, then the planet will also act as a lens, increasing the brightness of the background. An example of a microlensing event is shown in figure 1.4, where the brightness of the background object increases to a peak, determined by the mass of the foreground star and the geometry of the system, before decreasing back to its nominal brightness. The sharp spike observed $\sim$ 10 days after the peak increase in brightness is the effect of the orbiting planet *OGLE-05-390L b*, a $\sim 5.5\,M_\oplus$ super-Earth with an orbital period of $\sim$ 3500 days (Beaulieu et al., 2006).

The downside to these microlensing events is that the probability of such an event occurring is extremely small, so for proper detection and statistics, large areas of the

sky have to be continuously observed. Furthermore, microlensing events only occur once between distinct foreground and background stars, meaning no direct follow-up observations can be undertaken. However the large advantage of microlensing is the area of parameter space it is sensitive to on a mass versus period diagram. Whilst transit and radial velocity surveys are sensitive to either planets with short periods or large mass planets with long periods, microlensing can be sensitive to low mass planets on long periods, as it is only the mass of the planet and the geometry of the lens system that affects possible detection. To date, 16 exoplanets have been discovered using this technique, with these planets denoted by blue dots in figure 1.1. These discoveries are due to numerous large sky surveys such as *OGLE* or *MOA*.

1.2.4 Pulsar Timing

This method is credited as making the first exoplanet discovery in 1992, that of the planets orbiting the pulsar *PSR B1257+12* (Wolszczan & Frail, 1992). Pulsars are rapidly rotating neutron stars that emit beams of electromagnetic radiation from their magnetic poles. If the stars rotational axis is not aligned with its magnetic axis, the beams' orientation also rotates, appearing as a regular pulsating signal to a distant observer. Since the rotation rates of these stars are extremely regular, any deviation in the timings observed can be used to measure the pulsar's motion. These variations can be used to detect orbiting exoplanets similar to that described in section 1.2.2, but with extreme accuracy that even small planets of fractions of an Earth mass can be detected. To date, 10 exoplanets have been discovered using this method.

1.2.5 Astrometry

As discussed in section 1.2.2, an orbiting exoplanet will cause its parent star to orbit the centre of mass between the two objects. Whilst the radial velocity method detects this orbital signature through spectroscopy, it is also possible to detect the physical movement of the star in the sky. The detection of this astrometric wobble is possible when comparing the star's relative position compared to a stable background of fixed stars. When combined with parallax measurements that obtain the distance to the star, it is then possible to model the periodic oscillations in the star's movement, yielding masses and periods of orbiting exoplanets. Though no such detection via this method has happened yet, it is expected that *Gaia* will

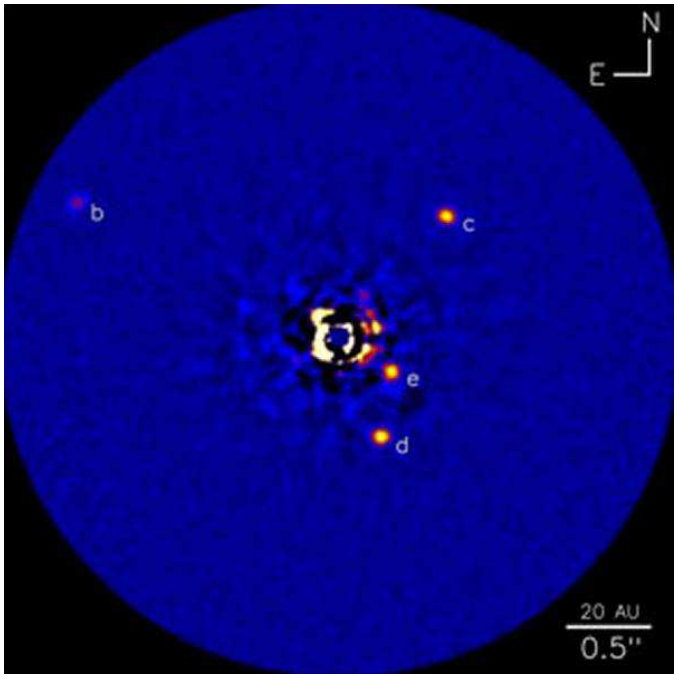

Figure 1.5: The directly imaged planets orbiting *HR 8799* (Marois et al., 2008).

detect thousands of exoplanets around Sun-like stars within 200 parsecs in the next few years (Anglada-Escudé et al., 2012; Casertano et al., 2008; Perryman et al., 2014).

1.2.6 Direct Imaging

While all other methods indirectly detect exoplanets by observing their effects on stellar fluxes, spectra or motions through the sky, direct imaging directly images the light emitted from an exoplanet. Directly imaging an exoplanet is extremely difficult however due to the overwhelming brightness of the parent star compared to that of the exoplanet, typically many orders of magnitude difference. Detection of an exoplanet is therefore easiest when the exoplanet and the star are widely separated, and when observations are performed in the infrared. This allows the brightness ratio between the star and planet to be at its smallest since exoplanets' peak thermal emission lies within the infrared. Use of a coronagraph, blocking the glare of the parent star, as well as adaptive optics also aids in detections. Currently this technique has detected 8 exoplanets with masses ranging between 0.5 and 9.5 Jupiter masses, and with periods between 20 and 1000 years. The most notable directly imaged exoplanets are those orbiting *HR 8799* (see figure 1.5), 4 exoplanets with masses between 4 and 10 Jupiter masses, and periods between 45 and 450 years (Marois et al., 2008).

1.3 Protoplantetary Discs

Before it is possible to discuss the formation and evolution of planetary systems, it is necessary to describe the formation and properties of the protoplanetary disc that planetary systems are thought to form out of.

1.3.1 Protoplanetarty Disc Formation

As a molecular cloud core collapses under its own gravity, the majority of the mass falls onto a point source forming a protostar, but a protoplanetary disc quickly forms as more distant material with higher angular momentum falls inward. As the core collapses, the disc cools down and its mass decreases as it accretes on to the star. The collapses of the core on to the disc opens a roughly spherical cavity in the surrounding envelope, evidenced by lower extinction in the mid-IR emissions than might be expected from a more centrally peaked core (Enoch et al., 2009). The system now contains a protostar surrounded by a protoplanetary disc and a surrounding envelope, and we begin to think of it as a star with a disc, a young stellar object, instead of a molecular cloud.

Young stellar objects (YSOs) fall into different classes, as described by Williams & Cieza (2011), separated by the gradient of the spectral energy distribution between about 2 and 25 μm. Class 0 YSOs are still embedded amongst a more massive envelope, and as such exhibit no optical or near-IR emission. Class I YSOs correspond to a star with a massive disc, roughly the same mass as the remaining envelope. Once the majority of the envelope has collapsed on to the star and disc, such the envelope can be thought to be virtually depleted, the star and disc are considered to be a class II YSO. The embedded class 0 and I phases last on average for ~ 0.5 Myr (Evans et al., 2009). The remaining disc in the class II stage typically has a mass equal to $\sim 1\%\mathrm{M}_*$, and is typically understood to be when planet formation occurs (though there is evidence that class I YSOs have planet formation processes in their discs). Finally class III YSOs have been observed to have negligible envelopes and low-mass, passive discs with little or no accretion on to the central protostar. The disc lifetime after the embedded phase is believed to be between 1–10 Myr (Wyatt, 2008).

From early observations of protoplanetary discs (those in the class I-III YSO stage where the envelope mass was either small or negligible), it was thought that the surface density and temperature radial profiles were smooth and could be approximated with a power law expression (Williams & Cieza, 2011). However as observing tech-

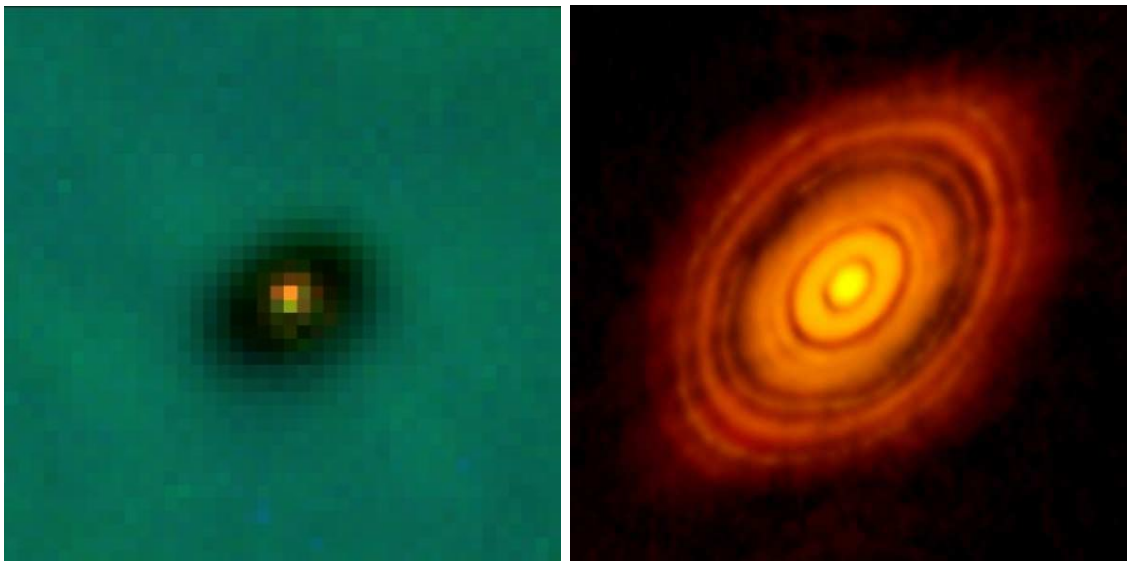

Figure 1.6: Left Panel: an image taken by the *Hubble Space Telescope* showing a young star surrounded by its disc (estimated to be 7.5 times the diameter of the Solar System) silhouetted against the background of the *Orion Nebula* (image credit: C.R. O'Dell/Rice University; NASA, news release STScI-1994-24c), Right Panel: *HL TAU* (estimated have a 100 AU radius) with radial structures observed by *ALMA* in 2014 (ALMA Partnership et al., 2015).

niques improved through the development of more sophisticated instruments and telescope arrays such as the *Atacama Large Millimeter Array (ALMA)*, it was found that protoplanetary discs are not as smooth as was initially thought. Instead, significant structuring has been observed in the form of axisymmetric rings (ALMA Partnership et al., 2015; Zhang et al., 2016). These features have been observed in both young massive protoplanetary discs (Andrews et al., 2016), and old depleted discs (ALMA Partnership et al., 2015). The right panel of figure 1.6 shows the radially structured protoplanetary disc *HL Tau*, and in chapter 5 I will explore the possible causes for this structuring before attempting to determine how they affect the types of planetary systems that form.

1.3.2 Minimum-mass Solar Nebula

In terms of the Solar system, the most recognised model of the protoplanetary disc is the Minimum Mass Solar Nebular model, or MMSN for short (Hayashi, 1981). The MMSN model estimates the original mass distribution of the protoplanetary disc that is thought to have formed the planets within the Solar System at or near their current locations. In order to construct the model, the total observed mass of heavy

elements within the Solar System was determined, along with their distributions. This determination included estimated heavy element masses for the giant and ice planets, calculated masses for the terrestrial planets, asteroids and comets, and a further estimate for the amount of dust in the Solar System. Once the total mass of heavy elements was determined, estimated as $15\,M_\oplus$, the total mass of the protoplanetary disc was then derived by assuming that its gas-to-solid ratio was equal to that found in the Sun. This yielded a total mass approximately 1.5% of a solar mass, spread out over a disc of radius $r_d \sim 40\,\text{au}$ with the following surface density profile:

$$\Sigma = 1731 \left(\frac{r}{1\,\text{au}}\right)^{-3/2} \text{g/cm}^2 \tag{1.3}$$

The associated volume density of the gas is equal to,

$$\rho(r, z) = \frac{\Sigma_g(r)}{\sqrt{2\pi}H} \exp(-z^2/H^2) \tag{1.4}$$

where H is the local disc scale height. To determine the heavy element profile, it is only necessary to multiply equation 1.3 by the solid-to-gas ratio, more commonly known as metallicity.

More recently work has been carried out to attempt to construct a model for extra-solar protoplanetary discs (Chiang & Laughlin, 2013). These models have been constructed in an attempt to explain the formation of super-Earths with small orbital periods, since the traditional MMSN model contains limited heavy element material close to the central star, insufficient to form super-Earths. However the necessity and validity of a universal minimum mass nebula is debated, since the expected mass distributions in observed multiple planet systems produce a diversity of mass profiles (Raymond & Cossou, 2014).

1.3.3 Snowline

The MMSN model outlines the protoplanetary disc's surface density profile. The model by Hayashi (1981) also includes a power law for the temperature of the gas disc:

$$T = 280 \left(\frac{r}{1\,\text{au}}\right)^{-1/2} \text{K}. \tag{1.5}$$

As can be seen, this equation allows the temperature to vary from 885 K at a distance of 0.1 au from the star, to 44 K at a much larger distance of 40 au. Within this range in temperatures, molecules and compounds are able to take different forms, depending on the local disc conditions. Generally considered to be the most impor-

tant of these compounds is water, where in the inner regions of the protoplanetary disc it is in gaseous form, whilst at larger orbital radii it is in solid form. Due to the low density and pressure within the protoplanetary disc, the liquid phase of water is not possible as there is insufficient force to contain the water molecules in a liquid form. The lack of a liquid phase results in there being only a single transition region for water molecules, known as the snowline or ice-line. At the snowline, water ice crossing into the disc interior to the snowline would sublimate into water vapour, whilst conversely water vapour crossing into the outer disc would undergo deposition, transforming directly from a gaseous to a solid phase. The various phases of water has important implications, especially in the outer regions of the protoplanetary disc where water ice is abundant. Here, as neighbouring water ice compounds coalesce they trap dust as well as other volatile compounds and gases, decreasing their overall bulk density. This freezing in of dust and volatiles into the ice enhances the surface density of solids from the nominal value of 7.1g/cm^2 interior to the snowline to 30g/cm^2 exterior, though recent results by Lodders (2003), have suggested that the ratio should instead be $\sim 2:1$ instead of $\sim 4:1$ as in the Hayashi (1981) model. Obviously there is not such a sudden switch at the snowline from one solid surface density to the another. Such a discontinuity is non-physical in nature, and as such is more likely to extend over a region surrounding the snowline, yielding a much smoother transition. It is worth noting that the fallout of this effect is observed today in asteroid belt compositions, where those in the inner asteroid belt, thought to have originated interior to the snowline, are volatile poor, whilst those that originated exterior to the snowline, now orbiting in the outer part of the belt are volatile rich (Gradie & Tedesco, 1982). It is within the protoplanetary disc, that planetesimals and protoplanets are thought to form. I will now discuss the two main avenues of planet formation: the gravitational instability model, and the core accretion model.

1.4 Planet Formation Models

1.4.1 Gravitational Instability

When protoplanetary discs are sufficiently massive, they can fragment and collapse under their own self gravity. This mechanism is thought to be the formation scenario for Brown Dwarfs and massive giant planets (Boss, 1997; Stamatellos & Whitworth, 2008). The gravitational collapse of these fragments is related to its cooling time

and the Toomre instability parameter,

$$Q = \frac{c_s \Omega}{\pi G \Sigma}, \tag{1.6}$$

where c_s is the sound speed of the gas, Ω is the local disc angular velocity and Σ is the gas surface density. Gravitational collapse of the disc occurs when $Q \leq 1$ and the cooling time, the time taken for a fragment that is hotter/cooler than its surroundings to return to equilibrium with its surroundings, $\tau_c \leq 3\Omega^{-1}$ (Gammie, 2001). In typical protoplanetary discs, the outer cooler regions are more susceptible to collapse than the inner warmer regions. Since collapse is also dependant on Σ^{-1}, it is more likely to occur in more massive discs.

Typically the gravitational instability model has been used to explain the formation of massive giant planets at large distances from their parent stars (e.g. the *HR 8799* system) (Matsuo et al., 2007), but has been unable to explain the formation of planets in the inner regions of the disc, where the fragments are unable to form due to long cooling time-scales. More recently a modified version of gravitational instability has been proposed, where tidal downsizing of inwardly migrating giant planets can reproduce the observed exoplanet statistics to some extent (Nayakshin, 2015).

1.4.2 Core Accretion

The other main branch of planet formation is the core accretion model where planets build from the bottom-up (i.e. from small dust grains into large planets).

Dust and volatile materials that have condensed out of the protoplanetary disc settle into the disc mid-plane. The settling time-scale is dependant on local disc density and temperature, the dust grain density, and the local angular velocity given as;

$$\tau_s = \frac{3\rho c_s}{4 R_{gr} \Omega^2 \rho_{gr}} \tag{1.7}$$

where ρ is the disc density, c_s is the sound speed of the gas, and R_{gr} and ρ_{gr} are the radius and density of the dust grain respectively. Typical dust settling times in typical protoplanetary discs range from $\sim 10^4$ years at 1 au, to $\sim 10^6$ years at 10 au. As these dust grains settle in the disc mid-plane, they clump together and grow through collisions (Helled et al., 2014). This continues until they become cm-sized, where coagulation of dust grains becomes inefficient since grains of this size either bounce off each other when collisional velocities are low, or fragment when collisions velocities are high. This is known as the 'bouncing barrier' (Blum & Wurm, 2008;

Kelling et al., 2014; Zsom et al., 2010) which limits the growth of grains beyond cm scales.

Once grains become large enough, they become uncoupled from the gas disc and experience aerodynamic drag, beginning to drift in towards the central star. For example, the drift of cm and m sized pebbles over the whole disc occurs on timescales of order $\sim 10^5$ years. This fast drift coupled with the inefficient growth due to the bouncing barrier makes it extremely difficult for bodies greater than 1 m to form before reaching the star at the centre of the disc. Recent studies have examined how to converge drifting pebbles and boulders in common locations. One such theory is known as the 'streaming instability' where pebbles that clump together into a dense layer accelerate the surrounding gas toward the Keplerian velocity, reducing their drift rate, since the relative velocity between the gas and pebbles becomes negligible (Johansen et al., 2007). The concentrations of these pebbles can continue to increase until they become gravitationally unstable, collapsing into larger kilometer-sized planetesimals. Collisions, mainly driven by the dispersion in radial velocities could also occur in the dense layer of pebbles, allowing the pebbles to collide and grow into larger boulders, which then undergo further collisional growth forming kilometer-sized planetesimals (Weidenschilling, 2000). As more planetesimals form in the disc, collisions between them occur, resulting in more massive planetesimals. As these collisions continue, the most massive planetesimals grow significantly faster due to gravitational focusing as their collisional cross-sections are increased by a factor of $\sqrt{1 + v_{\rm esc}^2/v_{\rm rel}^2}$, where $v_{\rm esc}$ is the escape velocity from the more massive body, and $v_{\rm rel}$ is the relative velocity of the less massive body being accreted. Once a small number of bodies become considerably more massive than the rest, such that their escape velocities dominate the average velocity in the disc, they undergo runaway growth quickly doubling their mass. Within the runaway growth regime, the doubling time is proportional to $M^{-1/3}$, and continues until the more massive planetesimals begin to stir the velocity dispersion of the remaining planetesimals in the disc, such that $v_{\rm esc} \approx v$. This regime is known as 'oligarchic growth' (Kokubo & Ida, 1998).

When large planetesimals become oligarchs, they no longer undergo runaway growth since the gravitational focusing effect is less efficient (Kokubo & Ida, 1998). In this regime the mass doubling time is proportional to $M^{1/3}$, slower than the runaway growth phase for the more massive bodies. In this regime, planetary embryos grow by accreting material in their feeding zones until they reach their isolation

masses, i.e. the feeding zones become empty. The isolation mass is given by,

$$M_{\rm iso} = \frac{(4\pi b a^2 \Sigma_{\rm s})^{3/2}}{\sqrt{3M_*}} \tag{1.8}$$

where a is the embryos location in the disc, $\Sigma_{\rm s}$ is the local solids surface density, and b is a constant defining the size of the feeding zone, typically equal to $2\sqrt{3}$. Multiple oligarchs are typically able to form in the disc, separated by a number of mutual Hill radii, typically 10.

Since the isolation mass scales as $M_{\rm iso} \sim a^3$, forming oligarchs have different masses. In regions close to the star, their masses are small, typically between a Mars and an Earth mass within the terrestrial zone. This low mass matches well with expected isolation masses that formed the precursors to the terrestrial planets in the Solar System (Chambers & Wetherill, 1998). At larger radii, this isolation mass is on the order of a few Earth masses, consistent with the expected core masses of the giant planets. Furthermore, the timescale for the formation of these oligarchs is on the order of a few million years, similar to the disc lifetime. Since these cores are able to easily form before the end of the disc lifetime, they can begin accreting gaseous envelopes. If they form early enough in the disc lifetime, they can accrete significant amounts of gas from the local disc and can undergo runaway gas accretion to become gas giants. The low hydrogen and helium content in the ice giants, Uranus and Neptune, compared to gas giants, Jupiter and Saturn, suggests that their core growth was much slower and that the gas disc had fully dissipated before they could undergo runaway gas accretion (Lissauer, 1995; Thommes et al., 2003).

The accretion of gaseous envelopes occurs once the escape velocity from the planet is greater than the sound speed of the local gas disc. Once the accreted gaseous envelope has a mass comparable to the core mass then the planet can undergo runaway gas accretion, becoming a gas giant. For low-mass planets this is a very slow process, since they have low escape velocities, resulting in negligible gaseous envelopes settling on to them over the disc lifetime. More massive cores will be able to accrete significant gaseous envelopes and undergo runaway gas accretion before the end of the disc lifetime. Pollack et al. (1996) found that a 10 Earth mass core was required for this to occur, but more recent work has found that cores with masses as low as 3 Earth masses are capable of becoming gas giants before the end of the disc lifetime if there are reductions in envelope opacity which can arise from grain growth and settling (Movshovitz et al., 2010).

The core accretion model is typically used to explain the formation of planets orbiting close to their central stars, including the terrestrial planets in the Solar

System (Chambers & Wetherill, 1998). However, it is unable to form long period giant planets (e.g. *HR 8799 b-d*) except in massive protoplanetary discs where the gravitational instability model is relevant and more effective. More recently, the accretion of pebbles on to small cores has been proposed as a formation mechanism for giant and terrestrial planets irrespective of radial location, both in the Solar System (Lambrechts et al., 2014; Levison et al., 2015a,b), and other planetary systems (Bitsch et al., 2015b; Chambers, 2014). Models of *in situ* formation have also been proposed for giant and terrestrial planets in the inner regions of the disc. In these models, planetary migration through interactions with the disc are neglected, and planets form through the accretion of material in their local vicinity arising from massively enhanced solid surface densities compared to those found in typical models of protoplanetary discs (Chatterjee & Tan, 2014, 2015; Chiang & Laughlin, 2013)

2 The Physical Model

In this section I will describe the basic physical model that was used for the simulations presented in this thesis. In the latter chapters, I include updates and additions to the physical model presented in this chapter. Those additions and updates will therefore be described in the appropriate chapter.

2.1 Disc Evolution

2.1.1 Initial Disc Profile

I initialise the gas surface density using the same power law profile expected in the MMSN model (Hayashi, 1981),

$$\Sigma_{\rm g}(r) = \Sigma_{\rm g}(1\,{\rm au}) \left(\frac{r}{1\,{\rm au}}\right)^{-1.5}, \tag{2.1}$$

where r is the radial distance from the central star and $\Sigma_{\rm g}(1\,{\rm au})$ is used to normalise the total disc mass. The temperature profile is initialised in a similar manner to the gas surface density, again using according to the MMSN model but with a power-law index of -0.5.

2.1.1.1 Snowline Enhancement

I enhance the surface density of solids beyond the snow line, taken as the radial location, $r_{\rm snow}$, where the disc temperature falls below 170 K, that being the temperature that water ice sublimates directly to water vapour, bypassing the liquid phase (Hayashi, 1981). To avoid sharp discontinuities, I transition the solids surface density to the enhanced values over a radial range of $\sim 1\,{\rm au}$,

$$\Sigma_{\rm s}(r) = \left\{\Sigma_1 + (\Sigma_2 - \Sigma_1)\left[\frac{1}{2}\left(\frac{r - r_{\rm snow}}{0.5\,{\rm au}}\right) + \frac{1}{2}\right]\right\}\left(\frac{r}{1\,{\rm au}}\right)^{-1.5} \tag{2.2}$$

I take a surface density enhancement due to the snowline as $(\Sigma_2/\Sigma_1) = 30/7.1$ as in Thommes et al. (2003).

2.1.2 Viscous Evolution

Whilst other models use an exponential decay to evolve the gas surface density over time (Cossou et al., 2014; Hellary & Nelson, 2012), I have adopted a 1-D viscous disc model for which the equilibrium temperature at each time step is calculated by balancing irradiation heating by the central star, viscous heating, and blackbody cooling. The disc surface density, Σ, is evolved by solving the standard diffusion equation

$$\frac{d\Sigma}{dt} = \frac{1}{r}\frac{d}{dr}\left[3r^{1/2}\frac{d}{dr}(\nu\Sigma r^{1/2}) - \frac{2\Lambda\Sigma r^{3/2}}{GM_*}\right] - \frac{d\Sigma_w}{dt}, \tag{2.3}$$

where ν is the disc viscosity, $d\Sigma_w/dt$ is the rate of change in surface density due to a photoevaporative wind, and Λ is the disc-planet torque that operates when a planet becomes massive enough to open a gap in the disc. The first term on the right-hand side of equation 2.3 represents the viscous diffusion of material throughout the disc. The second term represents the exchange of angular momentum between a planet that has opened a gap in the disc, and the disc material itself. The third term shows the loss of disc material due to a photoevaporative wind, where gas in the surface layers of the disc is heated to T$> 10,000$ K, giving it a thermal velocity greater than the escape velocity from the central star. The disc-planet torque per unit mass that applies for planets whose masses are large enough to open gaps is given by

$$\Lambda = \mathrm{sign}(r - r_\mathrm{p})q^2\frac{GM_*}{2r}\left(\frac{r}{|\Delta_\mathrm{p}|}\right)^4, \tag{2.4}$$

where q is the planet/star mass ratio, r_p is the planet orbital radius, and $|\Delta_\mathrm{p}| = \max(H, |r - r_\mathrm{p}|)$, where H is the local disc scale height. I use the standard α model for the disc viscosity (Shakura & Sunyaev, 1973)

$$\nu = \alpha c_\mathrm{s}^2/\Omega, \tag{2.5}$$

where c_s is the local sound speed, Ω is the angular velocity, and α is the viscosity parameter, taken to be $\alpha = 2 \times 10^{-3}$ in this thesis unless otherwise stated. I set a surface density floor of $\Sigma_\mathrm{min} = 10^{-5}\mathrm{g/cm}^2$, for computational efficiency. Protoplanetary discs generally have surface densities greater than $1\mathrm{g/cm}^2$, unless gap formation is occurring, leaving six orders of magnitude between normal disc surface densities and the minimum surface density, thus creating negligible effects on numerical simulations.

2.1.2.1 Finite Differencing Scheme

In order to computationally solve equation 2.3, I split the disc into a number of concentric rings, where I then used a finite differencing method to find new Σ values for all cells. Generally these schemes use cells of equal width, however my setup uses varied cell sizes to improve accuracy in certain regions of the protoplanetary disc, mainly the inner regions. The radial setup of my grid follows

$$r(i) = r_{\rm in} + (r_{\rm out} - r_{\rm in} + 1)\left(\frac{i-1}{N-1}\right) - 1 \tag{2.6}$$

where, $r_{\rm in}$ and $r_{\rm out}$ are the inner and outer boundaries respectively, and N is the total number of cells. This method gives a higher accuracy closer to $r_{\rm in}$ and lower accuracy near $r_{\rm out}$.

Rewriting equation 2.3 by expanding the differential and using $A = \nu\Sigma r^{1/2}$, and $B = \Lambda\Sigma r^{3/2}$, I get

$$\frac{d\Sigma}{dt} = \frac{3}{2r^{3/2}}\frac{dA}{dr} + \frac{3}{r^{1/2}}\frac{d^2A}{dr^2} - \frac{2}{rGM_*}\frac{dB}{dr} - \frac{d\Sigma_w}{dt} \tag{2.7}$$

If I now approximate the left-hand-side of this equation so that it uses finite differences instead of derivatives, it gives

$$\Sigma_{t+1} = \Sigma_t + \Delta t\left(\frac{3}{2r^{3/2}}\frac{dA}{dr} + \frac{3}{r^{1/2}}\frac{d^2A}{dr^2} - \frac{2}{rGM_*}\frac{dB}{dr} - \frac{d\Sigma_w}{dt}\right) \tag{2.8}$$

where Σ_{t+1} is the surface density at a very short time Δt after Σ_t. By using central differencing on the first two derivative terms of equation 2.8, the first derivative of A is given by

$$\frac{dA}{dr} = \frac{A_{i+1} - A_{i-1}}{dr_{i-1} + dr_i} \tag{2.9}$$

where i is the grid number. The second differential of A is given as

$$\frac{d^2A}{dr^2} = \frac{1}{dr_{i-1}}\left(\frac{dA_i}{dr_i} - \frac{dA_{i-1}}{dr_{i-1}}\right) \tag{2.10}$$

where the first derivative in this case is given as

$$\frac{dA_i}{dr} = \frac{A_{i+1} - A_i}{dr_i} \tag{2.11}$$

By expanding the second differential to include the new first derivative, yields

$$\frac{d^2A}{dr^2} = \frac{A_{i+1} - A_i}{dr_{i-1}dr_i} - \frac{A_i - A_{i-1}}{dr_{i-1}^2} \tag{2.12}$$

The two derivatives described above are the effects of viscous diffusion in the disc. The third derivative gives the effects of planet-disc interactions when planets are massive enough to exert a torque on the disc. The torque exerted on the disc is given by equation 2.4. For this derivative, upwind differencing is used instead of central differencing, where the sign of the radial velocity in the cell determines whether the differencing is upwind/downwind. The third derivative then becomes

$$\frac{dB}{dr} = \frac{B_{i+1} - B_i}{dr_i} \tag{2.13}$$

or

$$\frac{dB}{dr} = \frac{B_i - B_{i-1}}{dr_{i-1}} \tag{2.14}$$

for downwind/upwind differencing respectively.

2.1.2.2 Time step size calculation

The time step for each grid cell is calculated as the minimum between the n-body timestep (taken as $\sim 1/20^{\text{th}}$ of the innermost orbital period allowed), the timestep for a steady state disc,

$$\Delta t_{\text{steadystate,i}} = \frac{1}{10}\frac{\Delta r_i^2}{3\nu} \tag{2.15}$$

and that due to equation 2.3

$$\Delta t_{\text{diffusion,i}} = \frac{\Delta r_i}{v_{r,i}} = \frac{1}{10}\frac{\Delta r_i}{2\Lambda\sqrt{\frac{r_i}{GM_*}} - 3\frac{dA}{dr}(r_i\Sigma_i)^{-1/2}} \tag{2.16}$$

Cell time steps are calculated across the whole grid to give the final minimum timestep. The factor of a tenth in equations 2.15 and 2.16 is used to maximise the distance that gas can flow across a cell, so as to reduce numerical inaccuracies.

2.1.2.3 Boundary Conditions

The finite differencing scheme described above is sufficient for solving equation 2.3 in the central cells, however by design it will not work at the boundary cells. Therefore the change in surface density in the boundary cells has to be calculated in a different

manner. To calculate the change in the inner boundary cell, I have assumed that the flow of disc material is inwards towards the star (i.e. no disc mass can be added originating interior to the inner cell). Using this assumption the change in surface density at the inner boundary cell is equal to:

$$\Sigma_{t+1,1} = \Sigma_{t,1} + \frac{\Delta t}{dr_1}\left(v_{r,1}\Sigma_{t,1} - v_{r,2}\Sigma_{t,2}\frac{r_2}{r_1}\right) \tag{2.17}$$

where the first part of the brackets in right hand side of the equation is equal to the movement of material out of the inner cell onto the central star, and the second part is equal to the movement of material coming into the boundary cell from its neighbouring cell. Since it is not possible to use the diffusion equation to calculate the radial velocity of the inner cell, I calculate $v_{r,1}$ by

$$v_{r,1} = v_{r,2} - (v_{r,3} - v_{r,2}). \tag{2.18}$$

I limit the radial velocity of the first cell to

$$v_{r,1} = \min(v_{r,1}, 3\pi\nu_1\Sigma_1). \tag{2.19}$$

To calculate the outer boundary, I assume that the radial velocity of the outer cell is equal to 0. This leads to the calculation of the outer boundary to equal

$$\Sigma_N = \Sigma_{N-1}\frac{\nu_{N-1}}{\nu_N}\left(\frac{r_{N-1}}{r_N}\right)^{1/2}. \tag{2.20}$$

These boundary conditions were chosen to ensure the greatest numerical accuracy, ensuring that no excess mass is added into the simulation. Figure 2.1 shows the change in disc mass for a simulation using a typical $1 \times$ MMSN protoplanetary disc evolving for 10 Myr. The solid line, shows the actual change in disc mass in the calculation, and the dashed line shows the calculated change arising form material flowing out of the simulation domain at the inner and outer boundaries. As can be seen, there is a difference between the two lines, accumulating to $\sim 13\,\mathrm{M}_\oplus$ after 10 Myr, where the actual change in mass is greater than the calculated change. This means that more mass is lost from the disc than should be expected. By decreasing the timestep used, for example using a factor of a hundredth or a thousandth instead of a tenth in equations 2.15 and 2.16, the error is greatly reduced, however this greatly increases the computation time. However since the error calculated amounts to less than 0.25% over the course of the simulation, and is mostly concentrated

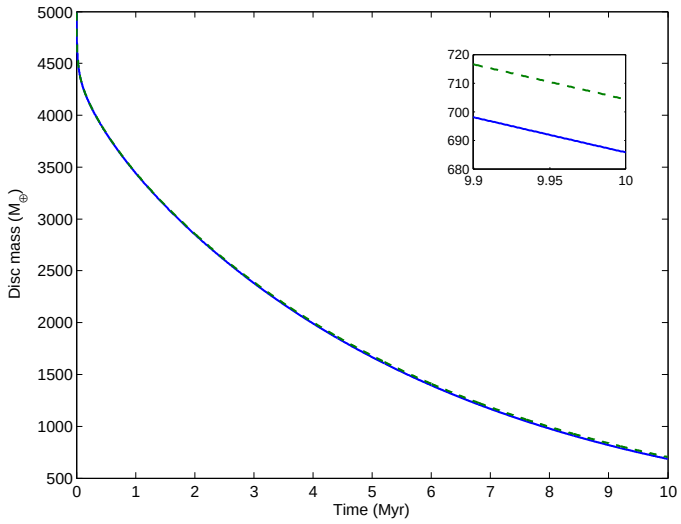

Figure 2.1: The change in disc mass of a typical simulation. The solid blue line shows the actual disc mass evolution, and the dashed green line shows the expected disc mass evolution.

near the disc boundaries, it should have negligible effects on the evolution and final outcomes of the simulations.

2.1.3 Temperature Determination

Protoplanetary discs are expected to remain in thermodynamic equilibrium, since any material that is not in equilibrium quickly returns to equilibrium due to short cooling times, typically less than a local orbital period. The temperature of the gas in the disc can therefore be determined by solving the equation for thermal equilibrium (D'Angelo & Marzari, 2012)

$$Q_{\rm irr} + Q_\nu - Q_{\rm cool} = 0, \tag{2.21}$$

where Q_ν is the viscous heating rate per unit area of the disc, $Q_{\rm irr}$ is the radiative heating rate due to the central star, and $Q_{\rm cool}$ is the radiative cooling rate. In the case of a Keplerian disc, the energy flux due to dissipation is given by Mihalas & Mihalas (1984) as

$$Q_\nu = \frac{9}{4}\nu\Sigma\Omega^2. \tag{2.22}$$

The heating rate due to stellar irradiation is given by Menou & Goodman (2004),

$$Q_{\rm irr} = 2\sigma T_{\rm irr}^4 \left(\frac{3}{8}\tau_{\rm R} + \frac{1}{2} + \frac{1}{4\tau_{\rm p}}\right)^{-1} \tag{2.23}$$

where σ is the Stefan-Boltzmann constant and $T_{\rm irr}$ is given by

$$T_{\rm irr}^4 = (T_{\rm S}^4 + T_{\rm acc}^4)(1-\epsilon)\left(\frac{R_{\rm S}}{r}\right)^2 W_{\rm G}. \tag{2.24}$$

Here, ϵ is the disc albedo (taken to be 0.5), $\tau_{\rm R}$ and $\tau_{\rm p}$ are the optical depths due to the Rosseland and Planck mean opacities, respectively (assumed to be equivalent in this thesis), $T_{\rm acc}$ is the contribution made to the irradiation temperature by accretion of gas onto the star,

$$T_{\rm acc}^4 = \frac{GM_{\rm S}\dot{M}_{\rm s}}{8\pi\sigma R_{\rm S}^3} \tag{2.25}$$

and $W_{\rm G}$ is a geometrical factor that determines the flux of radiation that is intercepted by the disc surface. This approximates to

$$W_{\rm G} = 0.4\left(\frac{R_{\rm S}}{r}\right) + \frac{2}{7}\frac{H}{r} \tag{2.26}$$

as given by D'Angelo & Marzari (2012), where H is the local disc scale height. Quantities with a subscript 'S' are the values for the central star. For disc cooling I adopt the equation given by Hubeny (1990)

$$Q_{\rm cool} = 2\sigma T^4\left(\frac{3}{8}\tau_{\rm R} + \frac{1}{2} + \frac{1}{4\tau_{\rm p}}\right)^{-1} \tag{2.27}$$

where T is the temperature of the disc midplane. To solve equation 2.21, I use Brent's method to find T, which utilises the fast-converging secant method, but reverts to the more robust bisection method when necessary (Press et al., 2007).

2.1.4 Opacities

I take the opacity, κ to be equal to the Rosseland mean opacity, with the temperature and density dependencies calculated using the formulae in Bell et al. (1997) for

temperatures below ∼3730 K, and by Bell & Lin (1994) above ∼3730 K[1]:

$$\kappa[\mathrm{cm}^2/\mathrm{g}] = \begin{cases} 10^{-4}\mathrm{T}^{2.1} & \mathrm{T} < 132\,\mathrm{K} \\ 3\mathrm{T}^{-0.01} & 132 \leq \mathrm{T} < 170\,\mathrm{K} \\ \mathrm{T}^{-1.1} & 170 \leq \mathrm{T} < 375\,\mathrm{K} \\ 5\mathrm{x}10^{4}\mathrm{T}^{-1.5} & 375 \leq \mathrm{T} < 390\,\mathrm{K} \\ 0.1\mathrm{T}^{0.7} & 390 \leq \mathrm{T} < 580\,\mathrm{K} \\ 2\mathrm{x}10^{15}\mathrm{T}^{-5.2} & 580 \leq \mathrm{T} < 680\,\mathrm{K} \\ 0.02\mathrm{T}^{0.8} & 680 \leq \mathrm{T} < 960^1\,\mathrm{K} \\ 2\mathrm{x}10^{81}\rho\mathrm{T}^{-24} & 960 \leq \mathrm{T} < 1570^1\,\mathrm{K} \\ 10^{-8}\rho^{2/3}\mathrm{T}^{3} & 1570 \leq \mathrm{T} < 3730^1\,\mathrm{K} \\ 10^{-36}\rho^{1/3}\mathrm{T}^{10} & 3730 \leq \mathrm{T} < 10000^1\,\mathrm{K} \end{cases} \tag{2.28}$$

To account for changes in the disc metallicity, I multiply the opacity by the metallicity relative to solar, since the opacity formulae in Bell & Lin (1994) and Bell et al. (1997) are for gas-to-dust ratios equal to Solar. I assume that the metallicity, dust size and solid/gas ratio remain constant throughout all simulations.

2.1.5 Photoevaporation

The absorption of UV radiation from the star by the disc can heat the disc above the local escape velocity, and hence drive a photoevaporative wind. Ultimately this photoevaporative wind is responsible for removing the final remnants of the gaseous protoplanetary disc. I adopt the formula provided by Dullemond et al. (2007) to calculate the rate at which the surface density decreases due to this wind

$$\frac{d\Sigma_w}{dt} = 1.16 \times 10^{-11} G_{\mathrm{fact}} \sqrt{f_{41}} \left(\frac{1}{r - r_{\mathrm{g}}}\right)^{3/2} \left(\frac{M_\odot}{\mathrm{au}^2\,\mathrm{yr}}\right) \tag{2.29}$$

where G_{fact} is a scaling factor defined as

$$G_{\mathrm{fact}} = \begin{cases} \left(\frac{r_{\mathrm{g}}}{r}\right)^2 e^{\frac{1}{2}\left(1-\frac{r_{\mathrm{g}}}{r}\right)} & r \leq r_{\mathrm{g}}, \\ \left(\frac{r_{\mathrm{g}}}{r}\right)^{5/2} & r > r_{\mathrm{g}}. \end{cases} \tag{2.30}$$

[1]Where the opacity is dependant on the local gas density, a density of $10^{-9}\mathrm{g/cm}^3$ is used to calculate the temperature ranges where that opacity law is appropriate.

Here, r_g is the characteristic radius beyond which gas becomes unbound from the system, which is set to 10 au in the simulations, and f_{41} is the rate at which extreme UV ionising photons are emitted by the central star in units of 10^{41} s^{-1}.

2.2 Accretion of Gaseous Envelopes

Once a protoplanet grows through mutual collisions and planetesimal accretion, it is able to accrete a gaseous envelope from the surrounding disc. To model envelope accretion, I have implemented an approximate scheme by calculating analytical fits to the results of the 1-D giant planet formation calculations presented in Movshovitz et al. (2010). Because Movshovitz et al. (2010) include the effects of grain growth and settling in their calculations, the opacity in the surface radiative zone of the atmosphere model falls well below the value appropriate to pristine interstellar grains. As a consequence, cores with masses as low as 3 Earth masses are able to accrete massive gaseous envelopes within reasonable protoplanetary disc life times (e.g. 2.7 Myr). I allow gas accretion to occur onto cores once their masses exceed 3 Earth masses in the simulations. The quality of the mass growth fits, compared to the calculations presented by Movshovitz et al. (2010), are demonstrated by figure 2 in Hellary & Nelson (2012). In units of Earth masses and Myr, this scheme gives a gas accretion rate of

$$\frac{dm_{\rm ge}}{dt} = \frac{5.5}{9.665} m_{\rm core}^{1.2} \exp\left(\frac{m_{\rm ge}}{5.5}\right) \tag{2.31}$$

This scheme allows the planet's core to continue to grow due to planetesimal accretion after a gaseous envelope has been acquired, while allowing the rate of envelope accretion to adapt to the varying core mass. This is in agreement with other studies, such as Pollack et al. (1996), that show that the rate of gas envelope accretion increases with the core mass. Furthermore, it is noted that these models also agree that gas accretion onto a planet transitions from slow settling to runaway accretion at a planet mass between 35–40 $M_\oplus$. I emphasise this latter point simply because the models that I present later in Chapter 3 have difficulty in forming significant numbers of planets that reach this runaway gas accretion mass due to the influence of migration.

Ideally, I would like to incorporate full 1-D models of gaseous envelopes in the simulations, but at present I have not developed a module for this in the code. While my adoption of fits to the Movshovitz et al. (2010) models allows gas accretion to occur at the rates prescribed in that paper, these fits do not change according to the local conditions in the disc, or according to the time varying planetesimal accretion

rate. This is something that will be addressed in future work.

The gas accretion rate given by equation 2.31 applies until the planet satisfies the gap formation criterion in section 2.3.3 (equation 2.68), after which the gas accretion rate switches to the minimum value of that obtained in equation 2.31 or the viscous supply rate

$$\frac{dm_{\rm ge}}{dt} = 3\pi\nu\Sigma_{\rm g}, \tag{2.32}$$

where $\Sigma_{\rm g}$ and ν are the gas surface density and viscosity at the disc location that is 5 planet Hill radii exterior to the planet's location. This prescription is chosen because the planet sits in a deep gap at this stage of evolution, and so the viscous supply rate of gas must be evaluated at a location in the disc that sits outside of the fully evacuated gap region. I note that the gas accretion routine is mass conservative as gas that is accreted onto the planet is removed from the disc.

2.3 Migration of Solids

Dust in protoplanetary discs is coupled to the gas. When dust grows into bodies that become weakly coupled to the gas, they begin to interact with it by exchanging angular momentum, and consequently altering their orbits. Below I discuss the different interactions that solids of different mass and size have with protoplanetary discs.

2.3.1 Aerodynamic Drag

Pebbles/boulders/planetesimals that are weakly coupled to the gas disc experience aerodynamic drag. This frictional drag force causes the objects to drift inwards toward the star as they experience a headwind from the surrounding sub-Keplerian disc. Gas drag also an efficient source of eccentricity and inclination damping, since it acts on all dimensions where there is a relative velocity between the gas and the object. In this thesis aerodynamic drag is applied to planetesimals initially through the use of Stokes' drag law (Adachi et al., 1976)

$$\mathbf{F}_{\rm st} = m_{\rm pl}\left(\frac{-3\rho_{\rm g}C_{\rm D}}{8\rho_{\rm pl}R_{\rm pl}}\right)v_{\rm rel}\mathbf{v}_{\rm rel}. \tag{2.33}$$

Here a subscript 'pl' corresponds to planetesimals, $\rho_{\rm pl}$ is the internal density of planetesimals, $R_{\rm pl}$ is the planetesimal radius, $C_{\rm D}$ is the dimensionless drag coefficient

(here taken as unity[2]), and $v_{\rm rel}$ is the relative velocity between the local gas disc and planetesimals, defined as:

$$v_{\rm rel} = v_{\rm pl} - v_{\rm K}(1-\eta) \tag{2.34}$$

where $v_{\rm pl}$ is the planetesimal velocity, $v_{\rm K}$ is the local Keplerian velocity given as

$$v_{\rm K} = \sqrt{\frac{GM_*}{r}} \tag{2.35}$$

and η is the fractional difference between the gas velocity and the local Keplerian velocity due to pressure support of the gas disc,

$$\eta = \frac{\pi}{16}(\alpha+\beta)\left(\frac{c_{\rm s}}{v_{\rm K}}\right)^2. \tag{2.36}$$

Here $c_{\rm s}$ is the local gas sound speed, whilst α and β are the exponents for power laws that can be applied to the local gas surface density and temperature respectively. Over the lifetime of the disc, planetesimals of size $\sim 1-10$km, located at 10 au will migrate inwards by less than 1 au. In chapter 4 I include an addition to the model where Epstein drag is considered for boulders/planetesimals that have $R_{\rm pl} < 9\lambda/4$, where λ is the local gas mean free path.

2.3.1.1 Atmospheric-drag-enhanced Capture Radius

Low mass protoplanets have an escape velocity that exceeds the speed of sound in the gas disc, allowing tenuous atmospheres to settle. Although these atmospheres are gravitationally negligible, they can have the important effect of increasing the planetesimal capture radius for the protoplanet through gas drag acting on bodies that have close encounters with it. This effect is modelled in this thesis by using the prescription described in section 2.5 of Inaba & Ikoma (2003). This model provides an estimate of atmospheric density as a function of radius, ρ(R). A planetesimal that passes through a protoplanet's Hill sphere at a distance $R_{\rm C}$ from the protoplanet will be captured if its physical radius is less than $R_{\rm crit}$ given by the following expression,

$$R_{\rm crit} = \frac{3}{2}\frac{v_{\rm rel}^2 + 2Gm_{\rm p}/R_{\rm C}}{v_{\rm rel}^2 + 2Gm_{\rm p}/r_{\rm H}}\frac{\rho(R_{\rm C})}{\rho_{\rm pl}}. \tag{2.37}$$

Here $\rho(R_{\rm C})$ is the local density of the protoplanet atmosphere, $\rho_{\rm pl}$ is the planetesimal internal density, $r_{\rm H}$ is the protoplanet's Hill radius, and $v_{\rm rel}$ is the relative velocity between the protoplanet and planetesimal.

[2]In chapter 4, $C_{\rm D}$ is not taken as unity, but instead as a function of the Reynolds number.

The atmosphere model in Inaba & Ikoma (2003) requires calculation of the protoplanet's luminosity. I assume that this is equal to the gravitational energy released by accreted solid material through planetesimal or protoplanet collisions

$$L_{\rm p} = \frac{G m_{\rm p}}{R_{\rm p}} \frac{dm_{\rm p}}{dt}, \tag{2.38}$$

where $R_{\rm p}$ is the radius of the protoplanet's core. The accretion rate of solids onto protoplanets is monitored to determine this accretion luminosity. Since this accretion is stochastic in nature, the accretion rate is smoothed by calculating and using the average luminosity over temporal windows of 200 local orbits, or 4000 years, whichever is smaller. Protoplanet luminosities are limited to lie in the range 10^{-9} to $10^{-4} L_{\odot}$.

The effective capture radius of a protoplanet is limited to a maximum of 1/20 of the protoplanet's Hill radius. This avoids overestimating the capture radius for larger protoplanets, as the Inaba & Ikoma (2003) model assumes the solid core is the main contributor to the gravitating mass. The transition to this limit is smoothed using the expression,

$$\begin{aligned} R_{\rm capture} = &\left[0.5 - 0.5 \tanh\left(\frac{m_{\rm p} - 30\,{\rm M}_{\oplus}}{5\,{\rm M}_{\oplus}}\right)\right] R_{\rm atmos} + \\ &\left[0.5 + 0.5 \tanh\left(\frac{m_{\rm p} - 30\,{\rm M}_{\oplus}}{5\,{\rm M}_{\oplus}}\right)\right] 0.05 r_{\rm H} \end{aligned} \tag{2.39}$$

Here $R_{\rm capture}$ is the effective capture radius and $R_{\rm atmos}$ is the atmosphere enhanced capture radius. The atmosphere enhanced capture radius is calculated by assuming that the outer edge of the atmosphere has the same properties as the surrounding disc material (i.e. same temperature and pressure), and by assuming that the atmosphere is of constant density and pressure. This last assumption is required to calculate R_{crit} as described in Inaba & Ikoma (2003), and should be valid for embedded planets as only very close to the planet's rocky surface does the atmosphere and pressure greatly increase. Ideally a full 1-D atmospheric model would be included to more accurately calculate a planetesimals trajectory as it passes through different layers of a planet's atmosphere, but this model can be computationally expensive and will be examined in future work.

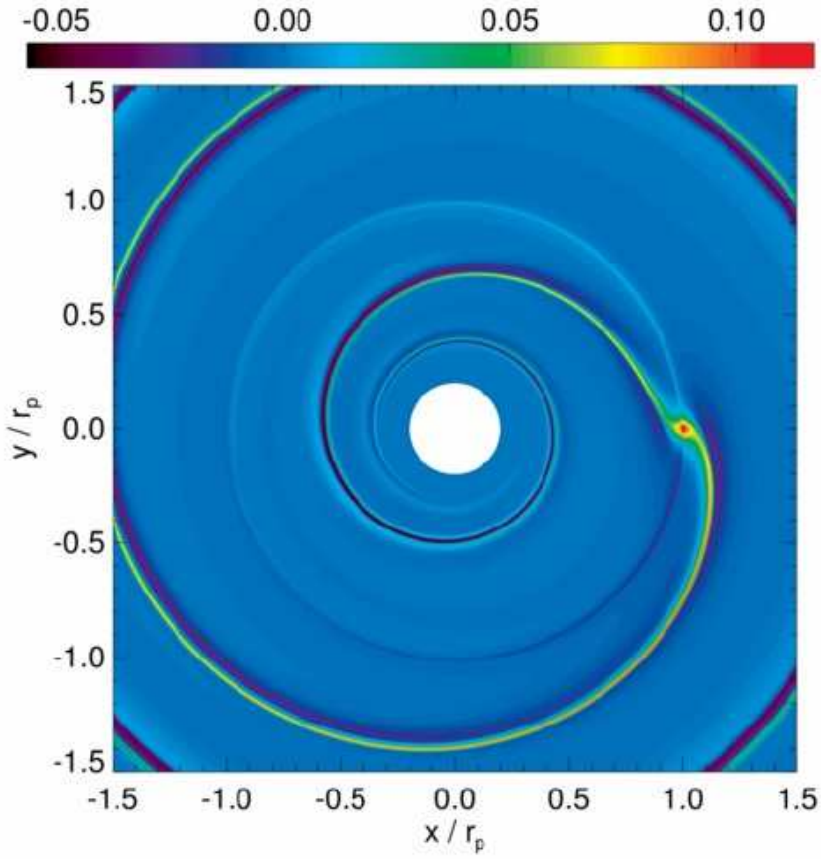

Figure 2.2: A 5 $M_\oplus$ planet embedded in a gas disc. Note spiral density wave pattern (driving Lindblad torques) and the density perturbation in the corotation region (driving corotation torques) (Baruteau et al., 2014).

2.3.2 Type I Migration

Planets that are greater than a Lunar mass begin to perturb the local gas disc. These perturbations (seen in figure 2.2 by the spiral density waves and increases/decreases in the corotation region of the planet) lead to exchanges in angular momentum between the disc and the planet, generally resulting in a net torque acting on the planet, causing it to radially migrate. The mass of the planet, along with the local disc conditions dictates the strength and direction of the net torque. Under certain conditions, such as for high-mass planets, the time-scale for the migration can be as little as 10^4 yr, but for low-mass planets, typical type I migration time-scales are 10^{5-6} yr. Below, I will describe the components that contribute to type I migration.

2.3.2.1 Lindblad Torque

When planets become massive enough, their gravity begins to exert a torque on the surrounding gas forming density waves. These density waves, shown in figure 2.2 are launched at the Lindblad resonances, both interior and exterior to the planet. This results in an exchange in angular momentum between the planet and the gas disc, exerting a torque on the planet. Torques exerted at the interior Lindblad resonances are positive due to the density wave being ahead of the planet azimuthally, pulling the planet forward in its orbit. However, torques from the exterior Lindblad resonances exert negative torques as the density wave lags behind the planet azimuthally, pulling the planet back. Generally the negative torques arising from the exterior density waves are stronger than those arising from the interior density waves, resulting in net negative torques, driving inward migration. The disparity of the interior and exterior torque strengths is due the disc being slightly sub-Keplerian which shifts the location of the Lindblad resonances so that the outer resonances lie closer to the planet.

Originally, linear analysis and perturbation theory were applied when considering the effects of Lindblad torques (Goldreich & Tremaine, 1979). In applying these equations, it was possible for migration time-scales for planets undergoing type I migration to be determined (Daisaka et al., 2006):

$$\tau_{\rm mig} = 0.23 \left(\frac{m_{\rm p}}{M_\odot}\right)^{-1} \left(\frac{\Sigma_{\rm g} r^2}{M_\odot}\right)^{-1} \left(\frac{c_{\rm s}}{r\Omega_{\rm p}}\right)^2 \Omega_{\rm p}^{-1}. \tag{2.40}$$

Without applying this equation to planet formation models, its effects can be quantitatively determined and compared to other time-scales, such as the disc lifetime. For example, if a Mars mass planet ($0.1\,\mathrm{M}_\oplus$) was embedded in a protoplanetary disc at 5 au, it would take approximately 5 million years to migrate to the central star, comparable to the lifetime of the disc. On the other hand, a $10\,\mathrm{M}_\oplus$ planet would only take 50,000 years to migrate that distance, considerably shorter than the disc lifetime. The latter example here has serious consequences for planet formation models. Planets of this mass are typically thought to be the cores of the giant planets, and if they migrate into the central star this quickly, then there is little time for them to accrete significant gaseous envelopes and become gas giants. Only by applying a reduction factor, on the order of 10-1000, was it possible for planet formation and population synthesis models to adequately recreate the observed distributions of exoplanets (Ida & Lin, 2008; Mordasini et al., 2009). The need for artificial reduction factors implied that improvements to the model were

required.

One such improvement to type I migration models was to consider that discs are non-isothermal, i.e. not a constant temperature. In considering protoplanetary discs as non-isothermal, the treatment of energy balance and transfer is more realistic, and has been shown to dramatically impact not only the net strength of type I migration, but also the net direction (Paardekooper & Mellema, 2006). This was found to be due to gradients in the local disc entropy, along with the corotation torque, discussed in section 2.3.2.2. In using non-isothermal 2-D discs Paardekooper et al. (2010) found that when applying power laws to the local disc surface density and temperature, e.g. $\Sigma_g \propto r^{-\alpha}$ and $T \propto r^{-\beta}$, the Lindblad torques departed from the linear equations previously used. This departure led to the following expression for the Lindblad torque

$$\gamma \frac{\Gamma_{\rm LB}}{\Gamma_0} = -2.5 - 1.7\beta + 0.1\alpha \tag{2.41}$$

where γ is the disc adiabatic exponent, and Γ_0 represents the normalisation of the torque,

$$\Gamma_0 = \frac{q^2}{h^2} \Sigma_{\rm p} r_{\rm p}^4 \Omega_{\rm p}^2 \tag{2.42}$$

where q is the ratio of the planet's mass to that of the central star, h is the aspect ratio of the disc, and the subscript 'p' represents that the quantity is evaluated at the planet's location.

2.3.2.2 Corotation Torque

Disc material that has a similar orbital radius to a planet will librate along horseshoe orbits relative to the planet. Goldreich & Tremaine (1979) also used linear analysis and perturbation theory to derive expressions for this so called 'linear corotation torque', showing that the torque exerted on to the planet scaled with the local vortensity gradients. It was shown, however, that for typical disc surface density profiles, the linear corotation torque is dominated by the Lindblad torque (Tanaka et al., 2002). More recently, (Paardekooper et al., 2010) derived an expression for the linear corotation torque;

$$\gamma \frac{\Gamma_{\rm c,lin}}{\Gamma_0} = 0.7 \left(\frac{3}{2} - \alpha - \frac{2\xi}{\gamma} \right) + 2.2\xi, \tag{2.43}$$

where $\xi = \beta - \alpha(\gamma - 1)$ is the exponent of the local entropy gradient.

An alternative approach in considering material in the corotation region was de-

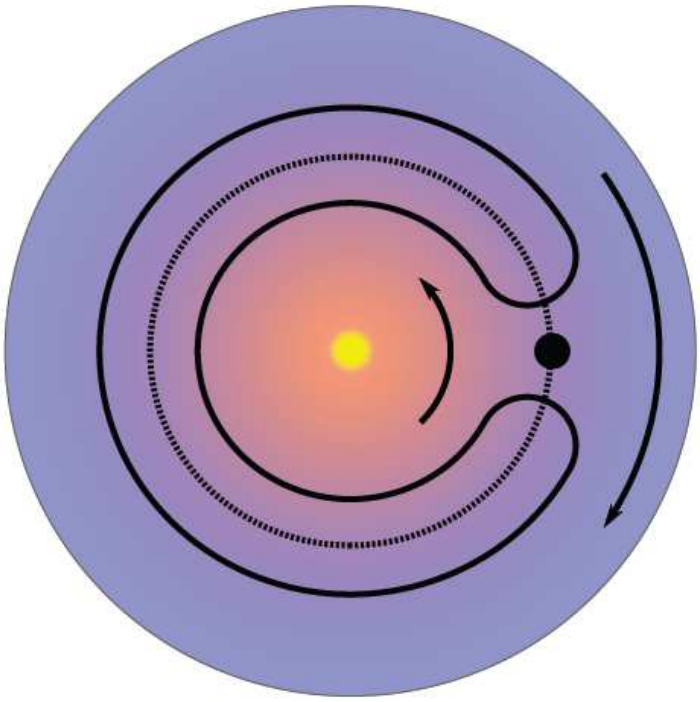

Figure 2.3: An example protoplanetary disc showing the orbit of material located in the corotation region of a planet. When material ahead of the planet undergoes a horseshoe turn, it moves from a slower-rotating cold outer disc into a faster-rotating hot inner disc, and vice versa for material behind the planet.

veloped by Ward (1991). They considered that disc material that is co-orbital with a planet will librate along horseshoe trajectories, moving from the inner to the outer disc, and vice versa, when encountering the planet, such as those shown in figure 2.3. These orbits are missing in linear theory where horseshoe turns do not exist. When there is an asymmetry between the exchanges of disc material from the outer to the inner disc on one side and from the inner to the outer disc on the other, there is a resultant torque acting on to the planet. This torque is known as the 'vortensity-related horseshoe drag', as local vortensity gradients create the asymmetries required. Since this torque has the same physical effect as the linear corotation torque, it was long unclear which expressions should be used. The relationship between the linear theory and horseshoe drag was shown by Paardekooper & Papaloizou (2009a,b) that whenever horseshoe turns occur, the linear corotation torque is replaced by the horseshoe drag, except when significant viscosities were present.

Another contribution to the non-linear corotation torque exists in adiabatic discs where entropy is conserved. This 'entropy-related corotation torque' causes an in-

crease in density of disc material that moves from a cool exterior disc to a warmer interior disc, and a decrease in density conversely.

These changes in local disc density maintain hydrostatic equilibrium in the disc (Baruteau & Masset, 2008; Paardekooper & Mellema, 2006; Paardekooper & Papaloizou, 2008). The localised regions of high density ahead of the planet, where cold disc material moves into a warmer environment as it encounters the planet, causes the planet to experience a positive torque, enabling the planet to migrate outwards.

Paardekooper et al. (2010) determined the following expressions for the full, non-linear horseshoe drag acting on a planet in a disc with surface density and temperature profiles, $\Sigma_g \propto r^{-\alpha}$ and $T \propto r^{-\beta}$;

$$\gamma \frac{\Gamma_{c,\mathrm{VHS}}}{\Gamma_0} = 1.1 \left(\frac{3}{2} - \alpha \right), \tag{2.44}$$

and

$$\gamma \frac{\Gamma_{c,\mathrm{EHS}}}{\Gamma_0} = 7.9 \frac{\xi}{\gamma}, \tag{2.45}$$

where ξ is the entropy exponent given above, and the equation 2.44 represents the vortensity–related corotation torque and the equation 2.45 represents the entropy–related corotation torque.

The expressions for the corotation torque described above only apply for inviscid discs. However, in an inviscid disc, the corotation region only has a finite reservoir of angular momentum that will eventually become depleted when exchanged with the planet on the horseshoe turns, flattening the vortensity and entropy gradients. When this occurs the corotation torque saturates, and is no longer applicable. In a viscous disc, the disc is continually evolving, maintaining vortensity and entropy gradients in the horseshoe region through the viscous and thermal diffusion of the disc. Paardekooper et al. (2011) examined the corotation torque in viscous discs, finding that a number of factors should be applied to the different components of the inviscid corotation torque to account for the viscous and thermal diffusion of the disc. They found that the corotation torque is strongest when the viscous and thermal diffusion time-scales of material crossing the horseshoe region, are roughly equal to half the horseshoe libration time, where

$$\tau_{\mathrm{lib}} = \frac{8\pi}{3\Omega_p x_s}, \tag{2.46}$$

is the horseshoe libration time,

$$\tau_\nu = \frac{x_\mathrm{s}^2 a_\mathrm{p}^2}{\nu}, \tag{2.47}$$

is the viscous diffusion time-scale, and

$$\tau_\mathrm{d} = \frac{x_\mathrm{s}^2 a_\mathrm{p}^2}{\mathrm{D}}, \tag{2.48}$$

is the thermal diffusion time-scale. The horseshoe width is given by x_s in the above equations, ν and D are the viscous and thermal diffusion coefficients, and any variable with subscript 'p' is calculated at the planet's radial location.

In following Paardekooper et al. (2011) I define two parameters that calculate the ratios between the viscous and thermal diffusion time-scales and the horseshoe libration time-scale:

$$p_\nu = \frac{2}{3}\sqrt{\frac{a_\mathrm{p}^2 \Omega x_\mathrm{s}^3}{2\pi\nu}}, \tag{2.49}$$

being the viscous diffusion parameter, and

$$p_\mathrm{d} = \frac{2}{3}\sqrt{\frac{a_\mathrm{p}^2 \Omega x_\mathrm{s}^3}{2\pi D}}, \tag{2.50}$$

being the thermal diffusion parameter. These parameters are then used to define the following factors that are applied to the components of the corotation torque (Paardekooper et al., 2011). The factors relating to the viscous diffusion parameter are as follows:

$$F_\nu = \frac{1}{1 + (p_\nu/1.3)^2}, \tag{2.51}$$

$$G_\nu = \begin{cases} \dfrac{16}{25}\left(\dfrac{45\pi}{8}\right)^{3/4} p_\nu^{3/2} & \text{if } p_\nu < \sqrt{8/45\pi)} \\ 1 - \dfrac{9}{25}\left(\dfrac{8}{45\pi}\right)^{4/3} p_\nu^{-8/3} & \text{if } p_\nu \geq \sqrt{8/45\pi)} \end{cases}, \tag{2.52}$$

$$K_\nu = \begin{cases} \dfrac{16}{25}\left(\dfrac{45\pi}{28}\right)^{3/4} p_\nu^{3/2} & \text{if } p_\nu < \sqrt{28/45\pi)} \\ 1 - \dfrac{9}{25}\left(\dfrac{28}{45\pi}\right)^{4/3} p_\nu^{-8/3} & \text{if } p_\nu \geq \sqrt{28/45\pi)} \end{cases}, \tag{2.53}$$

whilst the factors relating to the thermal diffusion parameter are:

$$F_\mathrm{d} = \frac{1}{1 + (p_\mathrm{d}/1.3)^2}, \tag{2.54}$$

$$G_{\rm d} = \begin{cases} \frac{16}{25}\left(\frac{45\pi}{8}\right)^{3/4} p_{\rm d}^{3/2} & \text{if } p_{\rm d} < \sqrt{8/45\pi)} \\ 1 - \frac{9}{25}\left(\frac{8}{45\pi}\right)^{4/3} p_{\rm d}^{-8/3} & \text{if } p_{\rm d} \geq \sqrt{8/45\pi)} \end{cases}, \tag{2.55}$$

$$K_{\rm d} = \begin{cases} \frac{16}{25}\left(\frac{45\pi}{28}\right)^{3/4} p_{\rm d}^{3/2} & \text{if } p_{\rm d} < \sqrt{28/45\pi)} \\ 1 - \frac{9}{25}\left(\frac{28}{45\pi}\right)^{4/3} p_{\rm d}^{-8/3} & \text{if } p_{\rm d} \geq \sqrt{28/45\pi)} \end{cases}. \tag{2.56}$$

In following Paardekooper et al. (2011) and combining these factors, with equations 2.43, 2.44, 2.45 and the equation for the Lindblad torque, equation 2.41, I obtain an expression for the total type I migration torque acting on a planet,

$$\begin{aligned} \Gamma_{\rm I,total} = \Gamma_{\rm LB} + \Gamma_{\rm VHS} F_\nu G_\nu + \Gamma_{\rm EHS} + F_\nu F_{\rm d}\sqrt{G_\nu G_{\rm d}} + \\ \Gamma_{\rm v-lin}(1 - K_\nu) + \Gamma_{\rm e-lin}\sqrt{(1 - K_\nu)(1 - K_{\rm d})}, \end{aligned} \tag{2.57}$$

where $\Gamma_{\rm v-lin} = 0.7(3/2 - \alpha)$, the first two terms of equation 2.43, and $\Gamma_{\rm e-lin} = 1.4\xi/\gamma + 2.2\xi$, the last two terms of equation 2.43.

2.3.2.3 Eccentricity and inclination attenuation

The total type I migration torque described in equation 2.57 is valid for planets with zero eccentricities, i.e. on circular orbits. However, planets embedded in protoplanetary discs are rarely on circular orbits. Interactions with over-dense regions of disc material, planet-planet interactions, are but a few sources that can excite planetary eccentricities. To this effect, it is necessary when calculating the torque exerted on a planet, to take into account the planet's eccentricity since the planet can undergo significant radial excursions, interacting more significantly with disc material contributing to either the Lindblad or the corotation torques. Bitsch & Kley (2010) examined the effect that a planet's eccentricity had on it's evolution, finding that depending on the planet's mass and eccentricity, the corotation torque can be heavily attenuated. More recently Fendyke & Nelson (2014) conducted 2-D hydrodynamical simulations of embedded eccentric low-mass planets, finding that the ratio between the planet's eccentricity 'e' and the local disc aspect ratio 'h' determined the reduction of the corotation torque.

A similar reduction in the total torque is found for inclined planets, since these planets spend significant portions of their orbit above/below the disc midplane, where the largest gas densities are found. In doing so, not only will they experience significantly reduced torques, but their horseshoe regions are likely to become

deformed.

To account for these reductions in the total type I migration torque, equation 2.57 becomes

$$\begin{aligned}\Gamma_{\rm I,total} = F_{\rm LB}\Gamma_{\rm LB} + \Big\{\Gamma_{\rm VHS}F_\nu G_\nu + \Gamma_{\rm EHS} + F_\nu F_{\rm d}\sqrt{G_\nu G_{\rm d}} + \\ \Gamma_{\rm v-lin}(1-K_\nu) + \Gamma_{\rm e-lin}\sqrt{(1-K_\nu)(1-K_{\rm d})}\Big\} F_{\rm e}F_{\rm i},\end{aligned} \tag{2.58}$$

where $F_{\rm LB}$ is the reduction factor for the Lindblad torque given by Cresswell & Nelson (2008)

$$F_{\rm LB} = \left[P_{\rm e} + \left(\frac{P_{\rm e}}{|P_{\rm e}|}\right) \times \left\{0.07\left(\frac{i}{h}\right) + 0.085\left(\frac{i}{h}\right)^4 - 0.08\left(\frac{e}{h}\right)\left(\frac{i}{h}\right)^2\right\}\right]^{-1} \tag{2.59}$$

where $P_{\rm e}$ is defined as

$$P_{\rm e} = \frac{1 + \left(\frac{e}{2.25h}\right)^{1/2} + \left(\frac{e}{2.84h}\right)^6}{1 - \left(\frac{e}{2.02h}\right)^4}. \tag{2.60}$$

$F_{\rm e}$ is the eccentricity reduction given by Fendyke & Nelson (2014)

$$F_{\rm e} = \exp\left(-\frac{e}{e_{\rm f}}\right), \tag{2.61}$$

where e is the planet's eccentricity, and $e_{\rm f}$ is defined as

$$e_{\rm f} = h/2 + 0.01. \tag{2.62}$$

The final reduction factor, $F_{\rm i}$ accounts for the effect of inclined planets on the corotation torque, and I define as

$$F_{\rm i} = 1 - \tanh(i/h), \tag{2.63}$$

where i is the inclination of the planet.

2.3.2.4 Eccentricity and inclination damping

In addition to experiencing migration through interactions with components of the gas disc, planets also undergo eccentricity and inclination damping. To damp ec-

centricities I use a simple time-scale damping formula, given as

$$F_{\mathrm{edamp,r}} = -\frac{v_{\mathrm{r}}}{t_{\mathrm{edamp}}},\ F_{\mathrm{edamp},\theta} = -\frac{-0.5(v_\theta - v_{\mathrm{K}})}{t_{\mathrm{edamp}}} \tag{2.64}$$

where

$$t_{\mathrm{edamp}} = \frac{t_{\mathrm{wave}}}{0.78} \times \left[1 - 0.14\left(\frac{e}{h}\right)^2 + 0.06\left(\frac{e}{h}\right)^3 + 0.18\left(\frac{e}{h}\right)\left(\frac{i}{h}\right)^2\right], \tag{2.65}$$

where t_{wave} is specified as

$$t_{\mathrm{wave}} = \left(\frac{m_{\mathrm{p}}}{M_\odot}\right)^{-1}\left(\frac{a_{\mathrm{p}}\Omega_{\mathrm{p}}}{c_{\mathrm{s}}}\right)^{-4}\left(\frac{\Sigma_{\mathrm{p}}a_{\mathrm{p}}^2}{M_\odot}\right)^{-1}\Omega_{\mathrm{p}}^{-1}. \tag{2.66}$$

I damp planet inclinations by using the prescription given in Daisaka et al. (2006), as adapted by Cresswell & Nelson (2008):

$$F_{\mathrm{idamp,z}} = \frac{0.544}{t_{\mathrm{wave}}}(2A_{\mathrm{cz}}v_{\mathrm{z}} + A_{\mathrm{sz}}z\Omega_p) \times \left[1 - 0.3\left(\frac{i}{h}\right)^2 + 0.24\left(\frac{i}{h}\right)^3 + 0.14\left(\frac{i}{h}\right)\left(\frac{e}{h}\right)^2\right]^{-1} \tag{2.67}$$

where $A_{\mathrm{cz}} = -1.088$ and $A_{\mathrm{sz}} = -0.871$.

2.3.3 Type II Migration

Where section 2.3.2 described the migration of embedded low-mass planets that have little influence on the structure of the disc, they do not apply when the disc is significantly altered by planetary torques. Torques exerted on the disc from low-mass planets are transported away from the planet along linear density waves, and as such do not significantly affect the structure of the disc. However for more massive planets, the density wave acts as a shock wave that deposits its angular momentum in the disc locally, altering the disc structure (Lin & Papaloizou, 1986) The planet begins to carve an annular gap centered on its orbital radius, until such a point that the viscous forces balance planetary torques, resulting in edges to the newly formed gap (see figure 2.4). More recent work by Crida et al. (2006), showed that not only viscous forces worked to balance planetary torques, but pressure forces arising from density waves launched by the planet assisted by transporting some of the gravitational torque away from the planet. In balancing viscous and pressure forces with gravitational torques, Crida et al. (2006) showed that a gap can be opened in

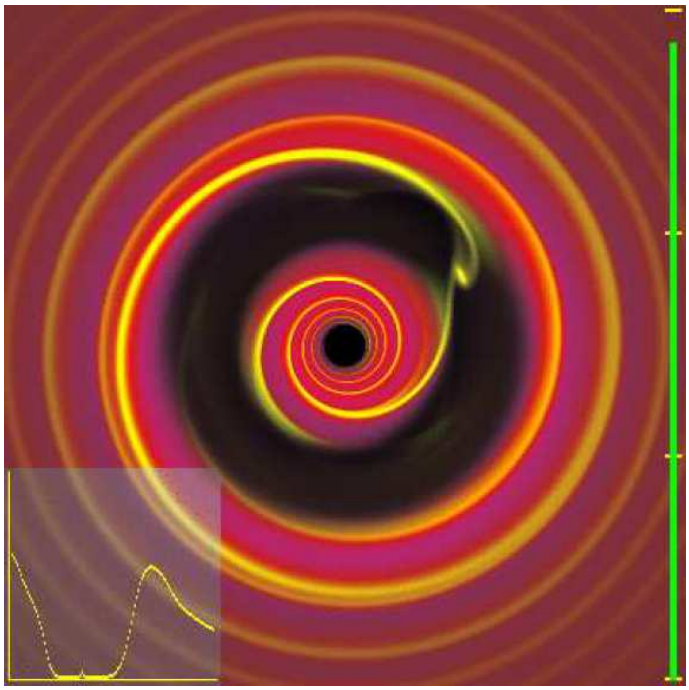

Figure 2.4: A giant planet opening a gap in a protoplanetary disc and undergoing type II migration (Armitage & Rice, 2005).

the disc when the following condition is satisfied

$$\frac{3}{4}\frac{H}{r_{\rm H}} + \frac{50}{qR} \leq 1, \tag{2.68}$$

where $r_{\rm H} = r_{\rm p}(q/3)^{1/3}$ is the planet's Hill radius, q is the planet/star mass ratio, and $R = r_{\rm p}^2\Omega_{\rm p}/\nu$ is the Reynolds number of the disc at the planet's location. Since I use a standard alpha model for disc viscosity where $\nu = \alpha H^2\Omega$ (Shakura & Sunyaev, 1973, equation 2.5), the gap-opening criterion reduces to

$$\frac{1.08h}{q^{1/3}} + \frac{50\alpha h^2}{q} \leq 1 \tag{2.69}$$

where h is equal to H/r. In typical scenarios of protoplanetary discs, the planet mass required to satisfy this criterion is on the order $m_{\rm p} \sim 100\,{\rm M}_\oplus$, but in regions of the disc close to the star, where the disc aspect ratio is small, Neptune mass planets ($m_{\rm p} \sim 20\,{\rm M}_\oplus$) are capable of opening a gap.

Since the planet exchanges angular momentum with the disc to open a gap, it receives torques from the disc forcing it to migrate when the interior and exterior torques are unbalanced. The total torque per unit mass acting on the planet is equal

to

$$\Gamma_{\rm II} = -\frac{2\pi}{m_{\rm p}} \int_{r_{\rm in}}^{r_{\rm out}} r\Lambda\Sigma_{\rm g} dr, \tag{2.70}$$

where Λ represents the disc-planet torques at individual locations:

$$\Lambda = {\rm sign}(r - r_{\rm p}) q^2 \frac{GM_*}{2r} \left(\frac{r}{|\Delta_{\rm p}|} \right)^4, \tag{2.71}$$

where $r_{\rm p}$ is the planet orbital radius, and $|\Delta_{\rm p}| = \max(H, |r - r_{\rm p}|)$. The direction of the planet's migration depends on the imbalance in torques acting from the interior and exterior gas discs. If greater torques originate from the gas disc interior to the planet, then the direction will be outwards, and naturally vice-versa when the torques from the exterior gas disc are stronger. Generally, type II migration acts to migrate the planet inwards towards the star, since viscous evolution of the disc tends to drive gas inwards, resulting in a depleting inner gas disc through accretion on to the central star, and a gas pile up in the outer disc at the outer gap edge. The typical time-scales for type II migration are therefore similar to the disc's viscous time-scale, $\tau_\nu = r_{\rm p}^2/3\nu$. For example, a Jupiter mass planet orbiting at 5 au in a typical protoplanetary disc, has a migration time of ~500,000 years.

To damp eccentricities and inclinations of planets undergoing type II migration, I implement the radial component of equation 2.64, and use a similar expression for inclination damping, where $v_{\rm r}$ is replaced by $v_{\rm inc}$. I use a damping time-scale of 10 local orbital periods.

2.3.3.1 Transition between type I and type II Migration

I transition smoothly between type I and type II migration by using the expression

$$\Gamma_{\rm eff} = \Gamma_{\rm II} f_{\rm trans} + \Gamma_{\rm I}(1 - f_{\rm trans}) \tag{2.72}$$

where $\Gamma_{\rm eff}$ is the torque applied during the transition, $\Gamma_{\rm I}$ is the type I torque and $\Gamma_{\rm II}$ is the type II torque. The transition function, $f_{\rm trans}$, is given by

$$f_{\rm trans} = 0.5 + 0.5 \tanh \left(\frac{m_{\rm p} - m_{\rm switch}}{1.5\,{\rm M}_\oplus} \right) \tag{2.73}$$

where $m_{\rm switch}$ is the planet mass that corresponds to the gap opening criterion (equation 2.68).

3 Formation of Planetary Systems via Oligarchic Growth

In this chapter I will present work that was published in the Monthly Notices of the Royal Astronomical Society (Coleman & Nelson, 2014), and as such this chapter closely follows that paper.

As discussed in chapter 1, the formation of planetary systems remains uncertain. A vast diversity in planets and planetary system architectures has led to the question of whether these diversities can be fully explained by a particular model of planet formation, or whether different models are required to explain the different architectures. The aim of the work presented in this chapter is to examine the types of planetary systems that emerge from the oligarchic growth of planetary embryos embedded in a gaseous protoplanetary disc, using the most up-to-date descriptions of migration and other processes such as gas accretion onto planetary cores. To begin answering this question, global models of planet formation that allows the formation and evolution of these systems over a large range of orbital-scales need to be constructed. I present here the results of simulations of oligarchic growth using the *Mercury-6* symplectic integrator (Chambers, 1999) that compute the dynamical evolution and collisional accretion of a system of planetary embryos and planetesimals. This is combined with a 1-D viscous disc model that incorporates thermal evolution through stellar irradiation, viscous heating and blackbody cooling. The simulations also incorporate models for planet migration, gas-envelope accretion, enhanced planetesimal capture by planetary atmospheres, and gas disc dispersal through photoevaporation over Myr time-scales. I explore a range of model parameters including disc mass, metallicity, and planetesimal radii to examine their influence on the types of planetary systems that emerge.

The work presented in this chapter uses the physical models described in chapter 2 and is presented as follows. I present the initial conditions for the simulations in section 3.1 and simulation results in section 3.2. The results are compared with observations in section 3.3. In section 3.4, I present an analysis of the conditions required for giant planet survival, and in section 3.5 I conclude the chapter.

Parameter	Value
Disc inner boundary	0.1 au
Planet inner boundary	0.1 au
Disc outer boundary	40 au
Number of cells	1000
$\Sigma_g(1\text{ au})$	1731 g cm^{-2}
Stellar Mass	$1\text{M}_\odot$
R_S	$2\text{R}_\odot$
T_S	4280 K
f_{41}	10

Table 3.1: Disc and stellar model parameters

3.1 Initial Simulation Conditions

The simulations were performed using the *Mercury-6* symplectic integrator (Chambers, 1999), adapted to include the physics discussed in chapter 2. In order to account for the total disc life time in all runs, the simulations were run until no protoplanets remained, or for 10 Myr.

All simulations were initiated with 36 planetary embryos, each of mass $0.3\,\text{M}_\oplus$, separated by 10 mutual Hill radii, and with semi-major axes lying between $1 - 20$ au. These were augmented by thousands of planetesimals, that were distributed in the same semi-major axis interval, with masses equal to $0.03\,\text{M}_\oplus$ and physical radii equal to either 1 or 10 km (ensuring that they experience appropriate accelerations due to the gas drag forces).

Eccentricities and inclinations for protoplanets and planetesimals were randomised according to a Rayleigh distribution, with scale parameters $e_0 = 0.01$ and $i_0 = 0.25°$, respectively. I ignore the effects of turbulent density fluctuations in the disc on the orbital evolution of embedded bodies, as I anticipate that the region of the disc that I simulate will sustain a significant dead zone, with only the innermost ~ 0.1 au of the disc supporting fully developed turbulence (Desch & Turner, 2015; Umebayashi & Nakano, 1988). The initial surface density of solids follows the same profile as the gas, but with an enhancement at and beyond the snowline, similar to the approach used in Hellary & Nelson (2012).

Collisions between protoplanets and other protoplanets or planetesimals were treated as being completely inelastic. A collision results in a single body containing all of the colliding mass. Planetesimal-planetesimal interactions and collisions were not considered in the simulations for reasons of computational speed, and this is one omission from the model that may have a significant influence on the simulation re-

Simulation	Disc mass (MMSN)	Metallicity (solar value)	Planetesimal radius (km)	Formation modes (A/B)
S111 A/B	1	1	1	LPG / LPG
S1110 A/B	1	1	10	LPG / LPG
S121 A/B	1	2	1	KN / KN
S1210 A/B	1	2	10	KN / KN,LFS
S211 A/B	2	1	1	KN,LFS / KN
S2110 A/B	2	1	10	KN / KN
S221 A/B	2	2	1	KN,KG / KN,KG
S2210 A/B	2	2	10	KN / KN
S311 A/B	3	1	1	KN / KN
S3110 A/B	3	1	10	KN / KN,LFS
S321 A/B	3	2	1	KN,KG / KN,KG
S3210 A/B	3	2	10	KN,KG / KN,KG
S411 A/B	4	1	1	KN / KN
S4110 A/B	4	1	10	KN / KN,KG
S421 A/B	4	2	1	KN,KG / KN,KG
S4210 A/B	4	2	10	KN,KG / KN,KG
S511 A/B	5	1	1	KN,KG / KN,KG
S5110 A/B	5	1	10	KN / KN,KG
S521 A/B	5	2	1	KN,KG,LFS / KN,KG
S5210 A/B	5	2	10	KN,KG / KN,KG

Table 3.2: Simulation parameters and planet formation modes displayed by the runs: LPG - *Limited Planetary Growth*, KN - *Kamikaze Neptunes*, KG - *Kamikaze Giants*, and LFS - *Late Forming Survivors*.

sults in regions of high planetesimal density where collisions may become disruptive. The simulations used a minimum time-step of 1 day, corresponding to a minimum semi-major axis of 0.15 AU. Bodies with semi-major axes less than this value are removed from the simulation and considered to have impacted onto the central star. Stellar and disc domain parameters can be found in table 3.1.

I ran simulations for disc masses lying in the range 1–5 times the mass of the Minimum Mass Solar Nebula (MMSN) (Hayashi, 1981), and I also vary the metallicity of the disc so that the initial ratio of solids to gas mass is either 240 or 120 interior to the snow line, the former value being the one expected for the MMSN with a metallicity equal to the solar value. I increase the mass of solids exterior to the snowline smoothly by a factor of 4, as described in Hellary & Nelson (2012). I track the changing compositions of planets during the simulations, as they accrete material that originates either interior or exterior to the snow line.

For each set of physical parameters, I ran two simulations which differed only in the random number seed used to generate the initial particle positions. The full set

Classification	Mass	Rock %	Ice %	Gas %
Rocky Terrestrial	$m_{\rm p} < 3\,{\rm M}_{\oplus}$	$> 95\%$	$< 5\%$	0%
Water-rich Terrestrial	$m_{\rm p} < 3\,{\rm M}_{\oplus}$	$< 95\%$	$> 5\%$	0%
Rocky super-Earth	$3\,{\rm M}_{\oplus} \leq m_{\rm p} < 10\,{\rm M}_{\oplus}$	$> 85\%$	$< 5\%$	$< 10\%$
Water-rich super-Earth	$3\,{\rm M}_{\oplus} \leq m_{\rm p} < 10\,{\rm M}_{\oplus}$	N/A	$> 5\%$	$< 10\%$
Mini-Neptune	$3\,{\rm M}_{\oplus} \leq m_{\rm p} < 10\,{\rm M}_{\oplus}$	N/A	N/A	$> 10\%$
Gas-rich Neptune	$10\,{\rm M}_{\oplus} \leq m_{\rm p} < 30\,{\rm M}_{\oplus}$	N/A	N/A	$> 10\%$
Gas-poor Neptune	$10\,{\rm M}_{\oplus} \leq m_{\rm p} < 30\,{\rm M}_{\oplus}$	N/A	N/A	$< 10\%$
Gas-dominated Giant	$m_{\rm p} \geq 30\,{\rm M}_{\oplus}$	N/A	N/A	$> 50\%$
Core-dominated Giant	$m_{\rm p} \geq 30\,{\rm M}_{\oplus}$	N/A	N/A	$< 50\%$

Table 3.3: Planetary classification parameters based on their composition and the mass fraction of their gaseous envelope. Note that water-rich planets are so-called because they accrete water ice in solid form that originates from beyond the snow-line.

of simulation parameters are detailed in table 3.2.

3.2 Results

In this section I will begin by discussing the common behaviour associated with the disc evolution and planet migration observed in the simulations. I will then present results of the full n-body simulations, where I divide the observed evolution into four distinct modes: *limited planetary growth*; *kamikaze neptunes*; *kamikaze giants*; *late forming survivors*. For each mode, I present the detailed results of one representative run. The modes displayed by each run are listed in table 3.2. As the names suggest, the behaviour associated with these different formation modes includes moderate mass growth of planets during the gas disc lifetime, formation of planetary cores that undergo large scale inward type I migration, formation of giant planets with masses $> 30\,{\rm M}_{\oplus}$ that undergo type II migration into the star (or at least through the inner boundary of the disc model), and formation of super-Earths and Neptune-mass planets late in the disc lifetime that avoid catastrophic migration because of disc dispersal. Not surprisingly, these different formation behaviours correlate with the initial disc mass, metallicity and planetesimal size, and I discuss how these influence the formation and evolution of planetary systems in the simulations. To assist in describing the outcomes of the simulations, I have developed a classification system for the different bodies that are formed, based on their masses and compositions. The classifications and associated parameters used in the definitions are described in table 3.3.

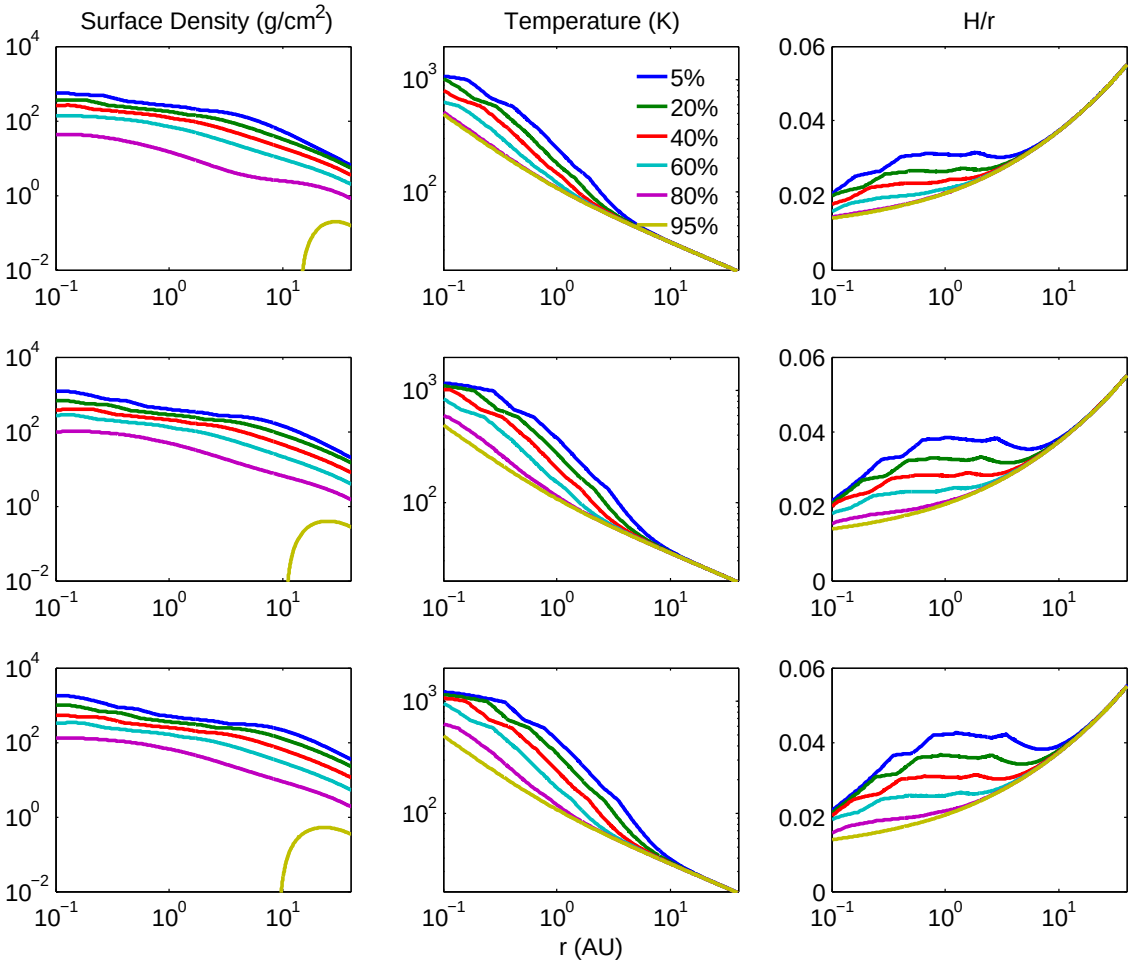

Figure 3.1: Gas surface densities, temperatures and aspect ratios for 5, 20, 40, 60, 80, 95% (top-bottom lines) of the disc lifetime in 1 × MMSN (top panels, life time: 4.8 Myr), 3 × MMSN (middle panels, lifetime: 8 Myr) and 5 × MMSN (bottom panels, lifetime: 9.5 Myr) discs.

3.2.1 Common behaviour

3.2.1.1 Gas disc evolution

The viscous and thermal evolution of three disc models are shown in figure 3.1. The top row shows the evolution of the surface density, temperature and H/r profiles for a disc with initial mass equal to 1 × MMSN. The middle and bottom rows show models with initial masses equal to 3 × MMSN and 5 × MMSN, respectively. The times corresponding to each profile displayed in the figures are indicated in the legend contained in the second panel on the top row, expressed as a percentage of the disc total lifetime. These lifetimes are 4.8 Myr for the 1 × MMSN disc, 8 Myr for the 3 × MMSN disc, and 9.5 Myr for the 5 × MMSN disc.

Figure 3.1 shows that the discs all evolve similarly, with the more massive discs maintaining higher temperatures and H/r values. As the discs evolve viscously, the surface density, temperature and H/r values decrease with time. The decreases in temperature and H/r arise because of the reductions in the viscous heating rates and opacities as Σ decreases. One effect of the decreasing values of H/r with both time and decreasing orbital radius is to allow gap formation to arise for planet masses significantly less than the Jovian mass, and this is one feature that is observed frequently in the n-body simulations: planets of moderate mass (e.g. $m_{\rm p} \gtrsim 10\,{\rm M}_{\oplus}$) migrating inward at late times and transitioning from type I to type II migration at disc radii $< 1\,{\rm au}$.

The final stages of disc evolution are characterised by the formation of an inner cavity, caused by the inner disc accreting viscously onto the central star while being starved of inflow from further out when the photoevaporative mass loss exceeds the viscous inflow rate (Clarke et al., 2001).

3.2.1.2 Migration behaviour driven by corotation torques

Hellary & Nelson (2012) performed simulations similar to those being presented in this chapter, but with simpler power-law disc models, where disc dispersal was modelled through an imposed self-similar exponential decay of the surface density. These models gave rise to a particular expectation for the influence of corotation torques on the migration of low mass planets, and Hellary & Nelson (2012) explored this behaviour through contour plots that displayed the strength of migration as a function of planet mass and orbital radius. Here, I also consider the expected migration behaviour in the disc models as a function of disc evolution time, planet mass and orbital radius, through the presentation of migration contour plots (or 'migration maps').

I begin by noting that the torque experienced by a low mass planet embedded in a disc arises because of two components: the Lindblad torque and the corotation torque. The Lindblad torque arises because of spiral density waves that are excited at Lindblad resonances in the disc, and it almost always drives rapid inwards migration of planets whose masses exceed an Earth mass. The corotation torque is a non-linear phenomena that is related to the horseshoe orbits followed by fluid elements located in the vicinity of the planet orbital radius. It originates from the entropy and vortensity gradients that exist in protoplanetary discs, and is usually positive, such that it tries to drive outward migration. If the viscous or radiative diffusion time scales across the horseshoe region are too long, then phase mixing of fluid

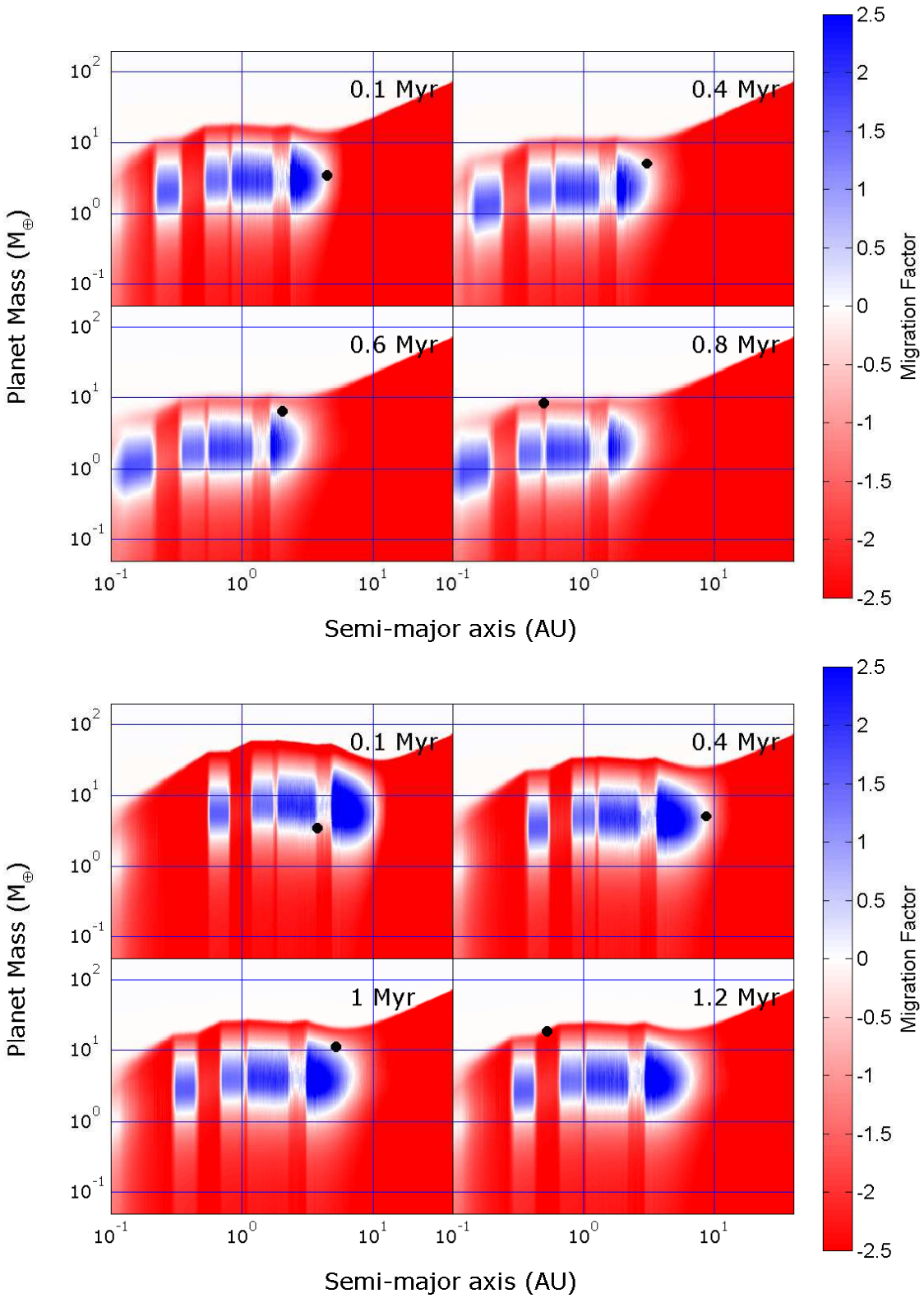

Figure 3.2: Upper panels: Contour plots showing regions of outward (blue) and inward (red) migration for a single planet in a $1 \times$ MMSN disc at $t = 0.1$ Myr (top left), $t = 0.4$ Myr (top right), $t = 0.6$ Myr (bottom left) and $t = 0.8$ Myr (bottom right). Lower panels: same as upper panels but for a $5 \times$ MMSN disc at times, 0.1, 0.4, 1 and 1.2 Myr. The black dots represents a single planet's mass and semi-major axis

elements in this region erases these gradients, and the corotation torque saturates (i.e. switches off). Corotation torques are maintained at their maximum values when the viscous/radiative diffusion time scale is approximately equal to the libration period associated with the horseshoe orbits, and can equal or exceed the Lindblad torque, leading to outward migration. When the viscous/radiative diffusion time scales are too short, then the corotation torque is reduced considerably in magnitude, and tends towards the value obtained in a linear perturbation analysis. This value is generally too small to counteract the inwards migration due to the Lindblad torque.

Considering the torques experienced by a planet with a low initial mass which grows over time, I note that a very low mass protoplanet will have a narrow horseshoe region, x_s, and the libration period associated with the horseshoe orbits will be very long relative to the viscous/radiative time scales. I therefore expect a low mass planet to experience a weak corotation torque that is equal to the linear value, and its orbital evolution to be dominated by Lindblad torques. As the planet mass grows, the horseshoe orbit times decrease and eventually equals the viscous and radiative diffusion time scales. The corotation torque will then be maximised, and the planet may migrate outward. Further increases in the planet mass cause the horseshoe orbit period to decrease below the viscous and thermal time scales. A sufficiently massive planet will lose its corotation torque due to saturation, and will migrate inwards rapidly due to the Lindblad torque.

I performed two separate 'single-planet-in-a-disc' simulations, where a $3\,M_\oplus$ planet is placed in a disc at $a_p = 5\,\text{au}$ with a prescribed mass growth rate, and its orbital evolution, due to the migration torques described in section 2.3.2, is followed and shown in figure 3.2. The upper panels in figure 3.2 show the migration behaviour for a planet embedded in a disc with mass equal to $1 \times \text{MMSN}$ as a function of time. Note that red contours correspond to rapid inwards migration due to the dominance of Lindblad torques, and blue contours correspond to strong outward migration. White contours correspond to 'zero-migration zones', where corotation and Lindblad torques balance each other. The structure of the migration contours depend on local disc conditions, and sharp changes in the opacity behaviour can cause sharp transitions in the expected migration behaviour, as shown by the migration maps in figure 3.2. At early times a planet with mass $\leq 1\,M_\oplus$, located at orbital distances in the range $0.3 \leq r \leq 5\,\text{au}$, will experience strong inwards migration. A planet in the same range of orbital distance with a mass in the interval $1 \leq m_p \leq 10\,M_\oplus$ will experience strong outward migration, and a planet with $m_p > 10\,M_\oplus$ will migrate inwards rapidly.

The location of the planet during the single planet simulations is denoted by the

black dot in figure 3.2.

After 0.1 Myr I see that it has migrated out to the zero-migration zone located at $\sim 5\,\mathrm{au}$. As the disc evolves, the migration contours evolve such that the outward migration region moves down in mass and in towards the central star. A planet sitting in a zero-migration zone will move inwards because of the disc evolution, even in the absence of further mass growth. In the single planet simulation, I see that further mass growth causes the planet to follow the outline of the zero-migration contour, and once its mass approaches $m_\mathrm{p} = 10\,\mathrm{M}_\oplus$ after 0.8 Myr, it is destined to migrate inwards due to the Lindblad torque.

The lower panels in figure 3.2 show a similar scenario, except for a model with disc mass equal to $5 \times$ MMSN. Here I see that the outward migration contours lie at higher masses and at further distance from the central star, but otherwise shows similar behaviour to the $1 \times$ MMSN case. The implications for planet formation arising from this mass dependency is simply that a planetary core which forms at early times may be driven outward to the zero-migration zone located at $r \sim 10\,\mathrm{au}$, where in principle it can sit and grow through mutual collisions with additional embryos and planetesimals. This core can grow to a larger mass in the heavier disc prior to saturation of the corotation torque, and may therefore avoid rapid inwards migration due to Lindblad torques for a longer period of time. This may not happen in practice, however, because being located in a heavier disc may allow the mass of the planetary core to grow rapidly to a mass at which the corotation torque saturates. Finally, I note that the transition from the red to the white contour at high masses in figure 3.2 corresponds to the planet reaching the local gap forming mass, at which point the planet will undergo type II migration. The contours show that for a more massive disc the transition to gap formation occurs for a higher planet mass, because of the previously mentioned higher temperatures and H/r values.

3.2.2 Limited planetary growth

In the oligarchic growth scenario, the collisional growth of planets within a disc containing a modest mass in solids is expected to proceed slowly. In the limit of a small enough disc mass, no planets will be able to form with masses that are large enough to accrete gaseous envelopes, even if the spatial density of protoplanets is increased by convergence in zero-migration zones. Planet formation in the lowest mass discs that I have considered, with standard solar metallicities, displays this

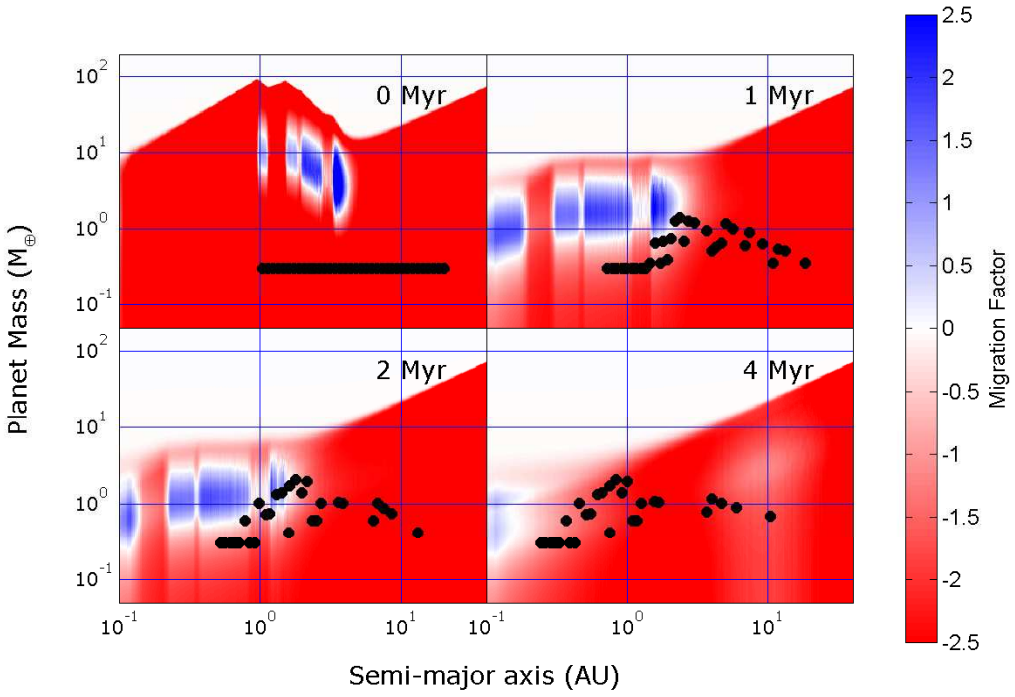

Figure 3.3: Contour plots showing regions of outward (blue) and inward (red) migration along with all protoplanets for simulation S111B at $t = 0$ yr (top left), $t = 1$ Myr (top right), $t = 2$ Myr (bottom left) and $t = 4$ Myr (bottom right).

behaviour, resulting in final systems of planets that are devoid of gaseous envelopes.[3] The simulations labelled as S111A, S111B, S1110A and S1110B displayed this mode of behaviour, and below I describe the results of run S111B in detail.

3.2.2.1 Run S111B

Run S111B had an initial disc mass equal to 1 × MMSN, solar metallicity, and planetesimal radii $R_{\rm pl} = 1$ km. The initial combined mass in protoplanets and planetesimals was equal to $42.5\,{\rm M}_{\oplus}$, distributed between disc radii $1 \leq r \leq 20$ au, with the mass in protoplanets being initially equal to $11\,{\rm M}_{\oplus}$.

The evolution of the protoplanets in the mass-radius plane is shown in figure 3.3, along with the evolution of the migration torques. The first panel shows that significant planetary growth must occur in order for planets to experience strong corotation torques. The evolution of the protoplanet masses, semimajor axes and eccentricities are shown in figure 3.4. Accretion of planetesimals by protoplanets,

[3] I note that planetary atmospheres may form *via* outgassing, but this effect goes beyond the range of physical processes considered in the models. Furthermore, H/He rich envelopes can settle onto relatively low mass planets (Lammer et al., 2014), and although I consider the effect of this on planetesimal accretion, I do not report gas envelope masses for planets with $m_{\rm p} < 3\,{\rm M}_{\oplus}$.

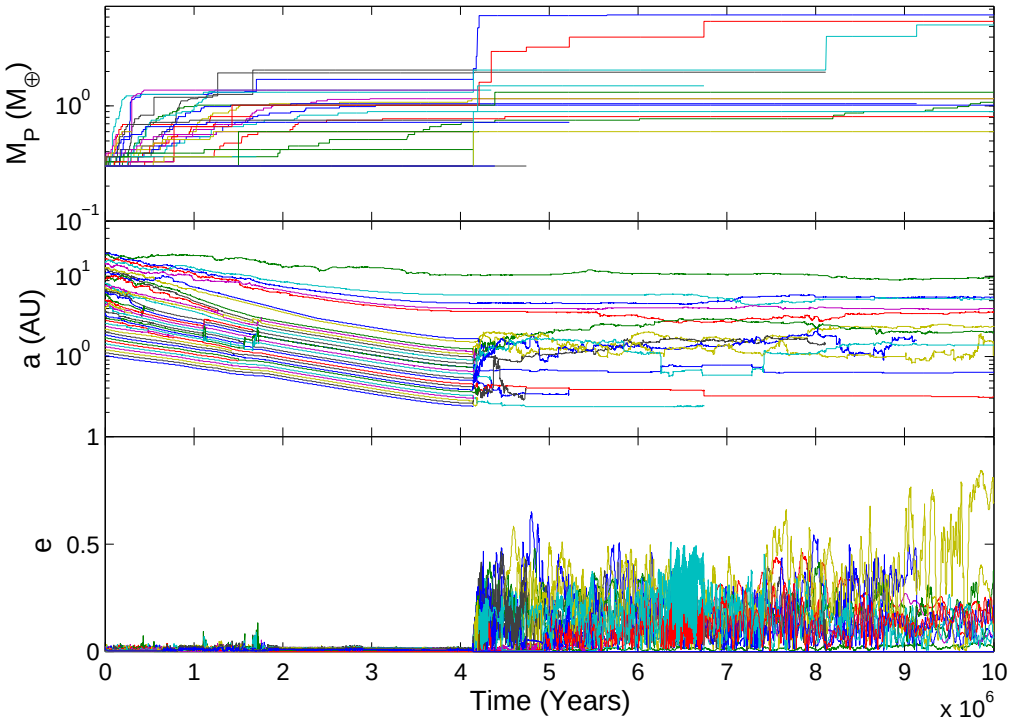

Figure 3.4: Evolution of masses, semi-major axes and eccentricities of all protoplanets in simulation S111B.

and their mutual collisions, quickly leads to the formation of protoplanets with masses $m_{\rm p} \simeq 1\,{\rm M}_{\oplus}$. These bodies experience strong corotation torques, and converge toward the zero-migration zone located at $\sim 3\,$au after 1 Myr. The population of planetary cores located initially beyond 10 au grow slowly, and remain in the outer disc throughout the simulation. These are the planets seen to remain at large distance in the middle panel of figure 3.4. The swarm of planets lying interior to this region are drifting in towards the central star slowly because they are being driven largely by the more massive planets that are sitting in the zero-migration zone, and as the gas disc evolves this zero-migration zone drifts toward the star on a time scale of $\sim$ 4.8 Myr, the gas disc lifetime. In spite of the convergence of protoplanets in the zero-migration zone, figure 3.4 shows that planetary growth leads to the formation of planets with maximum masses $m_{\rm p} \simeq 2\,{\rm M}_{\oplus}$ prior to the gas disc dispersing. Given that the model allows gas accretion to switch on only when the mass of a planet exceeds $3\,{\rm M}_{\oplus}$, this simulation does not result in the formation of any planets that reached the threshold for initiation of gas accretion.

As the gas disc begins to disperse after $\sim$ 4 Myr, I see that the planetary eccentricities grow dramatically due to the damping provided by the gas being removed. The planetary orbits begin to cross due to mutual gravitational interactions, and

mutual collisions lead to the formation of three super-Earths. The simulation ends at 10 Myr, and at this stage the chaotic orbital evolution and mutual collisions are on-going, such that I have not reached the point of having a final, stable planetary system. At 10 Myr, the three super-Earths have masses $5.5\,M_\oplus$, $6.25\,M_\oplus$ and $5.1\,M_\oplus$, and orbit with semimajor axes 0.31 au, 0.64 au and 1.39 au, respectively. In addition, there is a collection of lower mass planets with masses in the range $0.7 \leq m_{\rm p} \leq 1.5\,M_\oplus$ orbiting with semimajor axes between 1.5 and 10 au. All surviving planets are classified as being water-rich due to the accretion of material that originated beyond the snowline.

Considering the simulations that I have classed as displaying *limited planetary growth* as a whole (see table 3.2), the main difference was observed between runs with 1 km-sized planetesimals and those where planetesimal radii are 10 km. Due to the increased influence of gas drag in damping planetesimal random velocities, and in increasing the effective accretion cross-section of planetary embryos, I find that planet masses are generally larger in the runs with 1 km-sized planetesimals, and correspondingly migration plays a more important role in shaping the resulting planetary systems. Migration plays an important role in determining the overall architecture of all systems that display *limited planetary growth*, but is sufficiently modest that no planets are lost into the star. The final systems are distributed at large orbital distances compared to some of the highly compact systems that have been discovered in recent years, such as *Kepler-11*, *GJ 581* and *HD 69830*. In part, this result arises because I initiated the n-body simulations with the inner-most planetary embryos at 1 au, and a more realistic set-up would have embryos and planetesimals extending down to the sublimation radius at ~ 0.1 au. Including this interior population of embryos, however, would only add an additional $\sim 1\,M_\oplus$ of solid mass to the system, such that its inclusion would not lead to the formation of compact systems of super-Earths containing up to $\sim 30\,M_\oplus$ of solids as have been observed.

This somewhat crude approach to modelling the accretion of gaseous atmospheres prevents me from commenting in detail on the mass-radius relation displayed by this population, but I note that the four *limited planetary growth* simulations resulted in the following surviving planets: 47 terrestrials (semimajor axes in the range 0.3-18 au), of which 45 are classified as water-rich (the remaining 2 bodies being rocky); 7 water-rich super-Earths (semimajor axes in the range 0.3-1.4 au).

3.2.3 Kamikaze Neptunes

Increasing the initial mass in planetary embryos and planetesimals in the disc, either by increasing the mass of the disc as a whole, or by increasing the metallicity, should allow more massive planets to grow. At some point, such an enhancement of disc solids will enable the formation of planetary cores with masses $> 3\,\mathrm{M}_\oplus$, leading to the accretion of gaseous envelopes. Continued mass growth of these planets will eventually lead to saturation of their corotation torques, as described in section 3.2.1, causing rapid inward migration to arise because of Lindblad torques if this phase of evolution occurs in the presence of a substantial gas disc.

It was noted in section 3.2.1 that the decrease in H/r at smaller stellocentric distances allows planets of Neptune mass that orbit there to form gaps in the disc. I should then anticipate that the rapid inward migration of intermediate mass planets into this region will lead to a transition from type I to type II migration. The type II migration time scale for planets located at 1 au in the disc is $\tau \simeq 1 \times 10^5$ yr, so these planets are likely to migrate into the central star in the absence of a migration stopping mechanism, such as an interior magnetospheric cavity, or unless their inward migration is timed to coincide fortuitously with the final stages of disc dispersal through photoevaporation.

In this section I describe the results of simulations in which super-Earth and Neptune mass planets form relatively early in the disc life time, so that photoevaporation of the disc cannot halt their migration. These planets migrate through the whole system of embryos and planetesimals, and through the inner edge of the computational domain. This mode of evolution was observed in 18 of the 40 runs performed, as listed in table 3.2.

3.2.3.1 Run S211A

Simulation S211A has an initial disc mass equal to $2 \times$ MMSN, solar metallicity, planetesimal radii equal to 1 km, and an approximate gas disc lifetime of 6.7 Myr. The total initial mass in solids is equal to $84\,\mathrm{M}_\oplus$.

The full time evolution of the planet semimajor axes, eccentricities and masses are shown in figure 3.5. Snapshots showing the mass, orbital radii and migration behaviour of planets at key points during the of evolution, are shown in figure 3.6. During the first 0.5 Myr, planets with semimajor axes < 2 au migrate inwards slowly without accreting many planetesimals or experiencing mutual collisions, so their masses remain $< 0.5\,\mathrm{M}_\oplus$ during this time. Protoplanets with semimajor axes > 2 au accrete planetesimals and undergo mutual collisions, with three planets accreting

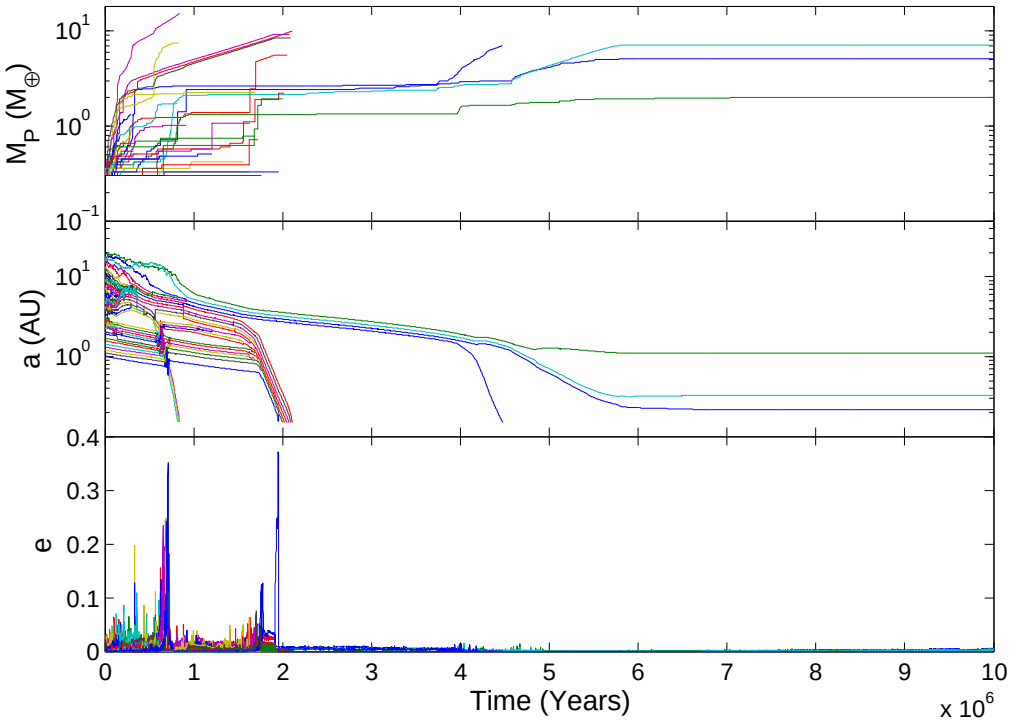

Figure 3.5: Evolution of masses, semi-major axes and eccentricities of all protoplanets in simulation S211A.

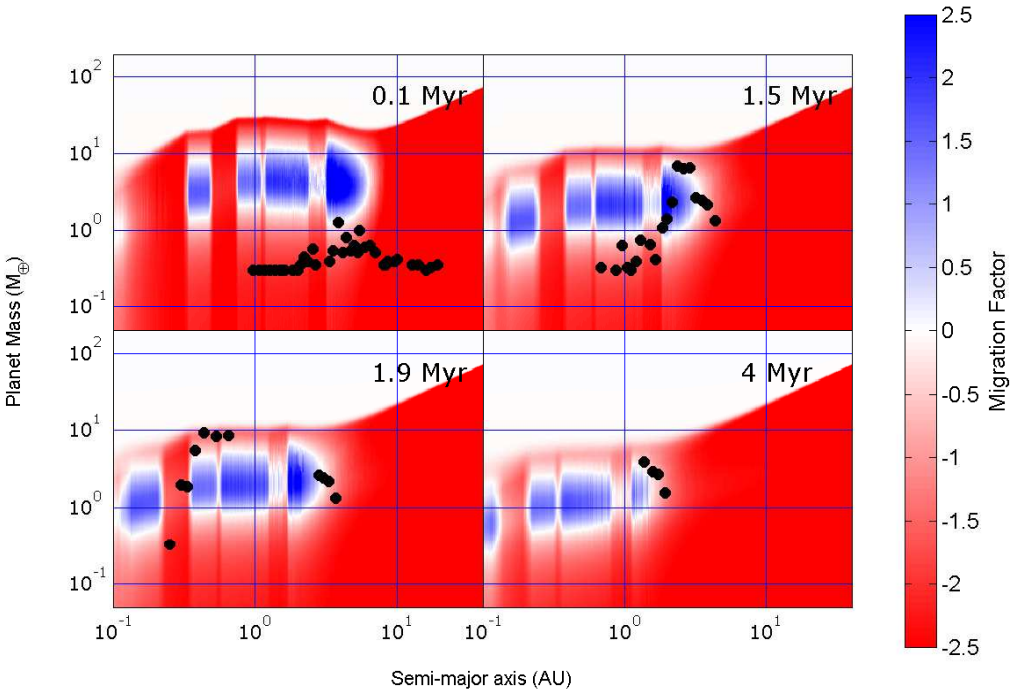

Figure 3.6: Contour plots showing regions of outward (blue) and inward (red) migration along with all protoplanets for simulation S211A at $t = 0.1$ Myr (top left), $t = 1.5$ Myr (top right), $t = 1.9$ Myr (bottom left) and $t = 4$ Myr (bottom right).

enough mass to initiate gas accretion. The most rapidly growing of these reaches mass $m_{\rm p} = 10\,{\rm M}_{\oplus}$ after 0.5 Myr, while orbiting at 5 au.

Over the next 0.25 Myr, the $10\,{\rm M}_{\oplus}$ planet continues to accrete gas and planetesimals, while migrating outward towards the zero-migration zone located at ~ 6 au. It grows massive enough for the corotation torque to saturate, leading to a period of rapid inwards migration. At 0.78 Myr, the now Neptune-mass planet opens a gap when it reaches semimajor axis 0.5 au, and transitions to type II migration. After a further 5×10^4 yr, this planet migrates through the inner boundary of the computational domain, taking two lower mass planets with it that are trapped in an interior resonant chain. During the large scale inwards migration, a large group of low mass planets is scattered to larger radii, instead of migrating in resonance with the migrating group, due to mutual gravitational interactions that cause them to leave the mean motion resonances and scatter off the Neptune-mass planet. This is a similar scenario, albeit with a lower mass primary migrator, to that of Jupiter-mass planets scattering terrestrial planets while migrating inward as described in Fogg & Nelson (2009).

Planetary accretion and migration continues among the exterior population of embryos during the migration and loss of the Neptune-mass planet. Looking at the top and middle panels of figure 3.5, I can see that three planets continue to grow slowly through planetesimal and gas accretion between 0.3 - 1.6 Myr. These planets drift inward slowly because they sit in a zero-migration zone that moves toward the central star as the disc evolves, as shown in the top right panel of figure 3.6. When the planets reach masses $\sim 8\,{\rm M}_{\oplus}$ the corotation torques saturate, and these planets migrate inward rapidly, catching a resonant chain of seven planets. The three most massive planets form gaps in the disc after 1.9 Myr when they reach semimajor axes ~ 0.5 au, before they all migrate past the inner boundary at 2.1 Myr. Low mass planets within the resonant chain either collided with the more massive planets, or were swept through the inner boundary. The most massive planet to pass through the inner boundary in this chain was $10\,{\rm M}_{\oplus}$, with a gaseous envelope that contained 68% of its total mass.

After 2.1 Myr, four planets remain in a resonant chain, orbiting at a few au, with masses $< 3\,{\rm M}_{\oplus}$. Slow inward migration continued for the next 2 Myr, at which point the innermost planet accreted a large number of planetesimals from a cluster that it encountered, increasing its mass above $3\,{\rm M}_{\oplus}$ and initiating gas accretion. 4 Myr after the start of the simulation, the corotation torque for this planet saturates, and it undergoes faster inward migration, before opening a gap at 0.5 au and type II migrating through the inner boundary at 4.5 Myr with a mass of $7\,{\rm M}_{\oplus}$. The

three remaining planets continue to drift in slowly due to the inward drift of the zero-migration zone, and for two of these three planets gas accretion was initiated after they accreted planetesimals so that their masses exceeded $3\,M_\oplus$. These planets underwent a period of more rapid migration, but because this last phase of evolution occurred as the gas disc was being dispersed, they accreted only limited amounts of gas and halted their migration without passing through the inner boundary. The final configuration of the system consisted of three surviving planets orbiting with semimajor axes 0.22 au, 0.33 au and 1.1 au, with masses $5.1\,M_\oplus$, $7.2\,M_\oplus$ and $2\,M_\oplus$. The innermost two planets have gas envelope fractions of 13% and 53% respectively, meaning they are classified as mini-Neptunes. The final low mass terrestrial planet is classified as water-rich owing to its initial location beyond the snowline.

A total of 18 other simulations showed similar evolution histories to that just described. These had disc masses varying between 1–5×MMSN. In each simulation, sub-Neptune and Neptune mass planets migrated inwards rapidly through type I migration, after saturation of their corotation torques, before entering a phase of type II migration when at orbital radii equal to a few tenths of an au. During the large scale migration, terrestrial-mass planets were scattered to larger radii, and some were forced to migrate inward in resonant chains. Surviving planets in these systems had a maximum mass of $7.2M_\oplus$ (from the run S211A described above), and the majority had masses between $1 - 5\,M_\oplus$.

It is worth noting that an individual run can display more than one mode of planet formation defined in the classification system. According to this nomenclature, run S211A displays the formation modes dubbed as *kamikaze neptunes* and *late forming survivors*.

3.2.4 Kamikaze Giants

For a disc with a significant mass in solids, either because it has a large overall mass, or because the disc has an enhanced metallicity, I might expect massive cores to form that are capable of accreting significant gaseous envelopes, leading to the formation of *giant planets* with masses $m_\mathrm{p} \geq 30\,M_\oplus$ (as per the definition of a giant planet given in table 3.3). As discussed in section 3.2.1, having a larger gas disc mass leads to higher temperatures and H/r values, and this pushes the zero-migration zones to larger radii and allows corotation torque saturation to occur only for higher mass planets, as demonstrated by figures 3.1 and 3.2. Higher mass planets are also likely to transition to slower type II migration at larger radii, and this combination of factors favours the growth of more massive planets by allowing them to remain

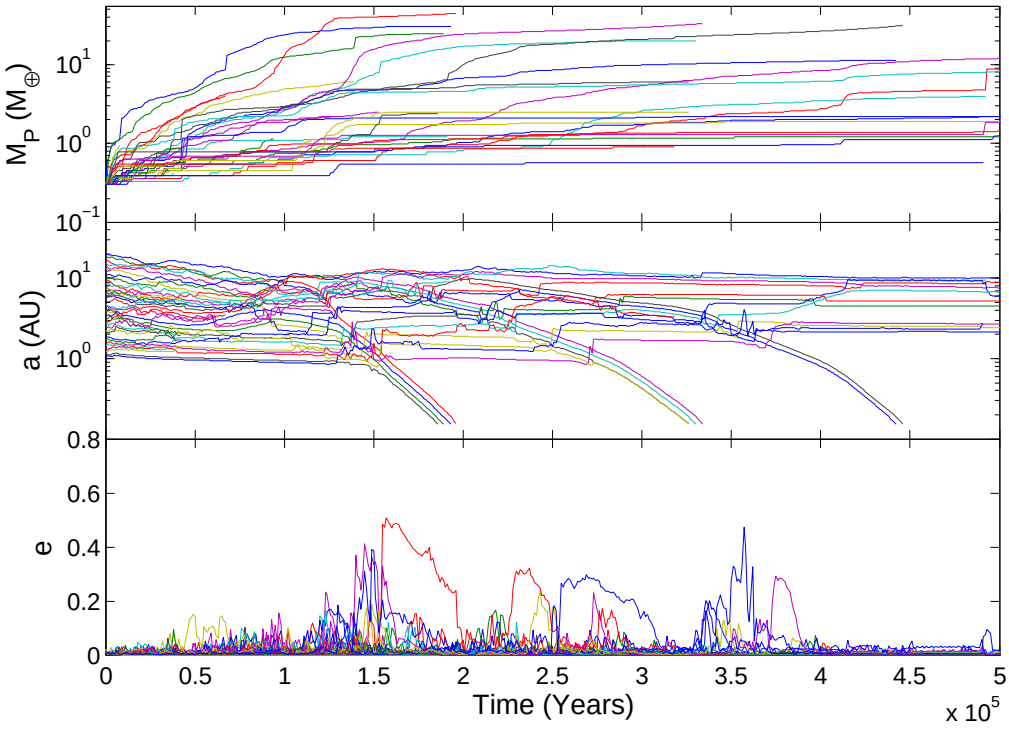

Figure 3.7: Evolution of masses, semi-major axes and eccentricities of all protoplanets for the initial 500,000 years in simulation S421A

in the disc for longer periods of time.

The following simulation provides a specific example of giant planets being able to form in more massive discs through the combination of the effects just discussed. As discussed later in section 3.4, the survival against migration of an isolated 30 $M_\oplus$ giant planet, that forms through gas accretion onto a 15 $M_\oplus$ core, can only occur if the planet opens a gap and starts type II migrating inward from an orbital radius $\gtrsim$ 6 au. The formation and survival of a jovian mass planet requires gap opening and the initiation of type II migration at orbital radii $\gtrsim$ 20 au. This sequence of events is not observed to occur in any of the simulations, such that all giant planets formed during the runs are lost via migration into the central star.

3.2.4.1 Run S421A

Run S421A has an initial disc mass equal to 4 × MMSN, and has twice the solar metallicity. Planetesimal radii are 1 km, and the approximate gas disc lifetime equals 8.8 Myr. The total mass of solids is equal to 337 $M_\oplus$, providing a substantial feedstock that enhances the likelihood of forming massive planetary cores.

The first 0.5 Myr of the evolution of planet semi-major axes, masses and eccentricities are shown in figure 3.7, and the full time evolution is shown in figure 3.8. A

mass-radius plot of the planets and their migration behaviour at specific moments during the evolution are shown in figure 3.9. Close inspection of the top two panels of figure 3.7 show that during the first 0.15 Myr, numerous embryos grow in mass, largely through the accretion of planetesimals, and start to accrete gas as their masses exceed $3\,M_\oplus$. These planets experience strong, unsaturated corotation torques, and migrate out towards their zero-migration zones that are located at between 4 and 8 au. Continued mass growth above $\sim 30\,M_\oplus$ for the outermost of these planets leads to saturation of the corotation torque, and a period of rapid inward migration. As this dominant planet migrates inward, it captures the two other massive planets in mean motion resonance, one of which tries to migrate outward because it experiences a strong, positive corotation torque from the disc, but is forced to move in with the dominant migrator because of the resonance. Some of the interior lower mass protoplanets are also captured into the resonant chain, whereas other bodies escape long term resonant capture, and are scattered outward through interaction with the three most massive planets. These scattering events lead to the bursts of eccentricity observed in the bottom panels of figures 3.7 and 3.8. The three massive planets start to form gaps in the disc when they reach semimajor axes ~ 0.8 au, and at this point their gas accretion rate is limited by the rate that gas can be supplied viscously, and their migration transitions from type I to type II. The planets then type II migrate into the central star on a time scale of 5×10^4 yr, with masses $45\,M_\oplus$, $30\,M_\oplus$ and $25\,M_\oplus$. I classify the first two of these planets as *core dominated giants*, because their early formation in the presence of a massive disc of solids leads to $> 85\%$ of their mass being in solids. The least massive planet of the three is classed as a *gas-poor Neptune*.

During the next 0.3 Myr, two massive, gas accreting planets form, causing two more periods of rapid inward migration that involve giant planets with masses $33\,M_\oplus$ and $31\,M_\oplus$, respectively. As with the initial large-scale migration episode described above, some small protoplanets were forced to migrate in resonance with the more massive planets, whilst other protoplanets were scattered outwards. As these planets accreted planetesimals at a slower rate, due to the planetesimal depletion caused by the earlier generation of planet formation and migration, the ratio of gas to solids in these planets was higher. As a result, the two core-dominated giants accreted gaseous envelopes that accounted for 30% and 37% of the total mass respectively. After 0.5 Myr has elapsed, 33% of the original protoplanets remain in the simulation.

Throughout the remainder of the simulation, three more massive planets form and undergo rapid inward type I migration before opening gaps at semimajor axes between 0.5 and 0.8 AU, and undergoing type II migration through the inner boundary

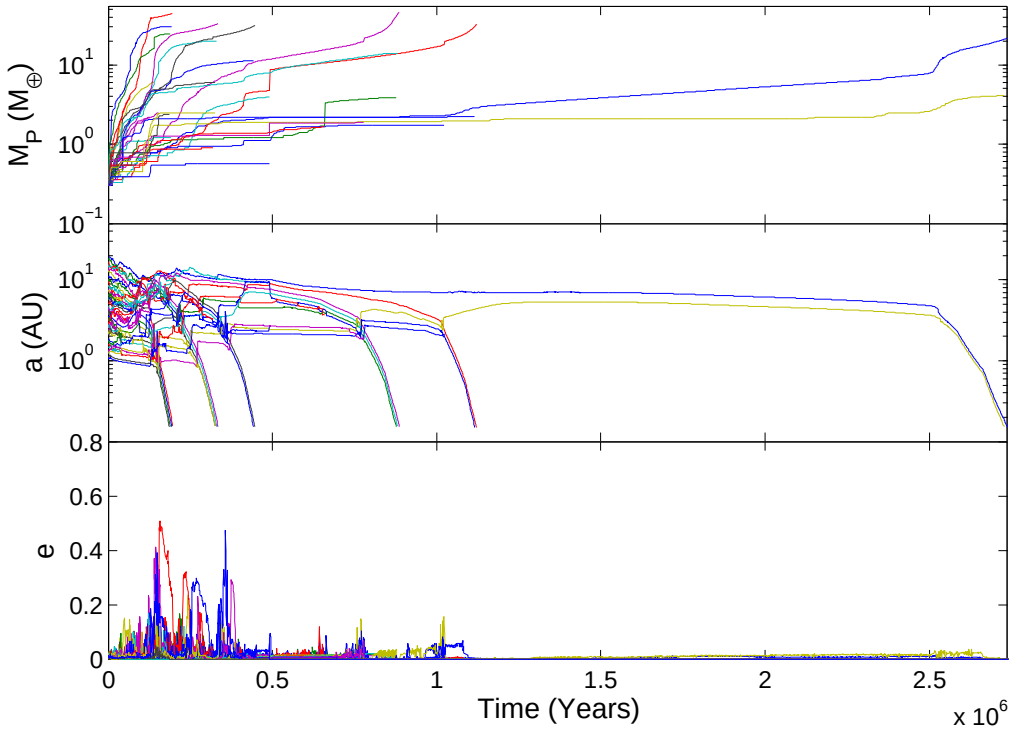

Figure 3.8: Evolution of masses, semi-major axes and eccentricities of all protoplanets in simulation S421A

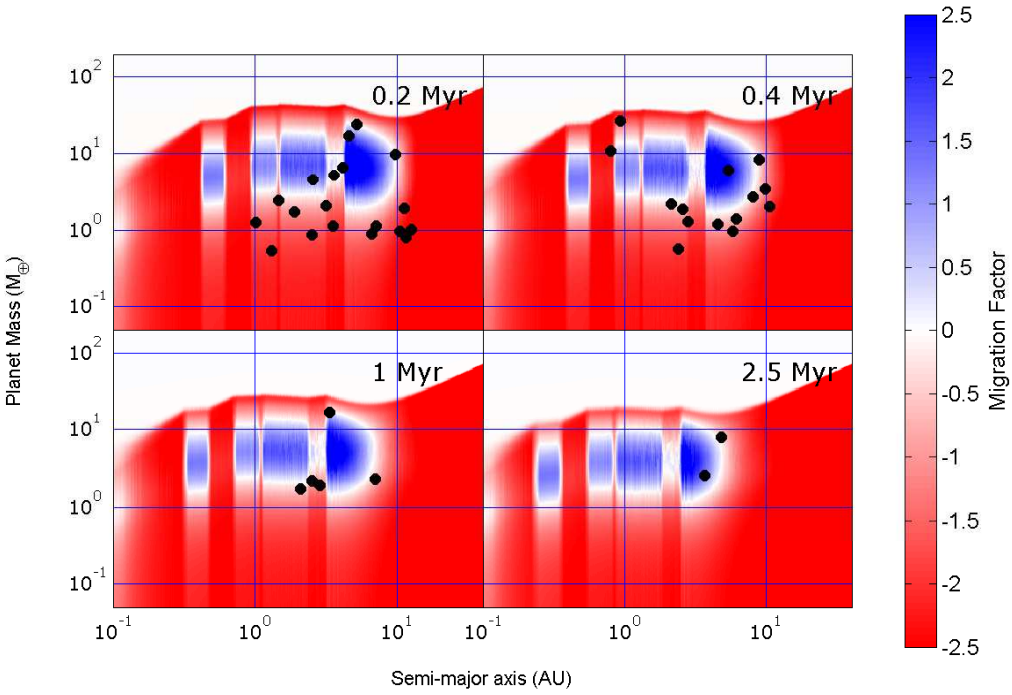

Figure 3.9: Contour plots showing regions of outward (blue) and inward (red) migration along with all protoplanets for simulation S421A at $t = 0.2$ Myr (top left), $t = 0.4$ Myr (top right), $t = 1$ Myr (bottom left) and $t = 2.5$ Myr (bottom right).

at times 0.9, 1.1 and 2.7 Myr, respectively, as illustrated by figure 3.8. The masses of these planets at this point are 47 $M_\oplus$, 32 $M_\oplus$ and 22 $M_\oplus$, with gas envelopes containing 71%, 67% and 53% of the total mass, respectively. The two most massive of these planets are therefore classified as *gas-dominated giants*, and the third planet is classified as a *gas-rich Neptune*. In comparing gas envelope percentages of late forming giant planets with those that formed earlier, it is observed that early forming giants are very heavy-element rich with modest H/He envelopes, while late forming giants are more abundant in H/He because of the depletion of planetesimals and embryos by the earlier generations of planet formation and migration. After the final rapid migration event, no protoplanets remained in the simulation, resulting in the end of the run before the disc had fully dispersed.

The general behaviour described above for run S421A is exhibited by a number of the runs whose evolution is classified as *Kamikaze Giants*, although some of the runs do retain a population of remnant low mass planets at the end, and some *late forming survivors*. Two runs that produced giant planets with significantly larger masses were S511A and S511B. In each of these runs, collisions involving already massive bodies, orbiting at between 2–2.5 au, resulted in the formation of a planet with a mass that was greater than the runaway gas accretion mass. Each of these planets opened gaps in the disc and type II migrated inward, reaching final masses of $\sim 90\,M_\oplus$ before migrating through the inner boundary of the disc. Simulations that formed giant planets, but which did not produce collisions involving already massive bodies, generally formed giant planets with masses in the range $30 \leq m_\mathrm{p} \leq 45\,M_\oplus$. This is because rapid inward type I migration led these planets to open gaps in the disc at small orbital radii ≤ 1 au before runaway gas accretion could occur, leaving minimal time to accrete gas while undergoing the final stages of type II migration. From a total of 18 simulations with comparable results, 57 giant planets were formed and migrated through the inner boundary, with a range of masses between 30 $M_\oplus$ and 92 $M_\oplus$.

3.2.5 Late forming survivors

As has been shown in sections 3.2.3 and 3.2.4, early forming Neptunes and giant planets are unable to survive in the disc if they form when the remaining disc life times exceed the migration time scales. If planets grow slowly, and survive early generations of giant planet formation and avoid large scale inward migration in resonant convoys, and begin accreting gas during the latter stages of the disc life time, then planets with significant gaseous envelopes can survive.

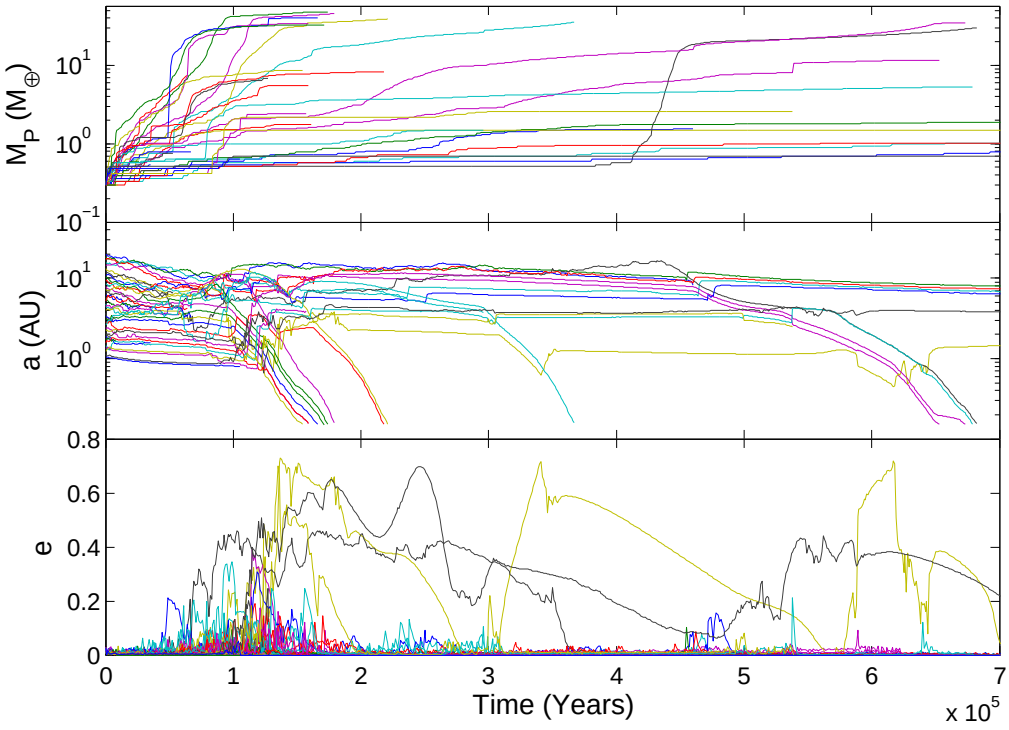

Figure 3.10: Evolution of masses, semi-major axes and eccentricities of all protoplanets for the initial 700,000 years in simulation S521A

In the following subsection I discuss one specific example of a simulation where the late formation and survival of gaseous planets occurs after earlier generations of Neptune-mass and giant planets have migrated through the system.

3.2.5.1 Run S521A

Simulation S521A had an initial disc mass equal to 5 × MMSN, twice the solar metallicity, 1 km-sized planetesimals, and an approximate disc life time of 9.5 Myr. The total mass of solids was equal to 421 $M_\oplus$.

The initial 0.7 Myr of evolution of the semimajor axes, eccentricities and masses are shown in figure 3.10, and the total time evolution is shown in figure 3.11. Migration maps are shown for the epochs 0.1, 0.3, 0.5 and 5 Myr in figure 3.12, with black dots denoting protoplanet positions in the mass-radius plane. As shown in figure 3.10, five massive planets form with masses between $12 - 42\,M_\oplus$ during the first 0.1 Myr. Rapid growth of solid cores and gas accretion cause the corotation torques for these bodies to saturate, and they undergo inward type I migration. Gap formation ensues for all these planets as they migrate interior to 1 au, and between the times 0.12 − 0.18 Myr they migrate through the inner boundary with final masses between $32 - 47\,M_\oplus$. These planets had gas envelope fractions between

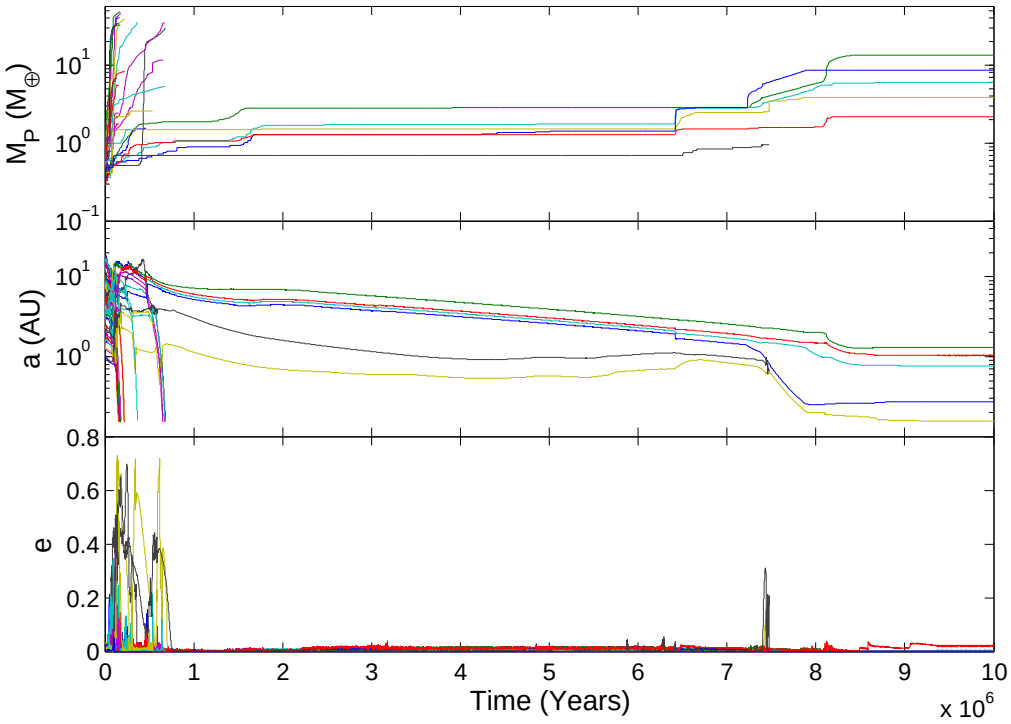

Figure 3.11: Evolution of masses, semi-major axes and eccentricities of all protoplanets in simulation S521A

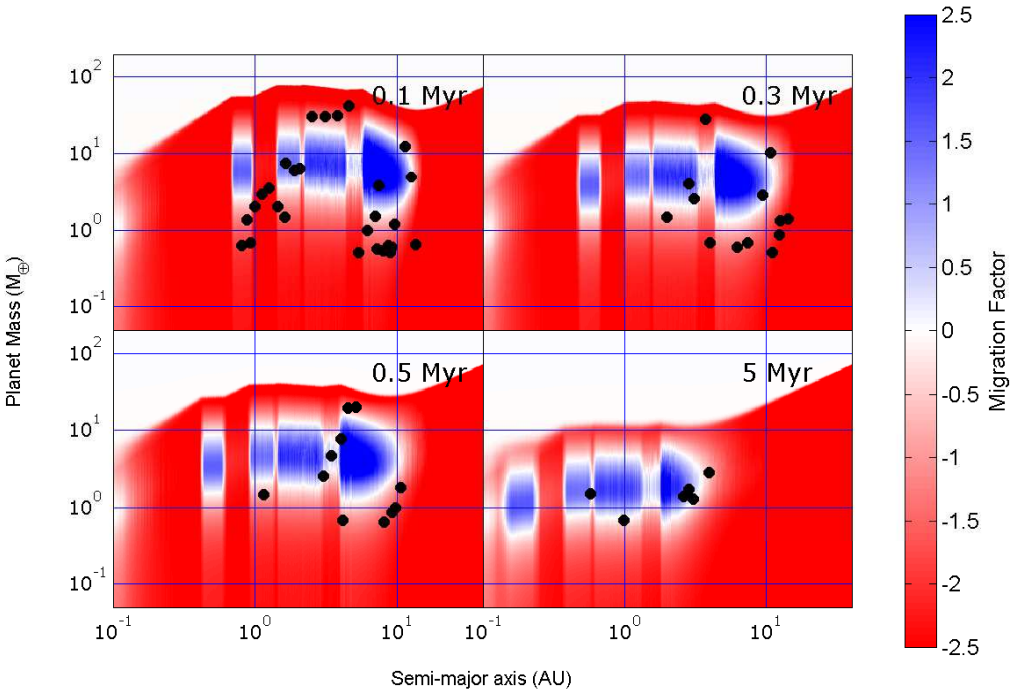

Figure 3.12: Contour plots showing regions of outward (blue) and inward (red) migration along with all protoplanets for simulation S521A at $t = 0.1$ Myr (top left), $t = 0.3$ Myr (top right), $t = 0.5$ Myr (bottom left) and $t = 5$ Myr (bottom right).

8% and 13%, so are all classed as *core-dominated giants*. After a further 5×10^4 yr, another core-dominated giant migrates through the inner boundary with a mass $m_{\rm p} = 39\,{\rm M}_\oplus$, and an envelope fraction of 16%. The large scale migration of these giant planets caused three low mass planets to migrate through the inner boundary, and inspection of figure 3.10 shows that numerous interior planets were scattered to larger orbital radii during this period of evolution.

Over the next 0.5 Myr, three additional giant planets accrete gas, before migrating through the inner boundary at times 0.36, 0.67 and 0.68 Myr respectively. These giant planets leave the simulation with masses $m_{\rm p} = 36\,{\rm M}_\oplus$, $34\,{\rm M}_\oplus$ and $30\,{\rm M}_\oplus$, with gas envelope fractions 34%, 54% and 35%, respectively. Two low mass planets resonantly migrate with the latter two giant planets, while six other low mass planets are scattered to larger radii. Figure 3.12 shows three of these migration events occurring, along with a snapshot of the system after 5 Myr showing the 6 remaining low mass planets. These six planets then drift inward while sitting in zero-migration zones for the next 6 Myr, while accreting planetesimals at a slow rate, and without accreting gas from the disc due to their masses being $< 3\,{\rm M}_\oplus$.

After 7.2 Myr, two planets accrete a swarm of planetesimals, allowing them to begin gas accretion. These planets then proceed to migrate inwards while accreting gas, and forming gaps within the disc, until the combined action of photoevaporation and viscous evolution begins to remove the inner disc after 7.9 Myr, leaving the planets stranded at small orbital radii. Complete disc dispersal occurs after 9.5 Myr, leaving a total of five planets: a $13\,{\rm M}_\oplus$ gas-rich Neptune with an $8\,{\rm M}_\oplus$ solid core and a $5\,{\rm M}_\oplus$ envelope orbiting at 1.3 au (not too different from interior models for Neptune and Uranus (Podolak et al., 2000)), an $8.6\,{\rm M}_\oplus$ mini-Neptune with gas envelope mass fraction equal to 41% orbiting at 0.27 au, and a $6\,{\rm M}_\oplus$ mini-Neptune orbiting at 0.77 au with gas envelope mass fraction equal to 31%. The two remaining planets were a $3.8\,{\rm M}_\oplus$ water-rich super-Earth orbiting at 0.16 au and a $2\,{\rm M}_\oplus$ water-rich terrestrial planet with semimajor axis ~ 1 au.

The late formation of these super-Earths/mini-Neptunes and gas-rich Neptune allowed them to survive migration into the star, while simultaneously limiting the amount of mass available to be accreted due to the earlier generations of planets that were lost from the system.

In section 3.4 I examine the conditions under which gas accreting planets can survive type II migration within the disc models that I present here, and the maximum masses that they can reach through gas accretion prior to removal of the disc by photoevaporation.

3.2.6 Summary of all runs

A suite of 40 simulations has been performed, with disc masses between $1 - 5 \times$ MMSN, metallicity being either solar or $2\times$ solar, and planetesimal radii being either 1 or 10 km. For each permutation of this parameter set, I ran two realisations by changing the random number seed used to set the initial particle positions and velocities. The final outcomes of all simulations, after 10 Myr of evolution, are shown in figure 3.13.

I now comment on how the different initial conditions in the simulations influenced their final outcomes by discussing briefly each of the panels in figure 3.13. I remind the reader that the labelling convention for the simulations is such that a run labelled S$N_1N_2N_3$ has disc mass $N_1 \times$ MMSN, metallicity enhancement factor N_2, and planetesimal radii N_3 km, where N_3 is either 1 or 10. Each panel contains both the set A simulation results (blue symbols) and those from set B (red symbols).

3.2.6.1 S111 and S1110

These models have the lowest disc masses and metallicites. The growth of planets occurred relatively slowly in all four runs, and the low mass of the gaseous disc resulted in only modest migration. No material was lost through the inner boundary of the computational domain in these runs. Systems of planets were formed consisting of more massive super-Earths orbiting with semimajor axes in the range $0.3 \leq a_{\rm p} \leq 1.4\,{\rm au}$, and less massive terrestrials orbiting at larger semimajor axes $0.3 \leq a_{\rm p} \leq 18\,{\rm au}$. The planetary systems continue to evolve through mutual interactions and collisions up to and beyond the end of the simulations.

3.2.6.2 S121 and S1210

These models initially have twice the mass in solids compared to the previous set. I see that doubling the mass in solids has the tendency of increasing the mass growth of planets, particularly those that are orbiting at greater distances from the central star. Planets were lost from the system by migrating into the central star in both of these run sets. I see that run S1210B results in a $9\,{\rm M}_\oplus$ planet orbiting at $a_{\rm p} \simeq 0.2\,{\rm au}$, and all runs result in systems of terrestrial and super-Earths orbiting between $0.6 \leq a_{\rm p} \leq 12\,{\rm au}$.

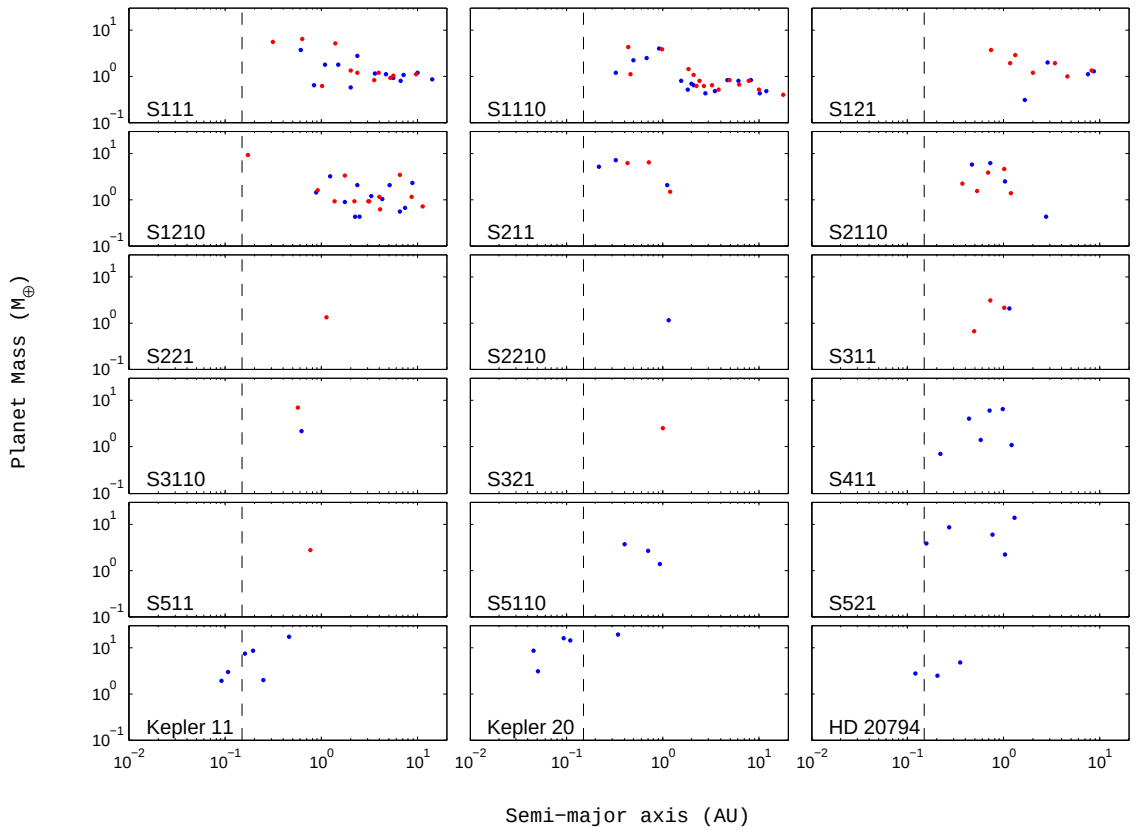

Figure 3.13: Final masses versus semimajor axes for all planets formed in all simulations. The blue symbols represent the set A simulations, and red symbols represent set B. The inner edge of the computational domain is shown by the vertical dashed line in each panel. For comparison, a selection of observed systems are also shown. Simulations that resulted in all planets migrating through the inner edge of the computational domain are not shown.

3.2.6.3 S211 and S2110

These models have double the disc mass in both solids and gas compared to runs S111 and S1110. I see that this enhances both the growth in mass of the final planets, and also increases the degree to which they have migrated. I note that these simulations result in substantial loss of solid material onto the central star through the formation and migration of super-Earth and Neptune-mass planets early during the disc life time.

3.2.6.4 S221 and S2210

Doubling the metallicity leads to a dramatic change in the results compared to runs S211 and S2110. I see that out of the four runs in the sets S221 and S2210, only

S221B and S2210A resulted in any surviving planets, and these are each $\sim 1\,M_\oplus$ bodies orbiting at $a_p \sim 1$ au. Planetary mass growth in these runs in the presence of a substantial gas disc results in almost all planets migrating into the central star.

3.2.6.5 S311, S3110, S321 and S3210

These runs continue the trend of almost all solid mass being evacuated from the disc through the formation of rapidly migrating giant planets ($m_p > 30\,M_\oplus$), or Neptunes and super-Earths, in the presence of a substantial gas disc.

3.2.6.6 S411, S4110, S421 and S4210

Of these runs, only S411A resulted in any planets surviving to the end of the simulations. S411A is an example of a run in which there is sufficient disc mass to allow multiple generations of planets to grow and migrate into the star, while leaving sufficient mass remaining in the disc near the end of the gas disc life time to allow a collection of terrestrial planets and super-Earths to form and survive.

3.2.6.7 S511, S5110, S521 and S5210

These runs follow the now familiar pattern of early formation of super-Earths, Neptunes and giant planets, resulting in them migrating into the central star. In all but run S521A, almost all of the solid mass is lost from the system prior to dispersal of the gas disc. S521A is another example of a simulation that resulted in late forming surviving planets, resulting in a system of 2 mini-Neptunes, a gas-rich Neptune, a water-rich super-Earth, and a water-rich terrestrial, with masses between $2 \leq m_p \leq 13\,M_\oplus$ and semimajor axes $a_p \leq 1.3$ au.

Considering the simulations collectively, I note that the final outcomes mirror the three essentially different modes of behaviour that were described in sections 3.2.2, 3.2.3, 3.2.4, and 3.2.5: (i) moderate growth and migration, resulting in closely packed systems of low mass super-Earths and terrestrials, but no neptunes or giant planets; (ii) growth of super-Earths, neptunes and giant planets early in the gas disc life time, resulting in catastrophic migration into the central star of all, or almost all, of the initial mass in solids; (iii) late formation of terrestrials, super-Earths and Neptunes from the material left over after previous generations of planet formation and catastrophic migration in high mass discs.

Across all simulations, 57 giant planets were formed, with none surviving migration. The largest planet formed was $92\,M_\oplus$ (two such planets formed in the

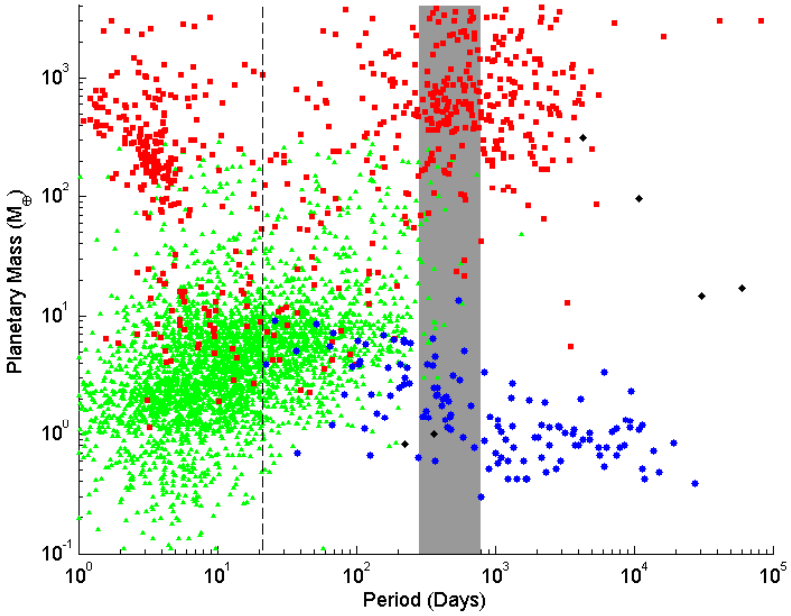

Figure 3.14: Mass vs period plot, comparing observed exoplanets (red squares) and *Kepler* candidates (green triangles) with simulation results (blue circles) and the Solar System (black diamonds). The dashed line indicates the 0.15 au cutoff point in our simulations, whilst the grey zone indicates the habitable zone (Kasting et al., 1993).

simulation suite), but due to its formation early in the disc life time it migrated through the inner boundary. Several Neptune-mass planets also followed this course of growth and migration, generally doing so in lower mass discs.

3.3 Comparison with observations

Although the simulation set does not constitute a population synthesis model, because I have not used a Monte Carlo approach to selecting initial conditions from a distribution of possibilities based on observational constraints, it is interesting nonetheless to compare the results with the observational data, so that I can see where model improvements are required. Figure 3.14 is a mass versus period diagram for the surviving planets from the simulations, along with all confirmed exoplanets and *Kepler* candidates (sourced from www.exoplanets.eu). The vertical dashed line located at ~ 20 days shows the position of the inner edge of the computational domain, so the simulation results cannot be compared with observed exoplanets with orbital periods less than this value.

The shorter period terrestrial-mass planets, super-Earths and Neptune-like planets from the simulations lie in the parameter space occupied by the confirmed ex-

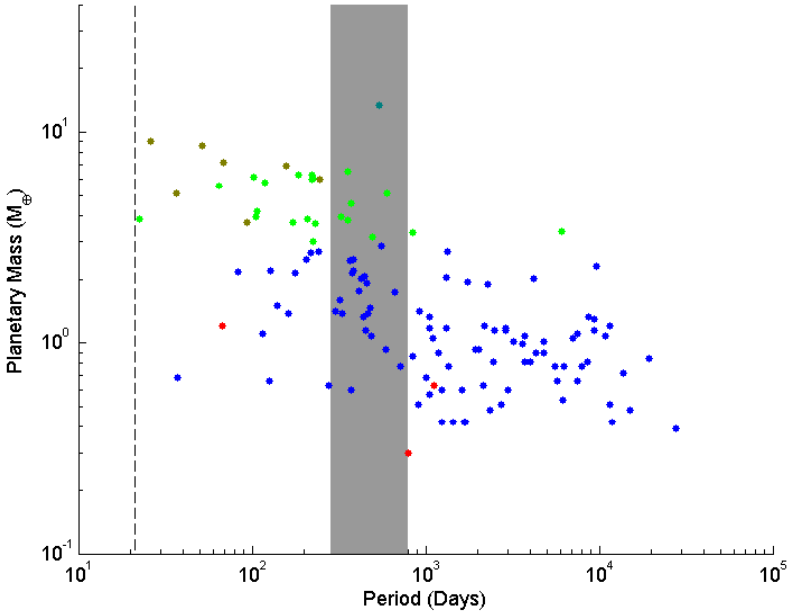

Figure 3.15: Mass vs period plot for the simulation results where symbol colour indicates planet classification. (Red: Rocky terrestrial. Blue: Water-rich terrestrial. Green: Mini Neptune. Brown: Water-rich super-Earth. Cyan: Gas-rich Neptune). The dashed line and grey zone are identical to that in figure 3.14.

oplanets and *Kepler* candidates. The longer period terrestrial-mass planets and super-Earths from the simulations, however, lie in an area that is sparsely populated by observed exoplanets because of observational biases in the radial velocity and transit techniques. These planets are best observed by the microlensing technique, but so far the yield from microlensing surveys is insufficient to provide strong constraints on models. In the future, the *PLATO* mission (Rauer et al., 2014) will provide information on this population of low-mass exoplanets on orbits with intermediate periods.

A clear failing in the simulation results is the lack of surviving giant planets at any orbital period. I explore this issue in greater depth in section 3.4 below, but the primary reason for this is that planets in the simulations rarely undergo runaway gas accretion because inward type I migration transports intermediate mass planets to small orbital radii, where gap formation and type II migration follow. The type II migration time scale for planets orbiting at orbital radii < 1 au is short, leading to the planets quickly migrating through the inner boundary of the simulation domain.

Figure 3.15 shows a mass versus period diagram for the surviving planets from the simulations, where the planets are colour-coded according to the classification scheme described in table 3.3. There is an abundance of water-rich terrestrials at

all semi-major axes due to large scale migration from beyond the ice-line bringing volatile-rich material into the inner regions. For planets with masses $> 3\,M_\oplus$, Mini-Neptunes are the dominant population, where planets have $> 10\%$ of their mass in gas. Gas-poor super-Earths typically formed at small semi-major axes, closer to the central star than the habitable zone. The largest surviving planet formed in the simulations is a gas rich Neptune located in the habitable zone, as discussed in section 3.2.5.

3.4 Conditions for giant planet formation and survival

As has been shown in sections 3.2 and 3.3, although the simulations managed to form giant planets with substantial gaseous envelopes, none of them managed to survive against migration into the star. I did not include the effects of an inner disc cavity in this chapter, which would stop migration and the loss of these giants, but inclusion of such a cavity would lead to a model prediction that essentially all stars have close-orbiting planets, contradicting the observational data. Furthermore, a central cavity cannot explain the longer period giant planet systems that are observed to exist in abundance, as illustrated by figure 3.14.

I now investigate the conditions required for a giant planet to form and survive within the context of the model. I present two suites of calculations below. The first adopts the standard model for gas accretion used in the simulations presented in previous sections. The second uses a model for accretion that is calibrated against a 2-D hydrodynamic simulation of an accreting and migrating planet that is embedded in a gaseous disc, following a similar approach to the runs presented in Nelson et al. (2000).

3.4.1 Standard accretion prescription

I ran a suite of single-planet simulations where a $15\,M_\oplus$ planetary core is embedded at various locations (1, 2, 3, ..., 20 au) in discs with masses that range between 0.2-$0.8\times$MMSN, in an attempt to find out what final planet masses and orbital radii are achieved. The initial conditions are such that I allow the $15\,M_\oplus$ core to accrete gas as described in section 2.2. This prescription uses analytical fits to the Movshovitz et al. (2010) gas envelope accretion calculations, and when the planet reaches the gap opening mass gas accretion changes to the rate at which gas can be supplied

viscously $\dot{m} = 3\pi\nu\Sigma$, where this quantity is calculated in the disc at a distance from the planet equal to $r - r_{\rm p} = 5r_{\rm H}$, to ensure that the location in the disc that the viscous supply rate of gas is evaluated, sits outside of the fully evacuated gap region. Type II migration is switched on when the gap opening mass is reached. Type I migration is neglected for these simulations so that the effects of type II migration can be analysed. To examine the potential effects of increasing the photoevaporation rate of the disc, I adapt the standard photoevaporation routine to account for an enhanced rate of dispersal when the disc interior to the planet's orbit has been cleared due to tidal truncation by the planet, allowing ionising photons to illuminate the inner edge of the disc directly. The direct photoevaporation prescription that I adopt is taken from Alexander & Armitage (2007) and Alexander & Armitage (2009), where the photoevaporative mass loss rate is given by

$$\frac{d\Sigma_{direct}}{dt} = 2C_2\mu m_H c_s \left(\frac{f_{41}}{4\pi\alpha_B h r_{in}^3}\right)^{1/2} \left(\frac{r}{r_{in}}\right)^{-2.42}. \tag{3.1}$$

Here, $C_2 = 0.235$, α_B is the Case B recombination coefficient for atomic hydrogen at 10^4K, having a value of $\alpha_B = 2.6 \times 10^{-19}\mathrm{m}^3\mathrm{s}^{-1}$ (Cox, 2000), and $r_{\rm in}$ is the radial location of the inner disc edge.

For the standard photoevaporation routine, I observe that in simulations starting with disc masses equal to 0.2 × MMSN, the starting semi-major axis for a 15 $\mathrm{M}_\oplus$ core that accretes gas, reaches the gap opening mass, and survives type II migration is 3 au, indicating that any planet that forms and opens a gap interior to 3 au will migrate into the star. Planets forming exterior to this radius will survive migration due to disc dispersal, and their final masses and stopping locations will depend on their initial formation semimajor axes. For higher mass discs, the formation zone that guarantees survival lies at increasing distance from the star, with the survival radii for 0.4, 0.6 and 0.8 × MMSN disc being 9, 14 and 18 au, respectively. The masses of these survivors are 126, 224 and 298 $\mathrm{M}_\oplus$, respectively. The top panel of figure 3.16 shows the starting and final semi-major axes, and the final planet masses, for all survivors as a function of disc mass and starting position. The final planet mass increases as the initial semi-major axis increases, as expected, since the planet has an increased local disc mass throughout its migration, along with an increased time to accrete. Figure 3.17 shows the evolution of the semi-major axes for the full set of 0.6 × MMSN simulations. Migration slows as planets reach the inner regions of the disc, where the amount of remaining disc mass determines if survival is possible. Planets forming exterior to 14 au were found to survive, where the disc life time for

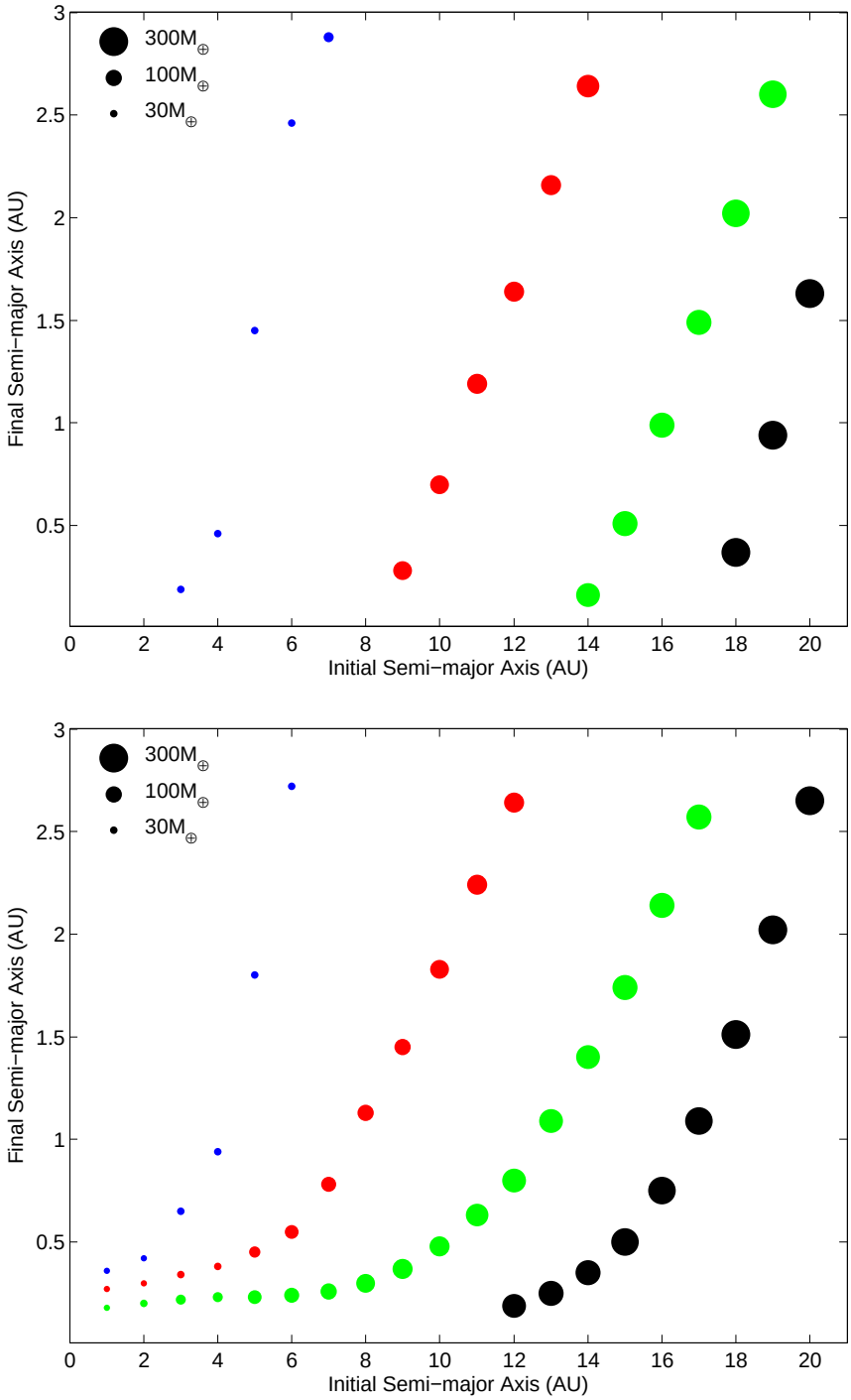

Figure 3.16: Final versus initial semimajor axes of planets in discs undergoing standard (top panel) and direct (bottom panel) photoevaporation that start with masses: 0.2 × MMSN (blue), 0.4 × MMSN (red), 0.6 × MMSN (green) and 0.8MMSN (black).

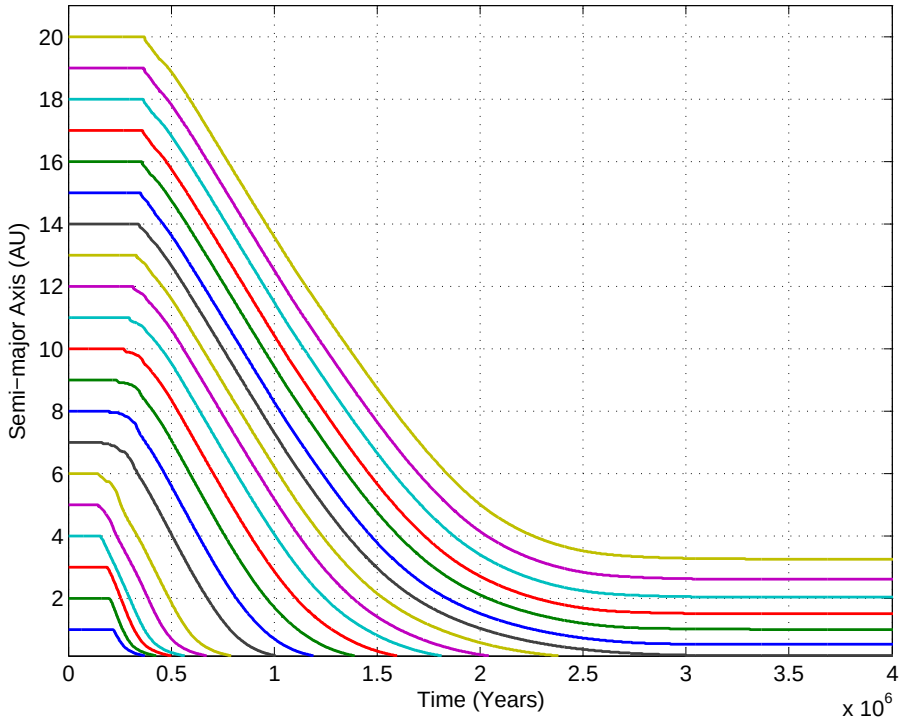

Figure 3.17: Semimajor axis evolution of 15 $M_\oplus$ gas accreting cores in discs with initial masses of 0.6 × MMSN.

this model is 2.9 Myr.

Results for the simulations that adopt the direct photoevaporation routine described above are shown in the bottom panel of figure 3.16. Planets forming between 1-20 au in discs with 0.2, 0.4 and 0.6 × MMSN discs all survive migration. The formation of a gap by a planet allows the inner disc to accrete onto the star within the time taken for the planet to migrate all the way to the inner boundary of the simulation domain. Consequently, as the planet migrates inward, the inner disc disappears, allowing rapid photoevaporation of the exterior disc through direct illumination. This planet-induced disc removal is rapid enough to ensure survival for all planets that form in the models described above. Simulations with disc mass 0.8 × MMSN result in planets migrating into the star unless they form with semi-major axes $\geq$ 12 au.

Planets with large initial semi-major axes in both sets of simulations behaved similarly, especially for larger disc masses. In both sets of simulations, a Jupiter mass planet formed by gas accretion onto the $15M_\oplus$ core only if the core started accreting gas beyond 20 au, and the initial disc mass was at least 0.8 times MMSN. This shows that Jupiters *can* form in the simulations, but only if the core starts to accrete gas at large distance from the central star, giving it sufficient time to accrete

a massive gaseous envelope prior to halting its migration due to disc dispersal. Higher mass discs will allow Jovian mass planets to form and survive, but as the disc mass increases, migration into the central star becomes more likely, so the initial formation radius must increase correspondingly.

In summary, in order for the standard model to form surviving Jupiters, it is necessary for planetary cores to accrete gas and open gaps at large semi-major axes. They must do this at a sufficiently late epoch, so that viscous evolution and photoevaporation have depleted the disc sufficiently that it will disperse before the planet migrates into the star. For the particular parameters adopted in the models, Jovian mass planets must initiate their formation through gas accretion onto solid cores out beyond 20 au. As described in previous sections, in almost all of the simulations in which a gas accreting core forms, it migrates inward to $r_{\rm p} \simeq 0.8\,{\rm au}$ before forming a gap and type II migrating into the star, preventing a massive gas giant planet from forming. In none of the simulations does a core form at, or experience disc-driven migration out to, the distance required for a gas giant planet to form and survive against type II migration. Furthermore, I do not observe any planet-planet scattering that results in planetary cores being flung out to these outer disc regions.

3.4.2 Alternative gas accretion prescription

In order to examine how well the results for gas accretion and migration agree with hydrodynamic models of planets embedded in discs, three 2-D simulations of migrating and accreting planets embedded in gaseous discs were performed[4]. In the fiducial hydrodynamic simulation, the parameters adopted were $\alpha = 2\times10^{-3}$, $H/r = 0.05$ and initial planet mass $m_{\rm p} = 50\,{\rm M}_{\oplus}$. The surface density profile $\Sigma(r) = \Sigma_0 r^{-1/2}$, and the disc mass was normalised so that the characteristic mass within the planet orbit $\pi r_{\rm p}^2 \Sigma(r_{\rm p}) = 264\,{\rm M}_{\oplus}$. The inner and outer boundaries of the computational domain were located at $0.1r_{\rm p}$ and $2.5r_{\rm p}$, respectively, where $r_{\rm p}$ denotes the initial orbital radius of the planet, here assumed to be $r_{\rm p} = 5\,{\rm au}$. The second simulation adopted identical parameters, except that $H/r = 0.0245$. The third simulation was the same as the first, except the initial disc mass was increased by a factor of 3. The simulations were performed using the NIRVANA code (Nelson et al., 2000; Ziegler & Yorke, 1997), with resolution $N_r = 800$ and $N_\phi = 400$, and adopted the accretion routine described in Kley (1999) that removes gas from within the planet Hill sphere

[4]2-D hydrodynamic simulations were set-up, run and completed by Richard Nelson. Analyses and comparison to 1-D models were performed by the author of this thesis.

on the dynamical time scale. The choice of initial planet mass $m_{\rm p} = 50\,{\rm M}_{\oplus}$ means that the planet should be in the runaway gas accretion regime from the beginning of the simulation (Movshovitz et al., 2010; Pollack et al., 1996).

In general, there is good agreement between the numerous hydrodynamic simulations that have been published concerning the gas accretion rate onto a giant planet (Bate et al., 2003; Bryden et al., 1999; D'Angelo et al., 2003; Gressel et al., 2013; Kley, 1999; Lubow et al., 1999; Nelson et al., 2000). It should be noted that these simulations do not resolve the gas flow all the way onto the surface of the planet, in general, and normally adopt a simple equation of state, and so essentially assume that gas accretion onto the planet itself occurs at the same rate that the surrounding protoplanetary disc supplies gas to the planet Hill sphere. In order to reach the planet, this gas must lose its angular momentum, and at the present time it is not known what mechanism is responsible for this angular momentum exchange, or how quickly it operates (Szulágyi et al., 2014). Putting these complications to one side, I simply note that the fiducial hydrodynamic simulation predicts that the planet accretes essentially all of the gas in its feeding zone (defined to be $m_{\rm iso} = 2\pi r_{\rm p} \Sigma_{\rm g}(r_{\rm p}) \Delta r$, where I set $\Delta r = 4\sqrt{3} r_{\rm H}$) during the gap formation process, and once this 'gas isolation mass', $m_{\rm iso}$, has been been reached, the planet continues to accrete at close to the viscous supply rate through the gap while undergoing type II migration. The second hydrodynamic simulation with $h = 0.0245$ was designed to test what happens when the planet is very close to, or equal to, the gap forming mass when it starts to undergo runaway gas accretion. In this case I find that only a fraction of the gas in the feeding zone is accreted because the planet efficiently opens a gap as it starts to accrete. The third simulation was designed to examine what happens when the planet is too low in mass to open a gap when it first enters the runaway gas accretion phase, but the feeding zone contains significantly more mass than is necessary for the planet to reach the local gap formation mass. In this case I find that the planet is able to efficiently accrete a large fraction of the mass in the feeding zone before transitioning to accretion at the viscous supply rate, because gas accretion occurs more rapidly than gap formation in this case.

Given the results of these hydrodynamic simulations, I have implemented a new model of gas accretion into the n-body plus 1-D disc code that matches the results of the hydrodynamic calculations. For a planet that reaches the runaway gas accretion phase prior to reaching the gap forming mass, I apply the following steps:
(i) Noting that a partial gap is formed even by a planet that is below the formal gap opening mass, I calculate the surface density fraction that is available for accretion as given by Crida & Morbidelli (2007)

$$F_{\Sigma}(P_{\Sigma}) = \begin{cases} \dfrac{P_{\Sigma} - 0.541}{4} & \text{if } P_{\Sigma} < 2.4646 \\ 1 - \exp\left(\dfrac{P_{\Sigma}^{3/4}}{-3}\right) & \text{if } P_{\Sigma} \geq 2.4646 \end{cases} \tag{3.2}$$

where

$$P_{\Sigma} = \frac{3H}{4r_{\rm p}\sqrt[3]{q/3}} + \frac{50\nu}{qr_{\rm p}^2\Omega_{\rm p}} \tag{3.3}$$

(ii) Calculate the gas isolation mass, $m_{\rm iso}$, given above using $\Sigma_{\rm g} = \Sigma_{\rm g} F_{\Sigma}$.
(iii) Allow the planet to grow rapidly to $m_{\rm iso}$ by removing gas from the disc around the planet and adding it to the planet. Once the planet reaches this mass it transitions to type II migration and accretes at the viscous supply rate.
When implementing the above prescription, I define the moment when runaway accretion occurs as being when $\frac{dm}{dt} \geq 2\,{\rm M}_{\oplus}$ per 1000 years. This value is chosen as I find that runaway gas accretion occurs shortly after the time that the gas accretion rate reaches this value. I note that a planet that does not reach the runaway gas accretion mass prior to reaching the local gap forming mass will instead transition directly to gas accretion at the viscous supply rate, and will undergo type II migration, without accreting the mass in its feeding zone. The gap formation criterion used in the calculations presented in this section is $3H/(4r_{\rm H}) + 50\nu/(qr_{\rm p}^2\Omega_{\rm p}) < 1$.

In figure 3.18 I plot the semimajor axis versus time, the mass versus time, and the mass versus semimajor axis for the fiducial 2-D hydrodynamic simulation, and a set of 1-D single-planet-in-a-disc runs where the viscous supply rate of gas is calculated at different locations in the disc that lie at different distances from the planet. Also plotted in this figure are the results obtained using the standard gas accretion routine used in the full n-body simulations presented in section 3.4.1. Close inspection of this figure shows that the new accretion routine is a dramatic improvement over the standard gas accretion prescription, with best agreement between 1-D models and the 2-D hydrodynamic simulation occurring when the viscous supply rate is calculated at 10 Hill radii exterior to the planet in the 1-D simulations. The standard accretion routine adopted for the n-body simulations presented earlier predicts too low an accretion rate compared to the 2-D hydrodynamic simulations, but it should be noted that this makes essentially no difference to the results of the full n-body simulations, as only 2 out of 40 runs resulted in a planet undergoing runaway gas accretion at an orbital radius > 0.8 au. Those simulations simply did not produce planets with properties that would allow the new accretion routine to significantly change the outcome of the simulations.

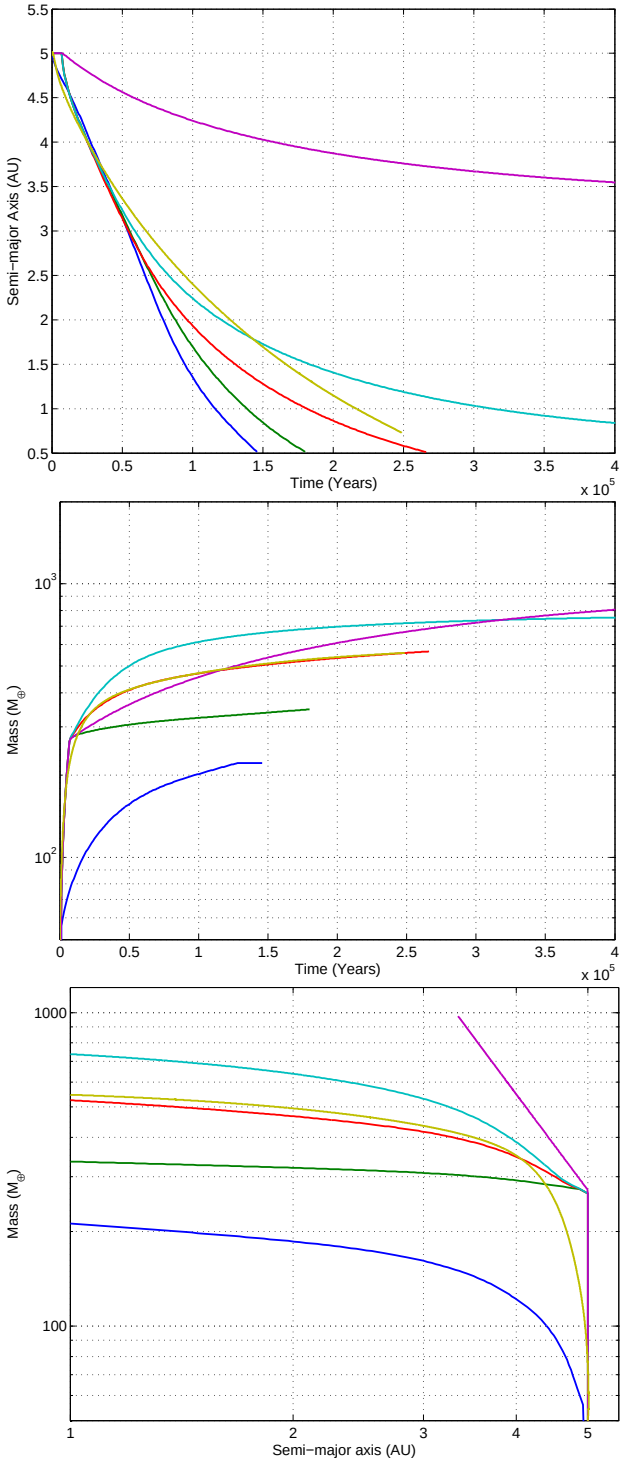

Figure 3.18: Upper panel: Semimajor axis versus time. Middle panel: Mass versus time. Lower panel: Mass versus semimajor axes. Each panel shows results for 50 $M_\oplus$ gas accreting cores in a $1 \times$ MMSN disc with different accretion routines: standard accretion prescription (blue), alternative accretion prescription evaluated at distances 5, 10, 15 R_H from the planet (green, red, cyan), results from 2-D hydro simulation (yellow), and results from Mordasini et al prescription (purple).

One issue of particular interest is why the n-body simulations presented in this chapter produce no surviving giant planets, whereas the population synthesis models of Mordasini et al. (2009), for example, are successful in forming large numbers of surviving gas giants. I have implemented the migration and gas accretion prescriptions for gap opening planets from Mordasini et al. (2009), and the results are shown by the purple curves in figure 3.18. I note that the gradient of the curve shown in the mass versus semimajor axis plot equals $-\pi$, in agreement with Mordasini et al. (2009). It is clear that there is strong disagreement between the results obtained using the Mordasini et al. prescriptions and the hydrodynamic simulation and best fit 1-D model presented in this chapter. The problem lies in their inclusion of the factor $2\Sigma_{\rm g} r_{\rm p}^2/m_{\rm p}$ in the migration torque when migration enters the so-called planet dominated regime with $m_{\rm p} > 2\Sigma_{\rm g} r_{\rm p}^2$, as this factor causes the migration to slow down too much while gas accretion continues to occur at the viscous supply rate. I note that fiducial hydrodynamic simulation was set up with $2\Sigma_{\rm g} r_{\rm p}^2 = 168\,{\rm M}_{\oplus}$, so that migration quickly enters the planet dominated regime when the planet reaches the jovian mass, which it does once reaching an orbital radius $r_{\rm p} \sim 4\,{\rm au}$. Towards the end of the simulation the planet mass reaches $550\,{\rm M}_{\oplus}$ while at an orbital radius $a_{\rm p} \sim 1\,{\rm au}$, such that the above migration slowing factor predicts that the migration speed will reduce by a factor of ~ 30. The hydrodynamic simulation does not reproduce this strong slowing of migration. The gradient observed in the mass versus semimajor axis plot for the hydrodynamic run approaches the value -0.1 rather than $-\pi$, because of the faster migration. This result suggests that the population synthesis calculations over estimate the number of gas giant planets that are able to form and survive in the models.

I have re-run the 1-D single planet simulations presented in section 3.4.1 to examine how the predictions of giant planet survival change with the new gas accretion prescription, and the results are shown in the top and bottom panels of figure 3.19 for the standard and direct photoevaporation prescriptions, respectively. I see that the conditions required for the survival of gas giants are now quite different from those obtained using the standard accretion routine, and suggest that surviving giant planets can form closer to the star. Nonetheless, I also see that giant planets must still start to undergo runaway gas accretion at orbital radii $r_{\rm p} \gtrsim 10\,{\rm au}$ in order for massive gas giant planets to survive. As such, this shows that inclusion of the new gas accretion prescription will not change the results of the simulations dramatically, because of the fact that type I migration of planetary cores to orbital radii $r_{\rm p} \sim 0.8\,{\rm au}$ almost always occurs prior to runaway gas accretion switching on. It therefore remains a significant challenge for the simulations to form cores that

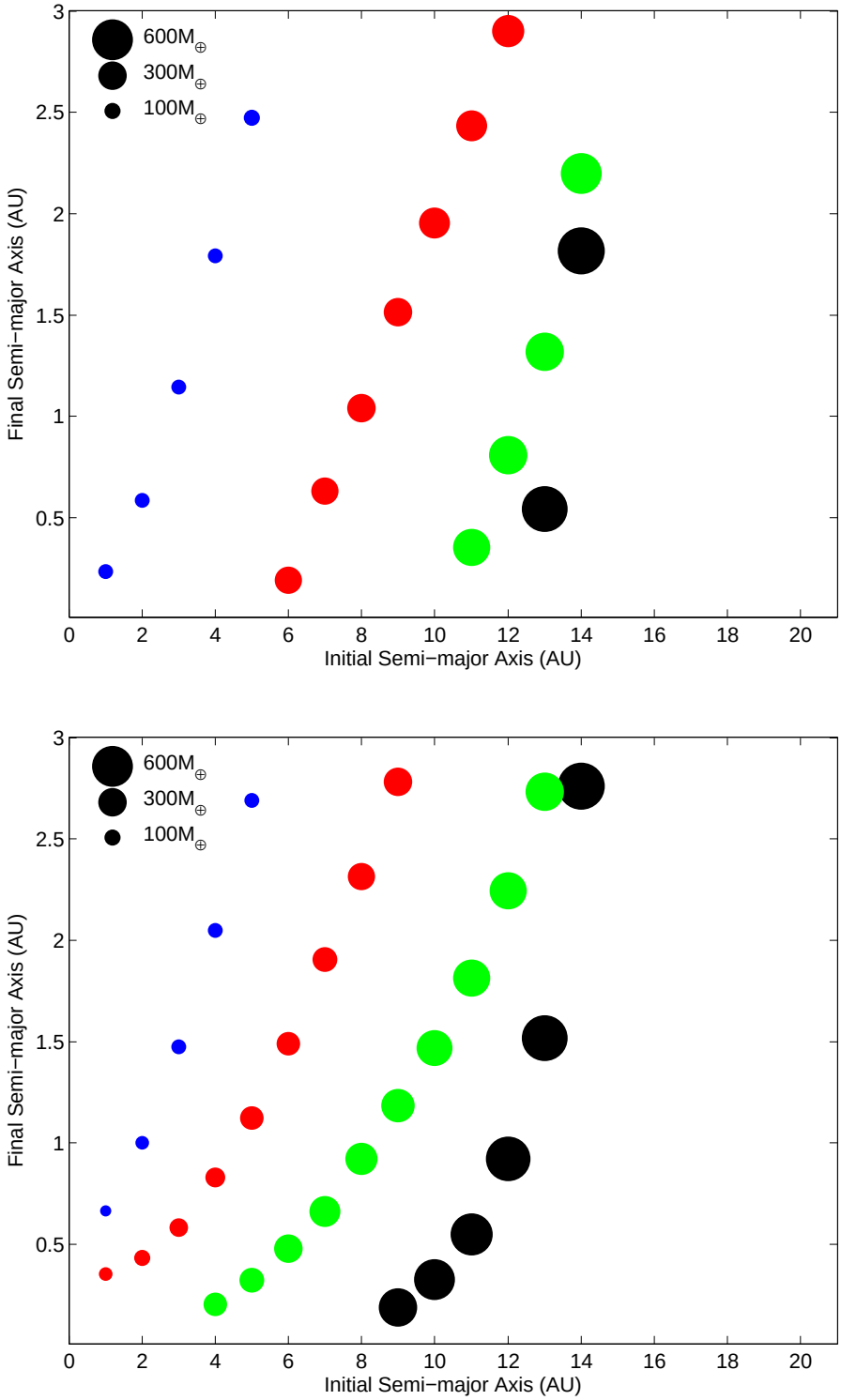

Figure 3.19: Plot of final semimajor axis versus initial semimajor axis of planets in discs undergoing rapid accretion and, standard (top panel), and direct (bottom panel) photoevaporation, starting with disc masses 0.2 × MMSN (blue), 0.4 × MMSN (red), 0.6 × MMSN (green) and 0.8 × MMSN (black).

undergo runaway gas accretion at large enough radii that they can survive as giant planets, even when a more efficient gas accretion prescription is adopted.

3.5 Discussion and Conclusions

I have presented the results of n-body simulations of planet formation in thermally evolving viscous disc models. The main results to come out of this study may be summarised as follows:

(i) Planetary growth in low mass discs (e.g. $\sim 1 \times$ MMSN) occurs relatively slowly, leading to the formation of closely-packed systems of terrestrial-mass and super-Earth planets that orbit with semimajor axes in the range $0.3 \leq a_{\rm p} \leq 20\,{\rm au}$. The close-packed nature of these systems means that they continue to evolve over time scales that are longer than the 10 Myr run times of the simulations. I anticipate these systems will achieve final stable architectures after a period of collisional accretion lasting $\gtrsim 100$ Myr.

(ii) Increases in the masses of solids available for planet building, either by increasing the solids-to-gas ratio in a disc, or by increasing the total disc mass (solids and gas), leads to multiple generations of Neptune-mass ($\sim 15\,{\rm M}_{\oplus}$) and giant planets ($\geq 30\,{\rm M}_{\oplus}$) forming and migrating into the star. This arises because the growth of planets to masses $m_{\rm p} \gtrsim 10\,{\rm M}_{\oplus}$ causes corotation torques to saturate, allowing rapid inward type I migration to occur. Once planets reach the inner disc regions where $H/r \sim 0.02$, these planets may form gaps and type II migrate into the central star. This process of formation and catastrophic migration of planets occurred in the majority of the simulations, resulting in either only low and intermediate mass planets surviving, or in extreme cases no planets surviving at all.

(iii) In a few cases, a final generation of super-Earths and Neptune-mass planets forms and migrates while the gas disc is undergoing its final stage of dispersal, allowing these final planets to survive.

(iv) The most massive planet to form in the simulations had $m_{\rm p} = 92\,{\rm M}_{\oplus}$, but was lost from the system due to type II migration. This planet formed through a collision between two already massive planets, leading to the formation of a body that was able to undergo runaway gas accretion while orbiting at $\sim 2.3\,{\rm au}$. Two out of forty simulations displayed this behaviour. More typically, giant planets in my simulations achieved final masses in the range $30 \leq m_{\rm p} \leq 45\,{\rm M}_{\oplus}$ before migrating into the star. The most massive surviving planet from all simulations was a gas-rich Neptune with $m_{\rm p} = 13\,{\rm M}_{\oplus}$.

(v) I have examined in detail the conditions required for gas giant planets to form and survive within the context of the model. I find that a planet must accrete gas, form a gap and initiate inward type II migration at an orbital radius $\gtrsim 20\,\mathrm{au}$ in order to form a surviving jovian mass planet. In my simulations, essentially all planets migrate into the inner disc regions, and reach the local gap forming mass prior to undergoing runaway gas accretion, explaining why the runs never form jovian mass planets.
(vi) Comparing 2-D hydrodynamic simulations of accreting and migrating planets with single planet calculations performed using the n-body code coupled to the 1-D disc model yields interesting results. First, this comparison has allowed me to develop a more accurate mass accretion prescription for planets that enter the runaway gas accretion phase prior to reaching the local gap forming mass. When applying this prescription to the question of when jovian mass planets can form and survive, I find that a planet must initiate runaway gas accretion at an orbital radius $\gtrsim 10\,\mathrm{au}$. Second, I find that planets migrate inward at a rate that is substantially faster than has been assumed in some population synthesis models (e.g. Mordasini et al., 2009), particularly when in the so-called 'planet dominated regime', explaining why these statistical models are more successful at forming giant planets that survive migration and grow to large masses than the models presented here. I suggest that the type II migration prescription being used in these population synthesis models causes planet migration to slow down too much, while allowing planets to accrete at the viscous rate. This suggests that the population synthesis models over-predict the numbers of gas giant planets that form and survive.

The conclusions that I have drawn about the formation and survival of gas giant planets imply that jovian mass exoplanets, and the gas giants in the Solar System, initiated formation much further out in the disc than their currently observed locations. The current understanding of disc driven migration makes it difficult to understand how this can happen for an isolated planet, as the 20–30 $\mathrm{M}_{\oplus}$ precursors to gas giant planets migrate inwards rapidly. If this conclusion is taken at face value, then one possible explanation for formation at large radius is that some cores are gravitationally scattered out to large radii through dynamical interactions between massive cores closer to the star, and these cores accrete gas as they type II migrate back into the inner disc regions. I note, however, that this mode of behaviour has not been observed in any of the simulations. A previously suggested explanation for the fact that the giant planets in our Solar System did not migrate over large distances is that Jupiter and Saturn entered into 3:2 mean motion resonance with each other, with Uranus and Neptune entering mean motion resonance with Saturn and

each other (Masset & Snellgrove, 2001; Morbidelli et al., 2007). This configuration can cause the sum of the migration torques to cancel, preventing migration of all the planets. This scenario, however, cannot be used to explain how the giant planets managed to form in the first place, as the cancellation of torques only operates once massive gap forming planets have formed. The most likely explanation of why the models fail to form surviving gas giant planets is that our current knowledge of planet migration and/or basic disc physics remains incomplete, and that some key ingredient is missing from the models that I have presented.

4 Low-mass Compact Planetary Systems

In this chapter I will present work that was published in the Monthly Notices of the Royal Astronomical Society (Coleman & Nelson, 2016a), and as such this chapter closely follows that paper.

Both radial velocity (Mayor et al., 2011) and transit surveys have shown conclusively that systems of low mass planets are common around main sequence stars, with the *Kepler* mission in particular providing some striking examples of short period compact multi-planet systems (Fabrycky et al., 2014; Lissauer et al., 2011). The most recent release of *Kepler* data contains over 4700 planet candidates, and more than 700 multi-planet systems (Mullally et al., 2015). Approximately 3000 systems show just a single transiting planet candidate, with orbital periods in the range $0.5 \leq P \leq 500$ days.

Analysis of the systems properties provides useful insight for understanding how these planets formed and evolved. One noticeable feature of the multi-systems is the paucity of first order mean motion resonances. The period ratio distribution shows features in the vicinity of the 2:1 and 3:2 resonances, suggesting that they have been dynamically important in the past, but relatively few systems are actually in a strict mean motion resonance (Fabrycky et al., 2014). Examples of systems of small planets that are in or very close to resonance, including 3 body resonances or resonant chains, include *Kepler-50* (6:5), *Kepler-60* (5:4, 4:3) (Steffen et al., 2012), *Kepler-221* (displays a 3 body resonance) (Fabrycky et al., 2014). In general the compact multi-planet systems appear to be composed of terrestrial planets, super-Earths and Neptune-like bodies. Mass estimates based on both radial velocity and transit timing variations suggest that there is a strong diversity in the mean densities of these objects, with some being rocky, some appearing to have a mixture of rock and water, and others being of very low density indicating the presence of significant fractions of H/He (Jontof-Hutter et al., 2015; Lissauer et al., 2011; Marcy et al., 2014; Wu & Lithwick, 2013). *Kepler-36* provides an example where a pair of neighbouring planets orbiting close to the 7:6 resonance have dramatically different

densities, characteristic of a rocky terrestrial inner body and an outer mini-Neptune (Carter et al., 2012). One of the most interesting facts to emerge from the data is the presence of low mass planetary systems around stars with a broad range of metallicities, including stars whose iron contents are factors of ~ 3 smaller than the solar abundance (Buchhave et al., 2014), a result that is supported by radial velocity discoveries of planets around metal-poor M dwarfs, such as *Kapteyn's star* (Anglada-Escudé et al., 2014).

A number of ideas have been put forward to explain the formation and early evolution of the compact *Kepler* and radial velocity systems, which in cases such as *Gliese 581* and *HD 69830* appear to contain in excess of $\sim 30\,M_\oplus$ of solid material within a few tenths of an au (Lovis et al., 2006; Udry et al., 2007). This concentration of solids close to the star led to classical core accretion models combined with disc driven migration being developed using population synthesis codes (Alibert et al., 2006). More recent population synthesis calculations that also include prescriptions for planet-planet interactions have also been presented (Ida & Lin, 2010). N-body simulations, combined with either hydrodynamic simulations or analytic prescriptions for migration and eccentricity/inclination damping of planetary growth, have also been used to examine the origins of such systems (Coleman & Nelson, 2014; Cossou et al., 2013; Cresswell & Nelson, 2006, 2008; Hands et al., 2014; Hellary & Nelson, 2012; McNeil & Nelson, 2009, 2010; Terquem & Papaloizou, 2007). A common outcome of these n-body simulations is the formation of resonant convoys of planets in the presence of convergent migration, an outcome that is not reflected in the *Kepler* systems. Various ideas have been put forward to explain why the resonances may be unstable, including tidal eccentricity damping followed by separation of the resonance for short period systems (Terquem & Papaloizou, 2007), stochastic migration due to local turbulence (Adams et al., 2008; Rein, 2012; Rein & Papaloizou, 2009) - a process that is likely to only operate close to the star where the disc can be thermally ionised (Desch & Turner, 2015; Umebayashi & Nakano, 1988), resonance breaking due to overstable librations (Goldreich & Schlichting, 2014), orbital repulsion due to non-linear spiral wave damping in planet co-orbital regions (Baruteau & Papaloizou, 2013; Podlewska-Gaca et al., 2012).

The paucity of mean motion resonances in the *Kepler* data has led to suggestions that the compact systems formed *in situ* through giant impacts, akin to the final stages of accumulating the terrestrial planets Chambers & Wetherill (1998), after the concentration of small planetesimals in the inner disc followed by their growth into planetary embryos (Hansen & Murray, 2012). Although this model has some success in generating non resonant multiple planet systems with inclinations that are

in good agreement with *Kepler* systems, there are difficulties in explaining how such large amounts of solids become concentrated in the inner disc, and the model fails to reproduce the numbers of single transiting planets detected by *Kepler* (Hansen & Murray, 2012). An alternative *in situ* model has been proposed by Chatterjee & Tan (2014) where pebbles/boulders concentrate and form a planet at the pressure maximum generated at the interface between the inner turbulent region of the disc and the dead zone, and exterior planets are spawned in succession by the disc being eroded outwards when the planets reach gap forming masses. While this model may be able to explain some systems, it is not clear that such a model can work for systems such as *Kepler-444* and *Kepler-186* where the planet masses are likely to be too small to form gaps, or for planetary systems in which the innermost planets orbit further from their stars than the fully active regions are expected to extend.

In this chapter I present the results from a suite of n-body simulations using an updated version of the planet formation and protoplanetary disc model presented in chapter 3. The main updates on chapter 3 include placing the inner boundary of the computational domain close to the star so that it is possible to simulate planets that can migrate to regions with orbital periods down to 1 day, addition of an active turbulent region (mimicked as a simple increase in viscosity) where disc temperatures exceed 1000 K, and a magnetospheric cavity close to the star into which planets can migrate. The aim of the work presented in this chapter is simply to examine whether or not such a comprehensive model of planet formation is able to produce planetary systems that are similar to those that have been observed, and if so under which set of conditions (disc mass, metallicity, planetesimal/boulder sizes) do these systems form.

The chapter is organised as follows. I present the physical model and numerical methods in section 4.1, and the simulation results in section 4.2. I compare the results with observations in section 4.3, and draw conclusions in section 4.4.

4.1 Physical model and numerical methods

The n-body simulations presented here were performed using the *Mercury-6* symplectic integrator (Chambers, 1999), adapted to include the disc models and physical processes described below. I use an updated version of the physical model described in chapter 3. The main elements of this model are described there, and the implemented updates are outlined in the following subsections. The basic model consists of 52 protoplanets, orbiting within a swarm of thousands of boulders or planetesi-

mals, embedded in a gaseous protoplanetary disc, all orbiting around a solar mass star. For each simulation, a single size for the boulders or planetesimals is adopted. Objects of radius $R_{\rm pl} = 10$ m are defined to be *boulders* and objects of radius $R_{\rm pl} \geq 100$ m to be *planetesimals*. These various sized objects differ from each other and from *protoplanets* or *planetary embryos* because they experience gas drag forces that vary with the size.

4.1.1 Model improvements and additions

4.1.1.1 Active turbulent region

Fully developed magnetohydrodynamic (MHD) turbulence is expected to arise in regions of the disc where the temperature exceeds 1000 K (Desch & Turner, 2015; Umebayashi & Nakano, 1988). To account for the increased turbulent stress, the viscous α parameter is increased when the temperature rises above 1000 K using the prescription

$$\alpha(r) = \begin{cases} 2 \times 10^{-3} & r > r_{\rm s}, \\ 2 \times 10^{-3} + 4 \times 10^{-3} & \\ \times \left(\tanh \left(\dfrac{3(r_{\rm s} - r - 5H(r))}{5H(r)} \right) + 1 \right) & r \leq r_{\rm s}, \end{cases} \tag{4.1}$$

where $r_{\rm s}$ represents the outermost radius with temperature greater than 1000 K, and $H(r)$ is the local disc scale height. This transition leads to a maximum $\alpha = 10^{-2}$ in the hottest parts of the disc sitting within ~ 0.5 au from the star at the beginning of the simulations.

4.1.1.2 Magnetospheric cavity and inner boundary

A rotating star with a strong dipole magnetic field may create an inner disc cavity through magnetic torques repelling the disc, and this can provide an effective mechanism for preventing planets migrating into their host stars (e.g. Lin et al., 1996). I include a cavity in the simulations by assuming that the outer edge of the cavity is truncated at 0.05 au, corresponding to an orbital period of ~ 4 d, in agreement with the spin periods of numerous T Tauri stars (Herbst & Mundt, 2005). Planets are able to migrate into this region through either type I or type II migration. A planet that has not reached the local gap opening mass halts its migration once it reaches the cavity edge (the assumption here is that strong corotation torques will stop its migration, as shown for migrating circumbinary planets (Pierens & Nelson,

Parameter	Value
Disc inner boundary	0.02 au
Cavity outer boundary	0.05 au
Disc outer boundary	40 au
Number of cells	1000
Σ_g(1 au)	1731 g /cm^2
Stellar Mass	1M$_\odot$
R_S	2R$_\odot$
T_S	4280 K

Table 4.1: Disc and stellar model parameters

2007), and those migrating in towards a single central star (Benítez-Llambay et al., 2011)). A gap forming planet continues to migrate into the cavity until it reaches the 2:1 orbital resonance with the cavity outer edge, at which point disc torques are switched off. This resonance is located at ~ 0.0315 au from the star. It should be noted that a second planet entering the cavity can nudge a planet sitting at the 2:1 resonance location on to a shorter period orbit. The inner boundary of the computational domain is located just inside 0.02 au (corresponding to an $\sim$ 1 d orbit period). Any planets whose semimajor axes are smaller than the boundary radius are removed from the simulation and are assumed to have hit the star. I note that the inner boundary adopted in chapter 3 corresponded to an orbital period of 20 d.

A summary of the disc and stellar parameters adopted in all simulations is given in table 4.1.

4.1.1.3 Opacity

I make a small change to the opacity prescription used in chapter 3 by assuming that half of the disc solids are in submicron sized dust particles, with the remainder being in planetary embryos and planetesimals/boulders. The opacity used to calculate the thermal diffusion time-scale in the disc is thus multiplied by the factor $F_{\rm opacity} = 1/2 \times {\rm M_{ratio}}$ where ${\rm M_{ratio}}$ is the ratio of the disc metallicity to the solar metallicity. $F_{\rm opacity} = 1/2$ for a disc with solar metallicity, 1/4 for a disc with half the solar metallicity, and 1 for a disc with twice solar metallicity. This modification of the opacity affects both the equilibrium disc temperature and estimates for when the corotation torques acting on planets saturate.

4.1.1.4 Gas envelope accretion

Once a protoplanet grows to a mass that exceeds 3 $M_\oplus$ it starts to accrete a gaseous envelope. I have improved on the fits to the 1-D giant planet formation models of Movshovitz et al. (2010) used in chapter 3. In units of Earth masses and Myr, the improved scheme gives a gas accretion rate of:

$$\frac{dm_{ge}}{dt} = \frac{4.5}{96.65} \exp\left(\frac{m_{ge}}{22}\right) m_{core}^{2.4} \exp\left(\frac{m_{ge}}{m_{core}}\right). \tag{4.2}$$

This scheme allows for the continuation of core growth after a gaseous envelope has been acquired, while allowing the rate of envelope accretion to adapt to the varying core and envelope mass. Figure 4.1 shows gas accretion on to 3, 10 and 30 $M_\oplus$ cores without the influence of migration or core growth. These are similar to the models in Hellary & Nelson (2012) and chapter 3, but are in better agreement with the models presented by Movshovitz et al. (2010). Ideally, I would incorporate self-consistent models of gas envelope accretion in the simulations, but unfortunately this is too expensive computationally to run within the current model. While the fits to the Movshovitz et al. (2010) models allows gas accretion to occur at the rates prescribed in that work, these fits do not change according to the local conditions in the disc, or to a time varying planetesimal accretion rate. This is something that will be addressed in future work.

The gas accretion rate given by equation 4.2 is valid until the planet forms a gap within the disc, after which the gas accretion rate switches to either the value obtained from equation 4.2 or the viscous supply rate given

$$\frac{dm_{ge}}{dt} = 3\pi\nu\Sigma_g, \tag{4.3}$$

whichever is smaller. Here Σ_g and ν are the surface density and viscosity of the gas that sits at a distance of 10 Hill radii exterior to the planet's location. This prescription is chosen because the planet sits in a deep gap and so the supply rate of gas must be evaluated at a location in the disc that sits outside the fully evacuated gap region. The precise value that is quoted here was determined in section 3.4.2 where different evaluation distances were tested against 2-D hydrodynamic simulations, and 10 Hill radii showed the best agreement. The gas accretion routine used here conserves mass by removing gas, that is accreted on to the planet, from the surrounding disc.

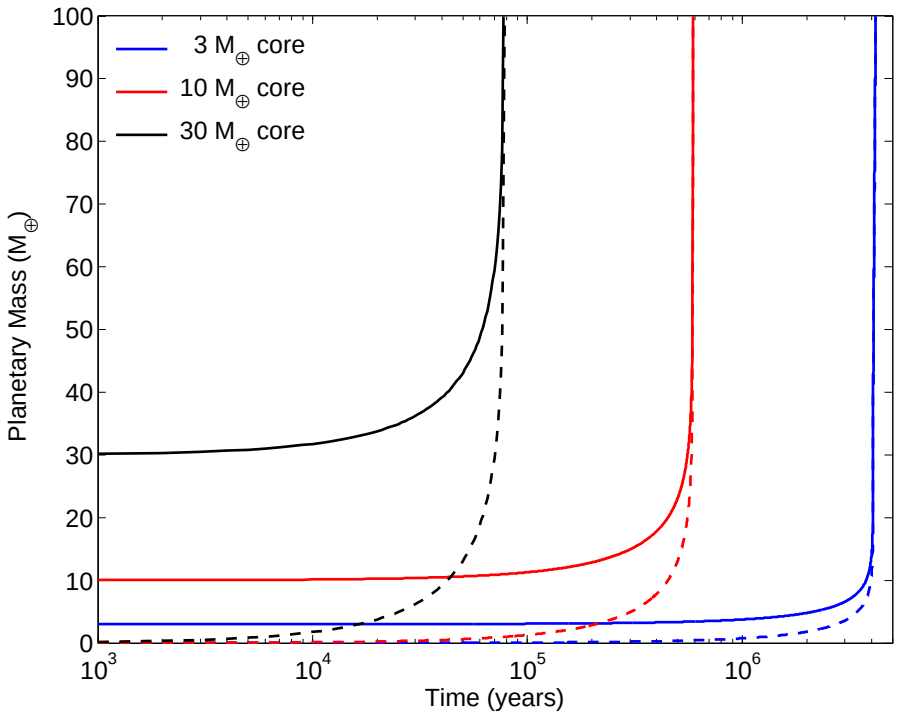

Figure 4.1: Gas accretion on to 3, 10, and 30 $M_\oplus$ cores versus time at 5 au. Solid lines denote total mass, whilst dotted lines denote the envelope mass.

4.1.1.5 Aerodynamic drag

Solid bodies experience aerodynamic drag, reducing semimajor axes whilst simultaneously damping eccentricities and inclinations. Stoke's drag is applied to planetesimals/boulders (Adachi et al., 1976) when the size of the body is greater than twice the molecular mean free path (λ). This switches to Epstein drag when the mean free path exceeds roughly half the planetesimal size (Weidenschilling, 1977). Here λ is given by

$$\lambda = \frac{\mu m_{\rm H}}{\sigma \rho_{\rm g}}, \tag{4.4}$$

where σ is the collision cross-section, μ is the gas mean molecular weight, and $\rho_{\rm g}$ is the local gas density. When the planetesimal size is greater than $\frac{9}{4}\lambda$, I use Stokes' drag law as (Adachi et al., 1976):

$$\mathbf{F}_{\rm st} = m_{\rm pl}\left(\frac{-3\rho_{\rm g}C_{\rm D}}{8\rho_{\rm pl}R_{\rm pl}}\right) v_{\rm rel}\mathbf{v}_{\rm rel} \tag{4.5}$$

Here, a subscript 'pl' corresponds to planetesimals, $\rho_{\rm pl}$ is the internal density of planetesimals, $R_{\rm pl}$ is the planetesimal radius and $v_{\rm rel}$ is the relative velocity between the gas and planetesimals. $C_{\rm D}$ is the dimensionless drag coefficient, taken as a

function of the Reynolds number ($R_{\rm e}$) given below

$$C_{\rm D} = \begin{cases} 24R_e^{-1} & R_e < 1 \\ 24R_e^{-0.6} & 1 \leq R_e < 800 \\ 0.44 & R_e \geq 800 \end{cases} \tag{4.6}$$

When the planetesimal size is equal to $9\lambda/4$, both drag regimes are equal, thus a transition to the Epstein drag law given as (Weidenschilling, 1977)

$$\mathbf{F}_{\rm ep} = m_{\rm pl} \left(\frac{\rho}{\rho_{\rm pl} R_{\rm pl}} \right) v_{\rm rel} c_s \tag{4.7}$$

When the planetesimal size is smaller than $9\lambda/4$ I only use the Epstein drag law.

4.1.2 Initial conditions

All simulations were run for 10 Myr, allowing the systems of formed planets to continue evolving through scattering and collisions after the dispersal of the protoplanetary discs. A run time of 10 Myr is insufficient for accretion between embryos orbiting at large distances to reach completion, and some of the simulations were halted when systems of planets on longer period orbits were still evolving. This is unavoidable for systems in which large-scale migration leads to the formation of short-period planets, with longer period planets remaining at larger semimajor axes, since the time steps become prohibitively short for Gyr run times to be achieved. For this reason, most of the discussion will focus on the short-period systems that arise in the simulations as these are dynamically much more mature than the longer period planets.

The runs were all initiated with 52 planetary embryos, of mass 0.1 $\rm M_{\oplus}$, separated by 10 mutual Hill radii, and with semimajor axes between 1 and 20 au. These were embedded in a swarm of thousands of planetesimals/boulders, that were distributed with semimajor axes between 0.5 and 20 au, and with masses either 10, 20 or 50 times smaller than the embryos, depending on the metallicity of the system. (This varying mass ratio between embryos and planetesimals was implemented to keep the numbers of planetesimals at a number that allowed the simulations to run on reasonable time-scales. Between 3000 and 8000 planetesimals/boulders were used and run times for the individual simulations varied between 3 and 9 months.) The effective physical radii of planetesimals were set to either 10 m, 100 m, 1 km and 10 km, such that the primary feedstock of the accreting protoplanets ranged from being boul-

Simulation	Disc mass (MMSN)	Metallicity (solar value)	Planetesimal radius (km)	Formation mode (A+B)
K10.50.01 A/B	1	0.5	0.01	LPG
K10.50.1 A/B	1	0.5	0.1	LPG
K10.51 A/B	1	0.5	1	LPG
K10.510 A/B	1	0.5	10	LPG
K110.01 A/B	1	1	0.01	MGM
K110.1 A/B	1	1	0.1	LPG
K111 A/B	1	1	1	LPG
K1110 A/B	1	1	10	LPG
K120.01 A/B	1	2	0.01	GFSM
K120.1 A/B	1	2	0.1	MGM
K121 A/B	1	2	1	LPG
K1210 A/B	1	2	10	LPG
K1.50.50.01 A/B	1.5	0.5	0.01	MGM
K1.50.50.1 A/B	1.5	0.5	0.1	LPG
K1.50.51 A/B	1.5	0.5	1	LPG
K1.50.510 A/B	1.5	0.5	10	LPG
K1.510.01 A/B	1.5	1	0.01	GFSM
K1.510.1 A/B	1.5	1	0.1	MGM
K1.511 A/B	1.5	1	1	LPG
K1.5110 A/B	1.5	1	10	LPG
K1.520.01 A/B	1.5	2	0.01	GFSM
K1.520.1 A/B	1.5	2	0.1	GFSM
K1.521 A/B	1.5	2	1	LPG
K1.5210 A/B	1.5	2	10	LPG
K20.50.01 A/B	2	0.5	0.01	MGM
K20.50.1 A/B	2	0.5	0.1	MGM
K20.51 A/B	2	0.5	1	LPG
K20.510 A/B	2	0.5	10	LPG
K210.01 A/B	2	1	0.01	GFSM
K210.1 A/B	2	1	0.1	MGM
K211 A/B	2	1	1	LPG
K2110 A/B	2	1	10	LPG
K220.01 A/B	2	2	0.01	GFSM
K220.1 A/B	2	2	0.1	GFSM
K221 A/B	2	2	1	MGM
K2210 A/B	2	2	10	LPG

Table 4.2: Simulation parameters with formation behaviours as follows: LPG - limited planetary growth, MGM - moderate growth and migration, GFSM - giant formation and significant migration.

Classification	Mass	Rock %	Ice %	Gas %
Rocky terrestrial	$m_{\rm p} < 3\,{\rm M}_{\oplus}$	$> 70\%$	$< 30\%$	0%
Water-rich terrestrial	$m_{\rm p} < 3\,{\rm M}_{\oplus}$	$< 70\%$	$> 30\%$	0%
Rocky super-Earth	$3\,{\rm M}_{\oplus} \leq m_{\rm p} < 10\,{\rm M}_{\oplus}$	$> 60\%$	$< 30\%$	$< 10\%$
Water-rich super-Earth	$3\,{\rm M}_{\oplus} \leq m_{\rm p} < 10\,{\rm M}_{\oplus}$	N/A	$> 30\%$	$< 10\%$
Mini-Neptune	$3\,{\rm M}_{\oplus} \leq m_{\rm p} < 10\,{\rm M}_{\oplus}$	N/A	N/A	$> 10\%$
Gas-rich Neptune	$10\,{\rm M}_{\oplus} \leq m_{\rm p} < 35\,{\rm M}_{\oplus}$	N/A	N/A	$> 10\%$
Gas-poor Neptune	$10\,{\rm M}_{\oplus} \leq m_{\rm p} < 35\,{\rm M}_{\oplus}$	N/A	N/A	$< 10\%$
Gas-dominated giant	$m_{\rm p} \geq 35\,{\rm M}_{\oplus}$	N/A	N/A	$> 50\%$
Core-dominated giant	$m_{\rm p} \geq 35\,{\rm M}_{\oplus}$	N/A	N/A	$< 50\%$

Table 4.3: Planetary classification parameters based on their composition and the mass fraction of their gaseous envelope. Note that water-rich planets are so-called because they accrete water ice in solid form that originates from beyond the snow line.

ders to being large planetesimals whose evolution differed principally because of the strengths of the gas drag forces that they experienced. Planetesimals/boulders in the simulations represent a larger group of particles, with realistic masses depending on their physical radii, whose averaged orbits allow them to be approximated as a single massive superparticle with an effective physical radius. Eccentricities and inclinations for protoplanets and planetesimals/boulders were randomized according to a Rayleigh distribution, with scale parameters $e_0 = 0.01$ and $i_0 = 0.^{\circ}25$, respectively.

Collisions between protoplanets and other protoplanets or planetesimals resulted in perfect sticking. I neglect planetesimal-planetesimal interactions and collisions in the simulations as their inclusion would greatly increase computation time.

The gas disc masses simulated were 1, 1.5 and 2 times the mass of the minimum mass solar nebula (Hayashi, 1981, MMSN). I also vary the disc metallicity so that the initial solids-to-gas mass ratios are equal to 0.5, 1 and 2 times the solar value for the different models. I smoothly increase the mass of solids exterior to the snow line by a factor of 4, as described in Hellary & Nelson (2012). I track the changes in planetary compositions throughout the simulations, as planets can accrete material originating either interior or exterior to the snow line.

Combining the three different gas disc masses, the three values of metallicity/solids-to-gas mass ratio, and the four different planetesimal/boulder sizes gives a total of 36 parameter variations. Two instances of each parameter set were run, where only the random number seed to generate initial particle positions and velocities was changed, giving a total of 72 simulations. The full set of run parameters are detailed in table 4.2.

4.2 Results

In order to provide context for the n-body simulations, I begin the discussion of the results by describing the general evolution of the disc models, and the orbital evolution of the protoplanets and planetesimals. I then describe the results of the new simulations. The simulation results are divided into three distinct categories: *limited planetary growth (LPG)*; *moderate growth and migration (MGM)*; *giant formation and significant migration (GFSM)*. For each category, I present the details of one or two representative runs, with table 4.2 listing the category for each run. Runs that displayed LPG resulted in no planet masses growing above $3\,M_\oplus$ during the gas disc lifetime (and hence the amount of type I migration was also modest), although further growth beyond $3\,M_\oplus$ could occur after dispersal of the gas disc. Runs showing MGM formed planets in the mass range $3 < m_p < 35\,M_\oplus$ during the gas disc lifetime. Simulations categorised as GFSM formed planets with masses $\geq 35\,M_\oplus$ during the gas disc lifetime, and generally displayed multiple bursts of planetary accretion accompanied by large scale migration that ended up with one or more planets migrating into the central star. The planets that are formed in the simulations have different compositions in terms of rocky, icy and gaseous material. I use a classification system for the planets based on their compositions, and these are defined in table 4.3.

4.2.1 Typical behaviour

4.2.1.1 Disc evolution with an active inner turbulent region

Figure 4.2 shows the evolution of a 1 × MMSN disc model. Disc surface density profiles are shown in the left-panel, temperature profiles are shown in the middle panel, and H/r profiles are shown in the right-panel. The times corresponding to each profile are indicated in the middle panel, expressed as a percentage of the disc lifetime. For a 1 × MMSN disc this is equal to 4.6 Myr. For a 1.5 × MMSN disc the lifetime is 5.5 Myr, and a 2 × MMSN disc disperses completely after 6.5 Myr. The inclusion of a turbulent inner region where $T > 1000$ K causes a dip in surface density due to the higher viscosity there, and it can be seen that as time progresses the location of the transition to the turbulent region moves in towards the star because the reduction in surface density reduces the viscous heating rate and the opacity. The turbulent region disappears when the disc temperature no longer exceeds 1000 K anywhere in the disc, as shown by the yellow line in figure 4.2. This happens in all of the disc models when the disc mass falls to approximately 10% of

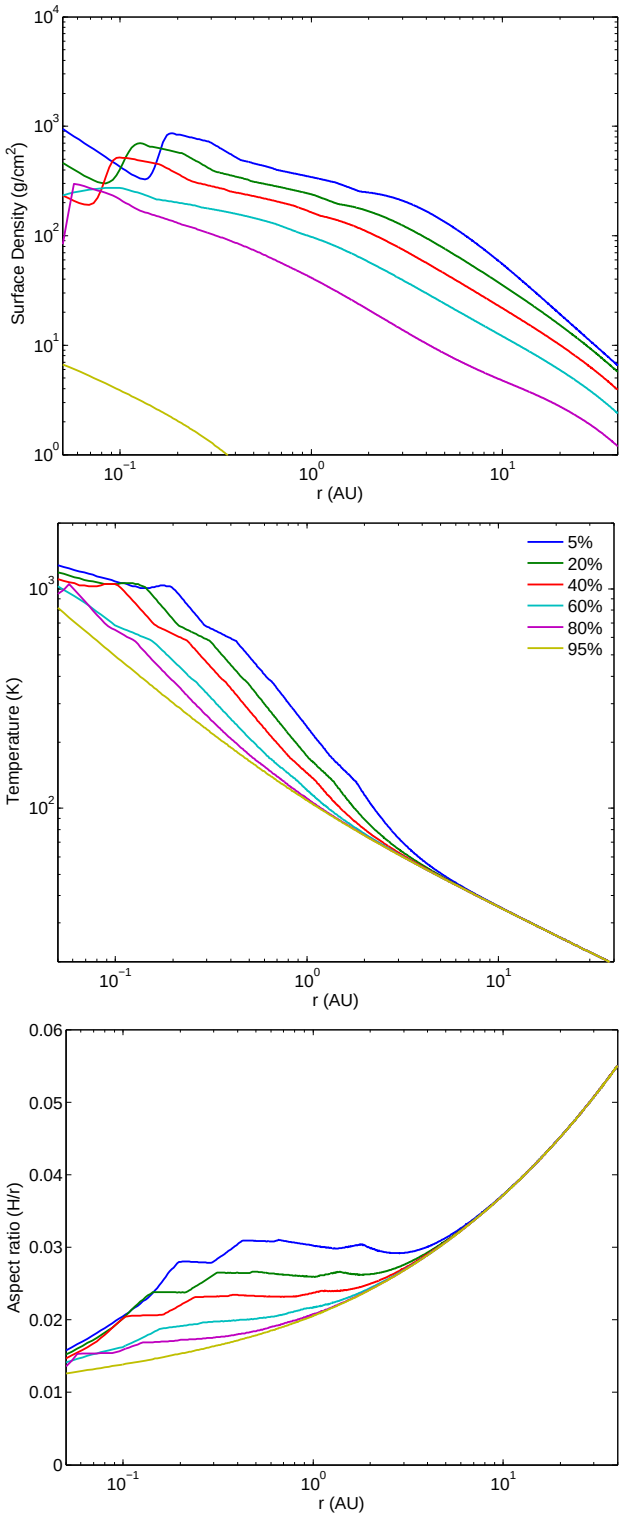

Figure 4.2: Gas surface densities, temperatures and aspect ratios for 5, 20, 40, 60, 80 and 95 per cent (top-bottom lines) of the disc lifetime in a $1 \times$MMSN disc (lifetime: 4.6 Myr)

the MMSN, which occurs 0.5 Myr before complete dispersal of the gas disc.

The drop in local surface density caused by the active turbulent region creates a planet trap for low-mass planets (Masset et al., 2006). The trap moves in with the active region until it reaches the inner disc edge located at 0.05 au (assumed in the model to be outer edge of the magnetospheric cavity). Once at the disc inner edge, the trap created from the active turbulent region disappears due to the temperature in the disc falling below 1000 K. However the outer edge of the magnetospheric cavity acts as a planet trap for low-mass planets, until they can open a gap in the disc and undergo type II migration into the cavity as discussed in section 4.1.1.2. It should be noted that the reduction of the temperature below 1000 K at all disc locations arises because of the adoption of a 1-D disc model which neglects irradiation heating of the disc along radial lines of sight.

On longer time-scales the removal of gas by the photoevaporative wind causes the disc to disperse. The loss of mass at large radius results in the inner disc emptying viscously on to the star, followed by removal of the remnant outer disc by the wind (Clarke et al., 2001).

4.2.1.2 Protoplanet migration

Type I migration of planets is controlled by both Lindblad and corotation torques. In the disc models Lindblad torques are negative and corotation torques are generally positive. Strong, positive corotation torques arise in regions where the radial entropy gradient is negative, and this is usually the case in the inner disc regions where viscous heating dominates over stellar irradiation. Corotation torques may saturate when either the viscous or thermal time-scale differs significantly from the periods of horseshoe orbits executed by gas in the corotation region. Figure 4.3 shows contours that illustrate the migration behaviour of planets as a function of their masses and semimajor axes in a 1 $\times$ MMSN disc with solar metallicity where half of the solid material is assumed to be in large bodies that do not provide any opacity. Dark blue regions correspond to strong outward migration, red regions correspond to strong inward migration, and white contours represent regions of parameter space where the corotation and Lindblad torques balance each other. These are referred to as *zero-migration zones*. The planet trap created by the inner turbulent region is shown by the innermost blue contour in the first three panels in figure 4.3. Planets in blue regions migrate outwards until they come to white regions where they stop migrating. These can and do act as planet convergence zones. Planets in red regions migrate inwards, and if their masses are in the appropriate range they stop when

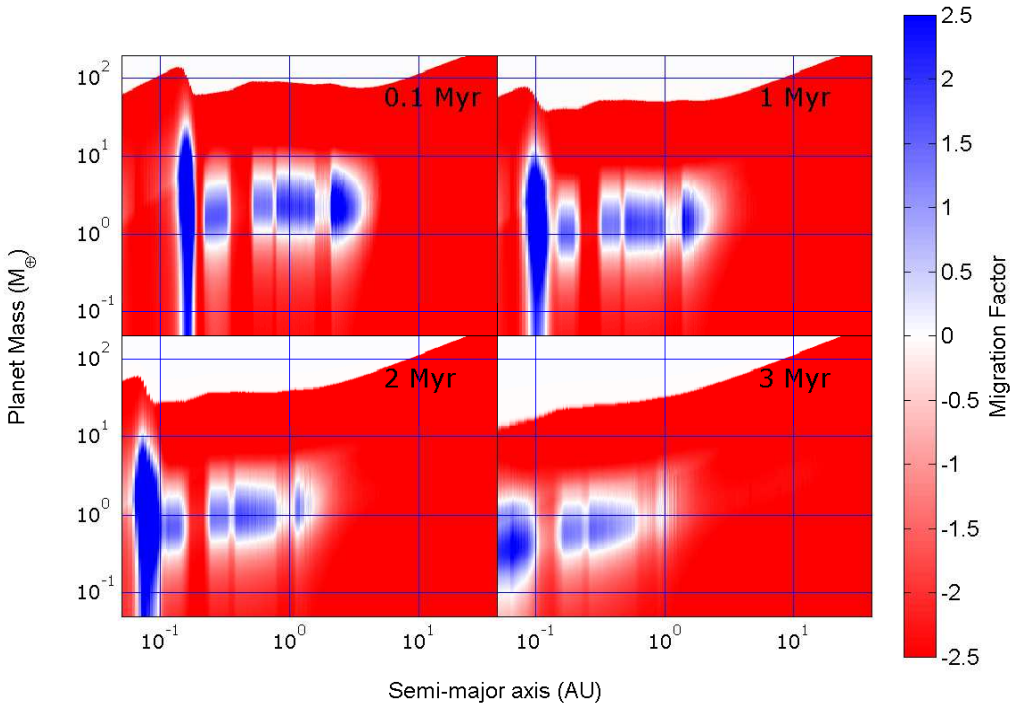

Figure 4.3: Contour plots showing regions of inwards (red) and outwards (blue) migration) in a $1 \times$ MMSN disc at t = 0.1 Myr (top left), 1 Myr (top right), 2 Myr (bottom left) and 3 Myr (bottom right).

they arrive at zero-migration zones. Over time the migration contours evolve as the disc surface density and thermal time-scale decrease, and planets sitting in zero-migration zones slowly drift in towards the star on the disc evolution time-scale. A planet that grows in mass so that it exceeds $\sim 10\,M_\oplus$ will be too massive to sit in a zero-migration zone in the main body of the disc, and will migrate inwards rapidly before being trapped at the transition to the inner turbulent region. As this disappears the planet will drift into the magnetospheric cavity interior to 0.05 au where it will stop if it is below the local gap forming mass. If it exceeds the gap forming mass then it will migrate to the 2:1 resonance location with the cavity outer edge before halting its migration. If another planet enters the cavity then it may push the previous one through the inner boundary of the computational domain interior to 0.02 au. The decrease in H/r values in the inner disc regions (and with time) means that it becomes possible for quite low-mass planets to open gaps in the disc and enter type II migration. Similarly, planets that accrete significant gas envelopes can become giant planets and open gaps. The transition to gap formation and type II migration is shown by the boundary between the red and white contours in the top regions of the panels in figure 4.3.

Each panel in figure 4.4 shows the migration histories of individual planets of

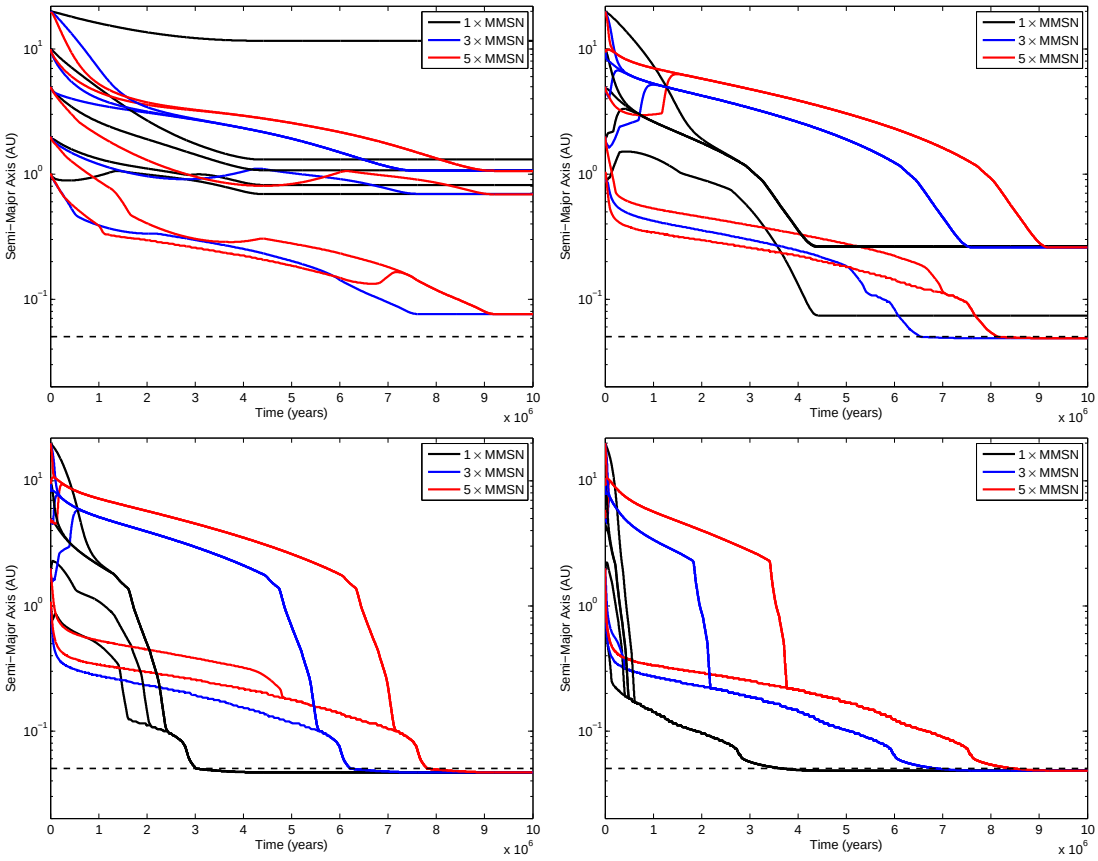

Figure 4.4: Semimajor axis evolution for planets with different masses in 1, 3 and 5 × MMSN discs: 1 $M_\oplus$ (top left), 3 $M_\oplus$ (top right), 5 $M_\oplus$ (bottom left) and 10 $M_\oplus$ (bottom right). The dotted line represents the disc inner edge.

mass 1 $M_\oplus$ (top left), 3 $M_\oplus$ (top right), 5 $M_\oplus$ (bottom left) and 10 $M_\oplus$ (bottom right) embedded in discs with masses 1, 3 and 5 × MMSN. In each panel, I plot the migration tracks of planets that have initial semimajor axes 1, 2, 5, 10 and 20 au. Note that I only consider disc masses in the range 1 - 2 × MMSN in the full n-body simulations described below, but larger disc masses are included in this discussion to illustrate how migration changes in significantly heavier discs. Looking at the 1 $M_\oplus$ migration trajectories, it is clear that planets starting with $a_p \geq 1$ au in a 1 × MMSN disc cannot migrate interior to 0.7 au because of the corotation torques. Even in heavier discs 1 $M_\oplus$ planets cannot migrate very close to the star and become stranded outside the magnetospheric cavity at ~ 0.07 au. The implications of this are clear. The origin of compact, short-period low-mass planet systems such as *Kepler-444* (Campante et al., 2015) or *Kepler-42* (Muirhead et al., 2012) cannot be explained by formation at significantly larger radii than where they are observed today, followed by large-scale inward migration. An *in situ* formation

model, perhaps aided by the inward drift of solids in the form of pebbles, boulders or small planetesimals would seem to be more plausible. More generally, *in situ* models of planet building cannot rely on the delivery of large numbers of low-mass protoplanets to inner disc regions through type I migration because they are not able to migrate across the required distances during gas disc lifetimes. Looking at the $3\,M_{\oplus}$ migration trajectories, I see that these planets are also unable to reach the inner magnetospheric cavity unless orbiting in heavier discs. Guaranteed arrival of planets to the very innermost regions of the disc only occurs when planet masses reach $m_{\rm p} \geq 5\,M_{\oplus}$. Periods of rapid migration observed in the lower left and right-panels of figure 4.4 arise when the planets saturate their corotation torques. Slow drift arises when the planets are sitting in zero-migration zones.

4.2.1.3 Planetesimal orbital evolution

Aerodynamic drag causes planetesimal eccentricities and inclinations to be damped and their semimajor axes to decrease. The 10 m boulders in the simulations experience rapid migration such that a body located initially at 1 au migrates to the inner turbulent region of the disc within approximately 10^3 yr, and a 10 m boulder located at 20 au reaches there in just over 10^6 years. A 100 m body located initially at 1 au reaches the inner turbulent region within $\sim$ 0.5 Myr, and one located initially at 10 au will reach $\sim$ 6 au within the disc lifetime. The larger 1 and 10 km bodies show very little drag-induced migration during disc lifetimes.

The levels of planetesimal/boulder eccentricity excitation due to gravitational stirring by protoplanets at the beginning of the simulations depends strongly on their sizes. I find that the mean eccentricity for the 10 m bodies is $e_{\rm pl} \sim 3$ - $5\ \times 10^{-4}$, for the 100 m bodies $e_{\rm pl} \sim 3$ - $4\ \times 10^{-3}$, for the 1 km bodies $e_{\rm pl} \sim 10^{-2}$ and for the 10 km planetesimals $e_{\rm pl} \sim 2$ - $3\ \times 10^{-2}$. Given the importance of gravitational focusing in determining planetary growth rates, it is clear that I should expect smaller boulders/planetesimals to accrete much more efficiently on to the protoplanets. The mobility of the boulders also means that planetary embryos can grow beyond their nominal isolation masses on short time-scales before they start to undergo significant type I migration. For protoplanets whose masses are too small for type I migration, it is the mobility of boulders and small planetesimals in the models that enables growth to occur above the isolation mass.

4.2.2 Limited Planetary Growth (LPG)

The mass growth of planets is expected to be slow when either the abundance of solids in the disc is small, and/or when the main feedstock for planet building is in the form of large planetesimals whose velocity dispersion is damped weakly by the gas disc. Consequently, in the limit of slow growth, no gas accreting cores with masses $m_{\rm p} \geq 3\,{\rm M}_{\oplus}$ will be able to form before dispersal of the gas disc, and planet migration will be modest. This outcome was obtained for all but one disc model that I considered with planetesimal sizes being either 1 or 10 km (the exception being the heaviest disc with mass 2 × MMSN, 2× solar metallicity and 1 km planetesimals). At the other end of the boulder/planetesimal size scale when 10 m boulders were included in the runs, this outcome was obtained only for the disc model with the lowest mass and metallicity. Overall, these results are in agreement with the low solid abundance models presented in chapter 3.

The simulations labelled as LPG in table 4.2 all displayed this mode of behaviour, and below I describe in detail the results of runs K10.50.01B and K2210B as they have very different disc properties, but result in similar outcomes.

4.2.2.1 Run K10.50.01B

Run K10.50.01B had a disc mass of $1 \times$ MMSN, $0.5\times$ solar metallicity, and boulder radii $R_{\rm pl} = 10$ m. The combined mass in protoplanets and boulders was equal to $11\,{\rm M}_{\oplus}$, distributed between $0.5 \leq r \leq 20\,{\rm au}$, with the mass in protoplanets being initially $5.2\,{\rm M}_{\oplus}$ (52 protoplanets each of mass $0.1\,{\rm M}_{\oplus}$).

The evolution of the protoplanet masses, semimajor axes and eccentricities are shown in figure 4.5 (note that boulders/planetesimals are not represented in this and similar plots). Accretion of boulders by embryos, and mutual collisions, led to the growth of protoplanets to masses in the range $0.6 \leq m_{\rm p} \leq 0.8\,{\rm M}_{\oplus}$ during the first 1 Myr. These embryos migrated towards the zero-migration zone located at $\sim 3\,{\rm au}$ and drifted in towards the star on the disc evolution time. Embryos located beyond 10 au grew more slowly, and remained near their initial locations throughout the simulation. I note that a couple of embryos at the inner edge of the solids disc experienced a short lived burst of migration by being shepherded inwards by a swarm of migrating boulders at the beginning of the simulation.

Despite the convergence of planets in the zero-migration zone, the frequency of collisions was limited by bodies entering mean motion resonances. Boulder collisions with embryos were scarce after 1 Myr, due to the drag-induced migration of boulders into the inner disc occurring on this time-scale. With the maximum mass of a

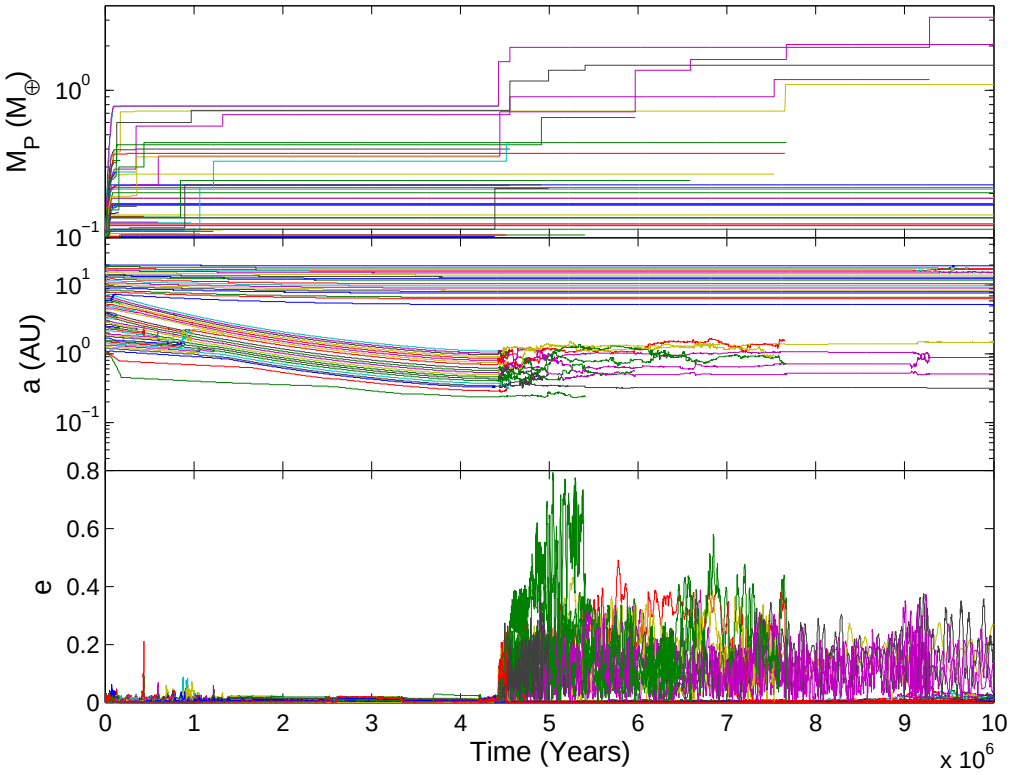

Figure 4.5: Evolution of masses, semimajor axes and eccentricities of all protoplanets in simulation K10.50.01B.

planetary embryo in the system being $0.8\,\mathrm{M}_\oplus$ throughout the lifetime of the gas disc, migration remained limited to a slow inwards drift. No planets accreted gaseous envelopes.

The disc photoevaporated after 4.6 Myr, allowing embryo eccentricities to grow dramatically through mutual encounters because gas disc damping had been removed. Collisions among the inner group of protoplanets led eventually to the formation of a system of four inner bodies with masses in the range $1.1 \leq m_\mathrm{p} \leq 3.4\,\mathrm{M}_\oplus$ after 10 Myr when the simulation ended. These bodies all accreted significant amounts of material from beyond the snowline, and I class them as either water-rich terrestrials or water-rich super-Earths, orbiting with periods $60 \leq P \leq 700$ d. There were a significant number of protoplanets orbiting exterior to 5 au still undergoing collisional evolution at 10 Myr when the simulation ended, and these would have continued accreting if the run had been extended.

4.2.2.2 Run K2210B

I turn now to run K2210B, for which the disc mass was $2 \times$ MMSN, the metallicity was $2 \times$ solar, planetesimal radii were 10 km, and the disc lifetime was 6.6 Myr. The

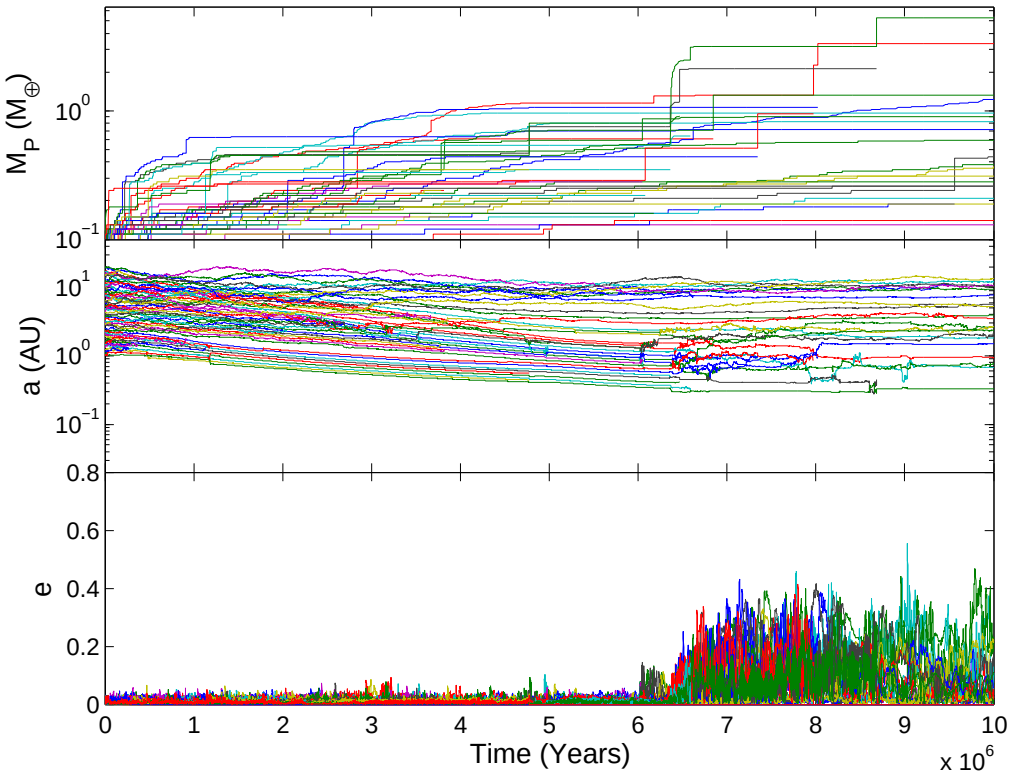

Figure 4.6: Evolution of masses, semimajor axes and eccentricities of all protoplanets in simulation K2210B.

initial mass in embryos and planetesimals was $87\,\mathrm{M}_\oplus$, this being the most solids-rich disc considered in this suite of simulations. In spite of this, planetary growth was very limited because of the weakly-damped planetesimals.

The evolution of protoplanet masses, semimajor axes and eccentricities are shown in figure 4.6. Protoplanets grew to masses $0.7\,\mathrm{M}_\oplus$ after 1 Myr, and when the disc dispersed the maximum embryo mass was approximately $2.5\,\mathrm{M}_\oplus$, there having been a couple of planets that accreted rapidly just prior to the final remnants of the gas being removed. Migration was limited, with the innermost body orbiting at 0.4 au at the point of gas disc dispersal. After removal of the gas the system entered a stage of chaotic evolution, with on-going collisions occurring within the embryo swarm when the run ended at 10 Myr. Approximately 20 planets remained at this stage, the most massive being $m_\mathrm{p} = 5.3\,\mathrm{M}_\oplus$. No planets accreted gaseous envelopes.

4.2.3 Moderate growth and migration (MGM)

Table 4.2 shows that a total of 16 out of 72 simulations exhibited *moderate growth and migration*. MGM runs are characterised by the formation of planets with masses $3 \leq m_\mathrm{p} < 35\,\mathrm{M}_\oplus$ before the end of the gas disc lifetime, with little or no loss of

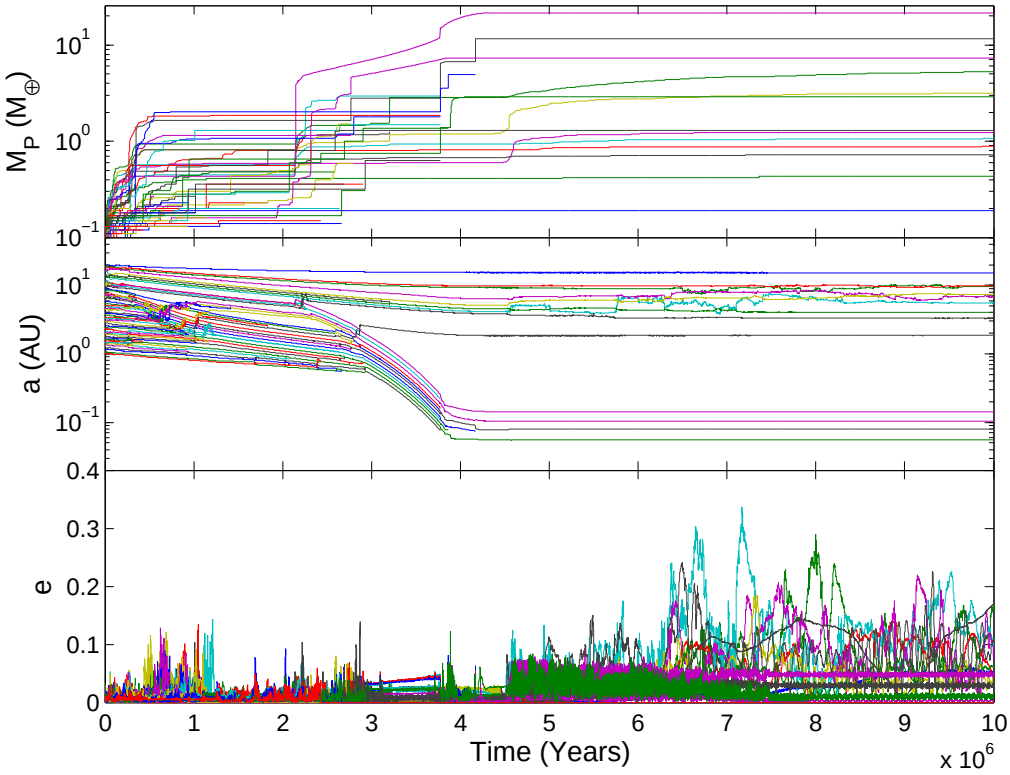

Figure 4.7: Evolution of masses, semimajor axes and eccentricities of all protoplanets in simulation K120.1B.

planets through the inner boundary of the computational domain. These simulations can result in two distinct planetary system architectures. One in which a dominant Neptune-mass body forms and migrates all the way into the magnetospheric cavity, and another where growth and migration of planets is more moderate, resulting in super-Earths and Neptunes orbiting at greater distances from the central star. Giants do not form because the growth of planets is slow enough that gas envelope accretion starts late during the disc lifetime, such that only moderate envelope masses have time to accrete. I discuss one representative example of an MGM run that led to the formation of a compact system of super-Earths and Neptunes on short-period orbits, but no planet orbiting within the magnetospheric cavity.

4.2.3.1 Run K120.1B

Run K120.1B had a disc mass of 1 × MMSN, 2× solar metallicity, and 100 m planetesimals. The total amount of mass in embryos and planetesimals was 43.5 $M_\oplus$.

The evolution of embryo masses, semimajor axes and eccentricities are shown in figure 4.7. Several planets grew to masses $m_p \sim 2\,M_\oplus$ during the first 0.5 Myr. A common phenomenon during the simulations involving 10 m boulders or 100 m

planetesimals was the formation of shepherded rings of boulders/planetesimals while the gas disc was present, similar to those observed in Biller et al. (2015) but formed through interactions with terrestrial mass instead of Jovian mass planets. From time to time rapid growth of a planet was observed if it crossed one of these rings through embryo-embryo scattering. At 2 Myr an embryo of mass $0.43\,\mathrm{M}_\oplus$ located at 5.8 au grew to $3.8\,\mathrm{M}_\oplus$ by accreting planetesimals from a shepherded ring, and hence started to accrete a gas envelope. The increase in mass eventually caused the corotation torques to saturate and the planet migrated in towards the star before forming a gap and transitioning to slower type II migration at ~ 4 Myr. Figure 4.7 shows that the inward migration of this planet created an inward-migrating resonant convoy, with collisions between embryos and with planetesimals leading to embryos growing within the convoy. Initially consisting of 12 protoplanets, the arrival of the convoy to the inner disc was followed by dynamical instability and collisions that left four short-period planets remaining at the end of the simulation. These consisted of (moving out from the star) a $2.9\,\mathrm{M}_\oplus$ rocky terrestrial planet, an $11.6\,\mathrm{M}_\oplus$ gas-poor Neptune, a $7.2\,\mathrm{M}_\oplus$ mini-Neptune, and a $21.4\,\mathrm{M}_\oplus$ gas-rich Neptune, with orbital periods of 4.7, 8.3, 12.4 and 19.5 d, respectively. As all of the orbital periods are less than 100 d, this inner group constitutes a compact system, within which only one resonant pair exists, that being a 3:2 resonance between the gas-poor Neptune, and its neighbouring mini-Neptune. Other resonances existed in this group of planets and their progenitors, but were broken when strong interactions and collisions occurred. This run provides a clear example of how a short-period compact system can form through concurrent growth and migration of planets.

In the outer disc regions beyond 2 au, the dispersal of the gas disc after 4.6 Myr led to dynamical excitation of the embryos orbiting there. Planetesimals rings that had been shepherded by the planets were disrupted, and a number of planets grew in mass by accreting these planetesimals. At the end of the simulation the outer region was still undergoing active accretion, and would have led eventually to the formation of long period water-rich terrestrial and super-Earth planets orbiting between $1.85 \leq r_\mathrm{p} \leq 15.2$ au if the run had been continued.

4.2.4 Giant formation and significant migration (GFSM)

Table 4.2 shows that only simulations with either 10 m boulders or 100 m planetesimals formed giant planets with masses $m_\mathrm{p} > 35\,\mathrm{M}_\oplus$. Out of 72 runs, 14 resulted in the formation of giants.

Gas giant planet formation ensues because a core with $m_\mathrm{p} > 3\,\mathrm{M}_\oplus$ forms early

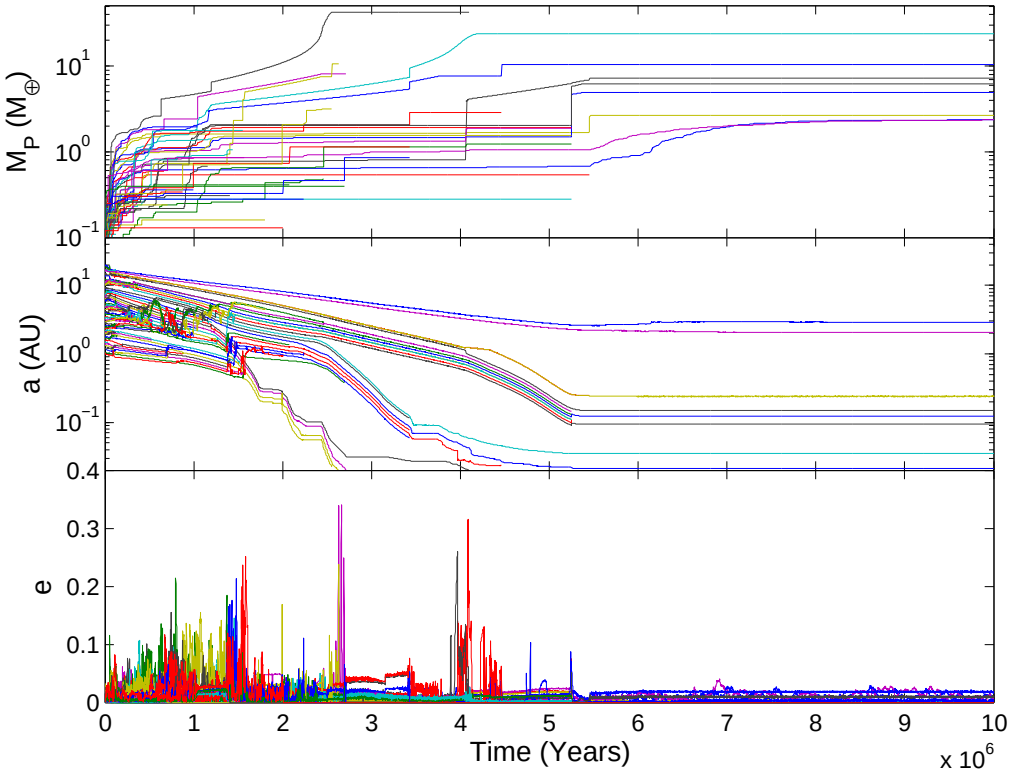

Figure 4.8: Evolution of masses, semimajor axes and eccentricities of all protoplanets in simulation K1.520.1A.

enough that a substantial gas envelope can accrete either before the disc disperses or before the planet migrates into the inner magnetospheric cavity. In agreement with the results of chapter 3, I find that discs capable of forming giant planets undergo multiple bursts of planet formation and migration, with the first generation of giants being lost through the inner boundary. Unlike chapter 3, however, the new model allows for the survival of migrating giants because they can become stranded within the magnetospheric cavity. Indeed, I formed a total of five surviving giants in the simulations, the most massive of which had $m_{\rm p} = 70\,{\rm M}_{\oplus}$. The most massive planet formed in any simulation had $m_{\rm p} = 160\,{\rm M}_{\oplus}$ (in model K220.01A), but was lost through the inner boundary because a second generation of planets arrived in the magnetospheric cavity and pushed it through the inner boundary interior to 0.02 au. I discuss one run below that formed giant planets that experienced significant migration.

4.2.4.1 Run K1.520.1A

Simulation K1.520.1A had an initial disc mass of 1.5 × MMSN, a solid abundance equal to 2 × solar and planetesimal radii 100 m. The mass in embryos and plan-

etesimals was $65\,M_\oplus$.

The evolution of protoplanet semimajor axes, masses and eccentricities are shown in figure 4.8. Two planets grew above $3\,M_\oplus$ and started accreting gas envelopes within the first Myr. The saturation of corotation torques for the most rapidly growing protoplanet caused it to migrate inwards, creating a resonant convoy of comigrating interior embryos, one of which also accreted gas. The largest mass body that drove the migration of the chain reached $m_\mathrm{p} = 40\,M_\oplus$ (with an envelope fraction of 87%) before the convoy entered the magnetospheric cavity. Gap formation prevented the $40\,M_\oplus$ planet from halting at the transition to the turbulent inner disc. The interior members of the group were pushed through the inner cavity and out of the computational domain, and the outermost planet stopped accreting gas and parked at the location of the 2:1 orbital commensurability with the outer edge of the cavity.

Shortly after 1 Myr another pair of planets exceeded $3\,M_\oplus$, accreted gas envelopes and started to migrate rapidly when their corotation torques saturated, driving another resonant convoy inwards. These planets halted when they arrived at the transition to the active turbulent region at approximately 3.4 Myr. The outer planet in the convoy grew to $24\,M_\oplus$, formed a gap and underwent type II migration into the magnetospheric cavity, pushing the resonant convoy and the earlier formed $40\,M_\oplus$ giant planet ahead of it. All the interior planets apart from an adjacent $10.5\,M_\oplus$ (formed by a collision within the cavity) were pushed through the inner boundary, leaving the $24\,M_\oplus$ and $10.5\,M_\oplus$ gas-rich Neptunes orbiting at 0.035 and 0.021 au at the end of the simulation, with gas envelope fractions of 77 and 32%, respectively.

In the interval between 2 and 4 Myr a group of $\sim$ Earth-mass protoplanets drifted in towards the star while sitting in a zero-migration zone, and halted their migration when the gas disc dispersed. Subsequent collisions resulted in the formation of two water-rich super-Earths, a mini-Neptune and a water-rich terrestrial planet orbiting between 0.09 and 0.24 au with masses in the range $2.3 \leq m_\mathrm{p} \leq 8\,M_\oplus$. At large radii (2 and 3 au, respectively) two water-rich terrestrial planets are formed by the accretion of planetesimals after gas disc dispersal, reaching masses $\sim 2.5\,M_\oplus$ at the end of the simulation at 10 Myr.

4.2.5 Summary of LPG, MGM and GFSM results

I now summarise the results obtained in the simulations according to which class of outcome they fall into.

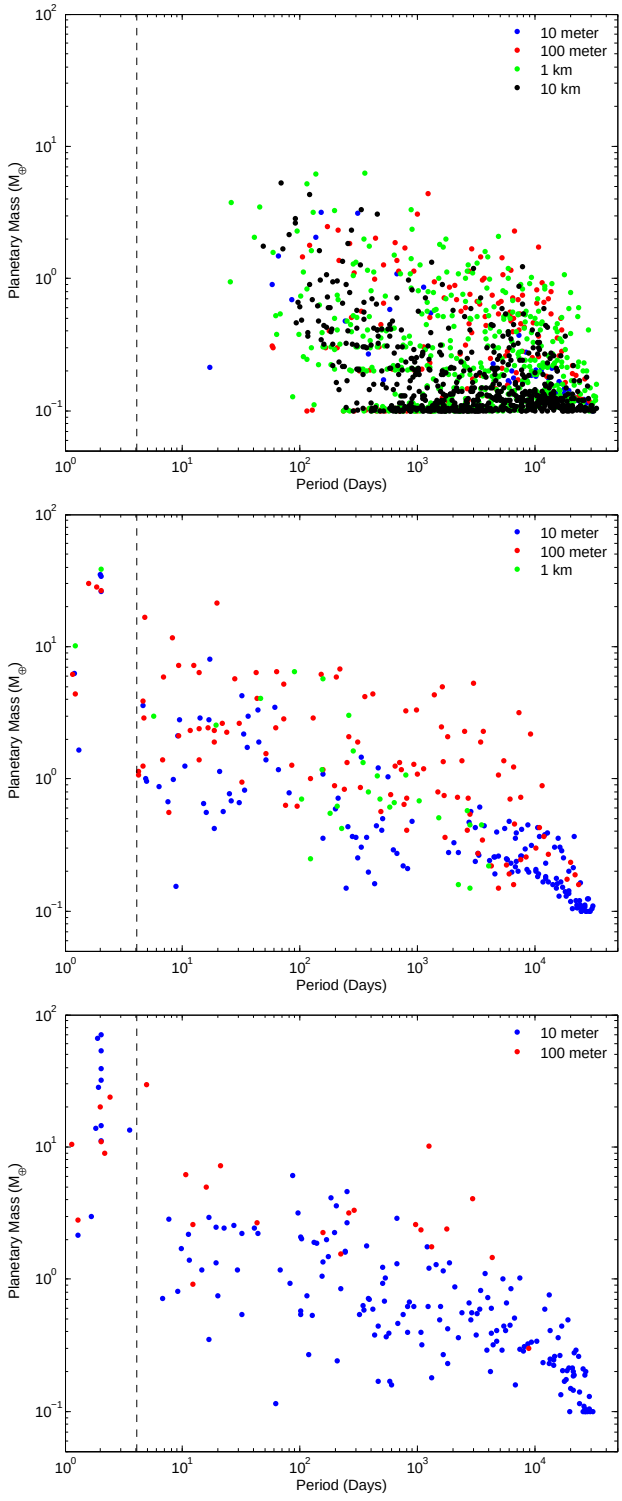

Figure 4.9: Final masses versus orbital period for all planets formed in all simulations displaying *limited planetary growth* (top panel), *moderate growth and migration* (middle panel) and *giant formation and significant migration* (right-hand panel). Note that the runs are colour coded according to the planetesimal/boulder size adopted, as indicated in the legend in each panel.

4.2.5.1 LPG

Simulations classified as showing LPG led to similar outcomes despite diverse initial conditions: (i) discs with low solids abundances containing boulders and small planetesimals; (ii) discs with relatively high abundances of solids in the form of large planetesimals. The final outcomes of these simulations are summarised in the mass versus period diagram shown in the top panel of figure 4.9. I see that no very short period planets were formed, and final masses are all below $10\,M_{\oplus}$. The inverse correlation between mass and semimajor axis arises because of modest disc-driven migration that caused the most massive bodies to drift in. The colour coding of the symbols shows that the final outcomes are similar for all boulder and planetesimal sizes.

4.2.5.2 MGM

The final states of all runs that exhibited MGM are shown in the middle panel of figure 4.9. Super-Earths and Neptune-mass planets on short period orbits are formed, and these occur almost always in compact systems (see the lower panels in figure 4.16 which shows the final outcomes of all individual runs that were classified as MGM). I note a strong inverse correlation between mass and orbital period in figure 4.9 caused by migration. Low-mass planets on short-period orbits were shepherded in as members of resonant convoys driven by more massive planets. Within individual systems this often led to a direct correlation between mass and orbital period because migration was driven by more massive bodies at the outer edge of migrating resonant chains.

Figure 4.9 shows that the most massive survivors have migrated into the magnetospheric cavity. Their migration was rapid enough to send them in this far, and they are often accompanied by short-period planets that are surviving members of a resonant convoy that avoided being pushed through the inner boundary. As mentioned briefly above, runs classified as MGM can be divided into two sub-classes: those that produce objects that migrate quickly enough to reach the magnetospheric cavity, and those which do not, with faster planet growth in more solids-rich discs and/or containing smaller planetesimals/boulders leading to the first sub-class.

4.2.5.3 GFSM

The final outcomes of runs classified as showing GFSM are presented in the bottom panel of figure 4.9. It is clear that all of the surviving gas giant planets have migrated

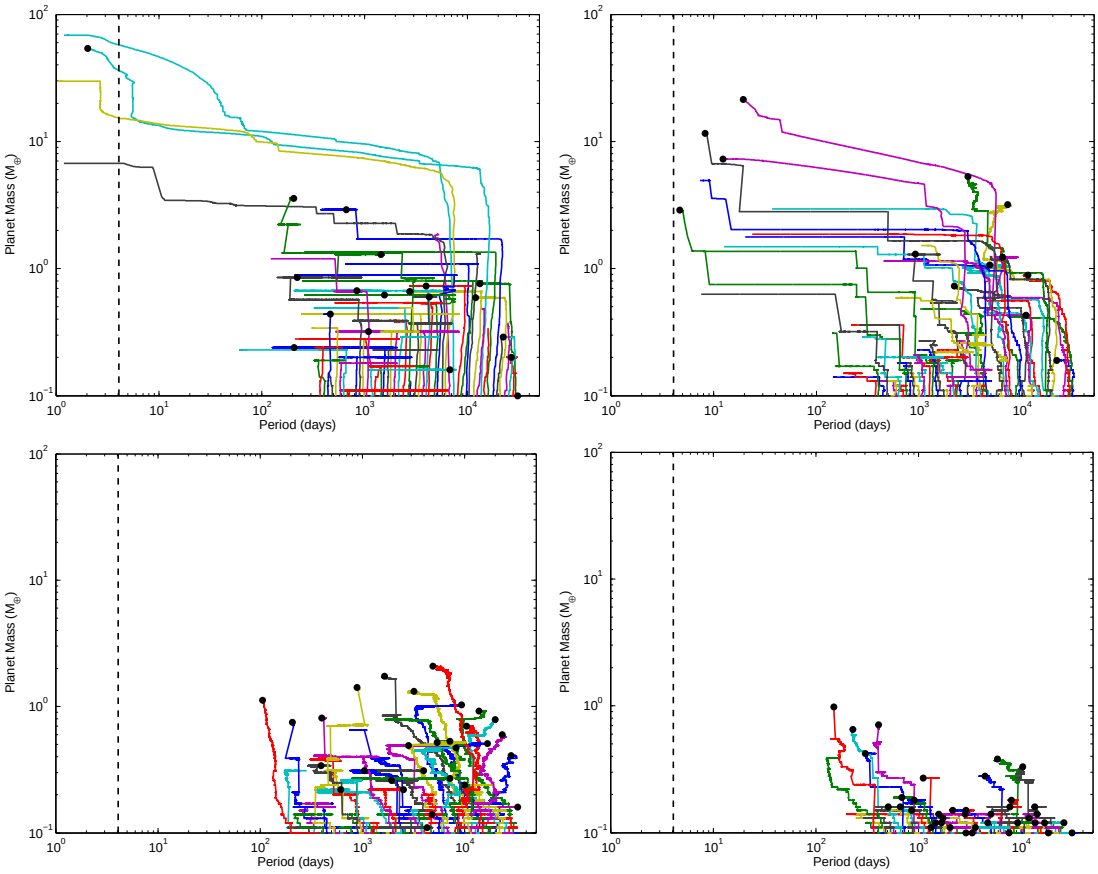

Figure 4.10: Evolution of planet mass versus orbital period for disc with mass 1 × MMSN and metallicity 2 × solar. Top left-hand panel: 10 m boulders. Top right-hand panel: 100 m planetesimals. Bottom left-hand panel: 1 km planetesimals. Bottom right-hand panel: 10 km planetesimals.

into the magnetospheric cavity, and some of them are accompanied by interior lower mass planetary companions.

Only models with 10 m boulders and 100 m planetesimals formed giant planets with masses $\geq 35\,M_{\oplus}$. All of these planets except for two were gas-dominated giants - the two exceptions being core-dominated giants (see table 4.3 for definitions). For 10 m boulders the abundance of solids required to build a gas giant is equivalent to an MMSN disc with metallicity 1.5× the solar value. For 100 m planetesimals a solids abundance equivalent to an MMSN disc with metallicity 3× the solar value is required. Simulations with 1 km and 10 km planetesimals presented in chapter 3 show that giants would have formed in the runs if disc models with a total solids abundance equivalent to an MMSN disc with 8× solar metallicity (e.g. a $4\times$MMSN disc with 2× solar metallicity/solids-to-gas ratio) were considered.

It is noteworthy that the most massive surviving (and non-surviving) planets all

formed in models with 10 m boulders. Fewer low-mass planets are left at large radii in the 100 m planetesimal runs because planet growth at these radii continues to larger masses in these runs as the planetesimals do not migrate inwards too rapidly. This allows the more massive planets formed there to also migrate inwards during the gas disc lifetime.

4.2.6 Evolution as a function of planetesimal radius

The simulation results show a very strong dependence on the planetesimal size adopted, and to highlight this point I have plotted planet evolution tracks in the mass–period plane in figure 4.10 for simulations with fixed disc properties (disc mass 1 × MMSN, metallicity 2× solar) and varying planetesimal/boulder sizes: 10 m - top left-hand panel; 100 m - top right-hand panel; 1 km - bottom left-hand panel; 10 km - bottom right-hand panel. Lines ending in a black filled circle represent the formation of a surviving planet. The top left-hand panel shows the formation and rapid inward migration of gas giant planets. The top right-hand panel shows the formation and inward migration of super-Earths and Neptune-mass planets. The bottom panels shows much slower growth of planets up to approximately one Earth mass and very little migration.

4.2.7 Evolution as a function of solid abundance

The simulation outcomes show strong dependence on the total mass in solids for a fixed planetesimal size. This is illustrated in figure 4.11, which shows mass-period evolution tracks for planets in discs of varying mass and metallicity for 100 m planetesimals. The upper panel shows results obtained from an anaemic disc with a mass 1 × MMSN and metallicity 0.5× solar. MGM is observed in the middle panel for a disc mass of 1.5 × MMSN and metallicity 1× solar. The lower panel shows the dramatic change in evolution when the solids abundance is raised, leading to the formation of numerous Neptune-mass and gas giant planets in successive bursts, with a $20\,M_{\oplus}$ gas-rich Neptune remaining in the magnetospheric cavity at the end of the simulation.

4.3 Comparison with observations

It is important to re-emphasise that the simulation set does not constitute an attempt at population synthesis. The aim is much simpler: to examine whether or

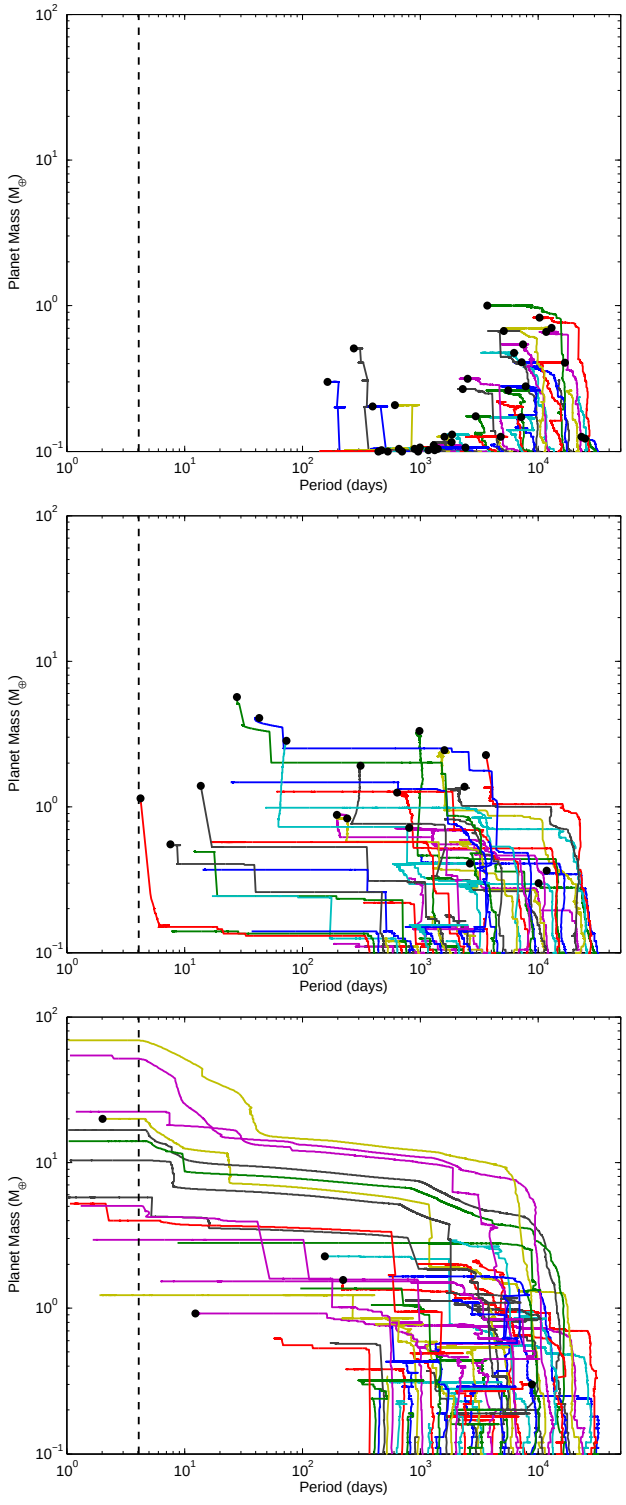

Figure 4.11: Evolution of planet mass versus orbital period for models with planetesimals sizes of 100 m. Upper panel: disc with low solid abundance - run K10.50.1A with disc mass 1 × MMSN, metallicity 0.5 × solar. Middle panel: disc with medium-level solid abundance - run K1.510.1A with disc mass 1.5 × MMSN, metallicity 1 × solar. Lower panel: disc with large solid abundance - run K220.1B with disc mass 2 × MMSN, metallicity 2 × solar.

not the model of planet formation and migration presented here is able to form planetary systems similar to those that have been observed within the context of plausible disc models. I have not used a Monte Carlo approach to select initial conditions from observationally derived distribution functions, and so the frequency with which different types of systems arise in the simulations is not relevant when judging whether or not the planet formation model is successful. Comparing with observations allows us to determine whether or not the model is capable of producing planets with properties that match those of the observed population (or at least a sub-set of it), and provides a guide for understanding where model improvements are needed.

4.3.1 Mass versus period

Figure 4.12 is a mass versus period diagram for the surviving planets from all simulations, along with all confirmed exoplanets (Han et al., 2014). The vertical dashed line located at ~ 4 d shows the position of the disc inner edge in the simulations (i.e. the location of the magnetospheric cavity).

The large number of long-period (> 365 d) low mass planets ($m_{\rm p} \lesssim 5\,{\rm M}_{\oplus}$) produced by the simulations arises because of the large number of runs that displayed limited growth (21 out of 36 disc models). These are located in a part of the mass-period diagram that is poorly sampled by radial velocity and transit surveys which are biased towards finding massive planets on short-period orbits. Microlensing surveys sample this region of parameter space and although relatively few planets have been discovered, constraints obtained from statistical analysis of the data suggest that planets should be common in this region of the diagram (Gould et al., 2010).

There is good overlap between the simulation outcomes and the large numbers of observed short period terrestrial/super-Earth/Neptune-mass planets. In the simulations these planets tend to form in compact multiplanet systems, similar to those discovered by *Kepler* (Fabrycky et al., 2014) and radial velocity surveys (Mayor et al., 2011), as discussed in more detail below. The observational data also indicate that there are numerous systems containing a single planet or which have low multiplicity. The most recent release of *Kepler* data, for example, contains more than 3000 single transiting planet candidates (Mullally et al., 2015). In general, the simulations only produce systems with a short-period planet and few objects (if any) orbiting significantly further out when a dominant object (Neptune or gas giant) forms and migrates through the system to the inner cavity. This scenario can clear other planets from the system, leading to low levels of multiplicity. Examples

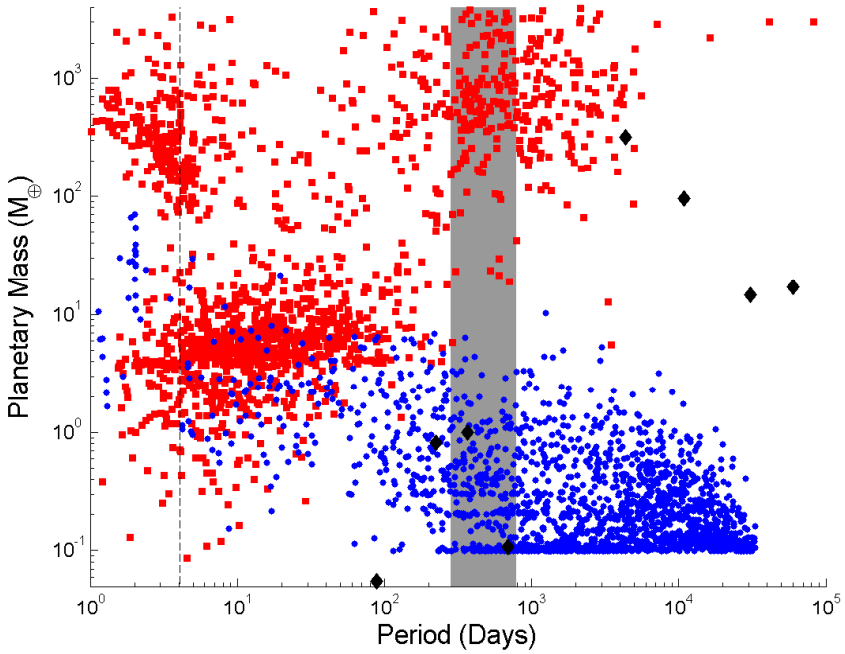

Figure 4.12: Mass versus period plot, comparing observed exoplanets (red squares) with simulation results (blue circles) and the Solar system (black diamonds). The dashed line indicates the disc inner edge of 0.05 au in the simulations, whilst the grey zone indicates the habitable zone (Kasting et al., 1993).

of where this occurred can be seen in figure 4.16, which shows the final outcomes from all runs with short-period planets. Forming single planets or low multiplicity systems without a close orbiting dominant body would seem to be difficult in the planet formation scenario presented here, and this may indicate that the choice of inserting 52 planetary embryos at the beginning of the simulations does not match the mode of planet formation occurring most commonly in nature. The prevalence of single or low multiplicity systems may be an indication that planet formation often proceeds by only forming relatively few embryos, in contrast to traditional scenarios of oligarchic and giant impact growth (Chambers & Wetherill, 1998; Ida & Makino, 1993).

The collection of very short period planets ($P < 2$ d) with masses in the range $2 \leq m_\mathrm{p} \leq 10\,\mathrm{M}_\oplus$ from the simulations all arose because they migrated into the magnetospheric cavity and were pushed closer to the star by an exterior body that was driving a resonant convoy. These outer planets, that stall finally near the 2:1 resonance with the cavity edge, are also apparent in figure 4.12 and sit in a region of parameter space where there are very few observed planets. I can ascribe these distinct orbital period features in the simulated planet population as being due

to adopting a single location for the cavity edge, whereas in reality it will vary from system to system (and with time) due to differences in stellar magnetic field strengths and accretion rates through protoplanetary discs. This will have the effect of blurring the locations of the planets at the 2:1 resonance location and the interior planets that have been pushed inwards. The group of more massive planets at 2 d have masses that are not commonly observed, and this may be an indication that the model fails because these bodies should have accreted more gas to become part of the hot-Jupiter population (represented by observed planets with masses $\gtrsim 100\,\mathrm{M}_\oplus$), or should experience substantial evaporation of their atmospheres by stellar X-ray irradiation on Gyr time-scales (Owen & Jackson, 2012), leaving planets with smaller masses in better agreement with observations. Erosion of the atmosphere through an evaporative wind can also exert a torque on the planet allowing the planet to migrate a few percent of its semimajor axis, if the wind is anisotropic (Teyssandier et al., 2015).

One clear failing in the simulation results is the lack of surviving giant planets with masses $\geq 100\,\mathrm{M}_\oplus$. As mentioned earlier, the most massive planet to form in the simulations had $m_\mathrm{p} = 160\,\mathrm{M}_\oplus$, but migrated into the star. The formation of giant planets within the simulation occurred in the inner regions of the disc (orbital radii $\leq 1\,\mathrm{au}$), and during times when there were significant amounts of gas remaining. These giants always migrated into the magnetospheric cavity, before getting trapped at the 2:1 resonance with the disc inner edge. Generally, the last planet that migrated into this region survived, along with a less massive companion if the companion migrated in convoy. Earlier arriving planets are pushed through the inner boundary of the disc by these late arrivers. The later formation time of these surviving planets causes their masses to be smaller, as the amount of material available for accretion was reduced, explaining why there are not any genuine hot Jupiters or hot Saturns remaining at the ends of the simulations. Once again, the high multiplicity of the simulated planetary systems may be causing short-period giant planets to be removed from the simulations, thus reducing the level of agreement between the models and the observations. In other words, the choice of initial conditions where embryos are equitably distributed throughout the disc may lead to too many planets forming, preventing the survival of early-forming gas giants.

Finally, I note that the models do not even come close to explaining the long-period cold-Jupiter population. This is a feature of the simulations that was discussed at length in chapter 3, where it was shown that for giant planets to have formed and survived type II migration in the simulations, they would have had to

have initiated runaway gas accretion at large orbital radii (typically > 8 au) and during sufficiently late periods of the disc lifetime when the total disc mass remaining was less than a few tenths of a minimum mass disc. Forming under these conditions would allow planets to undergo only a moderate amount of type II migration, allowing them to survive at large orbital radii. Trapping giant planet cores at large orbital radii until late times is difficult in the model, however, because the saturation of entropy-related corotation torques leads to rapid inwards type I migration. This point is illustrated by the migration contours shown in figure 4.3.

4.3.2 Comparison with *Kepler*-like systems

Figure 4.13 shows a comparison between a selection of compact *Kepler* systems, *Gliese 581* and *Wasp 47* and a selection of the simulated systems. Figure 4.16 shows all the simulated planetary systems that arose from runs resulting in either MGM or GFSM.

Inspection of the simulated planetary systems in figure 4.13 (and figure 4.16) shows that I obtain two basic architectures, one where either a gas-rich Neptune or a gas giant planet has migrated through the system into the inner cavity, and another where the migration has been more modest as planet masses have not grown so massive. The runs K221B, K20.50.01B, K120.1B and K1.50.50.01B displayed the latter type of behaviour, whereas runs K220.01B, K20.50.01A and K110.01A displayed the former type. I obtain outcomes in which the planets are well separated and not in resonance, such as K221B (for which there was a lot of scattering and growth after the gas disc dispersed) and outcomes such as K1.50.50.01B where the planets are in a chain of resonances at the end of the simulation. Note that figure 4.16 shows which pairs of planets in the final systems are in mean motion resonances. I also find a small number of co-orbital planets at the end of the runs (three trojan systems and one horseshoe system were found orbiting within 200 d across all runs. These systems are shown as being in 1:1 resonance in figure 4.16). All co-orbital planets were found in systems where at least one planet underwent rapid and large scale migration, causing bodies to be scattered on to eccentric orbits that quickly damped once the rapid migrator had passed through the system. This concurs with previous studies of co-orbital planet formation which showed that these bodies are a direct consequence of violent relaxation in a highly dissipative environment (Cresswell & Nelson, 2006).

While it is difficult to perform a quantitative comparison between the simulated and the observed planets, certain similarities can be noted. For example, *Kepler-444*

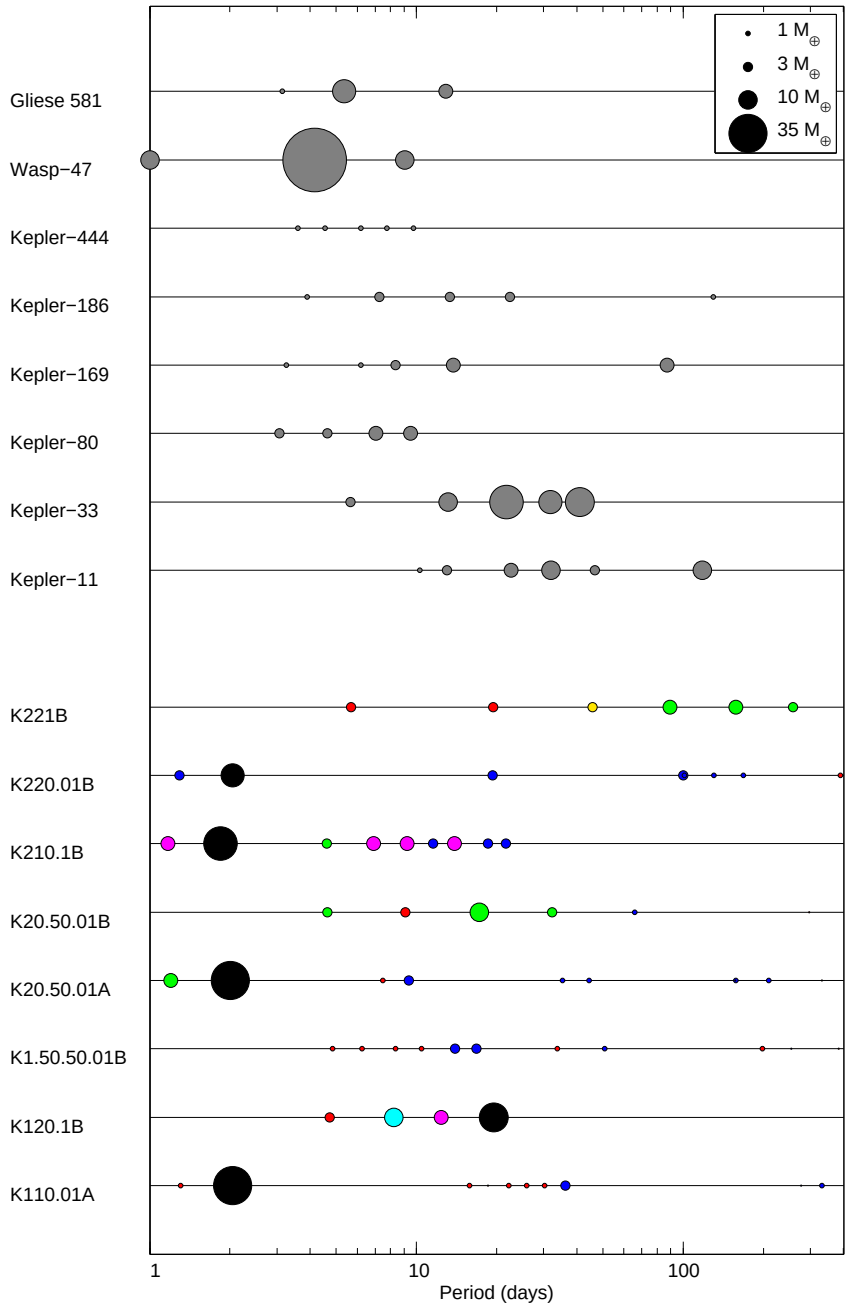

Figure 4.13: Plot comparing observed compact multiplanet systems (upper panels) with simulated systems (lower panels). Orbital period is indicated on the x-axis and planet masses are indicated by the symbol size (radius scales with the square-root of the planet mass) with reference sizes shown in the legend. Masses for observed systems are either measured masses, or where these are not available they are calculated using the formulae described in Han et al. (2014). The symbol colours in the lower panels indicate the classification of each planet: red = rocky terrestrial; blue = water-rich terrestrial; yellow = rocky super-Earth; green = water-rich super-Earth; magenta = mini-Neptune; cyan = gas-poor Neptune; black = gas-rich Neptune; brown = gas-dominated giant. See table 4.3 for definitions of planet types.

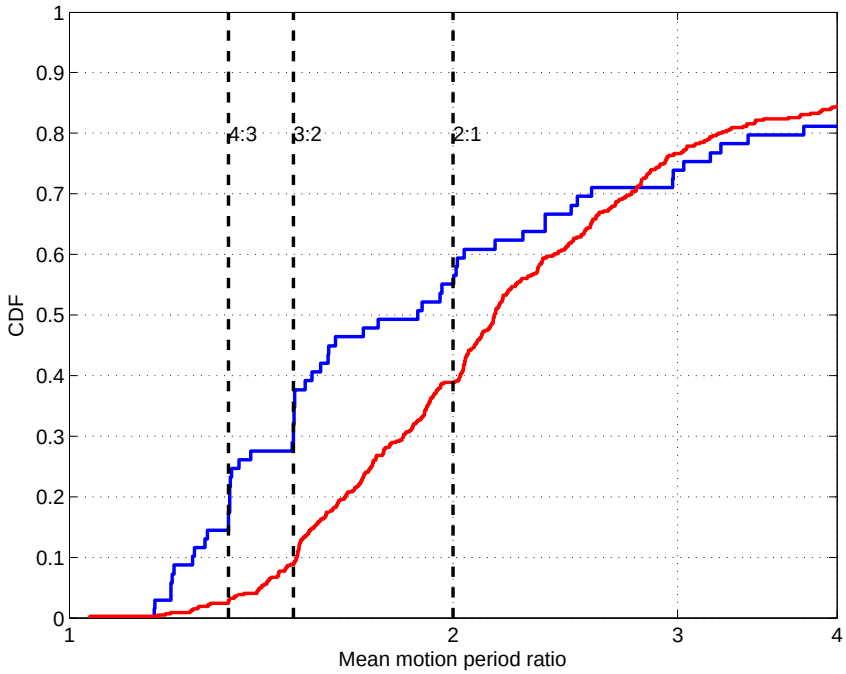

Figure 4.14: Cumulative distribution functions of period ratios between neighbouring planets with periods less than 100 d in the observations (red line) and simulations (blue line).

looks similar to the inner four planets of K1.50.50.01B. These four rocky-terrestrial planets were shepherded in by the exterior more massive water-rich terrestrials, and hence formed a resonant convoy. This is one way in which the *Kepler-444* planets could have arrived at their observed locations and provides an alternative to *in situ* formation (but relies on there being a more massive, undetected planet orbiting further from the star). *Kepler-169*, *186* and *80* look similar to K20.50.01B, and *Kepler-11* and *33* have broad similarities with K120.1B. Although the *Kepler* sample does not contain examples of compact multi-systems with massive, short-period planets (perhaps because these are more dynamically disturbed and therefore not transiting or close to resonances such that they are detectable through transit timing variations), *Gliese 581* and *Wasp 47* provide two examples that have architectures similar to K210.1B and K220.01B.

4.3.3 Period ratios and orbital spacings

Figure 4.14 compares the cumulative distributions of period ratios between neighbouring planets with masses $\geq 1\,M_\oplus$ and orbital periods less than 100 d obtained from the simulations (upper blue curve) and the *Kepler* systems (lower red curve).

The sample of *Kepler* planets was defined by choosing bodies with orbital periods ≤ 100 d and radii $\geq 1 R_{\oplus}$. This lower radius limit was adopted to account for possible incompleteness in the *Kepler* sample for planets with small radii. It is clear that the simulated systems are generally more closely packed after run times of 10 Myr, and the structure observed in the distribution shows that this is due in part to there being a number of planet pairs in resonance. The step-like features in the plot show that the 7:6, 6:5, 5:4, 4:3, 3:2 and 2:1 resonances are occupied. Whereas just an isolated pair of migrating planets are likely to be trapped in either the 2:1 or 3:2 resonances if they undergo smooth migration (Paardekooper et al., 2013), I find that migration in a crowded system allows diffusion through successive resonances to occur such that high degree resonances can be occupied, in agreement with earlier studies by Cresswell & Nelson (2006, 2008). Although resonant systems are relatively rare in the *Kepler* data, it is worth noting that *Kepler-36* has two planets very close to the 7:6 resonance (Carter et al., 2012; Paardekooper et al., 2013), and some of the planet pairs in *Kepler-444* are reported to be in 5:4 (Campante et al., 2015). Other examples of systems in resonance or near resonance, including three body resonances and resonant chains, are *Kepler-50* (6:5), *Kepler-60* (5:4, 4:3) (Steffen et al., 2012), *Kepler-221* (three body resonance where the mean motion combination $2n_{\rm in} - 5n_{\rm mid} + 3n_{\rm out}$ has been found to librate around 180 deg) (Fabrycky et al., 2014).

Furthermore, it has been noted in numerous studies (e.g. Fabrycky et al., 2014) that the distribution of planet period ratios contains an excess of planets just outside of 3:2 and 2:1, suggesting that the resonances have been dynamically important during the evolution but may have been broken by stochastic migration in a turbulent disc (Adams et al., 2008; Rein & Papaloizou, 2009), by tidal interaction with the central star (Terquem & Papaloizou, 2007), by orbital repulsion due to damping of non-linear spiral waves (Baruteau & Papaloizou, 2013), by overstability in librations about resonant centres (Goldreich & Schlichting, 2014), or because of scattering due to interactions with or accretion of residual planetesimals (Chatterjee & Ford, 2015). I observe that in a handful of simulations, planetesimal scattering after full gas disc dispersal does occur, breaking mean-motion resonances between neighbouring planets, in agreement with Chatterjee & Ford (2015). It is noteworthy that a number of the compact systems are orbiting in regions where their nascent protoplanetary discs are expected to have sustained MRI (Magnetorotational instability) turbulence due to the local temperature being in excess of 1000 K (Umebayashi & Nakano, 1988), and so may have been subjected to stochastic forcing of their orbits while the gas disc was present. To seek evidence for this transition to turbulence I have examined

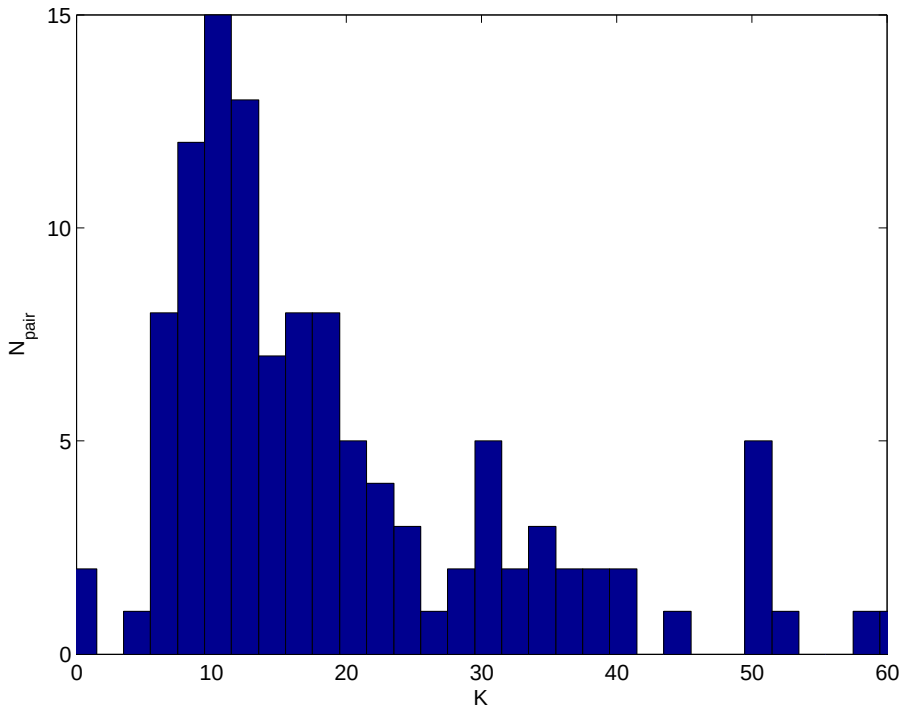

Figure 4.15: Histogram showing the distribution of separations between neighbouring planets with masses $\geq 1\,M_{\oplus}$, measured in units of the mutual Hill radius.

the minimum periods of planets in the compact *Kepler* multi-systems to see if they correlate with the effective temperature of the host star, but there is no evidence of a correlation. At present there is no clear evidence that the transition to turbulence in the inner regions of the protoplanetary discs that formed the *Kepler* systems played a decisive role in dynamically shaping these systems.

It is possible that a number of the simulated systems may be dynamically unstable on time-scales much longer than the 10 Myr run times, such that subsequent mutual collisions increase separations between adjacent planets. In a recent study, Pu & Wu (2015) used n-body simulations to show that compact *Kepler*-like multiplanet systems tend to remain stable for Gyr time-scales only if the typical mutual separation between neighbouring planets is approximately 12 mutual Hill radii. Figure 4.15 shows the distribution of separations between neighbouring planets present at the end of the simulations, and while many planet pairs are well separated there are a significant number whose orbital spacings may be too small for long-term stability. Running the simulations for long enough to test this goes beyond the scope of this thesis, but will be studied in future work as it may be the case that the mean motion resonances discussed above provide protection against instability. Note that

the objects with period ratios of unity shown in figure 4.15 are the co-orbital planets mentioned previously.

4.4 Discussion and conclusion

I have implemented a model of planet formation based on a scenario in which numerous planetary embryos are distributed across a wide range of semimajor axes, embedded in a sea of boulders or planetesimals that act as the primary feedstock for planetary growth. The model has a comprehensive list of ingredients: planetary embryo growth through boulder/planetesimal accretion and mutual collisions; a 1-D viscous gas disc model, subject to irradiation from the central star and a photoevaporative wind; type I migration using the most up-to-date prescriptions for Lindblad and corotation torques; a transition to gap formation and type II migration when gap formation criteria are satisfied; gas accretion on to solid cores. The disc has an increase in viscosity where the temperature $T > 1000$ K, to mimic unquenched MHD turbulence developing in the inner disc, and a magnetospheric cavity that creates an inner edge in the gas disc at an orbital period of 4 d. The aim of this study is to determine which types of planetary systems emerge from the planet formation model as a function of disc parameters (mass and metallicity) and planetesimal/boulder sizes. The main results from the simulations can be summarised as follows.

(1) System evolution can be categorised into three distinct modes that depend on the total amount of solids present in the disc and the sizes of the boulders/planetesimals.
(i) - When planetesimal/boulder radii are small (≤ 100 m) *limited planetary growth* arises when the inventory of solids is small. When planetesimal radii are large (≥ 1 km), limited growth arises for all discs models considered, except the one that is the most massive and solids-rich. Planets with maximum masses $\sim 3\,\mathrm{M}_{\oplus}$ form during the gas disc lifetimes, and show only very modest migration.
(ii) - *Moderate growth and migration* arises in only the most solids-rich disc considered when planetesimal sizes are 1 km, and for disc models with intermediate abundances of solids when the planetesimal/boulder sizes ≤ 100 m. Planets are able to grow to super-Earth or Neptune masses during the disc lifetime, and may undergo large-scale migration.
(iii) - *Giant formation and significant migration* is observed in the most solids-abundant discs when boulder/planetesimal sizes were ≤ 100 m, but did not arise in any of the runs with larger planetesimals. Generally, multiple episodes of planet formation occur, and gas giant planets with masses $\geq 35\,\mathrm{M}_{\oplus}$ form and undergo

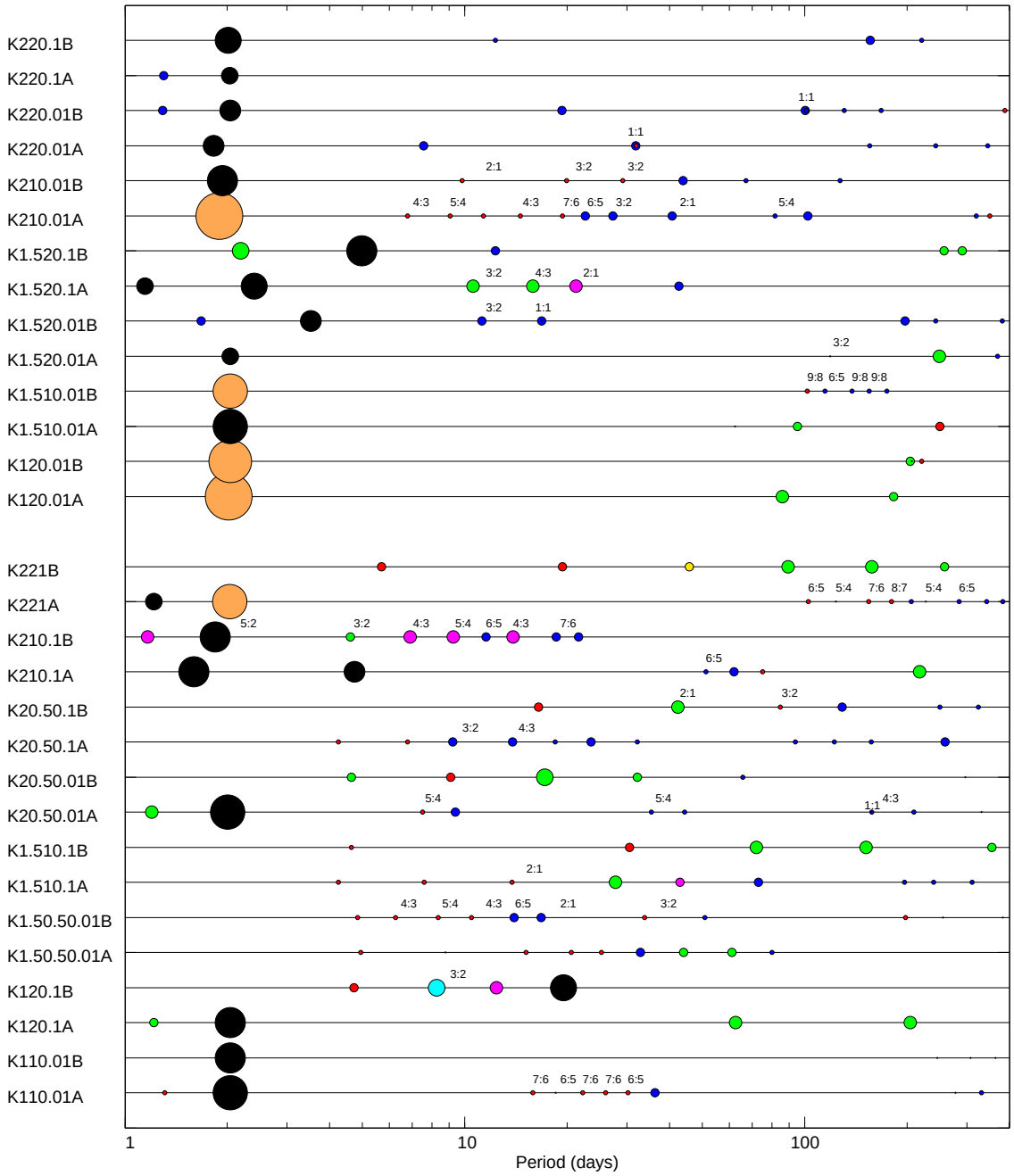

Figure 4.16: Plot showing all compact multiplanet systems formed in the simulations. The upper panels represent planets formed in runs classified as *giant formation and significant migration*, the low panels show outcomes from *moderate growth and migration* runs. Orbital periods are indicated on the x-axis and planet masses are indicated by the symbol size, as in figure 4.13. The symbol colours indicate the classification of each planet: red = rocky terrestrial; blue = water-rich terrestrial; yellow = rocky super-Earth; green = water-rich super-Earth; magenta = mini-Neptune; cyan = gas-poor Neptune; black = gas-rich Neptune; brown = gas-dominated giant. See table 4.3 for definitions of planet types.

large-scale migration before stalling in the magnetospheric cavity. The final surviving short period planets are normally the last ones to arrive in the magnetospheric cavity, with the earlier arrivals being pushed through the inner boundary by the planets that arrive there later.

(2) Considering systems of short-period planets, I can identify two basic architectures that emerge from the simulations. The first normally consists of a combination of terrestrial planets, super-Earths and low mass Neptunes, where no planet managed to migrate into the magnetospheric cavity. The shortest period orbits in these systems are normally 4-5 d. The second architecture consists of at least one dominant planet (a gas giant or a relatively massive Neptune) that migrated and stalled in the magnetospheric cavity with a period of ~ 2 d. In approximately 50% of cases, this planet has an interior companion (terrestrial planet, super-Earth or Neptune) which is almost never in resonance because of dynamical interactions and collisions with other planets during the evolution. In most cases where a dominant short-period planet formed, there are a number of exterior planets orbiting with periods in the range $5 \lesssim P \lesssim 80$ d.

(3) The planetary systems display a range of heterogeneity in composition versus orbital period. Systems that formed under relatively quiescent conditions, without a rapidly migrating gas giant or Neptune, have rocky bodies orbiting interior to volatile rich bodies. Systems that contained rapidly migrating giants or Neptunes, that end up in 2 d orbits, often experienced significant scattering, and these systems can have rocky bodies in exterior orbits in close proximity to volatile-rich bodies.

(4) The planetary systems that emerge from the simulations tend to be closer packed than the observed *Kepler* systems. The most common spacing between neighbouring planets is 10 - 12 mutual Hill radii, and Pu & Wu (2015) have shown that such systems are likely stable over Gyr time-scales. There are, however, numerous simulated planet pairs where the ratio of spacing to mutual Hill radius < 10, and these might cause the systems to evolve and change their spacing through collisions if evolved beyond the 10 Myr that I have considered, improving the agreement with observations. I note, however, that mean motion resonances may help stabilise the simulated systems compared with those considered by Pu & Wu (2015).

(5) One reason for the difference in the distributions of observed versus simulated period ratios is that mean motion resonances are common among the final planetary systems. I find examples of 7:6, 6:5, 5:4, 4:3, 3:2 and 2:1, with the latter three resonances being rather common. It is well known that most of the compact *Kepler* systems do not display mean motion resonances, even though there is evidence for the 2:1 and 3:2 resonances having been dynamically important in the past, and a few

individual systems appear to host resonant pairs or triples. One possible explanation for the greater numbers of resonant systems arising in the simulations is the neglect of stochastic forces in the inner disc regions due to MHD turbulence (Nelson, 2005; Nelson & Papaloizou, 2004) which can cause planets to diffuse out of resonance (Adams et al., 2008; Rein & Papaloizou, 2009). It remains to be seen whether or not inclusion of this effect can increase the agreement between observations and theory on the frequency of mean motion resonances. One further point worthy of note is that the frequency of resonances arising in the simulations is higher for those architectures that contain a dominant planet orbiting with a 2 d period. Systems without a dominant short period planet underwent more quiescent evolution during the gas disc lifetime, but also experienced more scattering after removal of the disc and this leads to systems that contain few resonances (see figure 4.16). Thus, it is important to note that there is a mode of planet formation that includes large scale migration but which does not result in systems that are members of resonant chains.

(6) A number of co-orbital planets were formed in the simulations (three trojan systems, and one undergoing mutual horseshoe orbits, were found to orbit with periods < 200 d). These all formed in systems where at least one dominant planet underwent migration through the planetary swarm, causing large amounts of scattering. In earlier work Cresswell & Nelson (2006, 2008) have shown that co-orbital planets arise as a consequence of violent relaxation in crowded planetary systems with strong eccentricity damping, and the results are in agreement with these earlier findings.

(7) Numerous gas giant planets were formed in the simulations, and some survived after migrating into the magnetospheric cavity. The most massive planet to form was a $160\,\mathrm{M}_\oplus$ gas giant, but this was pushed through the inner boundary of the computational domain by a planet that arrived in the magnetospheric cavity at a later time. The most massive surviving planet was a $70\,\mathrm{M}_\oplus$ "hot Saturn" on a 2 d orbit. In chapter 3 I undertook a detailed examination of the conditions required for the formation and survival of longer period giant planets against type II migration, and showed that a Jovian mass planet halting its migration at 5 au needs to start runaway gas accretion and type II migration at a distance of ~ 15 au from the central star. This has not occurred in any of the simulations (this chapter, or chapter 3, or in the many low-resolution test simulations that have been run but are not included in this thesis), because of the difficulty of forming a core and keeping it at such large orbital radius. I have concluded that forming and retaining long-period giant planets requires a set of disc conditions that are quite different from those that have been considered thus far. A potential solution to the problem will be presented in

chapter 5.

4.4.1 Formation of *Kepler-444* and *42*

The *Kepler-444* and *Kepler-42* systems are examples of short period compact low mass planetary systems. All have radii substantially smaller than the Earth's. *Kepler-444* is a five-planet system orbiting a 0.76 $M_\odot$ K0V star with [Fe/H] ~ -0.55, where the innermost orbital period is 3.6 d and the outer planets are close to the 5:4, 4:3, 5:4 and 5:4 mean motion resonances (Campante et al., 2015). *Kepler-42* is a three-planet system orbiting a 0.13 $M_\odot$ M3V star with [Fe/H] ~ -0.3. Orbital periods are 0.453, 1.214 and 1.865 d (Muirhead et al., 2012), so there are no first-order mean motion resonances. I showed in section 4.2 that planet masses need to be in excess of $\sim 3\,M_\oplus$ for migration over large distances to be effective, and given the low metallicities of these systems they are most likely explained by *in situ* formation after delivery of solids through drag-induced drift into the disc inner regions. Although large-scale migration of these planets is implausible, the resonant or near-resonant configuration of the *Kepler-444* planets suggests that modest migration may have occurred. The outermost planet being the largest (and presumably most massive) would lead to the necessary convergent migration.

4.4.2 Formation of short-period super-Earths in low-metallicity discs

The simulations demonstrate how difficult it is to grow planets that are massive enough to undergo significant type I migration during the gas disc lifetime when growth is dominated by the accretion of large (≥ 1 km) planetesimals in discs with a moderate inventory of solids. This is because growth time-scales are slow for large planetesimals. In addition, if a planet approaches its local isolation mass it will not be massive enough to migrate such that it can accrete from undepleted sources of planetesimals. The situation becomes more difficult in a low metallicity environment, and the existence of short-period super-Earths around stars such as *Kapteyn's star* (Anglada-Escudé et al., 2014), *Gliese 581* (Udry et al., 2007), *HD 175607* (Mortier et al., 2016) and the numerous low-metallicity hosts of *Kepler* systems (Buchhave et al., 2014) suggests that these planets did not form via the classical oligarchic growth picture of widely distributed embryos accreting from a swarm of large planetesimals. These systems instead point towards planetary embryos growing into type I migrating super-Earths by accreting from a supply of

highly mobile small planetesimals, boulders or pebbles (e.g. Lambrechts & Johansen, 2012; Ormel & Klahr, 2010), as this is the only means available of exceeding local isolation masses. On the other hand, the requirement for the local solids-to-gas ratio to be approximately twice solar in order for the streaming instability to operate and generate large planetesimals that can acts as the seeds of growing planets (Johansen et al., 2009b) suggests that small particles must first concentrate in specific disc regions due to the existence of zonal flows (Bai & Stone, 2014; Johansen et al., 2009a), vortices (Fromang & Nelson, 2005) or dead zone interfaces (Lyra et al., 2009) in order to create local enhancements of solids. Such a collect-and-grow scenario would appear to offer the best hope for explaining the existence of planets in the lowest metallicity environments.

5 Planet Formation in Radially Structured Protoplanetary Discs

In this chapter I will present work that has been accepted for publication in the Monthly Notices of the Royal Astronomical Society (Coleman & Nelson, 2016b), and as such this chapter closely follows that paper.

Ever since the discovery of the first extrasolar giant planet around a main sequence star (Mayor & Queloz, 1995), questions have been asked as to the formation and evolution of giant exoplanets. To date over 1600 confirmed extrasolar planets have been discovered, displaying a broad range of orbital and physical properties, and approximately 600 of these are believed to be gas giants (Han et al., 2014). Explaining the origins of the broad diversity of exoplanets remains a formidable challenge to planet formation theory, and even the more restricted challenge of explaining the orbital period distribution of giant exoplanets has not yet been addressed satisfactorily.

Observational biases, in particular the fact that ground based transit surveys are only sensitive to detecting giant planets with orbital periods $\lesssim 10$ days, and that radial velocity searches have surveyed stars that are more metal-rich than the average, give the impression that hot Jupiters are common. Recent studies that have examined data from the *Kepler* spacecraft and follow-up radial velocity measurements (Fressin et al., 2013; Santerne et al., 2016) find that hot Jupiters are expected to orbit only 1% of main sequence stars, while cold Jupiters have a higher occurrence rate of 17% (Cassan et al., 2012). The occurrence rate between the two populations does not increase linearly, however, as a 'period valley' exists between 10–85 days where there is a dearth of giant planet detections when accounting for observational biases. This period valley was first observed in radial velocity surveys (Cumming et al., 2008; Jones et al., 2003; Udry et al., 2003), and its existence has been supported by the aforementioned recent analysis of combined *Kepler* and radial velocity observations (Santerne et al., 2016). Individual theories have been put forward to explain this period valley (Alexander & Pascucci, 2012; Ercolano & Rosotti, 2015; Hasegawa & Pudritz, 2011), but none have been incorporated into ab initio models of planet formation to examine whether or not it is possible to explain this, and

other features in the giant planet distribution, from first principles.

Competing theories of giant planet formation, including the core-accretion and pebble-accretion models (e.g. Alibert et al., 2006; Bitsch et al., 2015b; Ida & Lin, 2004; Mordasini et al., 2009), and the tidal-downsizing model (e.g. Nayakshin, 2015), have been used to make predictions about the giant planet population for comparison with observations, and to examine the formation of giant planets in our Solar System (Levison et al., 2015a). The fact that many multiplanet systems have been discovered, containing various combinations of super-Earths, Neptunes and Jovian mass bodies (Becker et al., 2015; Muirhead et al., 2012; Neveu-VanMalle et al., 2016), often in compact systems (e.g. Becker et al., 2015; Lissauer et al., 2011), suggests that gravitational interactions, and perhaps competitive accretion, are essential components of the planet formation process. Furthermore, the fact that many giant planets appear to be on eccentric orbits suggests that dynamical instabilities involving initially compact giant planet systems, either during or after formation, are common and important for shaping planetary system architectures (e.g. Rasio & Ford, 1996). Chapters 3 and 4 examined the formation of planets in irradiated, viscous disc models that adopted the standard α prescription (Lynden-Bell & Pringle, 1974; Shakura & Sunyaev, 1973). Except for a small region close to the star where the temperature exceeds 1000 K, α was assumed to be constant, leading to smooth temperature and surface density profiles in the discs. The models have been successful in forming systems containing hot Jupiters, multiple super-Earths and Neptunes in compact configurations, and numerous terrestrial planets with a variety of compositions, but the models fail completely to form any surviving cold Jupiters. The main reason for this is that giant planet cores undergo rapid inward migration as they accrete gas, because the corotation torques that are needed to counteract the Lindblad torques become saturated (e.g. Paardekooper et al., 2011). These planets then end up as hot planets orbiting close to the star. In chapter 3 I undertook a detailed examination of the conditions required for giant planet formation and survival, and showed that a Jovian mass planet that settles into a final orbit at 5 au must have initiated runaway gas accretion and type II migration when at an orbital radius ~ 15 au, and this should have occurred late in the disc lifetime so that the gas disc disperses before the planet type II migrates all the way to the central star (or into the magnetospheric cavity if one is present). In this chapter, I address the question of whether or not radial structuring of a protoplanetary disc, because of spatial and temporal variations in the viscous stress, can prevent accreting giant planet cores from migrating inwards rapidly because of the 'planet traps' created by the surface density variations (Masset et al., 2006). Although I adopt a simple,

proof-of-concept 'toy model' for the generation of radial structuring of the disc, the results suggest that this may provide an effective means of allowing the formation of surviving cold Jupiters, and point the way to an avenue of potentially fruitful future research.

The chapter is organised as follows. I describe the updates to the physical model and numerical methods in section 5.1. I present the results in section 5.2, and draw conclusions in section 5.3.

5.1 Physical model and numerical methods

The n-body simulations presented here were performed using the *Mercury-6* symplectic integrator (Chambers, 1999), adapted to include the additional physical processes described below. Some of these are updated versions of those described in chapters 3 and 4, and some of the processes are new to this chapter.

5.1.1 Model improvements

5.1.1.1 Gas envelope accretion

A planet undergoes runaway gas accretion once the envelope and core are of comparable mass, and during this phase the planet rapidly accretes the material occupying its feeding zone, until it reaches its 'gas isolation mass', where the feeding zone is now empty and a gap has formed in the disc. In chapter 3 I obtained fits to the runaway gas accretion rates from 2-D hydrodynamic simulations, but those fits only considered the migration of the rapidly accreting planet after it had reached its 'gas isolation mass'. I have improved on the fits in chapter 3 by allowing the planet to migrate while undergoing runaway gas accretion. Including migration in the determination of the fits makes them more consistent with the hydrodynamic models.

Once a planet enters the runaway gas accretion phase prior to reaching the gap forming mass, the following steps are applied:
(i) Calculate the gas isolation mass, $m_{\rm iso}$, according to:

$$m_{\rm iso} = 2\pi r_{\rm p} \Sigma_g(r_{\rm p}) \Delta r \tag{5.1}$$

where $\Sigma_g(r_{\rm p})$ is the gas surface density taken at the planet's location, and Δr is given by

$$\Delta r = 6\sqrt{3} r_{\rm H} \tag{5.2}$$

where $r_{\rm H}$ is the planet's Hill radius.
(ii) Recalculate $m_{\rm iso}$ at each time step to account for the drop in $\Sigma_{\rm g}$ as the material in the planet's feeding zone diminishes.
(iii) Allow the planet to grow rapidly to $m_{\rm iso}$ by removing gas from the disc around the planet and adding it to the planet, using gas accretion rates obtained from the fits to the Movshovitz et al. (2010) models. Once the planet reaches $m_{\rm iso}$, it transitions to type II migration and begins accreting at the viscous rate.

When implementing the above prescription, I define the point at which the planet enters runaway gas accretion to be when $\frac{dm}{dt} \geq 2\,{\rm M}_{\oplus}$ per 1000 yr. When the gas isolation mass is calculated I assume a maximum gas isolation mass of $400\,{\rm M}_{\oplus}$, which accounts for when a planet enters the runaway gas accretion phase in a massive disc, where tidal torques from the planet would evacuate the feeding zone before the gas isolation mass was reached. I note that a planet that does not reach the runaway gas accretion mass prior to reaching the local gap forming mass would instead transition directly to type II migration without accreting the material within its feeding zone, and will begin accreting at the smaller of the rate obtained from the fits to Movshovitz et al. (2010), or the viscous supply rate. I note that all of the values displayed above have been determined to give the best agreement with 2D hydrodynamic simulations similar to those presented in section 3.4.

5.1.1.2 Migration during runaway gas accretion

Until the planet reaches the mass required for runaway gas accretion, it undergoes type I migration using the torque formulae of Paardekooper et al. (2010, 2011). Once it undergoes runaway gas accretion, the planet begins to carve a gap in the disc by rapidly accreting the surrounding material. To account for this change in conditions, the planet stops undergoing type I migration and begins to migrate at a rate with a timescale equal to the local viscous evolution time:

$$\tau_{\nu} = \frac{2r_{\rm p}}{3\nu}. \tag{5.3}$$

Migration at this rate continues until the planet reaches the gas isolation mass, where it transitions to self-consistent type II migration driven by the coupling to the viscous evolution of the disc via the impulse approximation (Lin & Papaloizou, 1986). I note that recent hydrodynamic simulations have indicated that the migration of gap forming planets does not necessarily occur at exactly the viscous flow rate of the gas in the disc (Duffell et al., 2014; Dürmann & Kley, 2015), due to residual

gas in the gap adding to the migration torque. For the disc and planet masses that are considered in this chapter, however, the migration rates provided by the impulse approximation are in reasonable agreement with those obtained in hydrodynamic calculations presented in section 3.4.2.

5.1.2 Disc radial structures

Simulations performed in chapters 3 and 4 failed to form any surviving gas giant planets, other than hot Jupiters that are only prevented from migrating into their host stars by the presence of a central magnetospheric cavity. An analysis of the conditions required for gas giants to form and survive outside of the central cavity presented in chapter 3 demonstrated that runaway gas accretion and the transition to type II migration needs to occur when the planets are distant from their stars. For example, for a Jovian mass planet to form and settle into a final orbit at ~ 1 au, requires type II migration to be initiated at ~ 6 au. A Jovian planet orbiting at ~ 5 au needs to initiate runaway gas accretion and type II migration at ~ 15 au. The time of formation also provides a constraint: form too early in the disc life time and a planet migrates all the way into the central cavity; form too late and there is insufficient gas available to build a gas giant. It is noteworthy that population synthesis simulations produce a large number of surviving cold gas giants (e.g. Mordasini et al., 2009). Chapter 3 examined the planet mass and orbital evolution obtained using the following three approaches: 1-D disc models similar to those presented in this paper; 2-D hydrodynamic simulations that were designed to match the conditions in the 1-D models; the prescriptions for mass growth and migration used in population synthesis models. I showed that the discrepancy obtained in giant planet survival rates between the modelling approaches arises because a migration-slowing factor is included in the population synthesis models when in the so-called planet-dominated regime, and this results in too much slowing of type II migration compared to that observed in the 2-D hydrodynamic simulations or in the 1-D viscous disc models.

Retaining the cores of gas giants at large orbital radii is difficult, especially late in the disc life time. The corotation and Lindblad torques need to balance, such that the core orbits in a "zero-migration zone" (Bitsch & Kley, 2011; Cossou et al., 2013; Hellary & Nelson, 2012). The corotation torque has entropy-related and vortensity-related components, and it is the entropy-part that is normally strongest and able to balance the Lindblad torque when the temperature profile decreases outwards steeply. In a viscous, irradiated disc, the inner regions of the disc, where the viscous

dissipation dominates the heating, have steep temperature gradients, and early in the disc life time the zero-migration zone can extend out to $\sim$ 10 au for planet masses $\gtrsim$ 10 $M_\oplus$ (Bitsch et al., 2015a; Bitsch & Kley, 2011; Coleman & Nelson, 2014; Cossou et al., 2013; Hellary & Nelson, 2012). As the disc evolves, however, the viscous heating rate decreases and the zero-migration zone moves into the inner 1–2 au and only prevents the migration of lower mass planets. Although the details of the evolution depend on input parameters such as the viscous stress and the opacity, it would seem to be difficult to maintain strong entropy-related corotation torques in the outer disc regions during the later phases of disc evolution. One alternative for maintaining cores at large radii might be for the vortensity-part of the corotation torque to be strengthened in regions where the surface density increases with radius, such as may occur if the disc surface density contains undulations . These regions might act as planet traps (Masset et al., 2006), as well as being regions where small sized bodies such as dust, pebbles, boulders and small planetesimals could concentrate (e.g. Pinilla et al., 2012). The main focus of this chapter is to examine the consequences of allowing protoplanetary discs to be radially structured because of radial variations in the viscous stress. My approach is to employ a very simple "toy model" for simulating these radial structures, but I derive motivation from recent observations of protoplanetary discs, and from the long history of MHD simulations showing that discs which support magnetorotational turbulence (Balbus & Hawley, 1991) often demonstrate radial structuring in the form of zonal flows.

5.1.2.1 Observed structures

Recent observations of the young class I T Tauri star, HL Tau, have shown the presence of a number of quasi-axisymmetric rings, corresponding to maxima and minima in the emitted intensity as a function of radius. The system of rings extends between 13–100 au (ALMA Partnership et al., 2015). A number of suggestions have been put forward to explain the rings, included embedded planets (Dipierro et al., 2015; Picogna & Kley, 2015), pressure bumps that trap dust (Flock et al., 2015), enhanced dust growth near ice lines (Zhang et al., 2015), and sintering of dust aggregates (Okuzumi et al., 2016). Even more recent ALMA observations of the disc around TW Hydra have also uncovered a series of rings (Andrews et al., 2016), suggesting that these really are common phenomena that arise during the evolution of protoplanetary discs. The closer proximity of TW Hydra to the Solar System allows regions of the disc that lie closer to the central star to be probed by the ALMA observations, and these have uncovered rings between orbital radii 1 –

40 au. Furthermore, although high resolution ALMA images of other protoplanetary discs have not yet been released, existing ALMA data for a number of other discs indicate that ring structures are present in the disc outer regions (Zhang et al., 2016), suggesting that these features are common phenomena that arise during the evolution of protoplanetary discs. Although I do not attempt to fit the simulations to these observations, I simply note that a plausible scenario for the origin of these rings is radial variation in the effective viscous/turbulent stresses that give rise to variations in the surface density.

5.1.2.2 Zonal flows in MHD simulations

Over a number of years, both global (Fromang & Nelson, 2006; Papaloizou & Nelson, 2003; Steinacker & Papaloizou, 2002) and local (Johansen et al., 2009b) simulations of magnetised discs have demonstrated the occurrence of persistent density/pressure maxima and minima as a function of radius, arising from localised magnetic flux concentration and associated enhancement of magnetic stresses. More recent simulations incorporating non-ideal MHD effects have also reported the existence of these features in local (Bai & Stone, 2014) and global (Béthune et al., 2016; Zhu et al., 2014) simulations. Density variations with amplitudes up to $\sim 50\%$ of the background have been reported (Bai & Stone, 2014). Being in geostrophic balance, these pressure bumps are often referred to as zonal flows (Johansen et al., 2009b). Simon et al. (2012) have recently observed long-lived zonal flows in simulations with radial domains up to 16 scale heights, and in these large shearing boxes they find that the outer radial scale of the zonal flows is $\sim 6H$, although they stress that simulations in larger domains are required to demonstrate convergence. Dittrich et al. (2013) ran shearing box simulations with radial domains up to $21H$ and also found the radial sizes of the axisymmetric zonal flows to be between 5 and $7H$. The study by (Bai & Stone, 2014) noted that zonal flows in radially-narrow shearing boxes tended to be intermittent, but runs in large shearing boxes of width $16H$ persisted for the full duration of the simulations, which had total run times of 400 orbits. Zonal flows are clearly able to live for long times, but at present it is not clear what their characteristic life times are.

Although I do not try to fit a model to these MHD simulations, and instead take the approach of employing a simple prescription to demonstrate "proof of concept", I note that global MHD simulations which display dust concentration in pressure bumps have been used to compare theoretical calculations with the observed structures in protoplanetary discs (Flock et al., 2015). Density and pressure bumps

Structure label	$r_{\rm min}$ (au)	$r_{\rm max}$ (au)	Lifetimes ($\times 10^3$ local orbits)
1	4.25	5.75	10, 50, 100
2	9.25	10.75	10, 50, 100
3	14.25	15.75	10, 50, 100
4	19.25	20.75	10, 50, 100

Table 5.1: Radial structure parameters

arising from variations in magnetic or turbulent stresses may be a common feature of planet forming discs. In addition to the zonal flows described above, similar features may also arise in regions where there is a transition from one non-ideal MHD process being dominant to another becoming dominant (i.e. a transition between Hall and ambipolar dominated regimes (Flock et al., 2015)), or at the interface between magnetically active and dead zones. In the presence of these transitions, the disc may not be able to maintain a constant mass flux through all radii at all times, and radial structuring may occur. For simplicity, in this chapter I just consider a rather crude model for disc structuring that is intended to mimic the growth and decay of zonal flows, but I note that radial structuring may also occur because of other physical processes that influence the local rate of mass flow through the disc.

5.1.2.3 A simple model for radial structuring

I incorporate radial structuring in the models by introducing a spatially and temporally varying viscous stress. At any one time, four structures are present in the simulations. While this number is arbitrary, it is similar to the number of rings observed in *HL Tau* and *TW Hydra*. Each one exists between specific, predefined radii ($r_{\rm min}$, $r_{\rm max}$), where the values are given in table 5.1. Each structure has a finite life time (see the final column of table 5.1), and as it decays a new structure grows within the same range of radii $r_{\rm min} < r < r_{\rm max}$. I initiate the structures 50,000 years after the start of the simulations, once the disc has reached a quasi-steady state, by increasing the viscosity parameter α up to a maximum strength of 1.5× that of the background value. This value was chosen to approximately match the $\sim 50\%$ variation in the surface density due to the zonal flows obtained in the MHD simulations of Bai & Stone (2014). For each structure, the maximum value of α is located at the centre of that structure, whilst I transition α to its background value over a distance of 3.5 local scale heights using a Gaussian kernel, giving each structure a width of 7 local scale heights. Once each of the structures begins to form, it does so over 100 local orbital periods by increasing α from the background value up to the

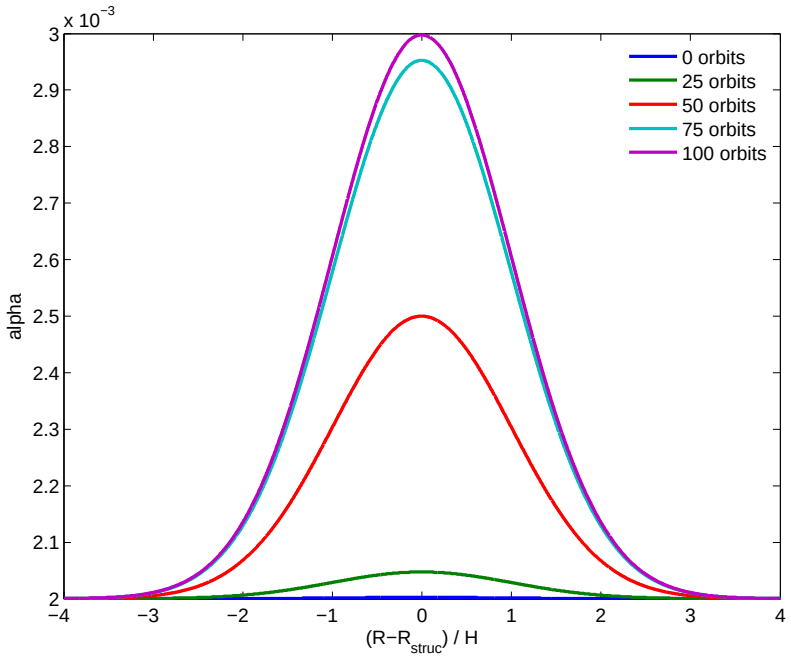

Figure 5.1: Plot showing the time variation of the viscous α associated with the formation of a radial structure over a time of 100 local orbits.

required value, as described below:

$$\alpha(r,t) = \alpha_{\rm b} + \frac{\alpha_{\rm b}}{2} r_{\rm new} t_{\rm new} \tag{5.4}$$

where $\alpha_{\rm b}$ is the background value, and $r_{\rm new}$ and $t_{\rm new}$ are the radial and time factors defined by

$$r_{\rm new} = \exp\left(\frac{-(r - r_{\rm struc})^2}{2H^2_{\rm struc}}\right) \tag{5.5}$$

$$t_{\rm new} = 0.5 \times \left(\tanh\left(\frac{6(t - t_{\rm start} - 0.5(t_{100} - t_{\rm start}))}{t_{100} - t_{\rm start}}\right) + 1\right) \tag{5.6}$$

where the subscript 'struc' denotes the radial location of the centre of the structure, $t_{\rm start}$ is the structure formation time, $t_{100} - t_{\rm start}$ represents the time interval of 100 orbital periods after the structure begins to form, evaluated at the structure's centre, and H is the local disc scale height. A formation time of 100 local orbital periods is chosen to allow a smooth transition between an unstructured and a structured disc. The shape and time evolution of the locally varying viscous α parameter associated with an individual structure as it forms is shown in figure 5.1, where the α parameter gradually increases to the required value, while maintaining a smooth profile.

The radial structures have specific lifetimes, and this is a parameter that I vary in the simulations described below. When a structure comes to the end of its lifetime

it quickly disappears over 100 local orbital periods. As one structure disappears, another one forms at a randomly chosen location within the range of allowed radii given in table 5.1. When the structure starts to disappear, α evolves according to:

$$\alpha(r) = \alpha_{\rm b} + \frac{\alpha_{\rm b}}{2} r_{\rm old}(1 - t_{\rm old}), \tag{5.7}$$

where $t_{\rm old}$ is given by

$$t_{\rm old} = 0.5 \times \left(\tanh \left(\frac{6(t - t_{\rm end} - 0.5(t_{100} - t_{\rm end}))}{t_{100} - t_{\rm end}} \right) + 1 \right). \tag{5.8}$$

Here, $t_{\rm end}$ is the time at which the structure begins to dissipate and t_{100} represents 100 orbital periods after this time. $r_{\rm old}$ is equal to equation 5.5 but with values taken for the old structure instead of a new one, as shown by this expression

$$r_{\rm old} = \exp \left(\frac{-(r - r_{\rm oldstruc})^2}{2H^2_{\rm oldstruc}} \right). \tag{5.9}$$

To account for a new structure being influenced by a dissipating older structure, equation 5.4 becomes

$$\alpha(r, t) = \alpha_{\rm b} + \frac{\alpha_{\rm b}}{2} (r_{\rm new} t_{\rm new} + r_{\rm old}(1 - t_{\rm old})) \tag{5.10}$$

This allows a smooth transition between two adjacent forming/dissipating structures.

Below I discuss the main effects of radial structures on the disc profile and migration of embedded low mass planets.

5.1.2.4 Effects on disc and planet evolution

Figure 5.2 shows the surface density evolution for a $1 \times$ MMSN disc in simulations without (top panel) and with (bottom panel) radial structuring. The drop in surface density in the inner regions of the discs arises because both models include an increase in α by a factor of 5 from the background values of either 2×10^{-3} or 6×10^{-3} where the disc temperature exceeds 1000 K (Coleman & Nelson, 2016a). The presence of the radial structures arising from the variations in α in the outer disc are evident in the right panel. While these surface density dips have little influence on the global disc evolution, they have a dramatic effect on planet migration.

Figure 5.3 shows contours that illustrate the direction and speed of type I planet migration as a function of planet mass and semimajor axis at different times in a

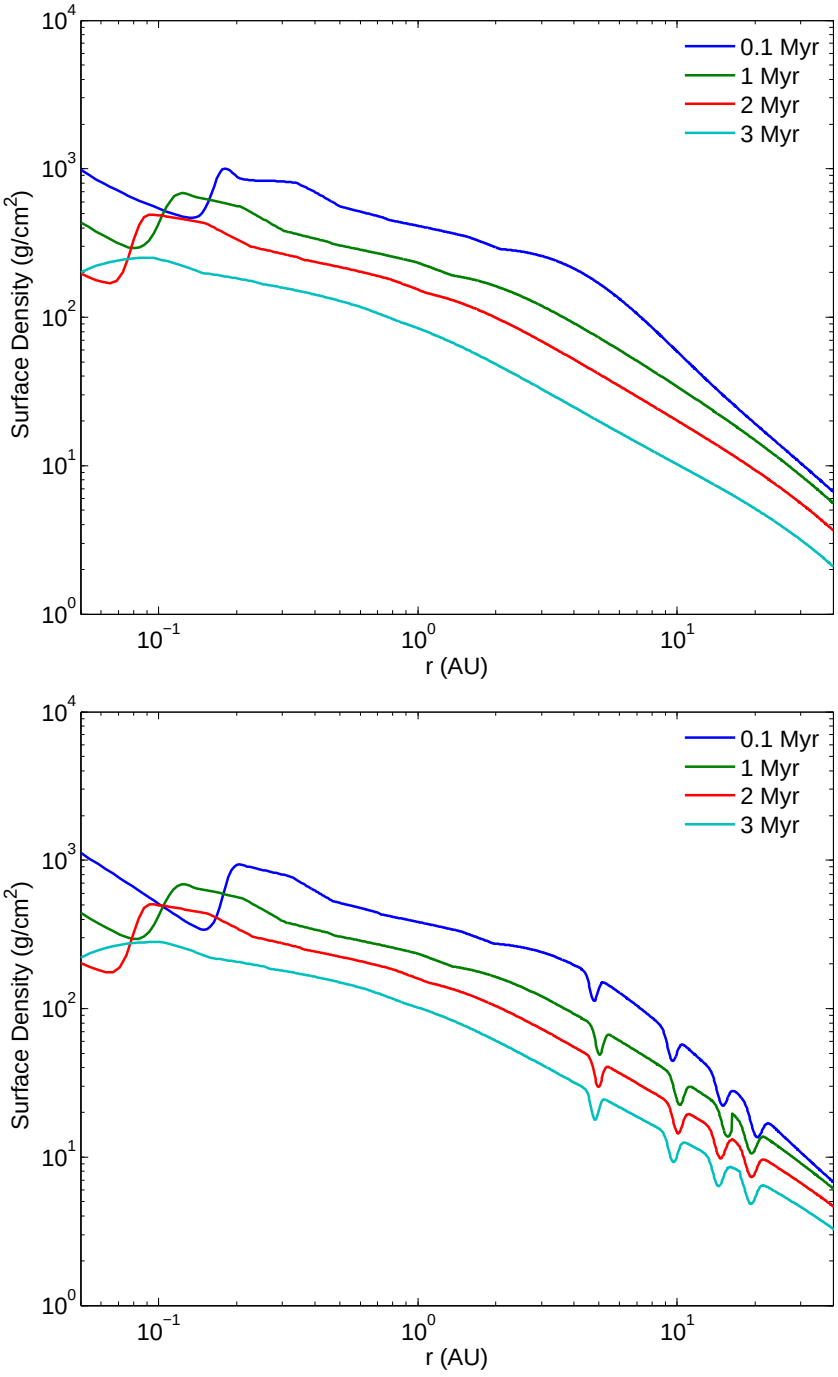

Figure 5.2: Surface density profiles at t = 0.1, 1, 2, 3 Myr for a 1×MMSN disc (total lifetime $\sim$ 5.5 Myr) without (top panel) and with (bottom panel) radial structuring.

$1 \times$ MMSN disc with solar metallicity. The left panel shows a simulation without radial structuring, and the right panel is for a run with structuring switched on. Red regions correspond to rapid inward migration, blue regions correspond to rapid outward migration, and white contours interspersed between the red and blue contours represent zero-migration zones where Lindblad and corotation torques cancel. The white contours at the top of the panels correspond to planets reaching the gap opening mass and undergoing type II migration. The planet trap arising from the inner fully-developed turbulent region is represented by the innermost blue contour, apparent in the first three frames of each simulation. As the surface density decreases, the zero-migration zones and extended regions of outward migration associated with strong entropy-related corotation torques slowly move in towards the star on the disc evolution time scale in both runs, but the run with radial structures maintains four zero-migration zones in the outer disc for the duration of the simulation, leading to the possibility of long-term trapping of planetary cores with masses up to $\sim 30\,\mathrm{M}_{\oplus}$.

If a planet core was to migrate to the edge of one of the four structures, then it would be trapped for the lifetime of the structure. The core is released from the structure when it comes to the end of its life, and the planet starts to migrate inwards. A new structure is formed locally to replace the old one, and this has some probability of being located inside the old one (that depends on the location of the old structure within its allowed range of radii). If the new structure sits inside the old one then the planet core can be trapped by it, but if it sits outside the planet location then the planet migrates inwards, either into one of the other three structures, or in towards the star if it has just escaped from the innermost structure. Furthermore, a rapidly migrating planet core can escape from a structure while it is decaying and before the next structure has developed fully. This shows that the long term orbital evolution of a planetary core has a stochastic element that depends on the detailed evolutionary histories of the radial structures in the disc. Some cores remain trapped at large radius over the disc lifetime, whereas other cores escape from the planet traps and migrate into the disc inner regions.

Gas accretion can occur onto a core that is trapped if its mass exceeds $m_{\mathrm{p}} \geq 3\,\mathrm{M}_{\oplus}$, and if it remains in the outer disc for an extended period of time then runaway gas accretion can occur and a giant planet can form. The planet would then open a gap in the disc, and begin to undergo type II migration as the planet traps are not effective for gap forming planets. The process of building planets at the planet traps is enhanced by the concentration of boulders and planetesimals at these locations, which can then be accreted efficiently by the growing planets. In general, I find that accretion of solids by planetary embryos occurs during an early burst, prior to

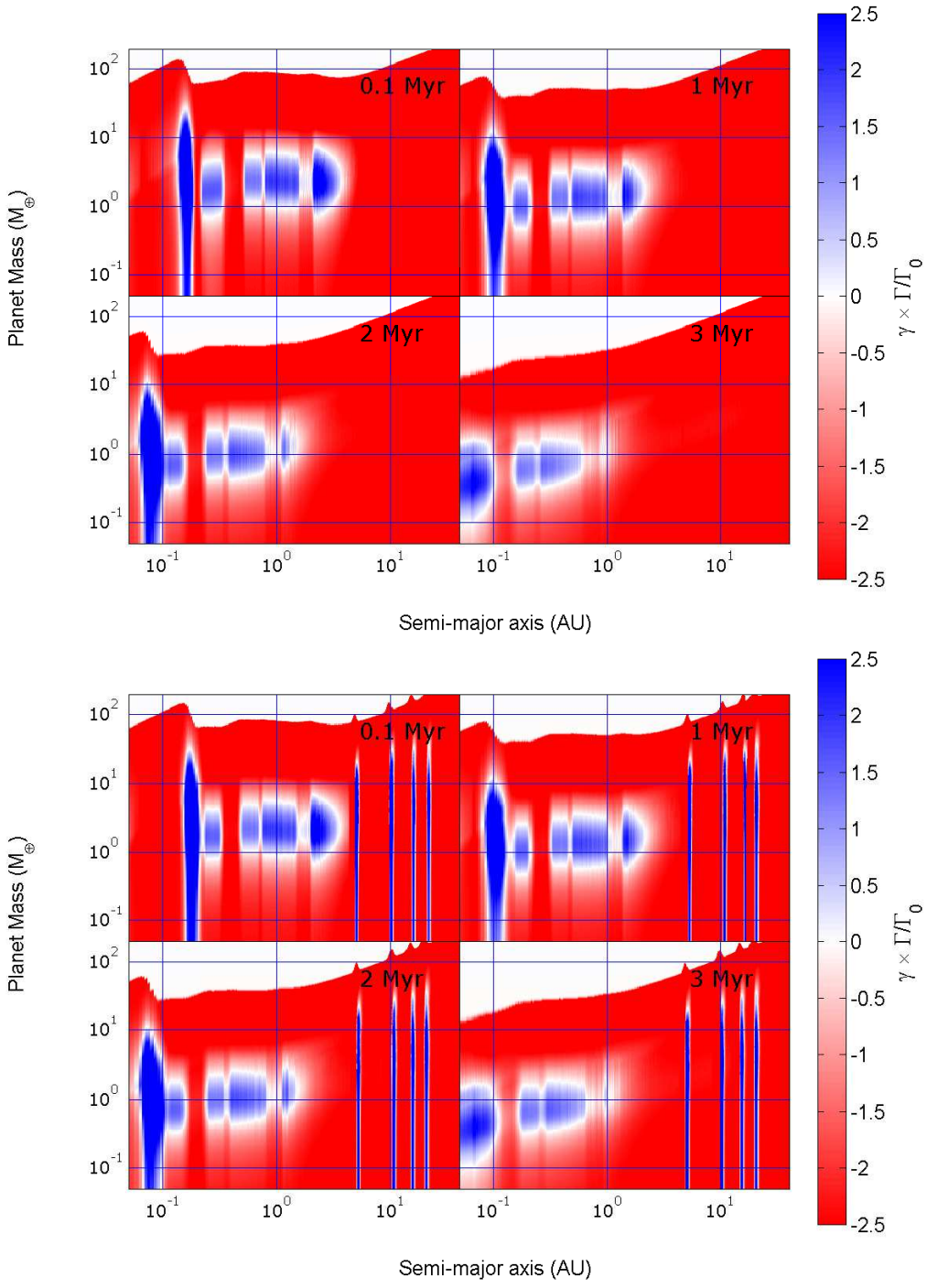

Figure 5.3: Contour plots showing regions of inwards (red) and outwards (blue) migration) in a $1\times$MMSN disc at t = 0.1 (top left), 1 (top right), 2 (bottom left) and 3 Myr (bottom right) for discs without (left panel) and with radial structuring (right panel). The white contours at the top of each panel corresponds to the planet reaching the local gap forming mass, at which point the planet will undergo type II migration. The contours represent values of $\gamma\Gamma/\Gamma_0$, where γ is the ratio of specific heats, Γ is the torque experienced by a planet and Γ_0 is a normalisation factor defined in Paardekooper et al. (2010).

Parameter	Values/Ranges
Disc mass	1, 2 ×MMSN
Disc metallicity	0.5, 1, 2 × Solar
Total solids mass	12.5–109 $M_\oplus$
Background viscous α	2×10^{-3}, 6×10^{-3}
Planetesimal radii	10 m, 100 m, 1 km, 10 km
Planetesimal mass	0.004, 0.01, 0.02 $M_\oplus$
Planetesimal number	1000 – 5000
Gas disc lifetimes	3.5 – 8.4 Myr

Table 5.2: Values, and the ranges of values, adopted for various simulation parameters.

the onset of the main gas accretion phase. Gas accretion is then accompanied by modest planetesimal accretion at rates that are similar to or below those prescribed in the Movshovitz et al. (2010) models that determine gas accretion rates in the simulations. Approximately 20% of the giant planets in the runs experience an episode of rapid and short-lived solids accretion, normally during the runaway gas accretion phase when the growth of the giant acts to destabilise the system. This burst of accretion can either arise from an impact with a low mass protoplanet, or through accretion of a local swarm of planetesimals over a time period that is less than ∼10,000 years. The fits to the Movshovitz et al. (2010) models do not allow the gas accretion rate to respond to this time-varying planetesimal accretion, and this is one area for future improvement of the model.

In summary, I have introduced a simple model for the radial structuring of protoplanetary discs that includes assumptions about the number of surface density features (planet traps) that are formed and their lifetimes. I present this model as a simple proof-of-concept, and do not include an extensive analysis of what happens when the model parameters are modified. It is reasonable to suppose, however, that reducing the number of planet traps and their lifetimes will result in less efficient trapping of planet cores, and hence less efficacious giant planet formation. Precisely how the formation of giant planets is affected by variation of model parameters will be examined in future work.

5.1.3 Initial conditions

Table 5.2 gives an overview of the parameters used in the simulations. All simulations were initiated with 44 planetary embryos, of mass 0.2 $M_\oplus$, with semimajor axes between 1 and 20 au and separated by 10 mutual Hill radii. These were em-

bedded in a swarm of thousands of planetesimals/boulders, that were distributed with semimajor axes between 0.5 and 25 au, with masses either 10, 20 or 50 times smaller than the embryos, depending on the metallicity of the system. (This varying mass ratio between embryos and planetesimals was implemented to obtain a planetesimal number that allowed the simulations to run on reasonable time scales. Between 1000 and 5000 planetesimals/boulders were used and run times for individual simulations varied between 2 and 6 months.) The total mass of solids ranges between 12.5–109 $M_\oplus$ depending on the disc mass and metallicity. The effective physical radii of planetesimals were set to 10 m, 100 m, 1 km or 10 km, such that the primary feedstock of the accreting protoplanets ranged from being boulders to large planetesimals whose evolution differed principally because of the strengths of the gas drag forces that they experienced. Initial eccentricities and inclinations for protoplanets and planetesimals/boulders were randomized according to a Rayleigh distribution, with scale parameters $e_0 = 0.01$ and $i_0 = 0.25°$, respectively.

Collisions between protoplanets and other protoplanets or planetesimals resulted in perfect sticking, which probably results in a slight overestimate of accretion rates in the simulations. I neglect planetesimal-planetesimal interactions and collisions in the simulations for reasons of computational speed.

The gas disc masses simulated were 1 and 2 times the mass of the minimum mass solar nebula (MMSN Hayashi, 1981). I also vary the metallicity so that the initial solids-to-gas mass ratios in the discs are equal to 0.5, 1 and 2 times the solar value for the different models. I define the solar metallicity to be equivalent to the solids-to-gas ratio introduced by Hayashi (1981). I smoothly increase the mass of solids exterior to the snow line by a factor of 4 by increasing the numbers of planetesimals, and the initial surface density of solids follows the initial gas surface density power law, as described in Hellary & Nelson (2012). I track the changes in planetary compositions throughout the simulations, as planets can accrete material originating either interior or exterior to the snow line.

I use two different values for the background α value, $\alpha = 2 \times 10^{-3}$ and 6×10^{-3}. These values of α correspond to disc lifetimes of 5.5 and 3.5 Myr respectively for a disc with mass equal to 1 × MMSN. I examine the effect of varying the lifetimes of the radial structures in the disc, with the three values assumed being 10^4, 5×10^4 and 10^5 local orbital periods. I ran two instances of each parameter set, where only the random number seed used to generate initial particle positions and velocities was changed, meaning that a total of 288 simulations have been run. The simulations were run for 10 Myr, or until no protoplanets remained.

I adopt an inner boundary to the simulation domain at 0.04 au, which is assumed

Classification	**Mass** $M_\oplus$	**Rock** %	**Ice** %	**Gas** %	**Final Number**
Earth					
Rocky	$m_p < 3$	> 70	< 30	0	1563
Water-rich	$m_p < 3$	< 70	> 30	0	4625
super-Earth					
Rocky	$3 \leq m_p < 10$	> 60	< 30	< 10	12
Water-rich	$3 \leq m_p < 10$	N/A	> 30	< 10	83
Gas-rich	$3 \leq m_p < 10$	N/A	N/A	> 10	69
Neptune					
Gas-poor	$10 \leq m_p < 35$	N/A	N/A	< 10	5
Gas-rich	$10 \leq m_p < 35$	N/A	N/A	> 10	79
super-Neptune					
Gas-poor	$35 \leq m_p < 100$	N/A	N/A	< 50	29
Gas-rich	$35 \leq m_p < 100$	N/A	N/A	> 50	147
Giant Planets					
Jupiter	$100 \leq m_p < 1000$	N/A	N/A	> 50	120
Super-Jupiter	$m_p \geq 1000$	N/A	N/A	> 50	12

Table 5.3: Planetary classification parameters based on their mass and composition. Note that water-rich planets are so-called because they accrete water ice in solid form that originates from beyond the snow-line. Characteristics that play no role in the classification of a planet are denoted by "N/A" in the relevant columns. Note all Jupiters and Super-Jupiters formed in the simulations had gas mass fractions $\geq 50\%$.

to represent the outer edge of an inner magnetospheric cavity. Any planet that enters this region no longer evolves, unless another planet enters the cavity, in which case the latter body is retained and the former one is assumed to have been pushed into the star. This is repeated for all subsequent planets that pass through the inner boundary (note that no sub-Neptune mass planets entered the cavity and pushed any giants into the star). When presenting the results in figures 5.6, 5.8, 5.9 and 5.10, the final semimajor axes of these inner planets are reassigned to straddle the stopping radius at 0.04 au, in order to mimic the expectation that the inner cavities will have a range of radii. This reassignment assumes that the distribution of cavity edges is Gaussian with standard deviation of 0.01 au.

5.1.4 Planet classification scheme

To assist in the discussion of simulation outcomes, I have developed a new classification system for the different bodies that are formed. As there are no formal IAU definitions for exoplanet classes relating to their masses and compositions, there

is freedom of choice in how planets should be classified. I have chosen a scheme that uses mass as the primary discriminant and composition as a secondary one. I use the labels "Earth", "Neptune" and "Jupiter", along with the prefix "super" to define six mass-based classes, and subclasses are defined according to the volatiles content, either in the form of ice or gas, of the planets. Definitions of the different planet classes are given in table 5.3. Note that when I use the term "gas giant" I am referring to Jupiters or super-Jupiters.

5.2 Results

I now present the results for the simulations. I begin by discussing a representative run in which multiple giant planets were able to form and survive. I then present an overview of all the simulation outcomes, before examining how modifying parameters such as the disc mass, metallicity, photoevaporation model etc. changes the results.

5.2.1 Run CJ120.1210A

Run CJ120.1210A had a disc mass of $1 \times$MMSN, $2\times$ solar metallicity, and contained planetesimals with radii $R_{\rm p} = 100$ m. The total mass in planetesimals was 43.2 $\rm M_{\oplus}$ and that in protoplanets was 8.8 $\rm M_{\oplus}$. The background $\alpha = 2 \times 10^{-3}$, and radial structures had a lifetime of 10,000 local orbits. The direct photoevaporation model was used.

The evolution of protoplanet masses, semimajor axes and eccentricities are shown in figure 5.4, and the final state of the system is also represented in figure 5.10 (the case with the label CJ120.1210A). I also show the mass versus orbital period evolution of all protoplanets in figure 5.5, where filled black circles represent surviving planets, and the evolution of the labelled planets is described below. The end state after 10 Myr consists of: an inner compact system comprising 3 super-Earths/Neptunes; a cool Neptune and Earth-mass planet orbiting between 2.5–3.4 au; two cold Jupiters orbiting between 6–12 au; a collection of low mass planets ('debris'), that failed to grow during the simulation, orbiting out beyond 20-30 au. I ignore the long period 'debris' in the discussion below, and just concentrate on the other planets that form.

5.2.1.1 Cold Jupiters

The cores of the two Jupiters (see planet labels 1 and 2 in figures 5.4 and 5.5) begin to form at orbital radii 15-25 au within the first 0.5 Myr of the simulation, through

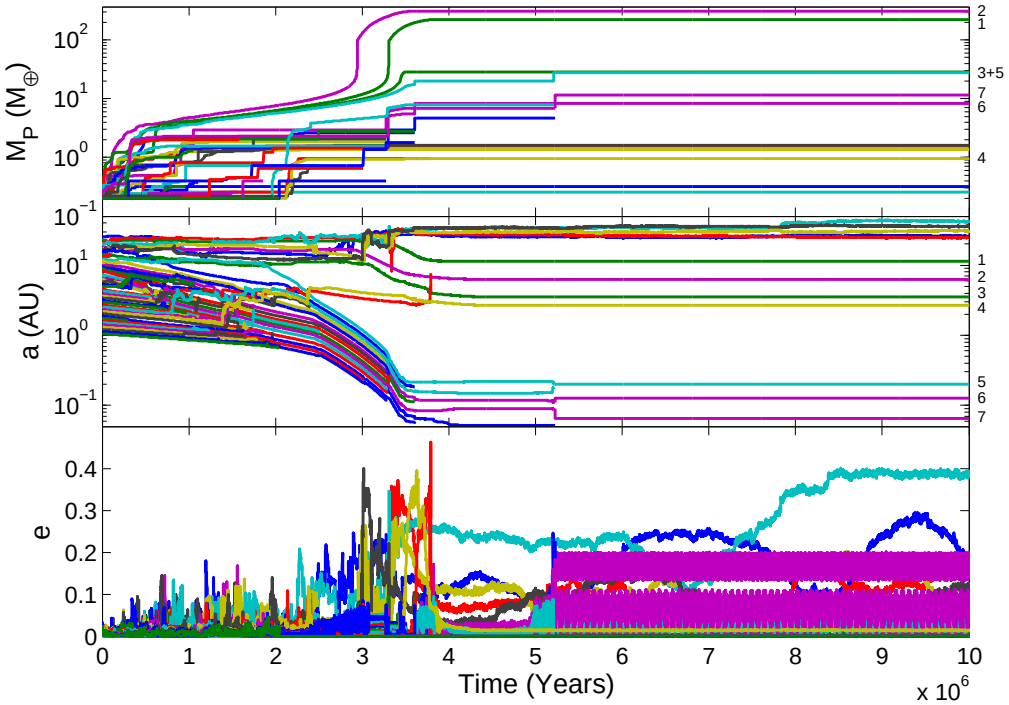

Figure 5.4: Evolution of masses, semimajor axes and eccentricities of all protoplanets in simulation CJ120.1210A. Note that formation histories of selected surviving planets are indicated by the labels on the right side of the mass and semi-major axis subplots.

a combination of planetesimal accretion and mutual collisions between embryos. Migration and trapping of planetesimals in the radial structures helps concentrate material which is then accreted by the embryos, stimulating rapid growth above $3\,M_\oplus$ such that gas accretion onto the growing cores can start. These proto-giant planets remain trapped at large radii by the radial structures, and continue to accrete gas steadily until runaway gas accretion is initiated at times just before and after 3 Myr, respectively (see the top panel of figure 5.4). The rapid burst of gas accretion takes the planet masses up to $\sim 100\,M_\oplus$, after which gap opening ensues. Initially both planets accrete at the viscous supply rate, but 'planet 1' truncates the disc exterior to it and prevents further gas accretion on to 'planet 2', which lies interior to 'planet 1'. The onset of gap formation allows the planets to type II migrate inwards until the gas disc is completely removed after ~ 4.5 Myr, although I note that the migration of 'planet 2' is slowed by the truncation of the disc by 'planet 1'. The gas giants have masses $306\,M_\oplus$ and $222\,M_\oplus$, gas mass fractions of 98%, semimajor axes 6.3 au and 11.4 au, orbital periods 15.8 yr and 38.5 yr and eccentricities ~ 0, respectively. While this pair of planets are far from being a perfect analogue to the Jupiter-Saturn system, there is an obvious similarity in terms of gross characteristics that is worthy

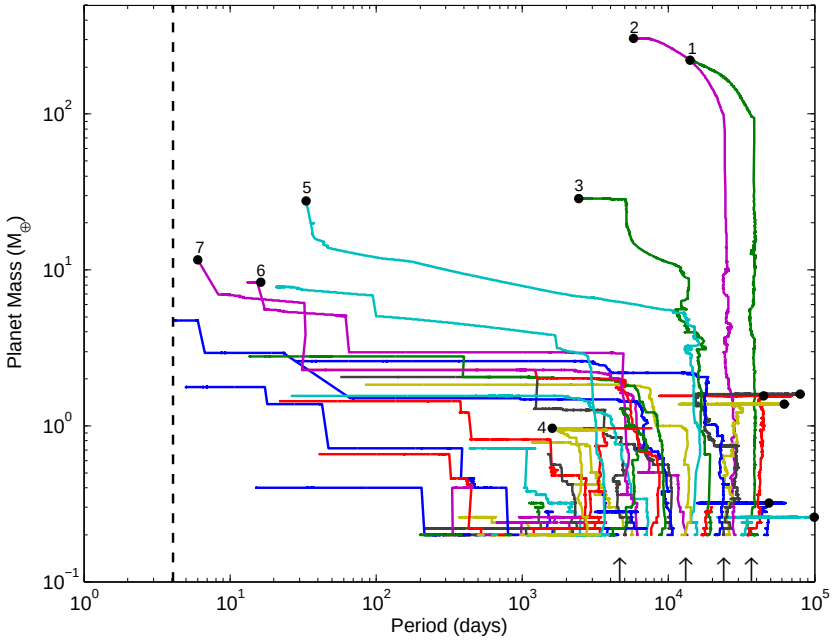

Figure 5.5: Evolution of planet mass versus orbital period for all protoplanets in simulation CJ120.1210A. Filled black circles represent final masses and orbital periods for surviving planets. Note that formation histories of selected surviving planets are indicated by the labels adjacent to the filled black circles. The dotted black line at $\sim$ 4d represents the inner edge of the simulated protoplanetary disc. The arrows above the x-axis indicate the average positions of the four radial structures.

of note (i.e. mass of inner planet $>$ mass of outer planet and semimajor axis ratio ~ 1.8).

5.2.1.2 Cool Neptune and Earth

These planets are labelled as 3 and 4 in figures 5.4 and 5.5. The cool Neptune begins its formation out beyond 10 au at the same time as the giant planet cores are forming, but interior to these two proto-giants. It also begins to accrete gas within the first 0.5 Myr, but at a slightly slower rate than the two proto-giants, and remains trapped by the radial structures during the first 3 Myr. The cool Neptune is nudged inwards when the innermost gas giant undergoes runaway gas accretion and starts type II migrating, and this allows the Neptune to escape the radial structures and migrate in towards the central star. Gas accretion onto the Neptune and its migration halt when the gas disc disperses after 3.5 Myr, leaving it with a mass of 28.6 $M_{\oplus}$, gas mass fraction of 86%, semimajor axis $\sim$ 3.5 au, orbital period 6.5 yr, and eccentricity $\sim$ 0. As this gas-rich Neptune escaped the radial structures and

migrated inwards it shepherded a $1\,M_\oplus$ water-rich terrestrial planet ahead of it, which had a final semimajor axis ~ 2.7 au and orbital period ~ 4.4 yr.

5.2.1.3 Compact inner system of super-Earths/Neptunes

The planets I discuss here have labels 5-7 in figures 5.4 and 5.5. This compact system forms from a combination of bodies that are initially orbiting interior to the radial structures and one dominant body that originates from larger radii. This more massive body grows through planetesimal accretion and collisions with neighbouring embryos out beyond 10 au, where it starts to accrete gas and remains trapped by the radial structures until 2 Myr. At this point its mass is $5\,M_\oplus$, and it is able to escape from the radial structures by migrating through them as they switch on and off, after which it undergoes rapid inward type I migration while continuing to accrete gas (becoming a gas-rich Neptune in the process). The gas-rich Neptune shepherds a large number of interior embryos in a resonant convoy as it migrates, and when the gas disc starts to disperse after ~ 3.5 Myr this convoy breaks up and mutual collisions between the numerous embryos lead eventually to the formation of a compact inner system comprised of 3 planets: a gas-poor Neptune with mass $11.6\,M_\oplus$, gas mass fraction 7%, semimajor axis ~ 0.07 au, orbital period 6 days and eccentricity 0.11; an icy super-Earth with mass $8.4\,M_\oplus$, gas mass fraction 6.5%, semimajor axis ~ 0.15 au, orbital period 16.2 days and eccentricity 0.2; a gas-rich Neptune with mass $27.6\,M_\oplus$, gas mass fraction 56%, semimajor axis ~ 0.2 au, orbital period 33.2 days and eccentricity 0.07. I note that the eccentricities of the these planets were pumped up to the values shown in the bottom panel of figure 5.4 during a late scattering event at 5.2 Myr.

5.2.2 Ensemble results

I now discuss the results of the simulations as a whole, focusing first on the masses and periods of the planets that form, and then on the eccentricity distribution.

5.2.2.1 Masses and periods

Considering the results of the simulations as a whole, 132 surviving giant planets are formed with masses ranging from $0.3\,M_{\rm Jupiter}$ to $4\,M_{\rm Jupiter}$, with periods from 5 days up to 24000 days (the smaller period being determined by the boundary conditions). The majority of these giant planets formed at the outer edges of radial structures, whilst a handful of less massive giant planets accreted the majority of their gas

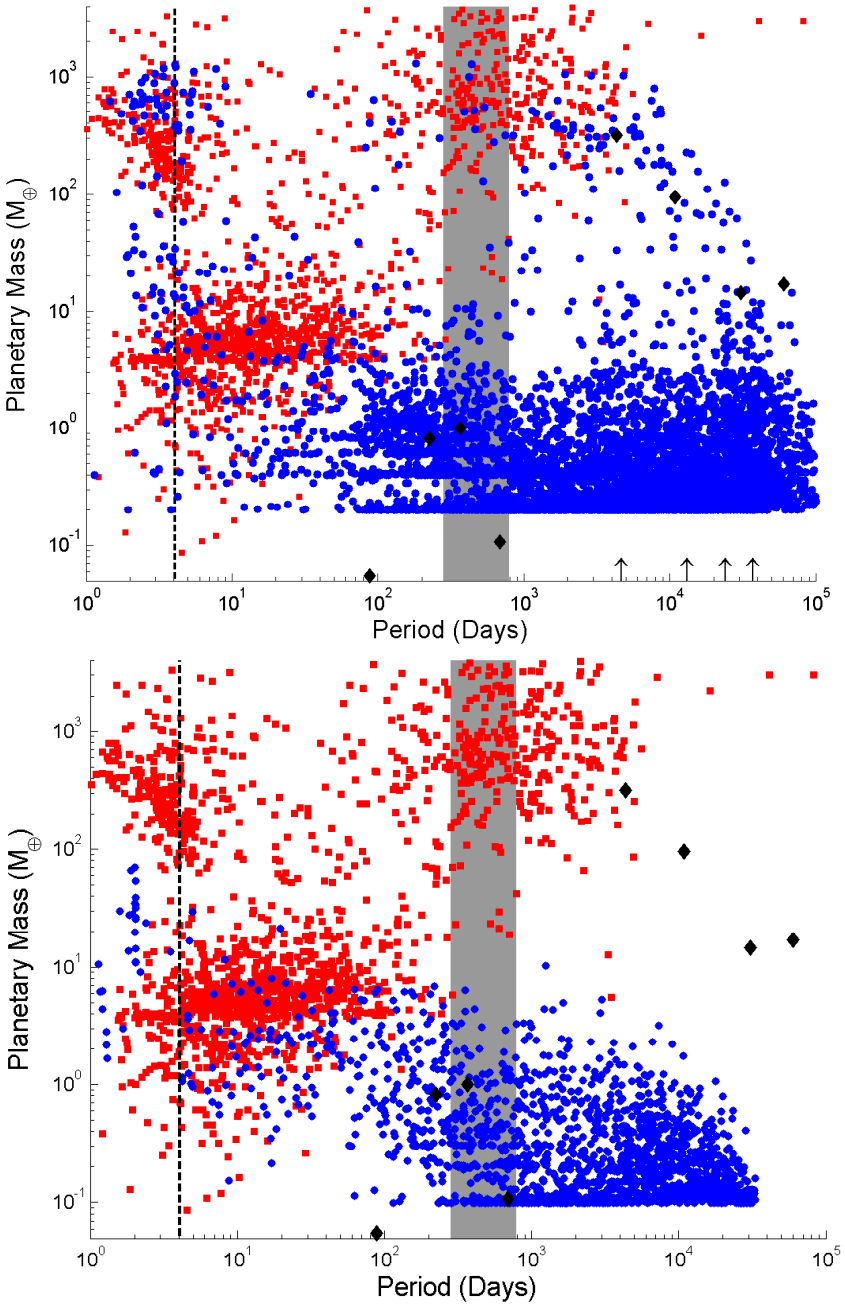

Figure 5.6: Upper panel: Mass vs period plot, comparing observed exoplanets (red squares) with the simulation results (blue circles) and the Solar System planets (black diamonds). Lower panel: Same as top panel but data taken from figure 4.12. The grey zones indicate the habitable zone (Kasting et al., 1993). The arrows at the bottom of the upper panel indicate the average positions of the four radial structures.

envelopes after escaping from the radial structures and type I migrating towards the central star. Figure 5.6 shows a mass versus period diagram for all of the surviving planets from the simulations, along with all confirmed exoplanets (Han et al., 2014).

The known exoplanets form three apparently distinct groups in the mass-period diagram: cold Jupiters with orbital periods $\gtrsim$ 100 days; hot Jupiters with orbital periods $\lesssim$ 10 days; super-Earths/Neptunes with periods between $2 \lesssim P \lesssim 100$ days. These features are affected by a number of observational biases, including the fact that ground based transit surveys are only sensitive to Jupiters with periods $\lesssim$ 10 days. Nonetheless, analysis of the period distribution of planets detected only by radial velocities seems to confirm that there is a real valley in the distribution between 10–100 days (Cumming et al., 2008; Udry et al., 2003). More recently, Santerne et al. (2016) have presented an analysis of giant planets discovered by the *Kepler* spacecraft that were followed-up using radial velocity measurements over 6 years, and they confirm that the period-valley also exists within this data set. One of the most striking features when comparing the results of the simulations with the observational data in figure 5.6 is the fact that the giant planets formed in the simulations are almost all hot Jupiters (periods $<$ 10 days) and cold Jupiters (periods $>$ 100 days), with only a few massive bodies being located in the region that corresponds to the observed period valley. Furthermore, the simulations produce numerous planets with masses in the range $0.5\,\mathrm{M}_\oplus \lesssim m_\mathrm{p} \lesssim 30\,\mathrm{M}_\oplus$ and periods between $2 \lesssim P \lesssim 100$ days, that correspond to the observed super-Earths and Neptunes. Some of these lower mass planets are in systems that contain giant planets, as described in the previous section for run CJ120.1210A, and some are devoid of any giants. Comparing the top panel of figure 5.6 with the bottom panel (a reproduction of figure 4.12), where similar n-body simulations, but without the inclusion of disc radial structures, were presented, I see that the agreement between the observed and simulated planet distributions is much improved in this chapter.

In the simulations, the origin of the two distinct populations of hot and cold Jupiters, and the period valley between them, can be explained as follows. Giant planets that form early in the disc lifetime migrate all the way into the magnetospheric cavity, and become hot Jupiters. Giant planets that are destined to *not* become hot Jupiters must form near the end of the disc lifetime, when photoevaporation plays an important role in the disc evolution. Photoevaporation, combined with viscous evolution, causes the disc to disperse from the inside out. There is a high probability that a giant forming towards the end of the disc lifetime will migrate towards the star when the disc interior to the critical radius for photoevaporation has been fully or partially evacuated, preventing it from migrating close to the star,

and ensuring that it remains as a cold Jupiter. Hence, the observed giant planet period distribution may arise as a combination of forming giant planets at large radius, having a stopping mechanism for migration at the inner edge of the disc (i.e. a magnetospheric cavity) and the inclusion of photoevaporation, which occurs outside a well-defined radius corresponding roughly to where a thermal wind can be launched. The influence of different models of photoevaporation on the results are discussed in more detail below, but I note that Alexander & Pascucci (2012) have suggested that disc clearing due to photoevaporation can be responsible for a pile-up of giant planets at 1 au, as planet migration is slowed when photoevaporation begins to dominate disc evolution. More recently Ercolano & Rosotti (2015) showed that different models of photoevaporation influence the pile-up location, with a thermal-wind launching inner radius of 1–2 au being preferred.

Low mass, compact systems that formed and migrated to the inner regions of the disc are seen in a number of simulations. The formation of these compact systems occurs similarly to those described in chapter 4, but some compact systems within this chapter contained giant planets with large orbital periods, as shown in section 5.2.1. The co-existence of long period giant planets and low mass compact systems in the simulation results seems to be in accord with the recent analysis of *Kepler* data indicating the presence of long period giant planets around stars known to host compact multi-systems (Kipping et al., 2016; Uehara et al., 2016).

5.2.2.2 Eccentricities of giant planets

The eccentricity distribution of observed giant ($m_{\rm p} \sin i \geq 100\,{\rm M}_{\oplus}$) exoplanets is shown in figure 5.7 for bodies with orbital periods > 10 days, along with the eccentricity distribution for planets in the same mass and period range that form in the simulations. It is clear that the eccentricity distribution associated with observed exoplanets is much broader than that generated in the simulations. The maximum eccentricity for a giant planet obtained in the simulations was $e_{\rm p} = 0.13$, whereas significant numbers of exoplanets are observed to have eccentricities > 0.3. I note that those simulated systems that resulted in modestly eccentric giants did so because the giant planets underwent strong gravitational scattering with other planets in the system, where the scattered bodies typically had masses $\simeq 20\,{\rm M}_{\oplus}$. Scattering between more massive bodies is required to obtain the larger eccentricities observed in the exoplanet data (e.g. Rasio & Ford, 1996).

Given that the simulations end after 10 Myr, it is possible that dynamical instabilities could occur on longer time scales in systems containing multiple giant

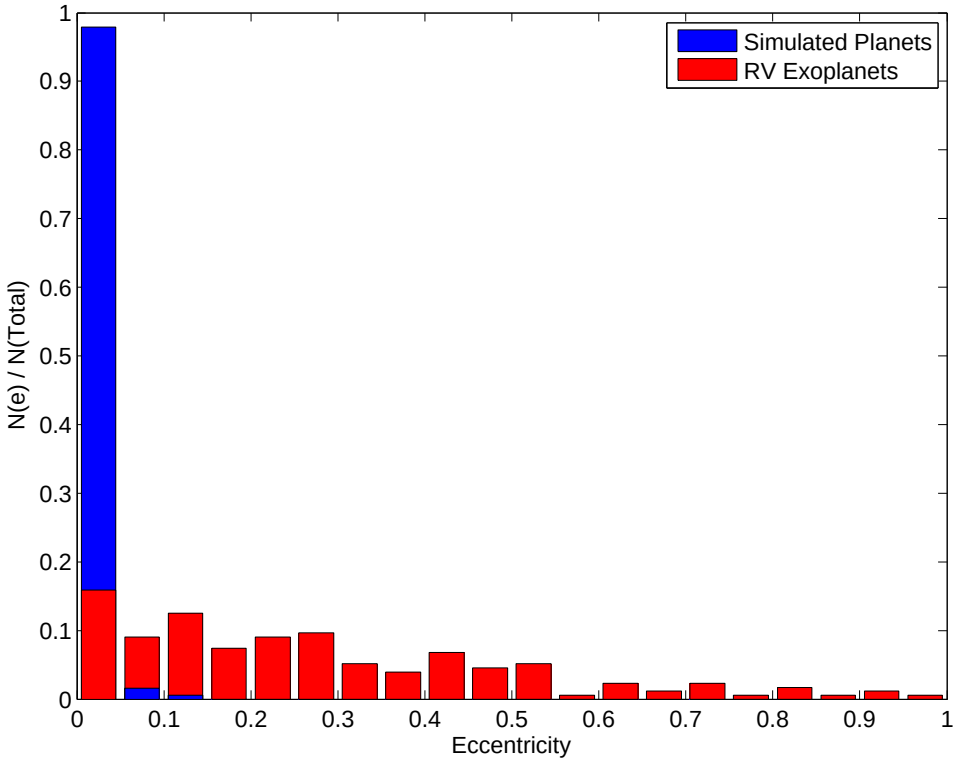

Figure 5.7: Distribution of observed giant exoplanet eccentricities (red) and the distribution arising from the simulations (blue).

planets, changing the statistics shown in figure 5.7. I have examined the distribution of mutual semimajor axis separations, expressed as a function of mutual Hill radii, to determine whether or not this is possible. I note that Marzari & Weidenschilling (2002) examined the dynamical stability of three Jovian-mass planets on initially circular orbits, and demonstrated that the instability time scale for such a system scales with the mutual Hill radius separation, with systems separated by ~ 6 mutual Hill radii having instability times of $\sim 10^9$ yr. All of the systems are at least as separated as this, with approximately half of the systems having semimajor axis separations between 6 and 12 mutual Hill radii, and the other half being more separated. This suggests that some of the simulated systems may undergo dynamical instabilities on time scales longer than 10 Myr, but it seems highly unlikely that running the simulations for Gyr time scales would result in an eccentricity distribution that matches the observed one.

Assuming that the observed eccentricity distribution of giant exoplanets arises primarily because of dynamical instabilities in multiplanet systems, and using the observed distribution as a constraint on viable formation scenarios, the data suggest that giant planets must often form in compact configurations, and do so more

frequently than occurs in the simulations.

Finally, I note that the simulations adopt a highly simplified prescription for the eccentricity damping experienced by gap forming planets, namely that the eccentricity is damped on a time scale of ~ 10 planet orbits. This is applied independently of the mass remaining in the gas disc, and so acts to bias the final systems towards having low eccentricities by reducing the likelihood of instabilities occurring while the gas disc is present. It is clear that a more sophisticated model will need to be adopted in future simulations if a more realistic assessment of the ability of the models to generate high eccentricity systems is to be undertaken.

5.2.3 Different photoevaporation models

5.2.3.1 Direct photoevaporation

Simulation CJ120.1210A, presented in section 5.2.1, was one of a group of simulations that allowed direct photoevaporation to impact the disc when the gas disc interior to the critical radius had accreted onto the central star. This can occur when a gap forming planet forms exterior to the critical photoevaporation radius, and the inner disc drains onto the star. In this scenario, the giant planet assists its own survival against migration by stimulating the onset of direct photoevaporation and reducing the disc lifetime. Figure 5.8 compares the cumulative distributions of giant planet periods from simulations with different photoevaporation models (colored lines) and observations (black lines). When comparing the observations, it is evident that for giant planets observed by *Kepler*, the ratio of hot Jupiters to cold Jupiters is lower than that found by radial velocity surveys. One possible reason for this is that the average of the metallicities of the *Kepler* stars is -0.18 dex (Huber et al., 2014), and this is lower than for stars in the solar neighbourhood where the average is -0.08 dex (Sousa et al., 2008). Comparing the observations with the simulations, it is clear that the blue line, representing simulations with direct photoevaporation, compares very reasonably with the observations, albeit with a higher fraction of hot Jupiters. Given that the simulations shown here have an average metallicity of 0.3 dex, the increased ratio is perhaps unsurprising, given that the boost in solid material can allow more rapid planet formation and therefore more time for migration. The period valley discussed above is also evident here, as is the good agreement between the simulated and observed cold Jupiter distributions.

Having observed the effect that direct photoevaporation has on the survival of giant planets with long orbital periods, I ran a further two sets of simulations with the same parameters as described in section 5.1.3, but with different photoevaporation

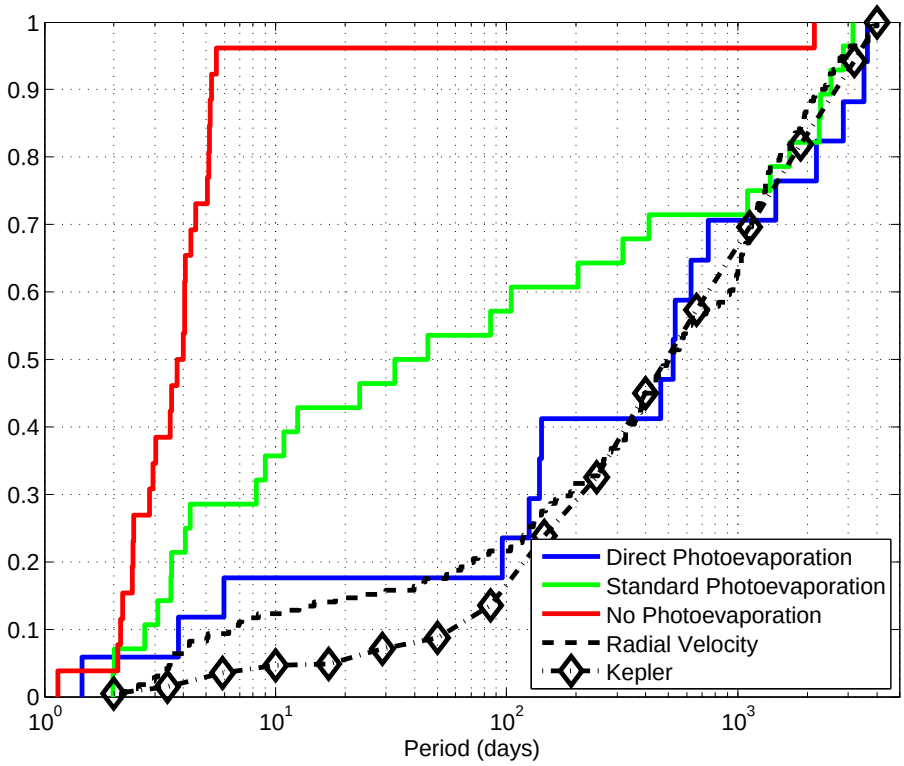

Figure 5.8: Normalised cumulative distribution functions of giant planet periods for radial velocity (black dashed line) and *Kepler* observed giant planets (black dot-dash line), and simulations with different photoevaporation regimes; direct (blue line), standard (green line), and none (red line). I define a giant planet in both simulations and observations as a planet with mass $m_{\rm p} \geq 100\,{\rm M}_{\oplus}$.

models, the standard one (obtained by just switching off direct photoevaporation) and no photoevaporation, in order to examine their effects on giant planet formation. The results of all simulations with disc mass 1× MMSN, metallicity 2× solar and $\alpha = 2 \times 10^{-3}$ are shown by the red (no photoevaporation) and green (standard) lines in figure 5.8 and are discussed in the following sections.

5.2.3.2 Standard photoevaporation

Given that only a modest number of the simulations containing large $\gtrsim 1$ km planetesimals formed giant planets, I only ran simulations with 10 m boulders or 100 m planetesimals to examine the influence of switching off direct photoevaporation and retaining the standard photoevaporation model. I note that when comparing the results of simulations that employed standard and direct photoevaporation models, evolution of the disc and planets are identical until the time that direct photoe-

vaporation is activated. This means that the formation pathways of giant planets is similar, and significant differences only arise for those cases where giant planet formation and migration occurs near to the end of the disc lifetime, when photoevaporation is strongly influencing the disc evolution. Direct photoevaporation causes the disc to be removed more rapidly, and so is more effective at stranding migrating planets at larger orbital radii. Planets that form and migrate in discs with standard photoevaporation are therefore more likely to form hot Jupiters, as indicated in figure 5.8.

5.2.3.3 No photoevaporation

In this set of simulations, I neglect photoevaporation entirely, such that the only processes that can deplete the gas disc are viscous evolution and accretion onto planets, significantly increasing disc lifetimes and the time periods over which migration can occur. I consider only models containing 10 m boulders and 100 m planetesimals.

The early formation and evolution of giant planets is similar to that seen in simulations with photoevaporation. Once a giant planet forms, however, the lack of an effective disc removal mechanism means that it will almost always migrate all the way to becoming a hot Jupiter, as shown by the red line in figure 5.8, where 95% of the giant planets formed are hot Jupiters. The giant planets that remain as cold Jupiters only did so because they formed late in the disc lifetime, where they survived migration by accreting the majority of the remaining gas disc. This ratio of hot Jupiters to cold Jupiters is not consistent with observations, and shows that recreating the observed distributions of giant planets is extremely difficult without a mechanism for disc dispersal.

5.2.4 Evolution as a function of model parameters

I now discuss the effects that varying the model parameters have on the formation and evolution of giant planets in the simulations. Since these effects are consistent across all photoevaporation models employed, I will only discuss the simulations that include direct photoevaporation. Figure 5.9 shows the cumulative distributions for simulated planets as a function of the different parameters considered.

5.2.4.1 Disc mass and metallicity

The simulation results show a strong dependence on the initial mass and metallicity of the disc. Simulations with small disc masses and sub-solar metallicities (e.g. 1×

MMSN and 0.5× solar metallicity) are unable to form any giant planets, due to the quantity of solid material in the disc being insufficient to form a massive planet core capable of accreting a massive gas envelope during the disc life time. Increasing the inventory of solids by increasing the total disc mass, or by increasing the metallicity, leads to the formation of giants. I see from figure 5.9 that the 1× MMSN, 2× solar metallicity runs form moderate numbers of hot Jupiters, with 90% of the giant planets having periods > 100 days. This is for the following reasons: the planet cores form quite late in the disc lifetime; the disc lifetime is shorter than for heavier discs; the low disc mass leads to slower type I migration. Increasing the disc mass and metallicity can be seen to dramatically increase the numbers of hot Jupiters, as planet cores form earlier, type I migration is faster and the disc lifetime is longer. Models with disc mass 2× MMSN and metallicity 2× solar form numerous giant planets, and 80% of these are hot Jupiters.

5.2.4.2 Planetesimal radii

The cumulative distributions for the giant planet orbital periods formed in simulations with different planetesimal radii are shown in the top-right panel of figure 5.9. No giant planets formed in simulations where the planetesimal size was 10 km, in agreement with the very anaemic growth found in chapter 4 for models with 10 km planetesimals. Large planetesimals do not migrate very far through the disc during its lifetime, and the relatively weak damping means that their accretion rate onto planetary embryos remains small because of their large velocity dispersion. Accretion rates are slightly higher for 1 km planetesimals, leading to 12 giant planets forming in these runs. Overall, only $\sim 5\%$ of all giant planets formed do so in simulations with 1 or 10 km sized planetesimals (half of all runs). When the planetesimal radius is decreased to 100 m, or 10 m boulders are considered, then giant planets form easily. In chapter 4 I found that planetary growth is efficient in the presence of small bodies that experience strong gas drag, since they can migrate over large distances (helping growing embryos to exceed their local isolation masses), and maintain a relative modest velocity dispersion due to strong eccentricity and inclination damping. The inclusion of radial structures allows small planetesimals and boulders to concentrate, and growing embryos to avoid rapid inward migration. Hence, the simulations form surviving giant planets with a broad range of orbital periods. Similar numbers of giant planets formed in simulations with 10 m and 100 m small bodies, while their orbital period distribution (i.e. number of hot Jupiters versus cold Jupiters) was also similar, as is shown by the cumulative distributions

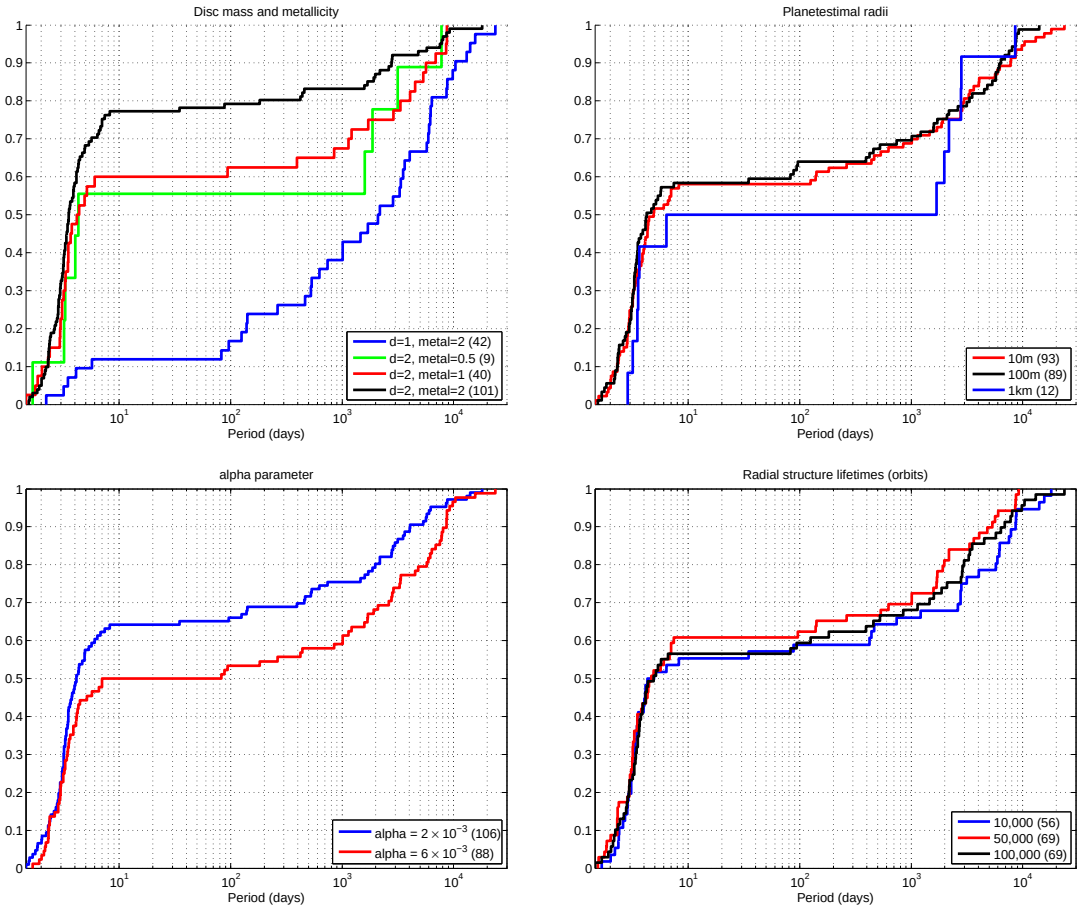

Figure 5.9: Normalised cumulative distributions of simulated giant planets as a function of different parameters. Top-left panel: Disc mass and metallicity. Top-right panel: Planetesimal radii. Bottom-left panel: α parameter. Bottom-right panel: Radial structure lifetimes. Bracketed values represent the number of giant planets in those cumulative distributions. I define a giant planet in both simulations and observations as a planet with mass $m_{\rm p} \geq 100\,{\rm M}_{\oplus}$.

in the top-right panel of figure 5.9.

5.2.4.3 α viscosity

The bottom-left panel of figure 5.9 shows that a lower viscosity (i.e. mass accretion rate through the disc for a given disc mass) gives rise to a larger ratio of hot to cold Jupiters. This is an effect of the shorter disc lifetimes associated with more viscous discs, by approximately 2 Myr in the simulations. A closely related effect is that the numbers of giant planets that form in higher viscosity discs is lower than in lower viscosity discs: 88 formed in the $\alpha = 6 \times 10^{-3}$ runs versus 106 in the $\alpha = 2 \times 10^{-3}$ simulations.

5.2.4.4 Radial structure lifetime

The cumulative distributions of orbital period for runs with different assumed lifetimes for the disc radial structures are shown in the bottom-right panel of figure 5.9. It is clear that varying these lifetimes between 10^4 and 10^5 local orbit periods has very little influence on the results, though the simulations with shorter lifetimes (10^4 orbital periods) did produce fewer giant planets. I therefore expect that shorter lifetimes than those considered in the runs would reduce the numbers of giant planets that form, since more growing cores could escape from the outer disc regions and migrate rapidly into the inner magnetospheric cavity before becoming giants. It is also likely that the mass distribution of the giants would be skewed towards lower masses, and the ratio of hot to cold Jupiters would increase. By decreasing the lifetimes of the radial structures to very short values the results presented in this chapter would eventually converge towards the results presented in chapter 4, where all surviving giant planets were hot Jupiters and had sub-Jovian masses.

5.2.5 Planetary system architectures

I find a diversity in the planetary system architectures arising from the simulations. An ensemble of simulated planetary systems displaying different architectures are shown in figure 5.10, where the different architectures are represented by different simulation label prefixes. Below I describe the different architectures, and the general physical conditions and modes of evolution associated with each of them:

(i) *Low-mass planetary systems* – These form in simulations where protoplanet growth rates are insufficient to form giant planets. In some cases these are compact planetary systems, with similar formation histories to those discussed in chapter 4. The systems with the prefix 'CS' (compact system) in figure 5.10 show the final configurations from these runs, where the lack of massive planets is evident along with their compactness. Generally, these systems arose in metal-poor low-mass discs with small planetesimals/boulders, or in more massive discs with large planetesimals (e.g. $R_{\rm pl} \geq 1$ km).

(ii) *Lonely hot Jupiters* – Systems containing only hot Jupiters formed in massive metal-rich discs. Typically multiple giant planets form in the outer regions of the disc and migrate to become hot Jupiters, where only the last hot Jupiter survives. Often accompanying these hot Jupiters are low-mass planets on long period orbits ($P_{\rm p} \geq 100$d), as shown by systems with prefixes 'HJ' (hot Jupiters) in figure 5.10. From an observational perspective, the low mass and long orbital periods of these companions would make the hot Jupiters appear singular.

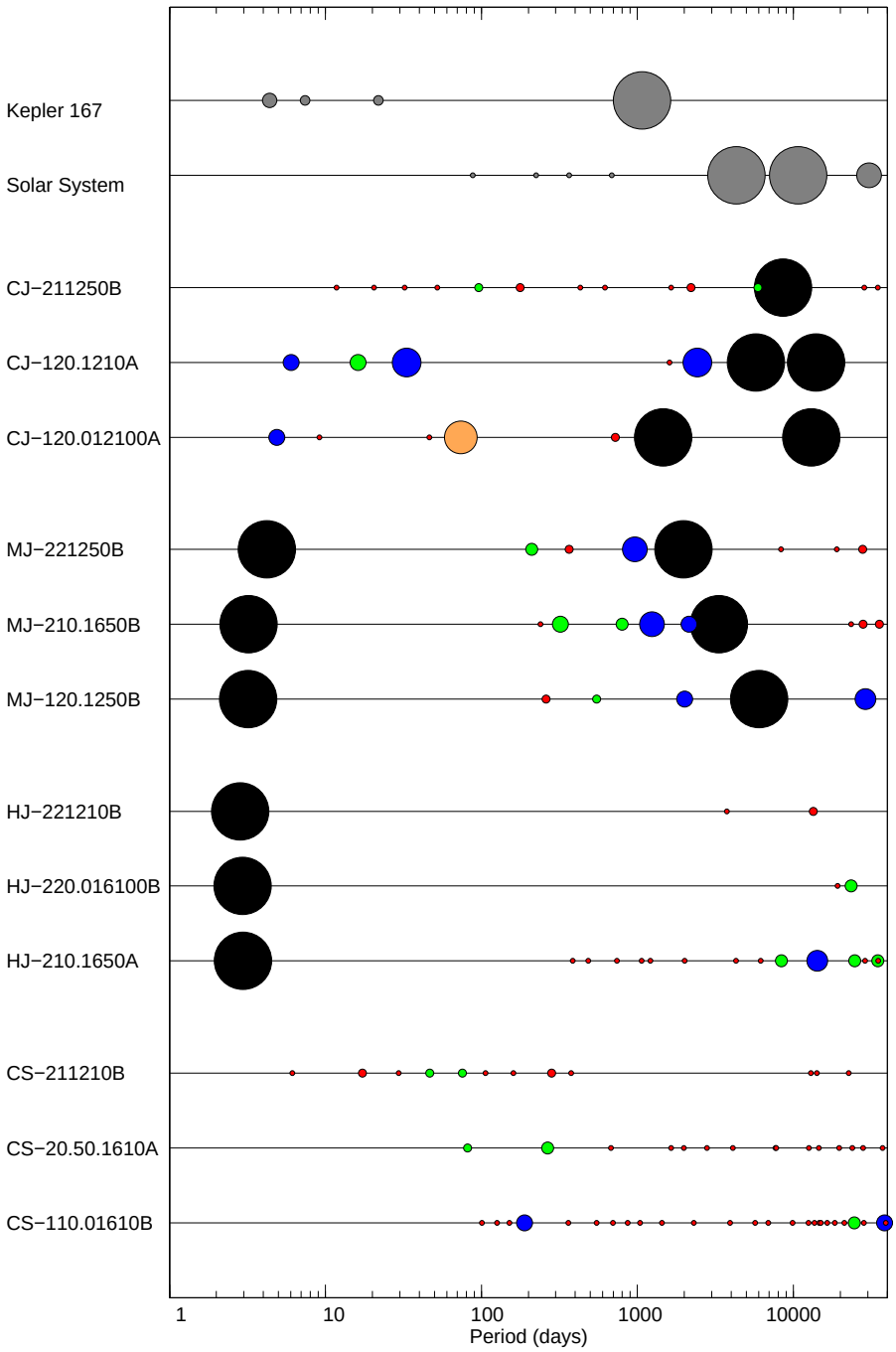

Figure 5.10: Plot comparing different architectures arising from the simulations, with the Solar System and *Kepler-167* included for comparison. Orbital period is indicated on the x-axis and planet masses are indicated by the symbol size (radius scales with the square-root of the planet mass). The symbol colours indicate the classification of each planet: red = Earths ($m_\mathrm{p} < 3\,\mathrm{M}_\oplus$); green = super-Earths ($3\,\mathrm{M}_\oplus \leq m_\mathrm{p} < 10\,\mathrm{M}_\oplus$); blue = Neptunes ($10\,\mathrm{M}_\oplus \leq m_\mathrm{p} < 35\,\mathrm{M}_\oplus$); orange = super-Neptunes ($35\,\mathrm{M}_\oplus \leq m_\mathrm{p} < 100\,\mathrm{M}_\oplus$); black = Jupiters and super-Jupiters ($m_\mathrm{p} > 100\,\mathrm{M}_\oplus$). See table 5.3 for definitions of planet types.

(iii) *Hot Jupiters with cold Jupiter companions* – Similar to the *lonely hot Jupiters*, planetary systems that contain both hot and cold Jupiters tend to arise from solids-rich discs. Hot Jupiters form early in the disc lifetime and migrate close to the central star, whilst late forming giant planets have insufficient time to migrate into the inner system, retaining long orbital periods as cold Jupiters. Typically, lower mass planets are found to occupy the space between the hot and cold Jupiters. Examples of these systems are shown in figure 5.10 by the prefix 'MJ' (multiple Jupiters), showing the diversity in planetary compositions in these systems.
(iv) *Cold Jupiters with low-mass companions* – When there is sufficient solid material in the disc, I find that giant planets can form simultaneously with inner systems of low mass planets. The late formation of giant planets enables them to remain as cold Jupiters at the end of the disc lifetime, whilst interior low-mass planets slowly accrete and migrate into the inner disc regions, becoming an inner system of low-mass planets, occasionally in a compact configuration. This architecture is similar to that found in the Solar System, and I note that recent analysis of *Kepler* light-curves indicates the existence of long period giant planets orbiting stars with known compact low mass systems, similar to the simulated cold Jupiters with short period low mass companions presented in this chapter (Kipping et al., 2016; Uehara et al., 2016). This planetary system architecture is shown by systems with the prefix 'CJ' (cold Jupiters) in figure 5.10.

5.3 Discussion and conclusions

I have presented the results of n-body simulations coupled with prescriptions for planetary migration, accretion of gaseous envelopes, self-consistent evolution of a viscous disc with an inner magnetospheric cavity and disc removal by a photoevaporative wind on multi-Myr time scales. A new addition, not considered in chapters 3 and 4, is radial structuring of the disc due to variations in the viscous stresses, leading to the formation of persistent planet traps at large orbital radii from the star. The main results from this chapter can be summarised as follows:
(i) Radial structuring of the disc allows gas giant planets to form. Protoplanets and planetesimals become trapped at the outer edges of the radial structures, due to strong corotation torques and positive pressure gradients, respectively. Giant planet cores capable of accreting gaseous envelopes are able to form due to efficient accretion of planetesimals/boulders by planetary embryos. Out of 288 simulations,

132 surviving giant planets were formed by having their cores trapped by radial structures. The final periods depend on the time and location of formation, as discussed in section 3.4, where early forming giant planets became hot Jupiters, and late forming giant planets remain as cold Jupiters.

(ii) When analysing the effects of changing specific parameters, the following trends are identified:

– In solid-poor simulations (low disc mass and metallicity) no giant planets are formed, as there is insufficient solid material to form giant planet cores. This is in agreement with the observations of Fischer & Valenti (2005) and Santos et al. (2004), where giant planets are preferentially found around metal-rich stars.

– When the planetesimal radii are large ($\geq$ 1km), giant planets are unable to form except in the most solids-rich environments. Giant planet formation is strongly favoured in models where the primary feedstock of planetary growth is in the form of small 100 m sized planetesimals or 10 m sized boulders. 95% of the giant planets that formed did so in simulations with small boulders/planetesimals. None were formed in models with 10 km planetesimals.

– I find that discs with higher viscosity form fewer giant planets than low viscosity discs, and the ratio of hot to cold Jupiters in higher viscosity discs is smaller than in lower viscosity discs. These effects are entirely due to the shorter disc lifetimes associated with higher viscosity.

(iii) Multiple giant planets are able to form when there is sufficient solid material. This occurred in numerous simulations with high disc masses and metallicities, resulting in systems with multiple cold Jupiters, or a hot Jupiter with cold Jupiter companions. The survival rate of warm Jupiters (those with periods between 10–100 d) also depends on the presence of outer giant companions. Outer giant planet companions can stem the flow of gas into the inner system, reducing the migration rate of planets in the inner system and allowing them to survive at longer periods than if there were no exterior giant planets.

(iv) The simulations reproduce the giant planet period valley between 10 and 100 days that is seen in the observed period distribution of giant planets. Analysis shows that this arises because of the inclusion of disc removal by photoevaporation in the simulations. The launching of a photoevaporative wind causes the disc to empty from the inside out at the end of its lifetime, causing the migration of planets to stall at periods $>$ 100 days, an effect that has been discussed previously by Alexander & Pascucci (2012) and Ercolano & Rosotti (2015).

(v) Simulations do not reproduce the broad eccentricity distribution of the observed giant exoplanets, and this is apparently because the multiple giant planet systems

are too well separated to undergo dynamical instabilities that lead to the formation of eccentric orbits. It is noted, however, that the use of a simple model for damping the eccentricity of gap forming planets in the presence of the gas disc may also bias the simulations towards producing low eccentricity systems. A definitive conclusion about the ability of the models to form a population of eccentric giants can only be made once an improved prescription for this has been implemented. A further point that is worth making is that systems of multiple giant planets form in the simulations when the system metallicity is high (as described above). Assuming that the primary mechanism leading to the observed giant exoplanets attaining their eccentric orbits was dynamical instability in multiplanet systems (possibly on time scales much longer than the formation time scales that I have considered), I note that this (not unexpected) correlation between metallicity and the multiplicity of giant planets that form in the simulations may also explain the positive correlation that exists between eccentricity and stellar metallicity for giant exoplanets discovered by radial velocity surveys[5]. I note that this correlation has also been pointed out by Dawson & Murray-Clay (2013).

(vi) Numerous compact systems of super-Earths and Neptunes were formed in the simulations, with formation histories similar to those discussed in chapter 4. If there was sufficient solid material, long period giant planets also formed in the same simulations as the compact systems of super-Earths/Neptunes.

The simulations presented here show that giant planets can form in discs containing radial structures that act as planet traps, while the combination of magnetospheric cavities and photoevaporative winds creates two populations of giant planets: hot Jupiters and cold Jupiters. It is likely that in more realistic discs, the location, size and evolution of radial structures will be quite different from what has been examined in this chapter. Running a full parameter study on the effects of radial structures in protoplanetary discs, however, goes beyond the scope of this study, which is intended to be a proof of concept rather than an exhaustive survey of parameter space.

[5]This correlation may be seen by plotting eccentricity versus stellar metallicity using the data on radial velocity planets available at exoplanets.org

6 Conclusions and Further Work

The diversity in exoplanets and exoplanetary systems has raised the question of whether a single model of planet formation can explain the diversity, or whether multiple models that operate under different conditions are required. In this thesis I have developed a model of planet formation to investigate what types of planetary systems can emerge from oligarchic growth, and what factors (such as disc mass, metallicity, planetesimal size, disc structuring) these outcomes depend on. The physical model has a comprehensive list of ingredients: planetary embryo growth through boulder/planetesimal accretion and mutual collisions; a 1-D viscous gas model, subject to irradiation from the central star and a photoevaporative wind; type I migration using the most up-to-date prescriptions for Lindblad and corotation torques, including eccentricity and saturation effects; a transition to gap formation and type II migration when gap formation criteria are satisfied; accretion of gaseous envelopes onto solid cores. In chapters 4 and 5, I include further physical prescriptions; an increase in viscosity when the the disc temperature exceed 1000 K, to mimic unquenched MHD turbulence developing in the inner disc; a magnetospheric cavity that creates an inner edge in the gas disc at an orbital period of 4 days; radial structuring of the disc due to variations in the viscous stresses.

The models of planet formation contained in this thesis demonstrate that the traditional understanding of oligarchic growth involving large kilometer sized planetesimals fails to reproduce observed planetary system architectures, unless large disc masses and metallicities are considered. Further research demonstrated that growth with boulders or small planetesimals (≤ 100 m) on intermediate time-scales, comparable to the disc lifetime can lead to the formation of planetary systems similar to those observed. I will now discuss the main results that have arisen from each project undertaken, whilst more complete discussions can be found in the respective chapters of this thesis.

In chapter 3 I explored a range of model parameters including disc mass, metallicity and planetesimal radii to examine their influence on the types of planetary systems that emerge. The results of that study showed that limited planetary growth occurred in low-mas discs (e.g. $\sim 1 \times$ MMSN), whilst multiple generations

of Neptune-mass and giant planets formed and migrated into the central star when the amount of mass in solids was substantially increased (i.e. large disc masses or solids-to-gas-ratios). Few giant planets were able to form in these simulations, since their cores migrated rapidly into the inner disc and on to the central star before they could undergo runaway gas accretion. In some cases, a final generation of super-Earths and Neptune-mass planets were able to form and migrate while the gas disc underwent its final stage of dispersal, allowing these planets to survive. The most massive planet to form in these simulations was $92\,M_{\oplus}$, but migrated into the central star, whilst the most massive surviving planet was a $13\,M_{\oplus}$ gas-rich Neptune. In observing that few giant planets formed in these simulations and that none survived migration, I conducted further research in determining the location that giant planets need to form in order to survive type II migration. I compared 1-D simulations to 2-D hydrodynamic simulations, which allowed me to improve the prescription for runaway gas accretion in the model. When applying this prescription, I found that a planet must initiate runaway gas accretion at an orbital radius $\geq 10\,\text{au}$ in order to survive with characteristics similar to Jupiter. I also found that planets migrate inwards at a faster rate than has been assumed in some population synthesis models (e.g. Mordasini et al., 2009), particularly when in the so-called planet-dominated regime, which explains why these statistical models are more successful at forming giant planets that survive migration and grow to large masses than the models presented in chapter 3. These results showed that improvements were required to the model either through additional physics or improved prescriptions, in order to examine to whether the oligarchic growth picture of planet formation, combined with our best understanding of migration and disc evolution, can generate planetary systems that match those observed.

A number of additions and improvements were included in the physical model in chapter 4. These included: an active turbulent region when disc temperatures exceeded 1000 K; a magnetospheric cavity; and pushing the inner edge of the simulation domain to a period of 1 day. The aim of this project was again to determine the types of planetary systems that emerged from a broader range of parameters to that studied in chapter 3. The results of this study showed three evolution modes of planetary systems. Limited planetary growth occurred when either there was a lack of solid material in the disc, or when planetesimals were large. The lack of planetary growth in these simulations resulted in no planet being more massive than $\sim 3\,M_{\oplus}$ during the gas disc lifetime, whilst only very modest migration occurred. However, with moderate growth rates, through either more massive discs or smaller boulders/planetesimals, multiple planets with super-Earth to Neptune masses were able

to form and undergo large scale migration, typically forming a compact planetary system close to the central star. When the abundance of solids was high and more mobile boulders were used, multiple giant planets with masses $\geq 35\,M_{\oplus}$ were able to form and undergo large scale migration into the magnetospheric cavity, where the last one to arrive pushed the earlier arrivals on to the central star, before residing within the cavity. In considering planetary systems of short-period planets, I identify two distinct architectures arising from these simulations: a combination of terrestrials, super-Earths and low-mass Neptunes, with no planets having migrated into the magnetospheric cavity; a system containing a gas giant or massive Neptune sitting within the magnetospheric cavity, along with an interior terrestrial or super-Earth in some cases, and a number of exterior planets with periods up to 80 days. I find good agreement when comparing simulated planetary system architectures with observed planetary systems, but simulated planets tend to be more closely packed that the observed *Kepler* systems. Mean-motion resonances are common in simulated systems, whilst compact *Kepler* systems do not display mean motion resonances, even though there is evidence for the 2:1 and 3:2 resonances having been dynamically important in the past. These results showed that the model is effective at forming compact systems of planets, as well as planet formation in low-metallicity discs where the lack of giant planets is expected. They do however fail to reproduce the observed giant planet populations, since the cores of the giant planets migrate into the inner regions of the disc before they can undergo runaway gas accretion. This results in only hot Jupiters being able to form, and only in discs with significant solid abundances

In chapter 5, I studied the effects that disc radial structuring had on planet formation, with a specific focus on giant planet formation. I incorporated four radial structures into the protoplanetary disc due to variations in the viscous stresses, leading to the formation of long-lived planet traps at large orbital radii. The results of this project showed that disc radial structuring allows gas giant planets to form and migrate, through having their cores trapped at the outer edges of the radial structures, allowing them to accrete significant gaseous envelopes and undergo runaway gas accretion at large orbital radii. This effect only occurred in discs that had significant planetary growth rates, where either planetesimals were small ($\leq$ 100m), or solid abundances were large. No giant planets were able to form in simulations that used 10km planetesimals, whilst only few formed in simulations with 1km planetesimals. The final masses and orbital periods of the giant planets depended on where and when they formed. Giant planets that formed early in the disc lifetime had sufficient time to migrate close to the central star becoming a hot Jupiter, whilst

those that formed near the end of the disc lifetime, had insufficient time to significantly migrate, and so became cold Jupiters. When looking at the giant planets that formed as a whole, I found two distinct populations, hot Jupiters and cold Jupiters with a dearth of giant planets in between. This bimodal distribution and period valley between 10–100 days is consistent with observed giant planet statistics. I show that the period valley is due to planet migration stalling at periods $\geq$ 100 days, as photoevaporative winds cause the disc to empty from the inside out at the end of the disc lifetime.

Whilst other theories of planet formation attempt to recreate the observed distributions of planets (Bitsch et al., 2015b; Ida et al., 2013; Mordasini et al., 2012), the work presented in this thesis attempted to recreate the observed diversities in planetary system architectures. Observed planetary system architectures ranging from *lonely hot Jupiters* to *low mass compact systems* were able to form in simulations under a range of different conditions. The conditions that led to the formation of these systems can lead to important insights in to how observed planetary systems formed and evolved, as well as indicating whether the observed systems can be considered "complete", such that their main bulk properties have been determined (i.e. the number of giant planets, terrestrial planets, etc). Though the work presented here goes a way to explain the observed diversity in planetary system architectures, it is by no means complete. Further improvements to the model are required to enhance the accuracy and realism currently provided by simple assumptions. Only when the model becomes more sophisticated will it be capable of reproducing all observed planetary system architectures as well as the observed exoplanet distributions and occurrence rates.

In future work I will aim to include the following improvements to the model to improve its realism and accuracy:

(1) Incorporate a more realistic migration model that takes into account 3-D effects (Fung et al., 2015), the influence of planet luminosity (Benítez-Llambay et al., 2015) and dynamical torques arising from the planet's migration (Paardekooper, 2014; Pierens, 2015).

(2) Calculation of a gas envelope accretion using self-consistent calculations that include the effects of changing local disc conditions (Papaloizou & Nelson, 2005), rather than using fits to the Movshovitz et al. (2010) models.

(3) A full collisions and fragmentation model, so that the outcomes of planet-planet and planet-planetesimal collisions can be accurately modelled, instead of the current simple assumption of perfect mergers.

(4) Incorporating fits to MHD simulations so that disc radial structures arising from

zonal flows and transitions between magnetically active and dead zones can be included in a more realistic fashion.
(5) Include sublimation of planetesimals and boulders as they migrate inwards from beyond the snowline.
(6) Include a realistic model for pebble accretion so that the effects of multiple embryos undergoing competitive pebble accretion can be studied.

Other areas of future work that I will focus on will be to examine plant formation around stars of different type. Currently most observations and research into planet formation, including the work in this thesis, have been biased towards solar type stars. However solar type stars only contribute to a small fraction of the total stars in the universe, and as such limiting planet formation theories to only them means that the study is incomplete. Future missions such as *PLATO* (Rauer et al., 2014) and *TESS* (Ricker et al., 2015) will increase the number of observed exoplanets around M dwarfs, which will ultimately require their formation and evolution to be explained. It is only by improving the physical model so that it can apply to stars and planets of all types, will it be possible to explain the formation and evolution of exoplanets already discovered and also those lying in wait.

References

ALMA Partnership , Brogan C. L., Pérez L. M., Hunter T. R., Dent W. R. F., Hales A. S., Hills R. E., Corder S., Fomalont E. B., Vlahakis C., Asaki Y., Barkats D., Hirota A., Hodge J. A., Impellizzeri C. M. V., Kneissl R., Liuzzo E., Lucas R., Marcelino N., Matsushita S., Nakanishi K., Phillips N., Richards A. M. S., Toledo I., Aladro R., Broguiere D., Cortes J. R., Cortes P. C., Espada D., Galarza F., Garcia-Appadoo D., Guzman-Ramirez L., Humphreys E. M., Jung T., Kameno S., Laing R. A., Leon S., Marconi G., Mignano A., Nikolic B., Nyman L.-A., Radiszcz M., Remijan A., Rodón J. A., Sawada T., Takahashi S., Tilanus R. P. J., Vila Vilaro B., Watson L. C., Wiklind T., Akiyama E., Chapillon E., de Gregorio-Monsalvo I., Di Francesco J., Gueth F., Kawamura A., Lee C.-F., Nguyen Luong Q., Mangum J., Pietu V., Sanhueza P., Saigo K., Takakuwa S., Ubach C., van Kempen T., Wootten A., Castro-Carrizo A., Francke H., Gallardo J., Garcia J., Gonzalez S., Hill T., Kaminski T., Kurono Y., Liu H.-Y., Lopez C., Morales F., Plarre K., Schieven G., Testi L., Videla L., Villard E., Andreani P., Hibbard J. E., Tatematsu K. The 2014 ALMA Long Baseline Campaign: First Results from High Angular Resolution Observations toward the HL Tau Region // ApJ Letters. VII 2015. 808. L3. 27, 145

Adachi I., Hayashi C., Nakazawa K. The gas drag effect on the elliptical motion of a solid body in the primordial solar nebula. // Progress of Theoretical Physics. XII 1976. 56. 1756–1771. 43, 104

Adams F. C., Laughlin G., Bloch A. M. Turbulence Implies that Mean Motion Resonances are Rare // ApJ. VIII 2008. 683. 1117–1128. 99, 132, 137

Alexander R. D., Armitage P. J. Dust dynamics during protoplanetary disc clearing // MNRAS. II 2007. 375. 500–512. 86

Alexander R. D., Armitage P. J. Giant Planet Migration, Disk Evolution, and the Origin of Transitional Disks // ApJ. X 2009. 704. 989–1001. 86

Alexander R. D., Pascucci I. Deserts and pile-ups in the distribution of exoplanets due to photoevaporative disc clearing // MNRAS. V 2012. 422. 82–86. 140, 162, 172

Alibert Y., Baraffe I., Benz W., Chabrier G., Mordasini C., Lovis C., Mayor M., Pepe F., Bouchy F., Queloz D., Udry S. Formation and structure of the three Neptune-mass planets system around HD 69830 // A&A. VIII 2006. 455. L25–L28. 99, 141

Alibert Y., Carron F., Fortier A., Pfyffer S., Benz W., Mordasini C., Swoboda D. Theoretical models of planetary system formation: mass vs. semi-major axis // A&A. X 2013. 558. A109. 16

Andrews S. M., Wilner D. J., Zhu Z., Birnstiel T., Carpenter J. M., Pérez L. M., Bai X.-N., Öberg K. I., Hughes A. M., Isella A., Ricci L. Ringed Substructure and a Gap at 1 au in the Nearest Protoplanetary Disk // ApJ Letters. IV 2016. 820. L40. 27, 145

Anglada-Escudé G., Amado P. J., Barnes J., Berdiñas Z. M., Butler R. P., Coleman G. A. L., de La Cueva I., Dreizler S., Endl M., Giesers B., Jeffers S. V., Jenkins J. S., Jones H. R. A., Kiraga M., Kürster M., López-González M. J., Marvin C. J., Morales N., Morin J., Nelson R. P., Ortiz J. L., Ofir A., Paardekooper S.-J., Reiners A., Rodríguez E., Rodríguez-López C., Sarmiento L. F., Strachan J. P., Tsapras Y., Tuomi M., Zechmeister M. A terrestrial planet candidate in a temperate orbit around Proxima Centauri // Nature. VIII 2016. 536. 437–440. 21, 22

Anglada-Escudé G., Arriagada P., Tuomi M., Zechmeister M., Jenkins J. S., Ofir A., Dreizler S., Gerlach E., Marvin C. J., Reiners A., Jeffers S. V., Butler R. P., Vogt S. S., Amado P. J., Rodríguez-López C., Berdiñas Z. M., Morin J., Crane J. D., Shectman S. A., Thompson I. B., Díaz M., Rivera E., Sarmiento L. F., Jones H. R. A. Two planets around Kapteyn's star: a cold and a temperate super-Earth orbiting the nearest halo red dwarf // MNRAS. IX 2014. 443. L89–L93. 99, 138

Anglada-Escudé G., Boss A. P., Weinberger A. J., Thompson I. B., Butler R. P., Vogt S. S., Rivera E. J. Astrometry and Radial Velocities of the Planet Host M Dwarf GJ 317: New Trigonometric Distance, Metallicity, and Upper Limit to the Mass of GJ 317b // ApJ. II 2012. 746. 37. 25

Armitage P. J., Rice W. K. M. Planetary migration // ArXiv Astrophysics e-prints. VII 2005. 55

Bai X.-N., Stone J. M. Magnetic Flux Concentration and Zonal Flows in Magnetorotational Instability Turbulence // ApJ. XI 2014. 796. 31. 139, 146, 147

Balbus S. A., Hawley J. F. A powerful local shear instability in weakly magnetized disks. I - Linear analysis. II - Nonlinear evolution // ApJ. VII 1991. 376. 214–233. 145

Baruteau C., Crida A., Paardekooper S.-J., Masset F., Guilet J., Bitsch B., Nelson R., Kley W., Papaloizou J. Planet-Disk Interactions and Early Evolution of Planetary Systems // Protostars and Planets VI. 2014. 667–689. 46

Baruteau C., Masset F. On the Corotation Torque in a Radiatively Inefficient Disk // ApJ. I 2008. 672. 1054–1067. 50

Baruteau C., Papaloizou J. C. B. Disk-Planets Interactions and the Diversity of Period Ratios in Kepler's Multi-planetary Systems // ApJ. XI 2013. 778. 7. 99, 132

Batalha N. M., Borucki W. J., Bryson S. T., Buchhave L. A., Caldwell D. A., Christensen-Dalsgaard J., Ciardi D., Dunham E. W., Fressin F., Gautier T. N. III, Gilliland R. L., Haas M. R., Howell S. B., Jenkins J. M., Kjeldsen H., Koch D. G., Latham D. W., Lissauer J. J., Marcy G. W., Rowe J. F., Sasselov D. D., Seager S., Steffen J. H., Torres G., Basri G. S., Brown T. M., Charbonneau D., Christiansen J., Clarke B., Cochran W. D., Dupree A., Fabrycky D. C., Fischer D., Ford E. B., Fortney J., Girouard F. R., Holman M. J., Johnson J., Isaacson H., Klaus T. C., Machalek P., Moorehead A. V., Morehead R. C., Ragozzine D., Tenenbaum P., Twicken J., Quinn S., VanCleve J., Walkowicz L. M., Welsh W. F., Devore E., Gould A. Kepler's First Rocky Planet: Kepler-10b // ApJ. III 2011. 729. 27. 13

Bate M. R., Lubow S. H., Ogilvie G. I., Miller K. A. Three-dimensional calculations of high- and low-mass planets embedded in protoplanetary discs // MNRAS. V 2003. 341. 213–229. 90

Beaulieu J.-P., Bennett D. P., Fouqué P., Williams A., Dominik M., Jørgensen U. G., Kubas D., Cassan A., Coutures C., Greenhill J., Hill K., Menzies J., Sackett P. D., Albrow M., Brillant S., Caldwell J. A. R., Calitz J. J., Cook K. H., Corrales E., Desort M., Dieters S., Dominis D., Donatowicz J., Hoffman M., Kane S., Marquette J.-B., Martin R., Meintjes P., Pollard K., Sahu K., Vinter C., Wambsganss J., Woller K., Horne K., Steele I., Bramich D. M., Burgdorf M., Snodgrass C., Bode M., Udalski A., Szymański M. K., Kubiak M., Więckowski T., Pietrzyński G., Soszyński I., Szewczyk O., Wyrzykowski Ł., Paczyński B., Abe F., Bond I. A., Britton T. R., Gilmore A. C., Hearnshaw J. B., Itow Y., Kamiya K., Kilmartin P. M., Korpela A. V., Masuda K., Matsubara Y., Motomura M., Muraki Y., Nakamura S., Okada C., Ohnishi K., Rattenbury N. J., Sako T., Sato S., Sasaki M., Sekiguchi T., Sullivan D. J., Tristram P. J., Yock P. C. M., Yoshioka T. Discovery of a cool planet of 5.5 Earth masses through gravitational microlensing // Nature. I 2006. 439. 437–440. 23

Becker J. C., Vanderburg A., Adams F. C., Rappaport S. A., Schwengeler H. M. WASP-47: A Hot Jupiter System with Two Additional Planets Discovered by K2 // ApJ Letters. X 2015. 812. L18. 14, 141

Bell K. R., Cassen P. M., Klahr H. H., Henning T. The Structure and Appearance of Protostellar Accretion Disks: Limits on Disk Flaring // ApJ. IX 1997. 486. 372–387. 40, 41

Bell K. R., Lin D. N. C. Using FU Orionis outbursts to constrain self-regulated protostellar disk models // ApJ. VI 1994. 427. 987–1004. 41

Benítez-Llambay P., Masset F., Beaugé C. The mass-period distribution of close-in exoplanets // A&A. IV 2011. 528. A2. 102

Benítez-Llambay P., Masset F., Koenigsberger G., Szulágyi J. Planet heating prevents inward migration of planetary cores // Nature. IV 2015. 520. 63–65. 177

Béthune W., Lesur G., Ferreira J. Self-organisation in protoplanetary discs. Global, non-stratified Hall-MHD simulations // A&A. IV 2016. 589. A87. 146

Biller B. A., Liu M. C., Rice K., Wahhaj Z., Nielsen E., Hayward T., Kuchner M. J., Close L. M., Chun M., Ftaclas C., Toomey D. W. The Gemini NICI Planet-Finding Campaign: asymmetries in the HD 141569 disc // MNRAS. VII 2015. 450. 4446–4457. 118

Bitsch B., Johansen A., Lambrechts M., Morbidelli A. The structure of protoplanetary discs around evolving young stars // A&A. III 2015a. 575. A28. 145

Bitsch B., Kley W. Orbital evolution of eccentric planets in radiative discs // A&A. XI 2010. 523. A30. 52

Bitsch B., Kley W. Range of outward migration and influence of the disc's mass on the migration of giant planet cores // A&A. XII 2011. 536. A77. 144, 145

Bitsch B., Lambrechts M., Johansen A. The growth of planets by pebble accretion in evolving protoplanetary discs // A&A. X 2015b. 582. A112. 33, 141, 177

Blum J., Wurm G. The Growth Mechanisms of Macroscopic Bodies in Protoplanetary Disks // Annual Review of Astronomy&Astrophysics. IX 2008. 46. 21–56. 30

Boss A. P. Giant planet formation by gravitational instability. // Science. 1997. 276. 1836–1839. 15, 29

Bryden G., Chen X., Lin D. N. C., Nelson R. P., Papaloizou J. C. B. Tidally Induced Gap Formation in Protostellar Disks: Gap Clearing and Suppression of Protoplanetary Growth // ApJ. III 1999. 514. 344–367. 90

Buchhave L. A., Bizzarro M., Latham D. W., Sasselov D., Cochran W. D., Endl M., Isaacson H., Juncher D., Marcy G. W. Three regimes of extrasolar planet radius inferred from host star metallicities // Nature. V 2014. 509. 593–595. 99, 138

Butler R. P., Marcy G. W., Vogt S. S., Apps K. A Planet with a 3.1 Day Period around a Solar Twin // PASP. XII 1998. 110. 1389–1393. 14

Butler R. P., Marcy G. W., Williams E., Hauser H., Shirts P. Three New "51 Pegasi-Type" Planets // ApJ Letters. I 1997. 474. L115–L118. 13

Cabrera J., Csizmadia S., Lehmann H., Dvorak R., Gandolfi D., Rauer H., Erikson A., Dreyer C., Eigmüller P., Hatzes A. The Planetary System to KIC 11442793: A Compact Analogue to the Solar System // ApJ. I 2014. 781. 18. 14, 19

Campante T. L., Barclay T., Swift J. J., Huber D., Adibekyan V. Z., Cochran W., Burke C. J., Isaacson H., Quintana E. V., Davies G. R., Silva Aguirre V., Ragozzine D., Riddle R., Baranec C., Basu S., Chaplin W. J., Christensen-Dalsgaard J., Metcalfe T. S., Bedding T. R., Handberg R., Stello D., Brewer J. M., Hekker S., Karoff C., Kolbl R., Law N. M., Lundkvist M., Miglio A., Rowe J. F., Santos N. C., Van Laerhoven C., Arentoft T., Elsworth Y. P., Fischer D. A., Kawaler S. D., Kjeldsen H., Lund M. N., Marcy G. W., Sousa S. G., Sozzetti A., White T. R. An Ancient Extrasolar System with Five Sub-Earth-size Planets // ApJ. II 2015. 799. 170. 112, 132, 138

Carter J. A., Agol E., Chaplin W. J., Basu S., Bedding T. R., Buchhave L. A., Christensen-Dalsgaard J., Deck K. M., Elsworth Y., Fabrycky D. C., Ford E. B., Fortney J. J., Hale S. J., Handberg R., Hekker S., Holman M. J., Huber D., Karoff C., Kawaler S. D., Kjeldsen H., Lissauer J. J., Lopez E. D., Lund M. N., Lundkvist M., Metcalfe T. S., Miglio A., Rogers L. A., Stello D., Borucki W. J., Bryson S., Christiansen J. L., Cochran W. D., Geary J. C., Gilliland R. L., Haas M. R., Hall J., Howard A. W., Jenkins J. M., Klaus T., Koch D. G., Latham D. W., MacQueen P. J., Sasselov D., Steffen J. H., Twicken J. D., Winn J. N. Kepler-36: A Pair of Planets with Neighboring Orbits and Dissimilar Densities // Science. VIII 2012. 337. 556–. 15, 99, 132

Casertano S., Lattanzi M. G., Sozzetti A., Spagna A., Jancart S., Morbidelli R., Pannunzio R., Pourbaix D., Queloz D. Double-blind test program for astrometric planet detection with Gaia // A&A. V 2008. 482. 699–729. 25

Cassan A., Kubas D., Beaulieu J.-P., Dominik M., Horne K., Greenhill J., Wambsganss J., Menzies J., Williams A., Jørgensen U. G., Udalski A., Bennett D. P., Albrow M. D., Batista V., Brillant S., Caldwell J. A. R., Cole A., Coutures C., Cook K. H., Dieters S., Prester D. D., Donatowicz J., Fouqué P., Hill K., Kains N., Kane S., Marquette J.-B., Martin R., Pollard K. R., Sahu K. C., Vinter C., Warren D., Watson B., Zub M., Sumi T., Szymański M. K., Kubiak M., Poleski R., Soszynski I., Ulaczyk K., Pietrzyński G., Wyrzykowski Ł. One or more bound planets per Milky Way star from microlensing observations // Nature. I 2012. 481. 167–169. 140

Chambers J. E. A hybrid symplectic integrator that permits close encounters between massive bodies // MNRAS. IV 1999. 304. 793–799. 16, 57, 58, 100, 142

Chambers J. E. Giant planet formation with pebble accretion // Icarus. V 2014. 233. 83–100. 33

Chambers J. E., Wetherill G. W. Making the Terrestrial Planets: N-Body Integrations of Planetary Embryos in Three Dimensions // Icarus. XII 1998. 136. 304–327. 32, 33, 99, 127

Chatterjee S., Ford E. B. Planetesimal Interactions Can Explain the Mysterious Period Ratios of Small Near-Resonant Planets // ApJ. IV 2015. 803. 33. 132

Chatterjee S., Tan J. C. Inside-out Planet Formation // ApJ. I 2014. 780. 53. 33, 100

Chatterjee S., Tan J. C. Vulcan Planets: Inside-out Formation of the Innermost Super-Earths // ApJ Letters. I 2015. 798. L32. 33

Chiang E., Laughlin G. The minimum-mass extrasolar nebula: in situ formation of close-in super-Earths // MNRAS. VI 2013. 431. 3444–3455. 28, 33

Clarke C. J., Gendrin A., Sotomayor M. The dispersal of circumstellar discs: the role of the ultraviolet switch // MNRAS. XII 2001. 328. 485–491. 62, 110

Cochran W. D., Hatzes A. P., Butler R. P., Marcy G. W. The Discovery of a Planetary Companion to 16 Cygni B // ApJ. VII 1997. 483. 457–463. 14

Coleman G. A. L., Nelson R. P. On the formation of planetary systems via oligarchic growth in thermally evolving viscous discs // MNRAS. XI 2014. 445. 479–499. 57, 99, 145

Coleman G. A. L., Nelson R. P. On the formation of compact planetary systems via concurrent core accretion and migration // MNRAS. IV 2016a. 457. 2480–2500. 98, 149

Coleman G. A. L., Nelson R. P. Giant planet formation in radially structured protoplanetary discs // MNRAS. VIII 2016b. 460. 2779–2795. 140

Cossou C., Raymond S. N., Hersant F., Pierens A. Hot super-Earths and giant planet cores from different migration histories // A&A. IX 2014. 569. A56. 35

Cossou C., Raymond S. N., Pierens A. Convergence zones for Type I migration: an inward shift for multiple planet systems // A&A. V 2013. 553. L2. 16, 99, 144, 145

Cox A. N. Allen's astrophysical quantities. 2000. 86

Cresswell P., Nelson R. P. On the evolution of multiple protoplanets embedded in a protostellar disc // A&A. V 2006. 450. 833–853. 99, 129, 132, 137

Cresswell P., Nelson R. P. Three-dimensional simulations of multiple protoplanets embedded in a protostellar disc // A&A. V 2008. 482. 677–690. 53, 54, 99, 132, 137

Crida A., Morbidelli A. Cavity opening by a giant planet in a protoplanetary disc and effects on planetary migration // MNRAS. V 2007. 377. 1324–1336. 90

Crida A., Morbidelli A., Masset F. On the width and shape of gaps in protoplanetary disks // Icarus. IV 2006. 181. 587–604. 54

Csizmadia S., Pasternacki T., Dreyer C., Cabrera J., Erikson A., Rauer H. The effect of stellar limb darkening values on the accuracy of the planet radii derived from photometric transit observations // A&A. I 2013. 549. A9. 20

Cumming A., Butler R. P., Marcy G. W., Vogt S. S., Wright J. T., Fischer D. A. The Keck Planet Search: Detectability and the Minimum Mass and Orbital Period Distribution of Extrasolar Planets // PASP. V 2008. 120. 531–554. 22, 140, 161

D'Angelo G., Kley W., Henning T. Orbital Migration and Mass Accretion of Protoplanets in Three-dimensional Global Computations with Nested Grids // ApJ. III 2003. 586. 540–561. 90

D'Angelo G., Marzari F. Outward Migration of Jupiter and Saturn in Evolved Gaseous Disks // ApJ. IX 2012. 757. 50. 39, 40

Daisaka J. K., Tanaka H., Ida S. Orbital evolution and accretion of protoplanets tidally interacting with a gas disk. II. Solid surface density evolution with type-I migration // Icarus. XII 2006. 185. 492–507. 16, 47, 54

Dawson R. I., Johnson J. A., Fabrycky D. C., Foreman-Mackey D., Murray-Clay R. A., Buchhave L. A., Cargile P. A., Clubb K. I., Fulton B. J., Hebb L., Howard A. W., Huber D., Shporer A., Valenti J. A. Large Eccentricity, Low Mutual Inclination: The Three-dimensional Architecture of a Hierarchical System of Giant Planets // ApJ. VIII 2014. 791. 89. 20

Dawson R. I., Murray-Clay R. A. Giant Planets Orbiting Metal-rich Stars Show Signatures of Planet-Planet Interactions // ApJ Letters. IV 2013. 767. L24. 173

Desch S. J., Turner N. J. High-temperature Ionization in Protoplanetary Disks // ApJ. X 2015. 811. 156. 58, 99, 101

Dipierro G., Price D., Laibe G., Hirsh K., Cerioli A., Lodato G. On planet formation in HL Tau // MNRAS. X 2015. 453. L73–L77. 145

Dittrich K., Klahr H., Johansen A. Gravoturbulent Planetesimal Formation: The Positive Effect of Long-lived Zonal Flows // ApJ. II 2013. 763. 117. 146

Duffell P. C., Haiman Z., MacFadyen A. I., D'Orazio D. J., Farris B. D. The Migration of Gap-opening Planets is Not Locked to Viscous Disk Evolution // ApJ Letters. IX 2014. 792. L10. 143

Dullemond C. P., Hollenbach D., Kamp I., D'Alessio P. Models of the Structure and Evolution of Protoplanetary Disks // Protostars and Planets V. 2007. 555–572. 41

Dürmann C., Kley W. Migration of massive planets in accreting disks // A&A. II 2015. 574. A52. 143

Enoch M. L., Corder S., Dunham M. M., Duchêne G. Disk and Envelope Structure in Class 0 Protostars. I. The Resolved Massive Disk in Serpens Firs 1 // ApJ. XII 2009. 707. 103–113. 26

Ercolano B., Rosotti G. The link between disc dispersal by photoevaporation and the semimajor axis distribution of exoplanets // MNRAS. VII 2015. 450. 3008–3014. 140, 162, 172

Evans N. J. II, Dunham M. M., Jørgensen J. K., Enoch M. L., Merín B., van Dishoeck E. F., Alcalá J. M., Myers P. C., Stapelfeldt K. R., Huard T. L., Allen L. E., Harvey P. M., van Kempen T., Blake G. A., Koerner D. W., Mundy L. G., Padgett D. L., Sargent A. I. The Spitzer c2d Legacy Results: Star-Formation Rates and Efficiencies; Evolution and Lifetimes // ApJS. IV 2009. 181. 321–350. 26

Fabrycky D. C., Lissauer J. J., Ragozzine D., Rowe J. F., Steffen J. H., Agol E., Barclay T., Batalha N., Borucki W., Ciardi D. R., Ford E. B., Gautier T. N., Geary J. C., Holman M. J., Jenkins J. M., Li J., Morehead R. C., Morris R. L., Shporer A., Smith J. C., Still M., Van Cleve J. Architecture of Kepler's Multi-transiting Systems. II. New Investigations with Twice as Many Candidates // ApJ. VIII 2014. 790. 146. 15, 98, 126, 132

Fendyke S. M., Nelson R. P. On the corotation torque for low-mass eccentric planets // MNRAS. I 2014. 437. 96–107. 52, 53

Fischer D. A., Valenti J. The Planet-Metallicity Correlation // ApJ. IV 2005. 622. 1102–1117. 172

Flock M., Ruge J. P., Dzyurkevich N., Henning T., Klahr H., Wolf S. Gaps, rings, and non-axisymmetric structures in protoplanetary disks. From simulations to ALMA observations // A&A. II 2015. 574. A68. 145, 146, 147

Fogg M. J., Nelson R. P. The effect of type I migration on the formation of terrestrial planets in hot-Jupiter systems // A&A. IX 2007. 472. 1003–1015. 16

Fogg M. J., Nelson R. P. Terrestrial planet formation in low-eccentricity warm-Jupiter systems // A&A. V 2009. 498. 575–589. 16, 71

Forgan D., Rice K. Towards a population synthesis model of objects formed by self-gravitating disc fragmentation and tidal downsizing // MNRAS. VII 2013. 432. 3168–3185. 15

Fressin F., Torres G., Charbonneau D., Bryson S. T., Christiansen J., Dressing C. D., Jenkins J. M., Walkowicz L. M., Batalha N. M. The False Positive Rate of Kepler and the Occurrence of Planets // ApJ. IV 2013. 766. 81. 140

Fromang S., Nelson R. P. On the accumulation of solid bodies in global turbulent protoplanetary disc models // MNRAS. XI 2005. 364. L81–L85. 139

Fromang S., Nelson R. P. Global MHD simulations of stratified and turbulent protoplanetary discs. I. Model properties // A&A. X 2006. 457. 343–358. 146

Fung J., Artymowicz P., Wu Y. The 3D Flow Field Around an Embedded Planet // ApJ. X 2015. 811. 101. 177

Gammie C. F. Nonlinear Outcome of Gravitational Instability in Cooling, Gaseous Disks // ApJ. V 2001. 553. 174–183. 30

Gilliland R. L., Marcy G. W., Rowe J. F., Rogers L., Torres G., Fressin F., Lopez E. D., Buchhave L. A., Christensen-Dalsgaard J., Désert J.-M., Henze C. E., Isaacson H., Jenkins J. M., Lissauer J. J., Chaplin W. J., Basu S., Metcalfe T. S., Elsworth Y., Handberg R., Hekker S., Huber D., Karoff C., Kjeldsen H., Lund M. N., Lundkvist M., Miglio A., Charbonneau D., Ford E. B., Fortney J. J., Haas M. R., Howard A. W., Howell S. B., Ragozzine D., Thompson S. E. Kepler-68: Three Planets, One with a Density between that of Earth and Ice Giants // ApJ. III 2013. 766. 40. 14

Goldreich P., Schlichting H. E. Overstable Librations can Account for the Paucity of Mean Motion Resonances among Exoplanet Pairs // AJ. II 2014. 147. 32. 99, 132

Goldreich P., Tremaine S. The excitation of density waves at the Lindblad and corotation resonances by an external potential // ApJ. XI 1979. 233. 857–871. 47, 48

Gould A., Dong S., Gaudi B. S., Udalski A., Bond I. A., Greenhill J., Street R. A., Dominik M., Sumi T., Szymański M. K., Han C., Allen W., Bolt G., Bos M., Christie G. W., DePoy D. L., Drummond J., Eastman J. D., Gal-Yam A., Higgins D., Janczak J., Kaspi S., Kozłowski S., Lee C.-U., Mallia F., Maury A., Maoz D., McCormick J., Monard L. A. G., Moorhouse D., Morgan N., Natusch T., Ofek E. O., Park B.-G., Pogge R. W., Polishook D., Santallo R., Shporer A., Spector O., Thornley G., Yee J. C., μFUN Collaboration , Kubiak M., Pietrzyński G., Soszyński I., Szewczyk O., Wyrzykowski Ł., Ulaczyk K., Poleski R., OGLE Collaboration , Abe F., Bennett D. P., Botzler C. S., Douchin D., Freeman M., Fukui A., Furusawa K., Hearnshaw J. B., Hosaka S., Itow Y., Kamiya K., Kilmartin P. M., Korpela A., Lin W., Ling C. H., Makita S., Masuda K., Matsubara Y., Miyake N., Muraki Y., Nagaya M., Nishimoto K., Ohnishi K., Okumura T., Perrott Y. C., Philpott L., Rattenbury N., Saito T., Sako T., Sullivan D. J., Sweatman W. L., Tristram P. J., von Seggern E., Yock P. C. M., MOA Collaboration , Albrow M., Batista V., Beaulieu J. P., Brillant S., Caldwell J., Calitz J. J., Cassan A., Cole A., Cook K., Coutures C., Dieters S., Dominis Prester D., Donatowicz J., Fouqué P., Hill K., Hoffman M., Jablonski F., Kane S. R., Kains N., Kubas D., Marquette J.-B., Martin R., Martioli E., Meintjes P., Menzies J., Pedretti E., Pollard K., Sahu K. C., Vinter C., Wambsganss J., Watson R., Williams A., Zub M., PLANET Collaboration , Allan A., Bode M. F., Bramich D. M., Burgdorf M. J., Clay N., Fraser S., Hawkins E., Horne K., Kerins E., Lister T. A., Mottram C., Saunders E. S., Snodgrass C., Steele I. A., Tsapras Y., RoboNet Collaboration , Jørgensen U. G., Anguita T., Bozza V., Calchi Novati S., Harpsøe K., Hinse T. C., Hundertmark M., Kjærgaard P., Liebig C., Mancini L., Masi G., Mathiasen M., Rahvar S., Ricci D., Scarpetta G., Southworth J., Surdej J., Thöne C. C., MiNDSTEp Consortium . Frequency of Solar-like Sys-

tems and of Ice and Gas Giants Beyond the Snow Line from High-magnification Microlensing Events in 2005-2008 // ApJ. IX 2010. 720. 1073–1089. 126

Gradie J., Tedesco E. Compositional structure of the asteroid belt // Science. VI 1982. 216. 1405–1407. 29

Gressel O., Nelson R. P., Turner N. J., Ziegler U. Global Hydromagnetic Simulations of a Planet Embedded in a Dead Zone: Gap Opening, Gas Accretion, and Formation of a Protoplanetary Jet // ApJ. XII 2013. 779. 59. 90

Han E., Wang S. X., Wright J. T., Feng Y. K., Zhao M., Fakhouri O., Brown J. I., Hancock C. Exoplanet Orbit Database. II. Updates to Exoplanets.org // PASP. X 2014. 126. 827–837. 13, 14, 18, 19, 126, 130, 140, 161

Hands T. O., Alexander R. D., Dehnen W. Understanding the assembly of Kepler's compact planetary systems // MNRAS. XI 2014. 445. 749–760. 99

Hansen B. M. S., Murray N. Migration Then Assembly: Formation of Neptune-mass Planets inside 1 AU // ApJ. VI 2012. 751. 158. 99, 100

Hasegawa Y., Pudritz R. E. The origin of planetary system architectures - I. Multiple planet traps in gaseous discs // MNRAS. X 2011. 417. 1236–1259. 140

Hayashi C. Structure of the Solar Nebula, Growth and Decay of Magnetic Fields and Effects of Magnetic and Turbulent Viscosities on the Nebula // Progress of Theoretical Physics Supplement. 1981. 70. 35–53. 27, 28, 29, 34, 59, 107, 154

Hellary P., Nelson R. P. Global models of planetary system formation in radiatively-inefficient protoplanetary discs // MNRAS. II 2012. 419. 2737–2757. 16, 35, 42, 58, 59, 62, 99, 103, 107, 144, 145, 154

Helled R., Bodenheimer P., Podolak M., Boley A., Meru F., Nayakshin S., Fortney J. J., Mayer L., Alibert Y., Boss A. P. Giant Planet Formation, Evolution, and Internal Structure // Protostars and Planets VI. 2014. 643–665. 30

Hellier C., Anderson D. R., Collier Cameron A., Doyle A. P., Fumel A., Gillon M., Jehin E., Lendl M., Maxted P. F. L., Pepe F., Pollacco D., Queloz D., Ségransan D., Smalley B., Smith A. M. S., Southworth J., Triaud A. H. M. J., Udry S., West R. G. Seven transiting hot Jupiters from WASP-South, Euler and TRAPPIST: WASP-47b, WASP-55b, WASP-61b, WASP-62b, WASP-63b, WASP-66b and WASP-67b // MNRAS. X 2012. 426. 739–750. 14

Herbst W., Mundt R. Rotational Evolution of Solar-like Stars in Clusters from Pre-Main Sequence to Main Sequence: Empirical Results // ApJ. XI 2005. 633. 967–985. 101

Howell S. B., Sobeck C., Haas M., Still M., Barclay T., Mullally F., Troeltzsch J., Aigrain S., Bryson S. T., Caldwell D., Chaplin W. J., Cochran W. D., Huber D., Marcy G. W., Miglio A., Najita J. R., Smith M., Twicken J. D., Fortney J. J.

The K2 Mission: Characterization and Early Results // PASP. IV 2014. 126. 398–408. 14

Hubeny I. Vertical structure of accretion disks - A simplified analytical model // ApJ. III 1990. 351. 632–641. 40

Huber D., Silva Aguirre V., Matthews J. M., Pinsonneault M. H., Gaidos E., García R. A., Hekker S., Mathur S., Mosser B., Torres G., Bastien F. A., Basu S., Bedding T. R., Chaplin W. J., Demory B.-O., Fleming S. W., Guo Z., Mann A. W., Rowe J. F., Serenelli A. M., Smith M. A., Stello D. Revised Stellar Properties of Kepler Targets for the Quarter 1-16 Transit Detection Run // ApJS. III 2014. 211. 2. 164

Hubickyj O., Bodenheimer P., Lissauer J. J. Accretion of the gaseous envelope of Jupiter around a 5 10 Earth-mass core // Icarus. XII 2005. 179. 415–431. 15

IAU . Final results of NameExoWorlds public vote released. 2015. Accessed: 2016-04-24. 13

Ida S., Lin D. N. C. Toward a Deterministic Model of Planetary Formation. II. The Formation and Retention of Gas Giant Planets around Stars with a Range of Metallicities // ApJ. XI 2004. 616. 567–572. 141

Ida S., Lin D. N. C. Toward a Deterministic Model of Planetary Formation. V. Accumulation Near the Ice Line and Super-Earths // ApJ. IX 2008. 685. 584–595. 47

Ida S., Lin D. N. C. Toward a Deterministic Model of Planetary Formation. VI. Dynamical Interaction and Coagulation of Multiple Rocky Embryos and Super-Earth Systems around Solar-type Stars // ApJ. VIII 2010. 719. 810–830. 16, 99

Ida S., Lin D. N. C., Nagasawa M. Toward a Deterministic Model of Planetary Formation. VII. Eccentricity Distribution of Gas Giants // ApJ. IX 2013. 775. 42. 16, 177

Ida S., Makino J. Scattering of planetesimals by a protoplanet - Slowing down of runaway growth // Icarus. XI 1993. 106. 210. 127

Inaba S., Ikoma M. Enhanced collisional growth of a protoplanet that has an atmosphere // A&A. XI 2003. 410. 711–723. 44, 45

Johansen A., Oishi J. S., Mac Low M.-M., Klahr H., Henning T., Youdin A. Rapid planetesimal formation in turbulent circumstellar disks // Nature. VIII 2007. 448. 1022–1025. 31

Johansen A., Youdin A., Klahr H. Zonal Flows and Long-lived Axisymmetric Pressure Bumps in Magnetorotational Turbulence // ApJ. VI 2009a. 697. 1269–1289. 139

Johansen A., Youdin A., Mac Low M.-M. Particle Clumping and Planetesimal Formation Depend Strongly on Metallicity // ApJ Letters. X 2009b. 704. L75–L79. 139, 146

Jones H. R. A., Butler R. P., Tinney C. G., Marcy G. W., Penny A. J., McCarthy C., Carter B. D. An exoplanet in orbit around τ^1 Gruis // MNRAS. V 2003. 341. 948–952. 140

Jontof-Hutter D., Rowe J. F., Lissauer J. J., Fabrycky D. C., Ford E. B. The mass of the Mars-sized exoplanet Kepler-138 b from transit timing // Nature. VI 2015. 522. 321–323. 15, 98

Kasting J. F., Whitmire D. P., Reynolds R. T. Habitable Zones around Main Sequence Stars // Icarus. I 1993. 101. 108–128. 83, 127, 160

Kelling T., Wurm G., Köster M. Experimental Study on Bouncing Barriers in Protoplanetary Disks // ApJ. III 2014. 783. 111. 31

Kipping D. M., Torres G., Buchhave L. A., Kenyon S. J., Henze C., Isaacson H., Kolbl R., Marcy G. W., Bryson S. T., Stassun K., Bastien F. Discovery of a Transiting Planet near the Snow-line // ApJ. XI 2014. 795. 25. 19

Kipping D. M., Torres G., Henze C., Teachey A., Isaacson H., Petigura E., Marcy G. W., Buchhave L. A., Chen J., Bryson S. T., Sandford E. A Transiting Jupiter Analog // ApJ. IV 2016. 820. 112. 162, 171

Kley W. Mass flow and accretion through gaps in accretion discs // MNRAS. III 1999. 303. 696–710. 89, 90

Kokubo E., Ida S. Oligarchic Growth of Protoplanets // Icarus. I 1998. 131. 171–178. 31

Lagrange A.-M., Gratadour D., Chauvin G., Fusco T., Ehrenreich D., Mouillet D., Rousset G., Rouan D., Allard F., Gendron É., Charton J., Mugnier L., Rabou P., Montri J., Lacombe F. A probable giant planet imaged in the β Pictoris disk. VLT/NaCo deep L'-band imaging // A&A. I 2009. 493. L21–L25. 14

Lambrechts M., Johansen A. Rapid growth of gas-giant cores by pebble accretion // A&A. VIII 2012. 544. A32. 139

Lambrechts M., Johansen A., Morbidelli A. Separating gas-giant and ice-giant planets by halting pebble accretion // A&A. XII 2014. 572. A35. 33

Lammer H., Stökl A., Erkaev N. V., Dorfi E. A., Odert P., Güdel M., Kulikov Y. N., Kislyakova K. G., Leitzinger M. Origin and loss of nebula-captured hydrogen envelopes from 'sub'- to 'super-Earths' in the habitable zone of Sun-like stars // MNRAS. IV 2014. 439. 3225–3238. 66

Léger A., Rouan D., Schneider J., Barge P., Fridlund M., Samuel B., Ollivier M., Guenther E., Deleuil M., Deeg H. J., Auvergne M., Alonso R., Aigrain S., Alapini A., Almenara J. M., Baglin A., Barbieri M., Bruntt H., Bordé P., Bouchy F., Cabrera J., Catala C., Carone L., Carpano S., Csizmadia S., Dvorak R., Erikson A., Ferraz-Mello S., Foing B., Fressin F., Gandolfi D., Gillon M., Gondoin P., Grasset O., Guillot T., Hatzes A., Hébrard G., Jorda L., Lammer H., Llebaria A., Loeillet B., Mayor M., Mazeh T., Moutou C., Pätzold M., Pont F., Queloz D., Rauer H., Renner S., Samadi R., Shporer A., Sotin C., Tingley B., Wuchterl G., Adda M., Agogu P., Appourchaux T., Ballans H., Baron P., Beaufort T., Bellenger R., Berlin R., Bernardi P., Blouin D., Baudin F., Bodin P., Boisnard L., Boit L., Bonneau F., Borzeix S., Briet R., Buey J.-T., Butler B., Cailleau D., Cautain R., Chabaud P.-Y., Chaintreuil S., Chiavassa F., Costes V., Cuna Parrho V., de Oliveira Fialho F., Decaudin M., Defise J.-M., Djalal S., Epstein G., Exil G.-E., Fauré C., Fenouillet T., Gaboriaud A., Gallic A., Gamet P., Gavalda P., Grolleau E., Gruneisen R., Gueguen L., Guis V., Guivarc'h V., Guterman P., Hallouard D., Hasiba J., Heuripeau F., Huntzinger G., Hustaix H., Imad C., Imbert C., Johlander B., Jouret M., Journoud P., Karioty F., Kerjean L., Lafaille V., Lafond L., Lam-Trong T., Landiech P., Lapeyrere V., Larqué T., Laudet P., Lautier N., Lecann H., Lefevre L., Leruyet B., Levacher P., Magnan A., Mazy E., Mertens F., Mesnager J.-M., Meunier J.-C., Michel J.-P., Monjoin W., Naudet D., Nguyen-Kim K., Orcesi J.-L., Ottacher H., Perez R., Peter G., Plasson P., Plesseria J.-Y., Pontet B., Pradines A., Quentin C., Reynaud J.-L., Rolland G., Rollenhagen F., Romagnan R., Russ N., Schmidt R., Schwartz N., Sebbag I., Sedes G., Smit H., Steller M. B., Sunter W., Surace C., Tello M., Tiphène D., Toulouse P., Ulmer B., Vandermarcq O., Vergnault E., Vuillemin A., Zanatta P. Transiting exoplanets from the CoRoT space mission. VIII. CoRoT-7b: the first super-Earth with measured radius // A&A. X 2009. 506. 287–302. 13

Levison H. F., Kretke K. A., Duncan M. J. Growing the gas-giant planets by the gradual accumulation of pebbles // Nature. VIII 2015a. 524. 322–324. 33, 141

Levison H. F., Kretke K. A., Walsh K. J., Bottke W. F. Growing the terrestrial planets from the gradual accumulation of sub-meter sized objects // Proceedings of the National Academy of Science. XI 2015b. 112. 14180–14185. 33

Lin D. N. C., Bodenheimer P., Richardson D. C. Orbital migration of the planetary companion of 51 Pegasi to its present location // Nature. IV 1996. 380. 606–607. 101

Lin D. N. C., Papaloizou J. On the tidal interaction between protoplanets and the protoplanetary disk. III - Orbital migration of protoplanets // ApJ. X 1986. 309. 846–857. 17, 54, 143

Lissauer J. J. Urey prize lecture: On the diversity of plausible planetary systems // Icarus. IV 1995. 114. 217–236. 32

Lissauer J. J., Fabrycky D. C., Ford E. B., Borucki W. J., Fressin F., Marcy G. W., Orosz J. A., Rowe J. F., Torres G., Welsh W. F., Batalha N. M., Bryson S. T., Buchhave L. A., Caldwell D. A., Carter J. A., Charbonneau D., Christiansen J. L., Cochran W. D., Desert J.-M., Dunham E. W., Fanelli M. N., Fortney J. J., Gautier T. N. III, Geary J. C., Gilliland R. L., Haas M. R., Hall J. R., Holman M. J., Koch D. G., Latham D. W., Lopez E., McCauliff S., Miller N., Morehead R. C., Quintana E. V., Ragozzine D., Sasselov D., Short D. R., Steffen J. H. A closely packed system of low-mass, low-density planets transiting Kepler-11 // Nature. II 2011. 470. 53–58. 15, 19, 20, 98, 141

Lodders K. Solar System Abundances and Condensation Temperatures of the Elements // ApJ. VII 2003. 591. 1220–1247. 29

Louden T., Wheatley P. J. Spatially Resolved Eastward Winds and Rotation of HD 189733b // ApJ Letters. XII 2015. 814. L24. 20

Lovis C., Mayor M., Pepe F., Alibert Y., Benz W., Bouchy F., Correia A. C. M., Laskar J., Mordasini C., Queloz D., Santos N. C., Udry S., Bertaux J.-L., Sivan J.-P. An extrasolar planetary system with three Neptune-mass planets // Nature. V 2006. 441. 305–309. 99

Lubow S. H., Seibert M., Artymowicz P. Disk Accretion onto High-Mass Planets // ApJ. XII 1999. 526. 1001–1012. 90

Lynden-Bell D., Pringle J. E. The evolution of viscous discs and the origin of the nebular variables. // MNRAS. IX 1974. 168. 603–637. 141

Lyra W., Johansen A., Zsom A., Klahr H., Piskunov N. Planet formation bursts at the borders of the dead zone in 2D numerical simulations of circumstellar disks // A&A. IV 2009. 497. 869–888. 139

Marcy G. W., Weiss L. M., Petigura E. A., Isaacson H., Howard A. W., Buchhave L. A. Occurrence and core-envelope structure of 1-4x Earth-size planets around Sun-like stars // Proceedings of the National Academy of Science. IX 2014. 111. 12655–12660. 15, 98

Marois C., Macintosh B., Barman T., Zuckerman B., Song I., Patience J., Lafrenière D., Doyon R. Direct Imaging of Multiple Planets Orbiting the Star HR 8799 // Science. XI 2008. 322. 1348–. 14, 25

Marzari F., Weidenschilling S. J. Eccentric Extrasolar Planets: The Jumping Jupiter Model // Icarus. IV 2002. 156. 570–579. 163

Masset F., Snellgrove M. Reversing type II migration: resonance trapping of a lighter giant protoplanet // MNRAS. II 2001. 320. L55–L59. 97

Masset F. S., Morbidelli A., Crida A., Ferreira J. Disk Surface Density Transitions as Protoplanet Traps // ApJ. V 2006. 642. 478–487. 17, 110, 141, 145

Matsuo T., Shibai H., Ootsubo T., Tamura M. Planetary Formation Scenarios Revisited: Core-Accretion versus Disk Instability // ApJ. VI 2007. 662. 1282–1292. 30

Mayor M., Marmier M., Lovis C., Udry S., Ségransan D., Pepe F., Benz W., Bertaux J. ., Bouchy F., Dumusque X., Lo Curto G., Mordasini C., Queloz D., Santos N. C. The HARPS search for southern extra-solar planets XXXIV. Occurrence, mass distribution and orbital properties of super-Earths and Neptune-mass planets // ArXiv e-prints. IX 2011. 98, 126

Mayor M., Queloz D. A Jupiter-mass companion to a solar-type star // Nature. XI 1995. 378. 355–359. 13, 22, 140

Mayor M., Udry S., Naef D., Pepe F., Queloz D., Santos N. C., Burnet M. The CORALIE survey for southern extra-solar planets. XII. Orbital solutions for 16 extra-solar planets discovered with CORALIE // A&A. II 2004. 415. 391–402. 13

McLaughlin D. B. Some results of a spectrographic study of the Algol system. // ApJ. VII 1924. 60. 20

McNeil D., Duncan M., Levison H. F. Effects of Type I Migration on Terrestrial Planet Formation // AJ. XII 2005. 130. 2884–2899. 16

McNeil D. S., Nelson R. P. New methods for large dynamic range problems in planetary formation // MNRAS. I 2009. 392. 537–552. 16, 99

McNeil D. S., Nelson R. P. On the formation of hot Neptunes and super-Earths // MNRAS. I 2010. 401. 1691–1708. 16, 99

Menou K., Goodman J. Low-Mass Protoplanet Migration in T Tauri α-Disks // ApJ. V 2004. 606. 520–531. 39

Miguel Y., Guilera O. M., Brunini A. The role of the initial surface density profiles of the disc on giant planet formation: comparing with observations // MNRAS. IV 2011a. 412. 2113–2124. 16

Miguel Y., Guilera O. M., Brunini A. The diversity of planetary system architectures: contrasting theory with observations // MNRAS. X 2011b. 417. 314–332. 16

Mihalas D., Mihalas B. W. Foundations of radiation hydrodynamics. 1984. 39

Morbidelli A., Tsiganis K., Crida A., Levison H. F., Gomes R. Dynamics of the Giant Planets of the Solar System in the Gaseous Protoplanetary Disk and Their Relationship to the Current Orbital Architecture // AJ. XI 2007. 134. 1790–1798. 97

Mordasini C., Alibert Y., Benz W. Extrasolar planet population synthesis. I. Method, formation tracks, and mass-distance distribution // A&A. VII 2009. 501. 1139–1160. 16, 47, 93, 96, 141, 144, 175

Mordasini C., Alibert Y., Benz W., Klahr H., Henning T. Extrasolar planet population synthesis . IV. Correlations with disk metallicity, mass, and lifetime // A&A. V 2012. 541. A97. 16, 177

Mortier A., Faria J. P., Santos N. C., Rajpaul V., Figueira P., Boisse I., Collier Cameron A., Dumusque X., Lo Curto G., Lovis C., Mayor M., Melo C., Pepe F., Queloz D., Santerne A., Ségransan D., Sousa S. G., Sozzetti A., Udry S. The HARPS search for southern extra-solar planets. XXXIX. HD 175607, the most metal-poor G dwarf with an orbiting sub-Neptune // A&A. I 2016. 585. A135. 138

Movshovitz N., Bodenheimer P., Podolak M., Lissauer J. J. Formation of Jupiter using opacities based on detailed grain physics // Icarus. X 2010. 209. 616–624. 32, 42, 85, 90, 103, 143, 153, 177

Muirhead P. S., Johnson J. A., Apps K., Carter J. A., Morton T. D., Fabrycky D. C., Pineda J. S., Bottom M., Rojas-Ayala B., Schlawin E., Hamren K., Covey K. R., Crepp J. R., Stassun K. G., Pepper J., Hebb L., Kirby E. N., Howard A. W., Isaacson H. T., Marcy G. W., Levitan D., Diaz-Santos T., Armus L., Lloyd J. P. Characterizing the Cool KOIs. III. KOI 961: A Small Star with Large Proper Motion and Three Small Planets // ApJ. III 2012. 747. 144. 112, 138, 141

Mullally F., Coughlin J. L., Thompson S. E., Rowe J., Burke C., Latham D. W., Batalha N. M., Bryson S. T., Christiansen J., Henze C. E., Ofir A., Quarles B., Shporer A., Van Eylen V., Van Laerhoven C., Shah Y., Wolfgang A., Chaplin W. J., Xie J.-W., Akeson R., Argabright V., Bachtell E., Barclay T., Borucki W. J., Caldwell D. A., Campbell J. R., Catanzarite J. H., Cochran W. D., Duren R. M., Fleming S. W., Fraquelli D., Girouard F. R., Haas M. R., Helminiak K. G., Howell S. B., Huber D., Larson K., Gautier T. N. III, Jenkins J. M., Li J., Lissauer J. J., McArthur S., Miller C., Morris R. L., Patil-Sabale A., Plavchan P., Putnam D., Quintana E. V., Ramirez S., Silva Aguirre V., Seader S., Smith J. C., Steffen J. H., Stewart C., Stober J., Still M., Tenenbaum P., Troeltzsch J., Twicken J. D., Zamudio K. A. Planetary Candidates Observed by Kepler. VI. Planet Sample from Q1–Q16 (47 Months) // ApJS. IV 2015. 217. 31. 98, 126

Nayakshin S. Tidal downsizing model - I. Numerical methods: saving giant planets from tidal disruptions // MNRAS. XI 2015. 454. 64–82. 30, 141

Nelson R. P. On the orbital evolution of low mass protoplanets in turbulent, magnetised disks // A&A. XII 2005. 443. 1067–1085. 137

Nelson R. P., Papaloizou J. C. B. The interaction of giant planets with a disc with MHD turbulence - IV. Migration rates of embedded protoplanets // MNRAS. V 2004. 350. 849–864. 137

Nelson R. P., Papaloizou J. C. B., Masset F., Kley W. The migration and growth of protoplanets in protostellar discs // MNRAS. X 2000. 318. 18–36. 85, 89, 90

Neveu-VanMalle M., Queloz D., Anderson D. R., Brown D. J. A., Collier Cameron A., Delrez L., Díaz R. F., Gillon M., Hellier C., Jehin E., Lister T., Pepe F., Rojo P., Ségransan D., Triaud A. H. M. J., Turner O. D., Udry S. Hot Jupiters with relatives: discovery of additional planets in orbit around WASP-41 and WASP-47 // A&A. II 2016. 586. A93. 14, 141

Okuzumi S., Momose M., Sirono S.-i., Kobayashi H., Tanaka H. Sintering-induced Dust Ring Formation in Protoplanetary Disks: Application to the HL Tau Disk // ApJ. IV 2016. 821. 82. 145

Ormel C. W., Klahr H. H. The effect of gas drag on the growth of protoplanets. Analytical expressions for the accretion of small bodies in laminar disks // A&A. IX 2010. 520. A43. 139

Owen J. E., Jackson A. P. Planetary evaporation by UV & X-ray radiation: basic hydrodynamics // MNRAS. X 2012. 425. 2931–2947. 128

Paardekooper S.-J. Dynamical corotation torques on low-mass planets // MNRAS. XI 2014. 444. 2031–2042. 177

Paardekooper S.-J., Baruteau C., Crida A., Kley W. A torque formula for non-isothermal type I planetary migration - I. Unsaturated horseshoe drag // MNRAS. I 2010. 401. 1950–1964. 48, 50, 143, 152

Paardekooper S.-J., Baruteau C., Kley W. A torque formula for non-isothermal Type I planetary migration - II. Effects of diffusion // MNRAS. I 2011. 410. 293–303. 17, 50, 51, 52, 141, 143

Paardekooper S.-J., Mellema G. Halting type I planet migration in non-isothermal disks // A&A. XI 2006. 459. L17–L20. 48, 50

Paardekooper S.-J., Papaloizou J. C. B. On disc protoplanet interactions in a non-barotropic disc with thermal diffusion // A&A. VII 2008. 485. 877–895. 50

Paardekooper S.-J., Papaloizou J. C. B. On corotation torques, horseshoe drag and the possibility of sustained stalled or outward protoplanetary migration // MNRAS. IV 2009a. 394. 2283–2296. 49

Paardekooper S.-J., Papaloizou J. C. B. On the width and shape of the corotation region for low-mass planets // MNRAS. IV 2009b. 394. 2297–2309. 49

Paardekooper S.-J., Rein H., Kley W. The formation of systems with closely spaced low-mass planets and the application to Kepler-36 // MNRAS. X 2013. 434. 3018–3029. 132

Papaloizou J. C. B., Larwood J. D. On the orbital evolution and growth of protoplanets embedded in a gaseous disc // MNRAS. VII 2000. 315. 823–833. 15

Papaloizou J. C. B., Nelson R. P. The interaction of a giant planet with a disc with MHD turbulence - I. The initial turbulent disc models // MNRAS. III 2003. 339. 983–992. 146

Papaloizou J. C. B., Nelson R. P. Models of accreting gas giant protoplanets in protostellar disks // A&A. IV 2005. 433. 247–265. 177

Perryman M., Hartman J., Bakos G. Á., Lindegren L. Astrometric Exoplanet Detection with Gaia // ApJ. XII 2014. 797. 14. 25

Picogna G., Kley W. How do giant planetary cores shape the dust disk?. HL Tauri system // A&A. XII 2015. 584. A110. 145

Pierens A. Fast migration of low-mass planets in radiative discs // MNRAS. XII 2015. 454. 2003–2014. 177

Pierens A., Cossou C., Raymond S. N. Making giant planet cores: convergent migration and growth of planetary embryos in non-isothermal discs // A&A. X 2013. 558. A105. 16

Pierens A., Nelson R. P. On the migration of protoplanets embedded in circumbinary disks // A&A. IX 2007. 472. 993–1001. 101

Pinilla P., Birnstiel T., Ricci L., Dullemond C. P., Uribe A. L., Testi L., Natta A. Trapping dust particles in the outer regions of protoplanetary disks // A&A. II 2012. 538. A114. 145

Podlewska-Gaca E., Papaloizou J. C. B., Szuszkiewicz E. Outward migration of a super-Earth in a disc with outward propagating density waves excited by a giant planet // MNRAS. IV 2012. 421. 1736–1756. 99

Podolak M., Podolak J. I., Marley M. S. Further investigations of random models of Uranus and Neptune // Planetary and Space Science. II 2000. 48. 143–151. 79

Pollack J. B., Hubickyj O., Bodenheimer P., Lissauer J. J., Podolak M., Greenzweig Y. Formation of the Giant Planets by Concurrent Accretion of Solids and Gas // Icarus. XI 1996. 124. 62–85. 15, 32, 42, 90

Press William H., Teukolsky Saul A., Vetterling William T., Flannery Brian P. Numerical Recipes 3rd Edition: The Art of Scientific Computing. New York, NY, USA: Cambridge University Press, 2007. 3. 40

Pu B., Wu Y. Spacing of Kepler Planets: Sculpting by Dynamical Instability // ApJ. VII 2015. 807. 44. 133, 136

Rasio F. A., Ford E. B. Dynamical instabilities and the formation of extrasolar planetary systems // Science. XI 1996. 274. 954–956. 141, 162

Rauer H., Catala C., Aerts C., Appourchaux T., Benz W., Brandeker A., Christensen-Dalsgaard J., Deleuil M., Gizon L., Goupil M.-J., Güdel M., Janot-Pacheco E., Mas-Hesse M., Pagano I., Piotto G., Pollacco D., Santos Ċ., Smith A., Suárez J.-C., Szabó R., Udry S., Adibekyan V., Alibert Y., Almenara J.-M., Amaro-Seoane P., Eiff M. A.-v., Asplund M., Antonello E., Barnes S., Baudin F., Belkacem K., Bergemann M., Bihain G., Birch A. C., Bonfils X., Boisse I., Bonomo A. S., Borsa F., Brandão I. M., Brocato E., Brun S., Burleigh M., Burston R., Cabrera J., Cassisi S., Chaplin W., Charpinet S., Chiappini C., Church R. P., Csizmadia S., Cunha M., Damasso M., Davies M. B., Deeg H. J., Díaz R. F., Dreizler S., Dreyer C., Eggenberger P., Ehrenreich D., Eigmüller P., Erikson A., Farmer R., Feltzing S., de Oliveira Fialho F., Figueira P., Forveille T., Fridlund M., García R. A., Giommi P., Giuffrida G., Godolt M., Gomes da Silva J., Granzer T., Grenfell J. L., Grotsch-Noels A., Günther E., Haswell C. A., Hatzes A. P., Hébrard G., Hekker S., Helled R., Heng K., Jenkins J. M., Johansen A., Khodachenko M. L., Kislyakova K. G., Kley W., Kolb U., Krivova N., Kupka F., Lammer H., Lanza A. F., Lebreton Y., Magrin D., Marcos-Arenal P., Marrese P. M., Marques J. P., Martins J., Mathis S., Mathur S., Messina S., Miglio A., Montalban J., Montalto M., Monteiro M. J. P. F. G., Moradi H., Moravveji E., Mordasini C., Morel T., Mortier A., Nascimbeni V., Nelson R. P., Nielsen M. B., Noack L., Norton A. J., Ofir A., Oshagh M., Ouazzani R.-M., Pápics P., Parro V. C., Petit P., Plez B., Poretti E., Quirrenbach A., Ragazzoni R., Raimondo G., Rainer M., Reese D. R., Redmer R., Reffert S., Rojas-Ayala B., Roxburgh I. W., Salmon S., Santerne A., Schneider J., Schou J., Schuh S., Schunker H., Silva-Valio A., Silvotti R., Skillen I., Snellen I., Sohl F., Sousa S. G., Sozzetti A., Stello D., Strassmeier K. G., Švanda M., Szabó G. M., Tkachenko A., Valencia D., Van Grootel V., Vauclair S. D., Ventura P., Wagner F. W., Walton N. A., Weingrill J., Werner S. C., Wheatley P. J., Zwintz K. The PLATO 2.0 mission // Experimental Astronomy. XI 2014. 38. 249–330. 84, 178

Raymond S. N., Cossou C. No universal minimum-mass extrasolar nebula: evidence against in situ accretion of systems of hot super-Earths // MNRAS. V 2014. 440. L11–L15. 28

Rein H. Period ratios in multiplanetary systems discovered by Kepler are consistent with planet migration // MNRAS. XI 2012. 427. L21–L24. 99

Rein H., Papaloizou J. C. B. On the evolution of mean motion resonances through stochastic forcing: fast and slow libration modes and the origin of HD 128311 // A&A. IV 2009. 497. 595–609. 99, 132, 137

Ricker G. R., Winn J. N., Vanderspek R., Latham D. W., Bakos G. Á., Bean J. L., Berta-Thompson Z. K., Brown T. M., Buchhave L., Butler N. R., Butler R. P., Chaplin W. J., Charbonneau D., Christensen-Dalsgaard J., Clampin M., Deming D., Doty J., De Lee N., Dressing C., Dunham E. W., Endl M., Fressin F., Ge J., Henning T., Holman M. J., Howard A. W., Ida S., Jenkins J. M., Jernigan G., Johnson J. A., Kaltenegger L., Kawai N., Kjeldsen H., Laughlin G., Levine

A. M., Lin D., Lissauer J. J., MacQueen P., Marcy G., McCullough P. R., Morton T. D., Narita N., Paegert M., Palle E., Pepe F., Pepper J., Quirrenbach A., Rinehart S. A., Sasselov D., Sato B., Seager S., Sozzetti A., Stassun K. G., Sullivan P., Szentgyorgyi A., Torres G., Udry S., Villasenor J. Transiting Exoplanet Survey Satellite (TESS) // Journal of Astronomical Telescopes, Instruments, and Systems. I 2015. 1, 1. 014003. 178

Rossiter R. A. On the detection of an effect of rotation during eclipse in the velocity of the brigher component of beta Lyrae, and on the constancy of velocity of this system. // ApJ. VII 1924. 60. 20

Santerne A., Moutou C., Tsantaki M., Bouchy F., Hébrard G., Adibekyan V., Almenara J.-M., Amard L., Barros S. C. C., Boisse I., Bonomo A. S., Bruno G., Courcol B., Deleuil M., Demangeon O., Díaz R. F., Guillot T., Havel M., Montagnier G., Rajpurohit A. S., Rey J., Santos N. C. SOPHIE velocimetry of Kepler transit candidates. XVII. The physical properties of giant exoplanets within 400 days of period // A&A. III 2016. 587. A64. 140, 161

Santos N. C., Israelian G., Mayor M. Spectroscopic [Fe/H] for 98 extra-solar planet-host stars. Exploring the probability of planet formation // A&A. III 2004. 415. 1153–1166. 22, 172

Seager S., Mallén-Ornelas G. A Unique Solution of Planet and Star Parameters from an Extrasolar Planet Transit Light Curve // ApJ. III 2003. 585. 1038–1055. 19

Shakura N. I., Sunyaev R. A. Black holes in binary systems. Observational appearance. // A&A. 1973. 24. 337–355. 35, 55, 141

Simon J. B., Beckwith K., Armitage P. J. Emergent mesoscale phenomena in magnetized accretion disc turbulence // MNRAS. V 2012. 422. 2685–2700. 146

Sousa S. G., Santos N. C., Mayor M., Udry S., Casagrande L., Israelian G., Pepe F., Queloz D., Monteiro M. J. P. F. G. Spectroscopic parameters for 451 stars in the HARPS GTO planet search program. Stellar [Fe/H] and the frequency of exo-Neptunes // A&A. VIII 2008. 487. 373–381. 164

Stamatellos D., Whitworth A. P. Can giant planets form by gravitational fragmentation of discs?. // A&A. III 2008. 480. 879–887. 15, 29

Steffen J. H., Ford E. B., Rowe J. F., Fabrycky D. C., Holman M. J., Welsh W. F., Batalha N. M., Borucki W. J., Bryson S., Caldwell D. A., Ciardi D. R., Jenkins J. M., Kjeldsen H., Koch D. G., Prša A., Sanderfer D. T., Seader S., Twicken J. D. Transit Timing Observations from Kepler. VI. Potentially Interesting Candidate Systems from Fourier-based Statistical Tests // ApJ. IX 2012. 756. 186. 15, 98, 132

Steinacker A., Papaloizou J. C. B. Three-dimensional Magnetohydrodynamic Simulations of an Accretion Disk with Star-Disk Boundary Layer // ApJ. V 2002. 571. 413–428. 146

Szulágyi J., Morbidelli A., Crida A., Masset F. Accretion of Jupiter-mass Planets in the Limit of Vanishing Viscosity // ApJ. II 2014. 782. 65. 90

Tanaka H., Takeuchi T., Ward W. R. Three-Dimensional Interaction between a Planet and an Isothermal Gaseous Disk. I. Corotation and Lindblad Torques and Planet Migration // ApJ. II 2002. 565. 1257–1274. 48

Terquem C., Papaloizou J. C. B. Migration and the Formation of Systems of Hot Super-Earths and Neptunes // ApJ. I 2007. 654. 1110–1120. 16, 99, 132

Teyssandier J., Owen J. E., Adams F. C., Quillen A. C. Torque on an exoplanet from an anisotropic evaporative wind // MNRAS. IX 2015. 452. 1743–1753. 128

Thommes E. W., Duncan M. J., Levison H. F. Oligarchic growth of giant planets // Icarus. II 2003. 161. 431–455. 32, 34

Udry S., Bonfils X., Delfosse X., Forveille T., Mayor M., Perrier C., Bouchy F., Lovis C., Pepe F., Queloz D., Bertaux J.-L. The HARPS search for southern extra-solar planets. XI. Super-Earths (5 and $8M_{\oplus}$) in a 3-planet system // A&A. VII 2007. 469. L43–L47. 99, 138

Udry S., Mayor M., Santos N. C. Statistical properties of exoplanets. I. The period distribution: Constraints for the migration scenario // A&A. VIII 2003. 407. 369–376. 140, 161

Uehara S., Kawahara H., Masuda K., Yamada S., Aizawa M. Transiting Planet Candidates Beyond the Snow Line Detected by Visual Inspection of 7557 Kepler Objects of Interest // ApJ. V 2016. 822. 2. 15, 162, 171

Umebayashi T., Nakano T. Chapter 13. Ionization State and Magnetic Fields in the Solar Nebula // Progress of Theoretical Physics Supplement. 1988. 96. 151–160. 58, 99, 101, 132

Ward W. R. Horsehoe Orbit Drag // Lunar and Planetary Science Conference. 22. III 1991. (Lunar and Planetary Inst. Technical Report). 49

Weidenschilling S. J. Aerodynamics of solid bodies in the solar nebula // MNRAS. VII 1977. 180. 57–70. 104, 105

Weidenschilling S. J. Formation of Planetesimals and Accretion of the Terrestrial Planets // Space Science Reviews. IV 2000. 92. 295–310. 31

Williams J. P., Cieza L. A. Protoplanetary Disks and Their Evolution // Annual Review of Astronomy&Astrophysics. IX 2011. 49. 67–117. 26

Wolszczan A., Frail D. A. A planetary system around the millisecond pulsar PSR1257 + 12 // Nature. I 1992. 355. 145–147. 13, 24

Wright J. T., Gaudi B. S. Exoplanet Detection Methods // Planets, Stars and Stellar Systems. Volume 3: Solar and Stellar Planetary Systems. 2013. 489. 17

Wright J. T., Upadhyay S., Marcy G. W., Fischer D. A., Ford E. B., Johnson J. A. Ten New and Updated Multiplanet Systems and a Survey of Exoplanetary Systems // ApJ. III 2009. 693. 1084–1099. 14

Wu Y., Lithwick Y. Density and Eccentricity of Kepler Planets // ApJ. VII 2013. 772. 74. 15, 98

Wyatt M. C. Evolution of Debris Disks // Annual Review of Astronomy&Astrophysics. IX 2008. 46. 339–383. 26

Zhang K., Bergin E. A., Blake G. A., Cleeves L. I., Hogerheijde M., Salinas V., Schwarz K. R. On the Commonality of 10-30 AU Sized Axisymmetric Dust Structures in Protoplanetary Disks // ApJ Letters. II 2016. 818. L16. 27, 146

Zhang K., Blake G. A., Bergin E. A. Evidence of Fast Pebble Growth Near Condensation Fronts in the HL Tau Protoplanetary Disk // ApJ Letters. VI 2015. 806. L7. 145

Zhu Z., Stone J. M., Rafikov R. R., Bai X.-n. Particle Concentration at Planet-induced Gap Edges and Vortices. I. Inviscid Three-dimensional Hydro Disks // ApJ. IV 2014. 785. 122. 146

Ziegler U., Yorke H. W. A nested grid refinement technique for magnetohydrodynamical flows // Computer Physics Communications. IV 1997. 101. 54–74. 89

Zsom A., Ormel C. W., Güttler C., Blum J., Dullemond C. P. The outcome of protoplanetary dust growth: pebbles, boulders, or planetesimals? II. Introducing the bouncing barrier // A&A. IV 2010. 513. A57. 31